Summer 1994

# Investigation of Wall Injectors for Supersonic Mixing Enhancement

Yaacov Haimovitch
*Old Dominion University*

# INVESTIGATION OF WALL INJECTORS FOR SUPERSONIC MIXING ENHANCEMENT

by

Yaacov Haimovitch
B. Sc. ( 1979 ), and M. Sc. ( 1981 ) – Aeronautical Engineering
Technion - Israel Institute of Technology, Haifa, Israel

A Thesis submitted to the Faculty of
Old Dominion University in Partial Fulfillment of the
Requirement for the Degree of

DOCTOR OF PHILOSOPHY

MECHANICAL ENGINEERING

OLD DOMINION UNIVERSITY
August, 1994

Approved by :

A. Sidney Roberts, Jr. (Director)

E. Gartenberg

G. B. Northam

S. Tiwari

O. Baysal

# ABSTRACT

## INVESTIGATION OF WALL INJECTORS FOR SUPERSONIC MIXING ENHANCEMENT

Yaacov Haimovitch
Old Dominion University, 1994
Director: Dr. A. Sidney Roberts, Jr.

A comparative study of the interaction between wall mounted swept-ramp injectors and injector nozzle shape has been conducted in a constant area duct to explore techniques to enhance mixing in scramjet combustors. The scramjet combustors are currently being developed for propulsion systems applications on the envisioned hypersonic vehicles. Short combustor residence time, a requirement for fuel injection parallel to the main flow in the combustor, and an overall strong sensitivity of the vehicle performance to the propulsion system motivated the investigation. The swept-ramp injector investigated in this study produces vortex shedding and local separation downstream of the injector's nozzle exit, at the ramp's base. Six different injector nozzle inserts for preconditioning the fuel flow were tested to explore the interaction between the preconditioned fuel jet and the vortical flowfield produced by the ramp. The six injector nozzle inserts were : circular nozzle (baseline), nozzle with three downstream facing steps in the divergent section, nozzle with four vortex generators, elliptical nozzle, tapered-slot nozzle, and trapezoidal nozzle, all having equal exit and

throat areas. The main flow was air at Mach 2, and the fuel was simulated by air injected at Mach 1.63 and by helium injected at Mach 1.7 . The main portion of the research involved a series of experiments conducted at the NASA Langley Research Center in the Mach 2 Traverse Jet Facility. Extensive flow field surveys, combined with Mie and Rayleigh scattering visualization were used to investigate the flow field. An existing three-dimensional Navier-Stokes code was used to conduct a numerical study which closely tracked the experimental effort. The injector perfomance was evaluated in terms of both the experimental and computational results. The different nozzle inserts showed only minor performance differences, indicating that the injectant/air mixing in the far-field is independent of the injector geometry, molecular weight of the injectant, and the initial convective Mach number. However, the nozzle with vortex generators displayed the highest mixing performance, and there is evidence that the tapered-slot nozzle has a promising mixing performance. In the vicinity of the ramp base, the flow is dominated by the strong vortical flow field generated by the swept-ramp while well downstream of the base ramp the quasi-axisymmetric flow pattern indicates a "loss of memory" of the near-field stirring, the flow being controlled by small-scale turbulence. The flow field characteristics (mixing and losses) of this mixing scheme are determined by the ramp, the injector inner geometry having a very little effect. The injectant penetration into the main flow at an average angle that is equal to the initial injection angle, suggests that the penetration can be controlled by changing the injection angle.

# ACKNOWLEDGEMENTS

Foremost I would like to express my love and gratitude to my family, especially to my wife Simona, for her patience, loving support, and sacrifices. Their love and encouragement provided me the ability to successfully complete this research.

Looking back at the wonderful time I had during my study program, it is a pleasant duty to acknowledge many people for their support and assistance in this research. First of all, I would like to express my gratitude to Dr. G. Burton Northam from Hypersonic Airbreathing Propulsion Branch, Gas Dynamic Division, for his support, advice, encouragement, and continuous care throughout this research. I would like to extent special thanks to my advisors, Drs. A. Sidney Roberts, Jr., and Ehud Gartenberg, for initiating this research, for the guidance and assistance they provided in performing this research, and for making my life at ODU and NASA very pleasant. Many thanks to Mr. Griffin Y. Anderson, Head of Hypersonic Airbreathing Propulsion Branch, Gas Dynamic Division, for making this research possible and for his continuous support. I am grateful to Dr. Andrew D. Cutler for his assistance regarding the visualization experiments, to Dr. Dean R. Eklund for the many patient discussions and advice regarding the computational work, and to Ms. Donna K. Kraus for her assistance with the experiments. Also, I greatly appreciate the willingness of all the members of the Experimental Methods Branch, Fluid Mechanics Division, without exception, to help and provide advice, and for their encouragement.

Conducting experimental research would not have been possible without help from many members of the technical staff at NASA Langley Research Center. To Mr. Clinton J. Reese, many thanks for his dedicated technical support.

This research was funded through NASA Grants NAS1-18584 Task 114, and NAS1-19858 Task 4, with Old Dominion University Research Foundation. Dr. G. Burton Northam was the grant technical monitor.

# TABLE OF CONTENTS

# LIST OF TABLES

# LIST OF FIGURES

**FIGURE** **PAGE**

# NOMENCLATURE

A = area

a = speed of sound

B = two-dimensional array representing a background image

$\mathbf{b_i}$ = body force vector of $i^{th}$ species

c = constant in turbulence model, Eq. 3.30

$C_p$ = specific heat at constant pressure

$C_{p,i}$ = mass constant pressure specific heat of $i^{th}$ species

$\hat{C}_{p,i}$ = molar constant pressure specific heat of $i^{th}$ species

d = diameter (in general) or jet diameter

$Da$ = Damköhler number

$\mathcal{D}$ = binary diffusion coefficient

$\mathcal{D}_{ij}$ = binary diffusion coefficient of $i^{th}$ and $j^{th}$ species

$D_i^T$ = thermal diffusion coefficient of $i^{th}$ species

E = two-dimensional array representing a processed image

$\mathbf{E}$ = flux of conserved variables in x-direction

F = two-dimensional array representing a flat-field image

$\mathbf{F}$ = flux of conserved variables in y-direction

G = flux of conserved variables in z-direction

H = the non-homogeneous term in Navier-Stokes equation

h = ramp's base height

$h_i$ = enthalpy of $i^{th}$ species

$h_i^R$ = reference enthalpy of $i^{th}$ species

I = two-dimensional array representing an image

$\hat{\mathbf{i}}$ = unit vector in x-direction

$\hat{\mathbf{j}}$ = unit vector in y-direction

$\hat{\mathbf{k}}$ = unit vector in z-direction

Kn = Knudsen number

l = length

L = length or turbulent length scale

$\dot{m}$ = mass flow rate

M = Mach number

$M_C$ = convective Mach number

$M_R$ = relative Mach number

$M_\infty$ = freestream Mach number

$\mathcal{M}_i$ = molecular weight of $i^{th}$ species

$\overline{\mathcal{M}}$ = injectant to freestream molecular weight ratio

N = number of points or number density

n = refractive index

$n_i$ = number of moles of $i^{th}$ species

$N_S$ = number of chemical species

p = static pressure

$P_t$ = total pressure

$P_0$ = stagnation pressure

$p_\infty$ = freestream static pressure

$\bar{p}$ = injectant to freestream static pressure ratio

Pr = Prandtl number

$q_x$ = heat flux in the x-direction

$q_y$ = heat flux in the y-direction

$q_z$ = heat flux in the z-direction

R = mixture gas constant

Re = Reynolds number

$R_i$ = gas constant of $i^{th}$ species

$R_u$ = Universal gas constant

Sc = Schmidt number

s = specific entropy

t = time

T = static temperature

$T_0$ = stagnation temperature

$T^R$ = reference temperature = 298 K

$\overline{T}$ = injectant to freestream static temperature ratio

U = velocity

$U_C$ = convective velocity

$\mathbf{U}$ = vector of conserved variables

$\mathbf{u}$ = velocity vector

u = velocity component in x-direction

$\tilde{\mathbf{u}}_i$ = diffusion velocity vector of $i^{th}$ species

$\tilde{u}_i$ = diffusion velocity of $i^{th}$ species in x-direction

v = velocity component in y-direction

$\tilde{v}_i$ = diffusion velocity of $i^{th}$ species in y-direction

$\overline{v}$ = injectant to freestream velocity ratio

$V$ = volume

$V_i$ = volume of $i^{th}$ species

w = velocity component in z-direction

$\tilde{w}_i$ = diffusion velocity of $i^{th}$ species in z-direction

x = streamwise, axial coordinate

$\overline{x}$ = non-dimensional distance downstream of injector plane, = x/h

$X_i$ = mole fraction of $i^{th}$ species

Y = mass fraction

$Y_i$ = mass fraction of $i^{th}$ species

y = cross-stream coordinate

$\overline{y}$ = non-dimensional cross-flow coordinate, = y/h

z = vertical coordinate

$\overline{z}$ = non-dimensional vertical coordinate, = z/h

## Greek Symbols

$\beta$ = shock angle

$\gamma$ = ratio of specific heats for gas mixture

$\gamma_i$ = ratio of specific heats for $i^{th}$ species

$\delta$ = shear layer width

$\overline{\delta}, \delta_2$ = central-difference operators

$\epsilon$ = total specific energy (internal and kinetic)

$\eta$ = efficiency

$\theta$ = cone half angle

$\kappa$ = coefficient of thermal conductivity

$\lambda$ = second viscosity coefficient or wavelength

$\lambda_B$ = Batchelor's scale ( diffusion microscale )

$\lambda_{mfp}$ = mean free path

$\mu$ = coefficient of dynamic viscosity

$\nu$ = coefficient of kinematic viscosity

$\xi$ = average depth of penetration of molecule due to diffusion

$\rho$ = density

$\overline{\rho}$ = injectant to freestream density ratio

$\sigma$ = scattering cross-section

$\sigma_x$ = normal stress in the x-direction

$\sigma_y$ = normal stress in the y-direction

$\sigma_z$ = normal stress in the z-direction

$\tau_B$ = Batchelor's time scale

$\tau_{xy}$ = shear stress in xy plane

$\tau_{xz}$ = shear stress in xz plane

$\tau_{yz}$ = shear stress in yz plane

$\phi$ = equivalence ratio

$\Omega$ = solid angle (steradian)

$\vec{\omega}$ = vorticity vector

$\dot{\omega}_i$ = production rate of $i^{th}$ species

## Subscripts

$C$ = convective

$c$ = calculated

gas = gas phase

$l$ = laminar

liq = liquid

$m$ = measured

mix = mixture

$p$ = particle

$r$ = recovery

$t$ = turbulent or partial derivative with respect to time

$x$ = x-direction or partial derivative with respect to x

$y$ = y-direction or partial derivative with respect to y

$z$ = z-direction or partial derivative with respect to z

0 = stagnation

1 = primary stream

2 = secondary stream

$\infty$ = freestream

### Superscripts

* = predicted value, also sonic throat in a nozzle

R = reference

### Abbreviations

A-to-D = Analog to Digital

CCD = Charge Coupled Device

CTE = Charge Transfer Efficiency

func = function ( in general )

KD*P = Potassium di-Deuterium Phosphate ( $KD_2PO_4$ )

LAF = Line Adjacency Fill algorithm

| | |
|---|---|
| LDV | = Laser Doppler Velocimeter |
| LHS | = Left Hand Side |
| Nd:YAG | = Neodymium : Yttrium Aluminum Garnet |
| PC | = Personal Computer |
| RHS | = Right Hand Side |
| RMS | = Root Mean Square |
| SNR | = Signal to Noise Ratio |
| STP | = Standard Temperature Pressure |
| scramjet | = Supersonic Combustion Ram Jet |
| UV | = Ultra Violet |

# Chapter 1

# INTRODUCTION

## 1.1 Motivation

The study of mixing enhancement of high speed flows has received considerable attention in the recent years in relation to the current effort to develop a single-stage-to-orbit ( SSTO ) hypersonic vehicle. Such hypersonic aircraft could be an alternative to low-orbit rocket launchers. Table 1.1 presents a comparison between a typical aircraft and a conventional rocket launcher. This table reveals that the oxygen represents most of the takeoff weight of rockets. Moreover, the large

Table 1.1 Typical takeoff weight fraction breakdowns

from Heiser et al.[1] p.16

| Takeoff Weight Fraction | Aircraft | Rocket |
|---|---|---|
| Payload | 0.15 | 0.04 |
| Empty | 0.55 | 0.07 |
| Fuel | 0.30 | 0.24 |
| Oxygen | 0.00 | 0.65 |

oxygen fraction comes at the expense of the payload and the empty weight, which

includes structure, tankage, power, controls, propulsion system, and life support systems. The alternative is a vehicle which relies primarily on airbreathing propulsion, and operates as an ordinary aircraft. The weight saved by using air would be used, as in ordinary aircraft, to increase payload as well as to make the aircraft smaller. Another important characteristic of a such vehicle is the reusability and the possibility to include life saving systems into the aircraft. Furthermore, aircrafts need no special ( and very expensive ) launching facilities — existing airfields may be used, allowing quick reaction and turnaround. In order to further reduce the takeoff weight, cryogenic hydrogen would be the fuel of choice, because of its high combustion specific energy, and because its potential to provide vitally needed cooling by its very low storage temperature and high specific heat.

The main propulsion system of a trans-atmospheric vehicle will be based on ramjet / scramjet propulsion. Ramjets are the engines of choice for flight in the Mach number range 3 – 6. In a ramjet engine the air flow is decelerated to subsonic speed, the combustion takes place in subsonic flow, after which the hot flow is accelerated to supersonic speed and finally exhausts into the atmosphere. When the flight Mach number exceeds about six, it is no longer advantageous to decelerate the flow to subsonic speed. The adverse consequences include pressure too high for the combustor structure, excessive wall heat transfer rates, high total pressure losses caused by strong shocks, and thermal energy losses to chemical dissociation. To minimize these problems, the oncoming air is not decelerated to subsonic speed, resulting in supersonic flow in the combustor. This engine is known as the supersonic-combustion-ramjet, or in short, a scramjet. Typical design requirements point to combustor flow Mach numbers between two and eight[2]. Consequently, the time available for the mixing of the hydrogen with the air is greatly reduced compared to a conventional subsonic

combustor. For example, a typical aircraft flying at Mach 15, may have the air in the combustor at Mach 5 with a velocity of about 4000 m/s. Given the fact that the combustion chamber can be only a few meters long, the residence time of the air within the combustor is of the order of 1 ms. Thus, the mixing between the air and the hydrogen must proceed very rapidly.

An additional concern over the mixing is caused by the very low growth rates of the shear-layers, which form between the fuel and the air. Experiments have shown that the growth rate and the turbulence levels in a supersonic mixing layer are significantly reduced as compared with the subsonic mixing layer[3,4]. Hence, the mixing caused by the shear of the flow is less than that in a conventional subsonic combustor. The problem is aggravated by the requirement that a major component of the injectant flow vector be directed parallel to the freestream to alleviate losses, and to derive as much thrust from the momentum of the fuel jet as possible[2]. All of these facts generate the need for mechanisms to augment the mixing process.

In conclusion, following takeoff, the vehicle must climb and accelerate rapidly to a speed where the principal propulsion system, a scramjet, takes over. Through much of its flight envelope, the aircraft will be propelled by the scramjet engines relying on hydrogen-air combustion. The overall performance of the vehicle will be very sensitive to the scramjet engine operation. Clearly, providing rapid and efficient mixing in the combustor is essential to a successful scramjet engine design, and therefore to a successful aircraft. However, such mixing can be achieved only by devising mixing enhancement techniques, which is the primary motivation for the present study of supersonic mixing.

## 1.2 Fuel-Air Mixing

This section presents a literature survey of supersonic mixing and of mixing enhancement techniques.

### 1.2.1 Basic Definitions

Gas-phase chemical reactions occur by the exchange of atoms between molecules as a result of molecular collisions. Consequently, fuel and air must be mixed to stoichiometric proportions at the molecular level before combustion can take place. Two fluids can be mixed to a very fine macroscopic scale, but still not to a molecular level. Such a mixture is called a bulk mixture, or a macromixture. A mixture which is homogeneous at the molecular level is called a micromixture. In steady state mixing the initial stirring or macromixing is called *near-field mixing*, and the subsequent molecular diffusion or micromixing is called *far-field mixing*. The sequence of events that characterizes all mixing processes is as follows : first, input of mechanical work ( usually drawn from the main flow ) that causes macromixing, followed by molecular diffusion ( micromixing ).

### 1.2.2 Compressible Shear Layers

The compressible free shear layer is a fundamental flow type concerning fuel-air mixing in parallel streams, that is central to the flow in a scramjet combustor. In recent years compressible turbulent mixing flows have been studied in great detail in an attempt to understand and control the physics governing them. Although much has been learned from these studies, attempts to significantly increase the mixing of two streams have been largely unsuccessful. Two adjacent compressible

fluid streams of different supersonic speeds mix much more slowly at their interface than the same fluids at subsonic speeds with the same velocity and density ratios. The most elementary feature that distinguishes a supersonic flow from a subsonic one is that in the supersonic case a disturbance does not propagate upstream and remains confined within a Mach cone, while in the subsonic case a disturbance is felt throughout the flowfield. Given the limited region of influence of a supersonic disturbance, it may be expected that a supersonic shear layer is more stable, therefore mixes more slowly, than a subsonic one. Density differences between the streams were originally suggested as the cause of this mixing decrease, but the work of Brown and Roshko[5] showed this is not the case. They found that large changes in the density ratio across the mixing layer had a relatively small effect on the spreading angle of the mixing layer, and concluded that the strong effects are due to compressibility effects. This effect was conclusively shown by Papamoschou and Roshko[3]. They correlated their shear layer spreading rate data, and results of earlier studies, using the convective Mach number ($M_C$) concept introduced by Bogdanoff[6]. Since large structures are present in the compressible mixing layer, a frame of reference moving with the convective speed $U_C$ of these structures was suggested by Papamoschou and Roshko[3]. The convective Mach numbers then are defined as follows

$$M_{C_1} = \frac{U_1 - U_C}{a_1} \tag{1.1}$$

$$M_{C_2} = \frac{U_C - U_2}{a_2} \tag{1.2}$$

where the subscripts 1 and 2 stand for the first and second stream respectively. In this coordinate system, there is a saddle point between the structures shown in an idealized view in the work by Papamoschou and Roshko[3]. It is a common stagnation point for both streams, where the pressure must balance. Assuming that the flow

comes to rest at the stagnation point isentropically, hence without shock wave losses, Papamoschou and Roshko[3] obtained the relation

$$\left(1+\frac{\gamma_1-1}{2}M_{C_1}^2\right)^{\frac{\gamma_1}{\gamma_1-1}}=\left(1+\frac{\gamma_2-1}{2}M_{C_2}^2\right)^{\frac{\gamma_2}{\gamma_2-1}} \tag{1.3}$$

Since $U_C$ is algebraically implicit in Eq. ( 1.3), it must be found iteratively, or by using a root-finder software on a computer. However, for $M_{C_1}$ and $M_{C_2}$ not very large and $\gamma_1$ and $\gamma_2$ not greatly different, the Eq. ( 1.3) can be approximated by

$$M_{C_2}=\left(\frac{\gamma_1}{\gamma_2}\right)^{\frac{1}{2}}M_{C_1} \tag{1.4}$$

Using Eq. ( 1.4), together with the convective Mach number definitions the convective velocity can be calculated as

$$U_C=\frac{\gamma_1^{0.5}a_2U_1+\gamma_2^{0.5}a_1U_2}{\gamma_1^{0.5}a_2+\gamma_2^{0.5}a_1} \tag{1.5}$$

Since the pressures of both streams are equal at the stagnation point, one can obtain

$$\frac{U_C}{U_1}=\frac{1+\frac{U_2}{U_1}\left(\frac{\rho_2}{\rho_1}\right)^{0.5}}{1+\left(\frac{\rho_2}{\rho_1}\right)^{0.5}} \tag{1.6}$$

For $\gamma_1=\gamma_2$, $U_C$ can be expressed in the form of a speed-of-sound weighted average as

$$U_C=\frac{a_2U_1+a_1U_2}{a_2+a_1} \tag{1.7}$$

It should be pointed out that Eqs. ( 1.6) and ( 1.7) are not restricted to compressible flow and are actually more accurate for incompressible flow. Papamoschou and Roshko give the following relation for the incompressible shear layer growth rate based on visual thickness[3]

$$\delta'_{incomp.}=0.17\frac{\left[1-\frac{U_2}{U_1}\right]\left[1+\left(\frac{\rho_2}{\rho_1}\right)^{0.5}\right]}{1+\frac{U_2}{U_1}\left(\frac{\rho_2}{\rho_1}\right)^{0.5}} \tag{1.8}$$

where $\delta' = d\delta/dx$. Then the normalized growth rate of the compressible shear layer may be expressed in the form

$$\frac{\delta'_{compres.}}{\delta'_{incomp.}} \approx func(M_C) \tag{1.9}$$

where "func" is a universal function valid over a wide range of $U_2/U_1$ and $\rho_2/\rho_1$. Hence the convective Mach number correlates the effect of compressibility on the compressible shear layer growth rate normalized by its incompressible counterpart at the same freestream velocity and density ratios. This normalized growth rate is drastically reduced with increasing $M_{C_1}$, until $M_{C_1}$ reaches about 0.8 . Beyond this point, the growth rate stays fairly constant at a value approximately one fifth of the incompressible one. However, there are studies that have documented large structure convection velocities that are substantially different from those predicted using the convective Mach number analysis, particularly at higher convective Mach numbers[7,8]. Due to apparent problems associated with this parameter, the relative Mach number, is also used as a compressibility parameter[9,10]. The relative Mach number is defined as

$$M_R = \frac{2\Delta U}{a_1 + a_2} \tag{1.10}$$

where $\Delta U$ stands for the freestreams velocity difference $U_1 - U_2$.

In the context of convective Mach number, Ragab and Wu[11] numerically calculated the linear spatial instability of a two-dimensional compressible laminar mixing layer, and investigated the effects of temperature and velocity ratios, Reynolds number, and convective Mach number. Their results substantiate the convective Mach number as a parameter which correlates the compressibility effects on the spreading rates of the mixing layers. Sandham and Reynolds[12] extended the numerical simulations to three dimensions and showed that the structures become increasingly

three dimensional as the convective Mach number is increased, becoming dominant for $M_C > 0.6$. Fourguette et al.[13] found experimentally that in an axisymmetric supersonic jet the structures in the mixing layer are three dimensional and are rotating while traveling with a velocity higher than the one predicted based on the convective Mach number. Nixon et al.[14] suggested, based on a theoretical study, that the main cause of the decrease in mixing as $M_C$ increases is that an increasing amount of the energy in the two streams goes into compression of the fluid during entrainment rather than being used to produce pure mixing (increase of mass within the shear layer). They theorized that the only way to increase mixing is to accentuate streamwise vorticity. McIntyre and Settles[8] have found experimentally that the axisymmetric turbulent mixing layers possess large scale poorly-organized turbulent structures. These structures are always inclined toward the faster of the two mixing streams. For $M_C > 1$ these structures are supersonic with respect to only one of the two mixing streams. Spectrum analysis of the velocity fluctuations exhibited a broad-band peak which shifted to lower frequencies with downstream distance, indicating growth of the structures with downstream location.

Although the convective Mach number correlates growth-rate data fairly well, questions remained as to the accuracy of the isentropic model when shocks form on the structure. Papamoschou[7] pointed out that the isentropic model for the turbulent large scale structures fails when the flow becomes highly compressible. Dimotakis[15] proposed a scheme which assumes that for low convective Mach numbers, shocks will form in one of the two shear layer free streams. He pointed out that the available data indicate a convection velocity $U_C$ that is closer to $U_1$ (the high speed stream velocity) when the low speed stream is subsonic, and closer to $U_2$ (the low speed stream velocity) when both streams are supersonic, resulting in an asymmetric

entrainment pattern. Zeman[16,17] suggested that growth inhibition in mixing layers is a consequence of additional (anomalous) dissipation due to the presence of fluctuating dilatation, which is proportional to the square of fluctuating divergence. This so-called dilatation dissipation occurs in regions where the flow becomes locally supersonic and form shock-like structures, or turbulent shocklets. The dilatation dissipation affects the turbulence so that the turbulent fluctuations and also the layer growth rate are determined by the local sonic velocity rather than by the velocity difference $\Delta U$, thus explaining the growth rate leveling for $M_C > 1.5$ . Zeman also pointed out that if the faster stream is denser (as in the case of a freestream of air and hydrogen fuel ), the average spatial growth will be lower than in the case of equal densities streams. A shear-layer drift toward the stream with the lower density was also observed. It has been found by Zeman[17] that the shear layer reaches a self-similar state when the shear layer relative Mach number exceeds a value of about three.

Elliot et al.[4,18,19] showed that both the growth rate and the turbulence quantities decrease with increasing convective Mach number. Further experimental results from Laser Doppler Velocimetry (LDV) investigations by Goebel and Dutton[9] showed that the transverse turbulence intensities and normalized kinematic Reynolds stresses decrease with increasing relative Mach number, whereas the streamwise turbulence intensities and kinematic Reynolds stresses remain relatively constant. Gruber et al.[10] experimentally corroborated the Goebel and Dutton results, implying that the primary effect of compressibility on the mixing layer is to suppress transverse velocity fluctuations. The result concerning the streamwise turbulence is somewhat different from that obtained by Elliot et al.[19], who found a reduction in streamwise turbulence similar to the transverse component. This decrease in the turbulent quantities reduces the small scale mixing, consequently the molecular mixing decreases. Hall et al.[20]

experimentally observed a reduction in molecularly mixed fluid inside the shear layer, in addition to the reduction in the overall growth rate. Specifically, they measured about 31% of molecularly mixed fluid at $M_C = 0.96$, compared to 49% in incompressible flow. A contradictory result was experimentally observed by Clemens et al.[21]. Their results suggest that in a moderately compressible layer, a larger fraction of the fluid ( 15% to 25% more ) exists in a mixed state as compared to the incompressible layer. This controversy shows that the molecular mixing in compressible shear layers is still an unresolved issue. On one hand the increased three dimensionality of the shear layer suggests that an increase in the molecular mixing is to be expected. On the other hand, suppression of the vortex pairing process tends to reduce the molecular mixing.

In conclusion, the compressible shear layers suffer from a significantly reduction in the growth rate and in the turbulence quantities as well as an increase in the stability, as compared to the incompressible shear layers with the same velocities and densities ratios. Therefore the mixing of the two streams is reduced. Various mixing augmentation techniques have been proposed to enhance mixing in shear layers. All of them have in common the basic objective of increasing the mixing by extracting a fraction of the main flow energy, and applying it into the shear layer. The various methods will be discussed in the next subsection.

### 1.2.3 Mixing Augmentation Methods

To date, several techniques have been proposed for mixing enhancement. The methods may be sorted into three principal classes :

1. Methods which provide for conditioning of the flow field into which the fuel is injected by varying the injector/combustor wall geometry. These techniques are

also known as "Contoured wall injectors".

2. Preconditioning of the fuel through various turbulence and vorticity generating devices within the injectors themselves, including the use of non-circular nozzles.

3. Direct interaction between the injectant jet and freestream flows.

The following survey does not intend to cover all the work done in the field of mixing enhancement, but is intended to point-out different methods which have demonstrated improved supersonic mixing. Additional details and references can be found in the works cited here.

#### 1.2.3.1 Contoured wall injectors

This technique involves shaping the combustor wall geometry or the external injector geometry, thus conditioning the flow field into which the fuel is injected.

One type of injector from this class employs a ramp for generating streamwise vorticity. This type was studied extensively at NASA Langley Research Center , Hampton, VA, USA, by Northam et al.[22,23], Riggins et al.[24–26], and elsewhere by Davis et al.[27], Hartfield et al.[28], and Donohue et al.[29,30]. Ramp injectors generate streamwise vorticity when high pressure air compressed by the top of the ramp spills over the ramp corners to the lower pressure region between the ramps. The effect is enhanced if the ramp side walls are swept so that the region between the ramps diverges in the streamwise direction. Air is accelerated and expanded in this region to a lower pressure pulling more air over the corners. The injectant jet is highly deformed by those vortices, and it is almost split and lifted into two completely separate counter-rotating cores. In the case of swept side-wall ramp, the mixing is augmented in comparison with the straight wall ramp and requires less length. But

the swept-ramp incurs higher total pressure loss than the unswept ramp.

Another injector type which belongs to this class is the one which augments mixing by baroclinic vortex generation. It is designed so that the jet intersects an oblique shock. Vorticity is formed at any point where the gradients of pressure and density are non-parallel. Thus, intersection of a shock (pressure gradient) with a non-parallel fuel/air density gradient will cause a baroclinic generation of vorticity[31,32–34]. The rate of change of vorticity, $\vec{\omega}$, is derived by taking the curl of the momentum equation and can be written in the following form :

$$\frac{D\vec{\omega}}{Dt} = -\frac{1}{\rho^2}(\nabla p \times \nabla \rho) + (\vec{\omega} \bullet \nabla)\mathrm{u} - \vec{\omega}(\nabla \bullet \mathrm{u}) + \nu\nabla^2\vec{\omega} + (\nabla\nu) \times \nabla^2\mathrm{u} \qquad (1.11)$$

The first term on the RHS is called the "*baroclinic torque*" which exists when the pressure and density gradients are not parallel. When a shock wave intersects a jet of different density to the surrounding flow, such as a hydrogen fuel jet in air, the pressure gradients across the shock interact with the density gradient between the hydrogen jet and the air and generate vorticity. The studies showed an increase in the interface area between the air and the fuel resulting in an increase in the mixing. The jet was lifted-off the wall and complete separation from the wall occured streamwise within one injector height. The performance of these injectors is strongly affected by the boundary layer thickness which acts to modify the effective wall geometry. The impact of the boundary layer varies with the spacing in the injector array and upstream conditions. Widely spaced arrays were less influenced by the boundary layer thickness. Another parameter which affects the mixing enhancement is the injectant to free stream static pressure ratio. Pressure ratio near unity ( matched pressure injection) yields strong jet penetration and good mixing, compared with pressure ratios greater than unity (under expanded jets)[32]. However, it is not clear whether the gain in mixing enhancement due to the vorticity generated by baroclinic torque is

sufficient to justify the additional loss of total pressure caused by the oblique shock, through which the entire airstream must pass.

#### 1.2.3.2 Preconditioning the fuel

This method preconditions the fuel flow through various devices within the injectors themselves. Several techniques were employed including non-circular nozzle geometries. The elliptic and rectangular jets had a better mixing performance, and displayed greater spreading rate relative to the circular jets, especially in the minor axis plane, which was attributed to the higher pressure fluctuations measured in this plane. The higher spread was accompanied by faster decay of the mean velocity along the jet axis and amplification of turbulent small-scale fluctuations[35]. For noncircular nozzles with corners, e.g. triangles, rectangles or squares, a significant amplification of turbulent small scale fluctuations was observed due to axial vortices formed in the corners of the nozzle[36].

Other techniques precondition the fuel through various turbulence and vorticity generating devices. Schadow et al.[37] used a circular nozzle with several downstream facing steps upstream of its exit plane. Cold flow tests showed turbulence levels increased up to six times the initial turbulence level relative to a circular nozzle. Samimy et al.[38,39] and Zaman et al.[40] used vortex generators in the form of tabs projecting into the flow at the exit plane of the nozzle. The jet cross section was distorted. As a result of this distortion the entrainment region and the mixing were substantially increased. In an experimental study, Yu et al.[41] used a ramp nozzle that creates large scale structures which are responsible for the shear layer growth enhancement. Gutmark et al.[42] studied experimentally the performance of a jet injected from a supersonic tapered-slot nozzle. The jet spreads primarily at the

conical section with small spread at the major axis side. The growth rate of the turbulent level in the core region, as well as in the jet's circumference, was higher than in the circular or elliptic jets. The increased turbulence production was attributed to the axial vorticity component generated by the nozzle's geometry. The turbulent intensity level is lower at the center, but it is uniformly distributed accross the jet, with the highest relative intensity concentrated in the shear layer of the jet (the jet's circumference).

Based on studies made mainly under subsonic conditions, Swithenbank and Chigier[43], proposed to enhance supersonic mixing by swirl. Tangential injection of fuel into a centrally located swirl chamber results in a spiral flow within the chamber, and the generation of a swirling jet at the nozzle exit. Fluid emerging from the jet has a tangential velocity distribution in addition to the axial and radial components of velocity encountered in nonswirling jets. The rate of entrainment and mixing is substantially increased as compared with nonswirling jets. Recently Settles[44], using swirl vanes mounted upstream of the nozzle in order to obtain swirling jets, found that swirl enhances compressible mixing. The amount of mixing enhancement increases with increasing swirl. Cutler et al.[45,46] and Kraus[47] generated swirl by using tangential injection into a plenum chamber ahead of a convergent-divergent nozzle. The mixing layers growth rates with matched exit pressure were shown to increase up to three times with the addition of swirl. When operated overexpanded, considerable turbulence was produced caused by shock interactions and probable vortex breakdown.

#### 1.2.3.3 Direct interaction technique

This technique relies upon injectant interaction with the freestream to generate convective mixing. Low angled transverse injection has been studied where the fuel is injected from ports in a flat combustor wall at angles of 10 to 30 degrees relative to the freestream flow direction[48,49]. The injection with low transverse angle could increase the mixing rate and jet penetration while retaining the majority of the injectant thrust[49]. It was found by Fuller et al.[49] that coupling low tranverse angle with yaw angle may affect the mixing in different ways, depending upon the conditions : free stream Mach number, injection pressure, transverse angle, and yaw angle. It may increase the overall plume cross section, thus making the mixing layer larger ( Mach 3 and transverse injection angle of 30° ), but under other conditions ( Mach 6 and transverse injection angle of 15° ) it may degrade the mixing rate and decrease the penetration. Other results showed that the entire injectant plume remained supersonic and that moderate total pressure losses were found by Fuller et al.[49] . A new injector concept has been studied by Cox et al.[50], in which an array of flush-wall injectors was arranged in such a way as to induce large vortical structures in the main stream, that increase entrainment and mixing — a sort of "aerodynamic ramp". Their experimental and computational results demonstrated the creation of large-scale vortices in the mixing region with reasonably low losses and good mixing. A particular case of the transverse injection is the **normal injection**, in which all the injector thrust is lost. In addition, the shock wave system generated by such geometry, the shock-shock interactions, and the shock-boundary layer interactions cause substantially total pressure losses. In two recent works, the complex flowfields induced by gaseous secondary flow injected normally into a supersonic mainstream have been studied experimentally. Aso et al.[51] experimentally studied the normal

injection of nitrogen into a $M = 4$ air stream through a single transverse slot nozzle mounted on a flat plate model. As the freestream is partially blocked by the secondary flow, a strong bow shock wave is formed in front of the injection point. Ahead of the injection point the boundary layer separates due to the interaction between the shock wave and the boundary layer, and a separation shock wave is generated ahead of the bow shock that causes a shock-shock interaction with the bow shock. Just after the injection point the boundary layer reattaches and a recompression shock wave is generated. Hollo et al.[52] investigated a staged transverse injection of air into a M= 2 freestream of air. The interaction between the injectors accounts for the dramatically increased mixing rate produced by the staged injectors compared to a single injector. A subsonic region was observed just upstream of the second injector. It is significant to note that the far-field mixing is approximately the same as in the parallel injection schemes ! The near-field mixing in normal injection schemes is dominated by the large-scale vortices generated by the jet/freestream interaction, whereas the far-field mixing depends on small-scale turbulence, such that the far-field mixing essentially has no "memory" of the near-field stirring, the transition from near-field to far-field mixing taking place about 10 to 20 jet diameters downstream[52].

Because shocks and expansion waves are basic features of a supersonic flowfield, mixing augmentation may be obtained by the interaction of the injectant with expansion fans or with shock waves. When a hydrogen flow was accelerated into an air flow by an expansion fan, the interface was unstable, and rapid development of large scale structures was evident[53]. These large structures play an important role in mixing augmentation. The effect of shock impingement on the mixing and combustion was numerically simulated by Domel et al.[54]. A streamwise oblique shock was impinged on a hydrogen jet which was injected behind a backward facing step in a direction

parallel to a supersonic freestream of air vitiated with $H_2O$. The results showed that the shock impingement enhanced mixing and combustion.

Another mixing augmentation attempt was made by impinging spanwise shock waves against a supersonic mixing layer[55]. A shock wave emanated from a disturbance on the sidewall of the combustor (or test cell) and intersected with the supersonic shear layer formed between the fuel and the air stream. The pressure discontinuity across the wave could not be sustained by the mixing layer and an apparent vortex was formed.

Mixing improvement has also been achieved by employing an oscillating shock. This method was studied numerically by Kumar et al.[56], and options for producing such shock waves were discussed.

#### 1.2.3.4 Summary of mixing techniques

A review of the high speed mixing experimental database is presented by Thomas et al.[57]. They plotted the decay of maximum injectant concentration versus $x/d$ for the studies they reviewed, where $x$ was the distance downstream and d was a characteristic physical scale of the geometry, typically the diameter of the injection nozzle. The data were plotted on a log-log scale and fit with a power law. The data were categorized as free jets, transverse jets, wall slot jets, and hybrid jets. Due to the variety of experimental conditions, direct comparisons were not warranted. Considered as a whole, the data were grouped around a decay exponent of $-0.8$ .

### 1.2.4 Mixing and Combustion

The combustion of the fuel in the combustor releases energy which is, at best, partially recovered in the nozzle and along the afterbody generating useful thrust.

The time required for the heat release process to go to completion, and hence the length of the combustor, is dependent upon the time needed to mix the fuel and air, and the time needed for it to react. In practice, these two processes are occuring simultaneously[58], however to obtain complete combustion, the fuel and the air must be mixed in the correct proportions down to the molecular level. Waitz[32] cited an unpublished work by Yeung in which the hydrogen-air reaction has been modeled for conditions corresponding to a variety of flight Mach numbers. The time required for initiation of a hydrogen-air reaction in a typical scramjet combustor is of the order of 25 $\mu s$. Swithenbank et al.[58] claim that for their conditions the hydrogen-air reaction time is of the order of 1 $\mu s$. While strongly dependent on the pressure and on the local static temperature, the two values for the chemical kinetic time allow estimation of the extent to which supersonic combustion is controlled by mixing. Once the reaction is initiated, complete combustion can occur within a very short distance, on the order of millimeters.

The pertinent non-dimensional number is the first Damköhler number, $Da$, defined as the ratio of the flow characteristic time to the reaction characteristic time. Reactions with $Da \gg 1$ are mixing controlled. For example, a typical aircraft flying at Mach 15, may have the air in the combustor at Mach 5 with a velocity of 4000 m/s. For these conditions $Da = 1$ is obtained at a distance of 0.1 m downstream to the injector. Given the fact that the combustion chamber can only be a few meters long, ( taking a typical value of 4 m ) the Damköhler number at the end of the combustor is, $Da = 40$. Mungal and Frieler[59] found, in an experimental study on two-dimensional subsonic shear layer, that the mixing limited regime is reached when $Da_x > 40$, where the subscript $x$ stands for the local station coordinate. The flow characteristic time is defined as the streamwise distance between the measuring

station and the mixing transition point divided by the average velocity of the two streams : $(U_1 + U_2)/2$. The distance downstream of the splitter plate at which a significant amount of mixed fluid is first present is called the mixing transition point. Finite rate chemistry effects appear below this value.

The effects of the heat release associated with the combustion on the mixing were discussed in several papers. The heat release associated with the combustion produces an upstream shock compression and thereby changes the upstream flow conditions in the combustor. Two principal effects of heat release on the mixing layer have been observed, both theoretically and experimentally. First, at any axial location, both the shear layer and the included mixing layer occupy a greater volume fraction of the combustor, due to the volume dilation resulting from the temperature rise caused by the combustion at essentially constant pressure. The second effect is to reduce the rate of growth of the mixing layer. Menon et al.[60] studied numerically the effects of compressibility on the large scale structures of the reacting mixing layers. They confirmed that at low convective Mach numbers heat release reduces the growth rate of the shear layer and the amount of product formed, but at high Mach numbers heat release increases the growth rate of the shear layer. Sekar and Mukunda[61] conducted numerical simulations of high speed reacting and non-reacting flows for a hydrogen-air system. They found that the growth rate with heat release is only 7% lower and the entrainment is 25% lower with heat release than without. Their conclusion was that high speed mixing is not severely hampered by heat release. In three-dimensional numerical simulations conducted by Planche and Reynolds[62] the central role of streamwise vortices was demonstrated. The streamwise vortices strongly increase the mixing and the total reaction rate. Riggins and McClinton[25] point-out that reaction dramatically increases the rate of decay of vorticity and this

may decrease the rate of mixing. Vuillermoz et al.[63] numerically solved the two-dimensional, compressible, and reactive mixing layer between hydrogen and air. They found that for $Da \approx 1$, there are homogeneous pockets of radicals not yet converted to product. In this region the chemistry is strongly affected by the flow dynamics. For $Da \gg 1$ the result is a stretched flame and the reactions are completed by the end of the mixing period.

The conclusion is that combustion in typical scramjet applications will not be mixing controlled in the classical sense. It will, however, be mixing dominated. For example, 80% mixedness would correspond to 80% complete combustion[58]. The heat release associated with chemical reaction has little influence on the mixing. To minimize the chemical kinetic limitations, the local static temperatures must be sufficiently high so that the ignition time plus the reaction time are less than the time of the flow through the combustor. Hence, the investigation of mixing enhancement is germane to combustion enhancement.

### 1.2.5 Mixing and Losses

Any mixing augmentation scheme will increase the irreversible losses, decrease the axial momentum and eventually diminish the engine thrust so that there is always a trade off to be considered[26]. There is probably some optimum trade between the total pressure losses induced by the fuel injection and mixing augmentation process and the resulting increase in combustion efficiency. As pointed out by Swithenbank et al.[58], there is a competitive balance between irreversibilities produced by mixing enhancement and the advantage gained by additional reaction due to the enhanced mixing. The two extrema are high total pressure loss ( high mixedness ) leading to high combustion efficiency but low overall engine performance, and low total

pressure loss ( low mixedness ) causing low combustion efficiency and again leading to low overall performance. The practical realization of an optimum combustor requires proper mixing within in a short length because wall friction losses in ducted supersonic flows are extremely large. The flow losses incurred by placing a ramp in a supersonic airstream must not negate the benefit which is obtained by the mixing enhancement. Flow losses for a ramp configuration include shocks, frictional and pressure drag on the face of the ramp, vorticity generation losses, base pressure drag, and flow recirculation[26]. There are also practical difficulties with operating ramp type injectors in extremely high enthalpy flows within a scramjet combustor, and although the present study does not address these practical issues, it is necessary to point them out. Because the ramp injector performance depends on ramp's geometry and relies heavily on sharp corners, the effectiveness over long periods of time in such a harsh environment is questionable.

### 1.2.6 Mixing Efficiency

In order to compare the different mixing techniques an appropiate global value of "mixedness", varying only in the axial (downstream from the injector ) direction, $x$, has to be defined. Riggins[24] defines the mixing efficiency as the amount of fuel that would react if complete reaction occurred without further mixing divided by the amount of fuel that would react if the mixture were uniform. Heiser et al.[1], p.303, formulate the above definition as follows : if the far-field equivalence ratio is denoted by $\phi_{FF}$, then the mixing efficiency, $\eta_M(x)$ is defined as :

- For $\phi_{FF} \leq 1$, $\eta_M(x)$ is the fraction of fuel which is micromixed with air at any location $x$.

- For $\phi_{FF} > 1$, $\eta_M(x)$ is the fraction of air which is micromixed with fuel at the axial location $x$.

The equivalence ratio is the fuel-to-air ratio ( on a mass basis ) divided by the fuel-to-air ratio under stoichiometric conditions. Therefore, $\eta_M(x)$ measures the completeness of micromixing of either fuel or air, depending on whether the overall equivalence ratio $\phi_{FF}$ is less than or greater than one, respectively. Other mixing-efficiency definitions could possibly be defined. According to Swithenbank et al.[58], mixing efficiency means a cost/benefit ratio, where the "cost" is the mechanical energy drawn from the air or fuel stream and expended on stirring, and the "benefit" is either increased rate of growth of the near-field mixing layer or reduced axial distance required for complete micromixing. In the present study the mixing efficiency is defined according to Riggins[24].

## 1.3 Scope of the Investigation

It is likely that some combination of mixing enhancement methods may be required to obtain the required mixing for a supersonic combustor. Hence the goal of the work presented here was to evaluate the performance of injectors which combine different mixing enhancement techniques, looking for constructive coupling between them. This work addressed the mixing enhancement in the near-parallel injection schemes. Parallel injection schemes have two clear advantages over transverse injection :

1. Additional thrust is generated by injecting fuel in the downstream direction.
2. The strong bow shocks generated by transverse fuel injection into a supersonic stream are eliminated, minimizing the stagnation pressure losses.

Based on previous work in this area, the swept-ramp appears to be a practical injection scheme. Therefore, in this study the swept-ramp injector developed at NASA Langley Research Center by Northam et al.[22] was further investigated as a mixing augmentation device. The swept-ramp injector configuration was designed to generate vortical flow ( streamwise vorticity ) and local recirculation regions downstream from the ramp base similar to the rearward facing step that has been used for flame holding in supersonic flows. The fuel was injected at a low injection angle ( 10° ) which provided for the penetration of the fuel into the air, while preserving most of the fuel momentum. In addition, fuel preconditioning devices within the injector's nozzle were experimentally explored in order to further improve the mixing by coupling the preconditioned injectant flow with the vortical flow generated by the ramp. This combination of mixing augmentation techniques was intended to provide the necessary mixing with reasonable losses in total pressure. A coordinated experimental and computational program was carried-out, utilizing experimental techniques and computational methods.

### 1.3.1 Experimental Scope

The experiments were conducted on a single fuel injector placed in a rectangular cross-section duct. Injection of helium at Mach 1.7 into a Mach 2 air stream simulated hydrogen injection into a typical scramjet combustor. Experiments with air as fuel were also conducted. The air "fuel" was injected at Mach 1.63 into Mach 2 air stream. Of primary interest in these tests was the definition of the flow field features, particularly those related to the mixing enhancement by the fuel preconditioning devices. However, this study was limited by using helium and air to simulate the hydrogen fuel, and by conducting only cold flow experiments. The mixing performance was

evaluated from spatial scales which were discernable within the experimental and computational resolution. Increase in large-scale mixing of the flow field increases the molecular-scale mixing by increasing the interfacial shear surface area, thus facilitating the diffusion process. Lack of temporal resolution precluded the measurements of time-fluctuating component of the flow field. The phenomena associated with time-fluctuations were inferred from the mean flow field. Mean flow observations enabled estimates of the importance of these effects, but did not provide sufficient information for detailed analysis.

### 1.3.2 Computational Scope

An existing three-dimensional Navier-Stokes code was used to conduct a numerical study which closely tracked the experimental one. Modeling and simulation allowed the analysis of global aspects of the injector performance. The numerical results provided knowledge of flow variables at every point in the computational domain, and allowed study of derived quantities such as vorticity. The numerical data complemented the experimental effort, provided insight into the general flow phenomena, and enhanced the understanding provided by the experimental data.

# Chapter 2

# EXPERIMENTAL METHODS AND APPARATUS

## 2.1 Test Facility

The tests were conducted in the NASA Langley Transverse Jet Facility shown schematically in Fig. 2.1. This is an open-loop blowdown facility, with a rectangular, Mach 2 convergent-divergent nozzle section. A rectangular cross-section duct assembly is connected at the nozzle exit. The duct has a uniform and constant cross section of 1.52″ by 3.46″. The measurements were taken at the exit plane of the duct. In order to allow measurements at different cross-sections downstream of the injection plane, the duct can be extended by adding inserts in steps of two inches, from 4.5″ total length up to 10.5″ total length. The flow through the duct is unheated air at a nominal static pressure of one atmosphere, that discharges into the ambient air. Unless otherwise stated, the stagnation conditions for these tests were : $P_0 = 115.5 \pm 0.5$ psia, and $T_0$ equal to the ambient temperature, measured to $\pm 0.5°$ C. The repeatability of the total pressure between runs was within $\pm 0.5$ psia. The mass flow rate of the air at these conditions is $\approx 8.0$ lb/s ( $\approx 3.6$ kg/s ).

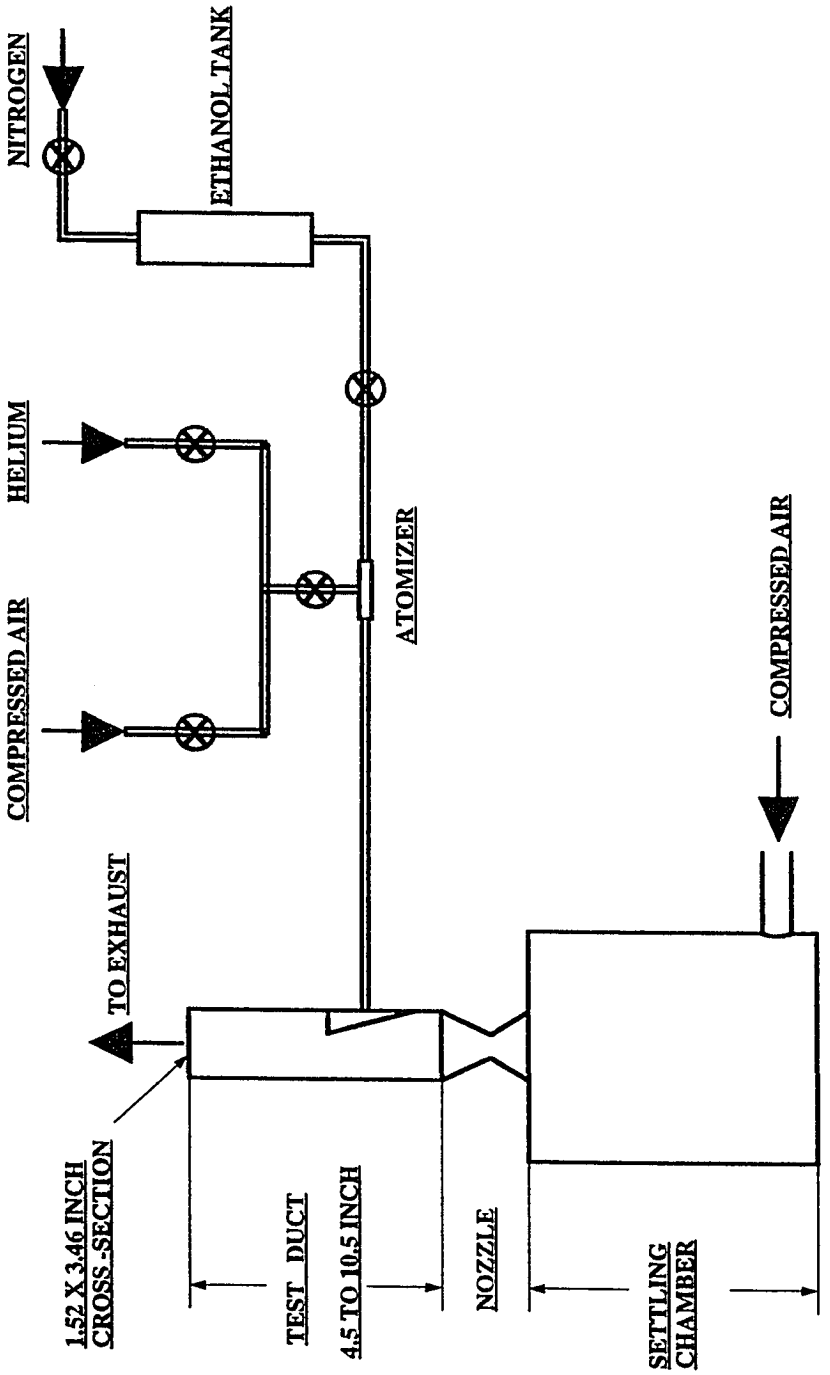


Fig. 2.1 Schematic of experimental facility

The "fuel" supply system designed and constructed for these studies is shown in Fig. 2.1. The system is capable of supplying air or helium at controlled conditions. The system provides air up to a maximum of 1000 psia from the compressed air plant, and helium up to a maximum of 2000 psia from 10 compressed manifolded bottles. Hence the helium supply is restricted to short runs. The system also has the ability to seed the injectant with ethanol for visualization tests. The ethanol injection is achieved by pressurizing the ethanol tank with nitrogen, at 100 psia higher than the pressure of the injected gas ( the "fuel" ). The flow rate of the ethanol injected into the fuel line is regulated by means of a fine needle valve. An ample length of pipe ( $\approx$ 60 feet ) with several elbows ensures evaporation and mixing ahead of the injector's nozzle.

## 2.2 Injector Model

The injector model shown in Fig. 2.2 has one swept-ramp located in the middle plane of the duct. The top wall of the ramp is inclined 10.3° relative to the duct wall. The side walls of the ramp are swept back at an 80° angle relative to the main flow direction which is parallel to the duct walls. The ramp ends in a nearly square base, ( 0.685″ wide by 0.639″ high ), corresponding to an area blockage of less than 9%. On both sides of the middle ramp there are swept sidewalls simulating adjacent ramps, thus the geometrical influence of an array of ramps can be tested in these experiments. The middle ramp is equipped with an injector connected to the "fuel" supply system. The injection line is at a 10.3° angle relative to the main flow. The injector consists of a convergent-divergent nozzle insert. The six different nozzle inserts used in the experiments are described in the following section.

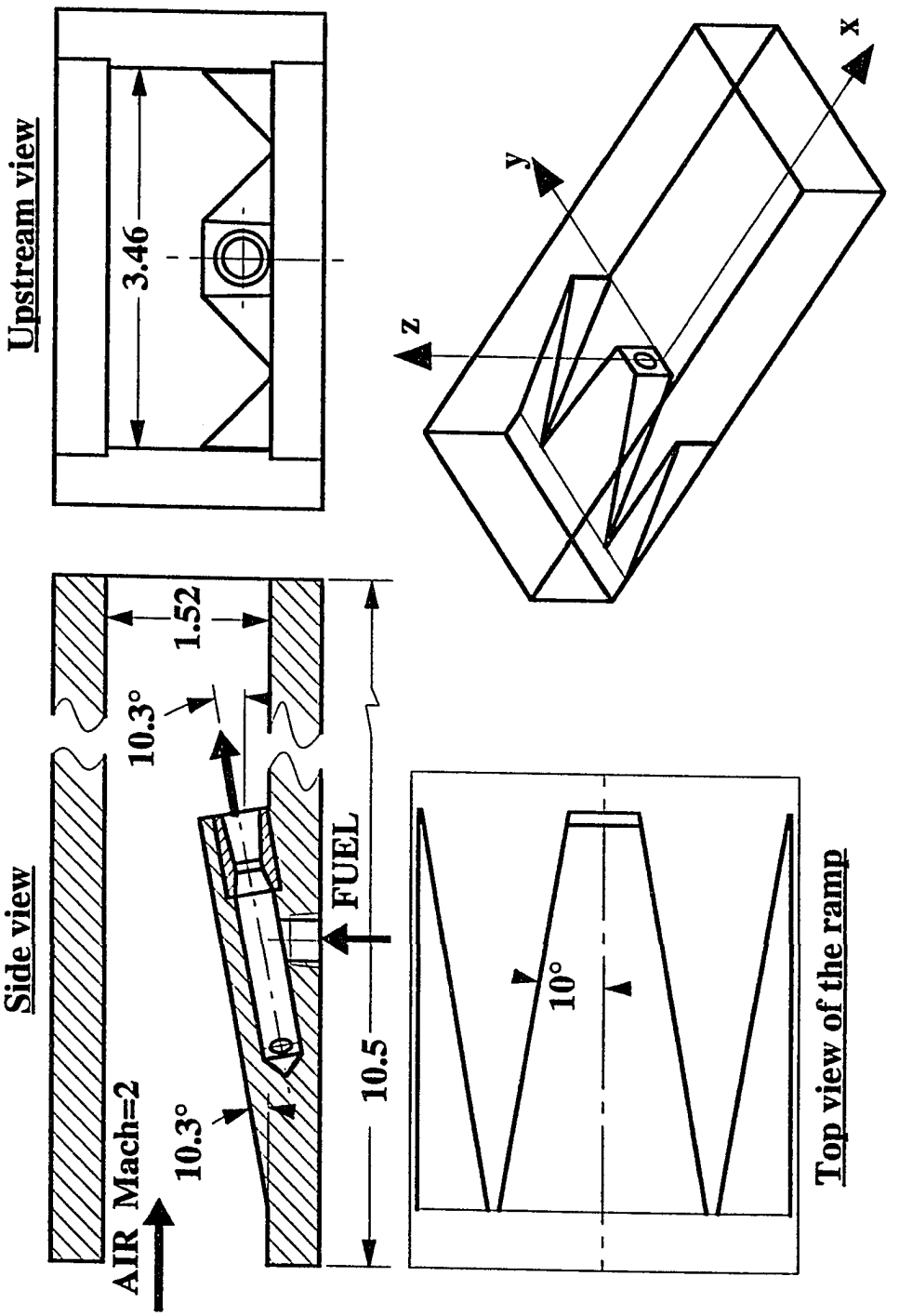


Fig. 2.2 Schematic of the injector model ( dimensions in inches )

## 2.3 Injector Nozzle Inserts

Six different nozzle inserts were made separately and then inserted into the ramp. A set-screw held the nozzle inserts in place. All the nozzles had the same exit area and the same throat area, hence they had the same exit Mach number and the same mass flow rate for each gas used. The calculated exit Mach number for helium was 1.7, and the calculated exit Mach number for air was 1.63. The six nozzle inserts shown in Fig. 2.3, were as follows :

1. **Circular nozzle**, Fig. 2.3a : This nozzle was the baseline configuration. It was a convergent-divergent nozzle with a circular cross section, a throat diameter of 0.250″ and an exit cross section diameter of 0.282″ . The area ratio $A/A^*$ was 1.272 .

2. **Nozzle with three downstream facing steps**, Fig. 2.3b : This nozzle had a circular cross section with three downstream-facing steps in the divergent section, each having a length-to-step height ratio of 16. These steps enhanced the small scale turbulence[37].

3. **Elliptical nozzle**, Fig. 2.3c : Only the divergent section of the nozzle was elliptical with an aspect ratio of 1.2 . The elliptical nozzle is known to have a higher spreading rate higher in the minor axis plane than in the major axis plane[35]. The higher spread is accompanied by a faster decay of the mean velocity along the jet axis and a higher amplification of turbulent small scale fluctuations. This nozzle was tested in two positions : first, where the major axis was horizontal, and the second, where the major axis was vertical.

4. **Nozzle with vortex generators**, Fig. 2.3d : This was a circular cross section conical nozzle with four vortex generators in the exit plane, corresponding to an area blockage of about 5%. The vortex generators were rectangular tabs, 0.02″ × 0.04″, projecting normally into the jet. The tabs introduced a significant distortion of the jet cross section. The mixing/entrainment area was substantially increased due to these distortions[38,40]. This nozzle insert was tested in two positions : with the vortex-generator tabs in cross orientation, and with the tabs rotated 45° relative to the previous position, thus obtaining an "X" orientation.

5. **Tapered-slot nozzle**, Fig. 2.3e : The tapered-slot nozzle had a rectangular-slot throat that blended smoothly into the conical inlet and exit sections. The tapered-slot nozzle jet spreads primarily at the conical section with small spread at the major axis side. There is also an increase in the turbulence production due to the axial vorticity component generated by the nozzle's geometry[42]. The turbulent intensity level is lower at the center, but it is uniformly distributed across the jet, with the highest relative intensity concentrated in the shear layer of the jet (the jet's circumference). This nozzle insert was tested in two positions : with the throat vertical, and horizontal.

6. **Trapezoidal nozzle**, Fig. 2.3f : This nozzle generates axial vortices at the corners inside the nozzle, yielding a significant amplification of turbulent small scale fluctuations[36].

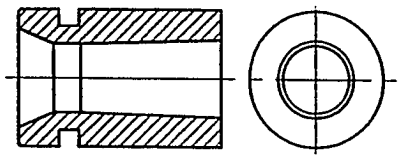

a. Circular nozzle

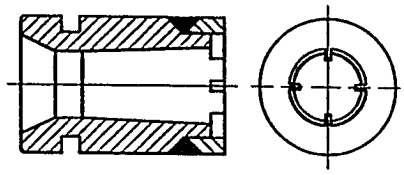

d. Nozzle with vortex generators

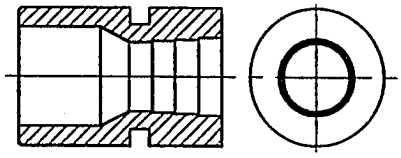

b. Nozzle with three steps

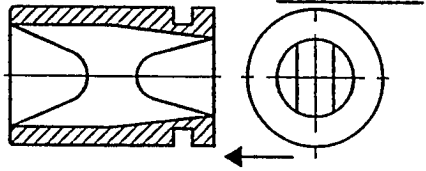


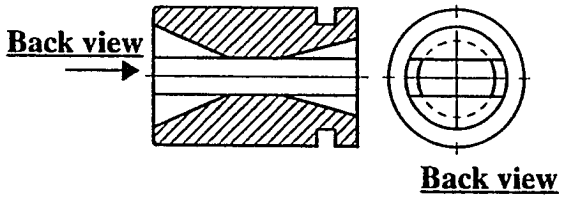


e. Tapered slot nozzle

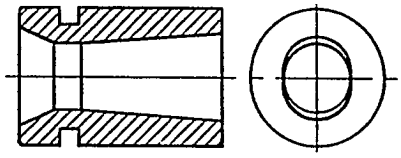

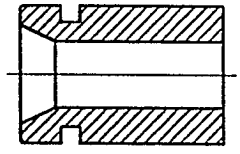

c. Elliptical nozzle

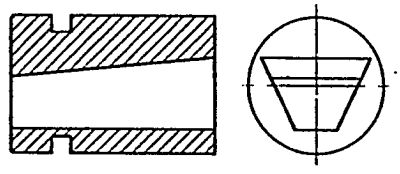

f. Trapezoidal nozzle

**For all nozzles : Ae / At = 1.272**

**Fig. 2.3 Injector - nozzle inserts**

## 2.4 Flow Field Survey Apparatus

Twelve rake-mounted probes were used to investigate the flow field : four pitot pressure probes, four cone static pressure probes, and four total temperature probes. Given the measurements from these twelve probes, Mach number, density, and static temperatures were determined. The pressure probes were connected to pressure transducers which were calibrated on-site using the same analog-to-digital converter ( A-to-D ) and the same personal computer ( PC ) used for acquiring the experimental data. The transducers were calibrated just before the beginning of the probe experiments. Periodic checks of the transducers response showed that the error was less than $\pm$ 0.5 psia. The power supply to the pressure transducers was held at 5 $\pm$0.0010 volts. The sampling loop delay chosen for the probes measurements (4 sec.) was sufficient to avoid measuring the transient due to the stage movement. The pressure transducers were hooked-up to a Hewlett-Packard 3497A data acquisition and control unit[64] which is controlled by a PC. The measurements were taken at a sampling rate of 50 Hz.

### 2.4.1 Probe Rake

A schematic of the rake is shown in Fig. 2.4. The rake assembly is mounted on a translation stage ( Thomson 2DB-12-OUB-B ) which is controlled by a PC, moving the rake according to a pre-determined plan ( see Sec. 2.6 : "*Data Acquisition*" ). The spacing between the total temperature probe and the pitot pressure probe was 0.145", centerline to centerline. The centerline of the conical static probe was set 0.29" away from the centerline of the neighbor probes to eliminate undesirable interference from the other probes. The probes extended 0.75" from the rake to minimize rake

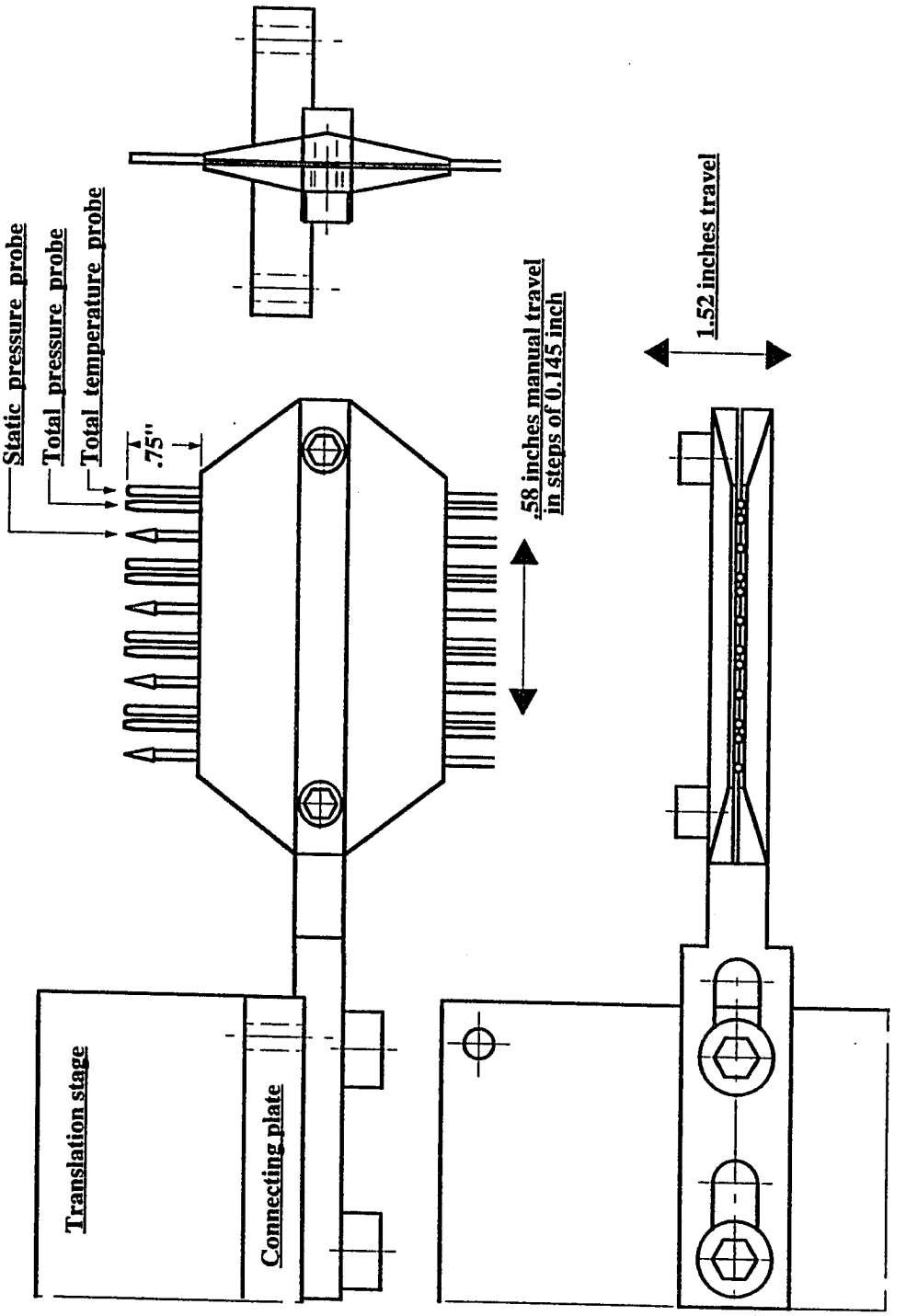


Fig. 2.4 The probes rake

interference. The probes are described in the following paragraphs.

#### 2.4.1.1 Total pressure probes

A drawing of the probe is shown in Fig. 2.5a. Each probe used had a 0.030″ diameter sensing orifice, and was connected to a pressure transducer by a 6 feet long, 0.04″ internal diameter stainless steel tubing. Strain-gage pressure transducers with a range extending to 300 psia and an accuracy of 0.5% full scale were used to measure the total pressures.

#### 2.4.1.2 Static pressure probes

The static pressure was measured on a cone of 10 degrees half angle. The probe is shown in Fig. 2.5b. Four 0.020″ diameter holes were drilled perpendicular to the surface of the cone, 90 degrees apart. Approximately 6 feet stainless steel tubing of 0.04″ internal diameter ran between the probe and the transducer. The strain-gage type pressure transducers had a range extending to 50 psia with a quoted accuracy of 0.1% full scale.

#### 2.4.1.3 Total temperature probes

A copper-constantan thermocouple (type "T" junction[65]) probe, shown in Fig. 2.5c, was used to measure the total temperature. The diameter of the bead was about 0.03″, and the conduction errors were minimized by using fine wire ( 0.01″ diameter ). The thermocouple was enclosed in a 0.060″ internal diameter radiation shield. Two 0.030″ diameter vent holes were located in the radiation shield downstream of the thermocouple. Due to the size of the radiation shield, the capture area of this probe was significantly greater than that of the other probes thus reducing the resolution of this

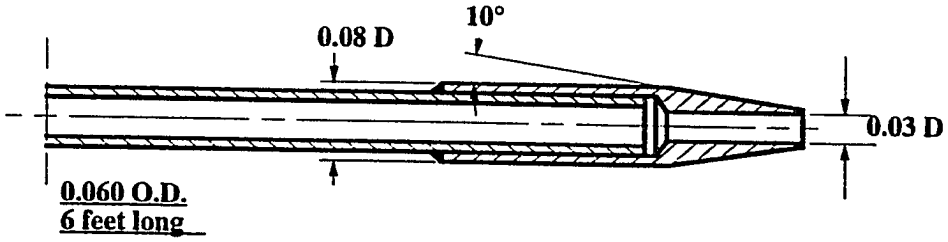


a. Pitot pressure probe

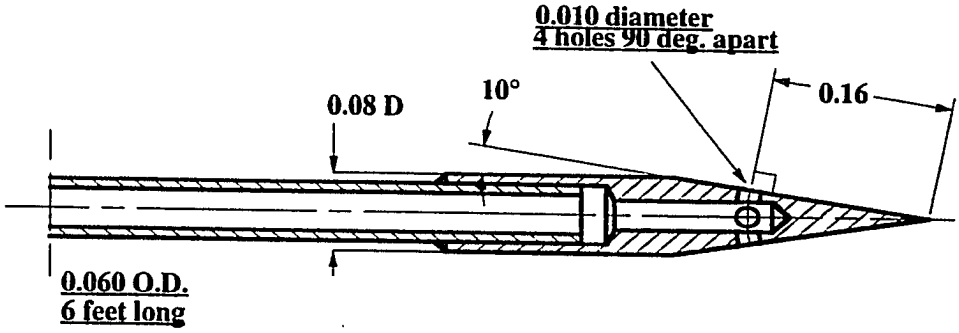


b. Static pressure probe

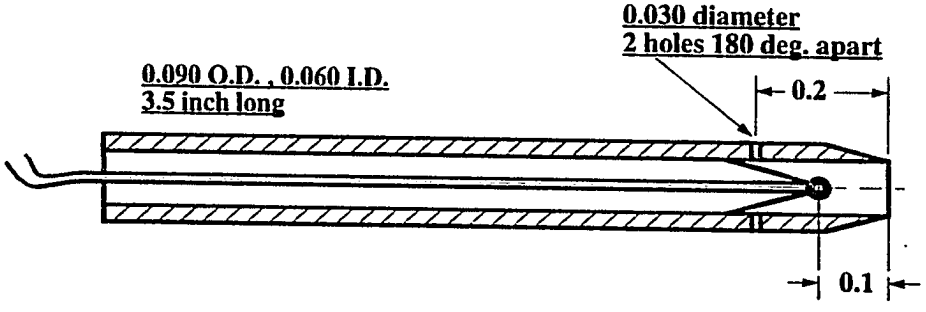


c. Total temperature probe

**Fig. 2.5 Flow field survey probes**

probe in comparison with the pressure probes. The thermocouples were hooked-up to an Hewlett-Packard 3497A data acquisition and control unit[64] which was controlled by a PC. The measurements were taken at a sampling rate of 50 Hz. The thermocouple voltage was reduced using a cold junction signal on the data acquisition multiplexer board. Comparison of the output of the total temperature probe with air plenum chamber total temperature was used to determine the effective recovery factor for the probe. In all cases, the probe measurement was about 99% $\pm$ 0.5% of the settling chamber temperature.

### 2.4.2 Errors in Probes Location

The experimental sampling grid is shown in Fig. 2.6. The error in the grid points ( probes coordinates ) are estimated in the present sub-section. The error due to the accuracy of the driving screw of the translation stage was very small. The screw has 5 mm/revolution, the stepping motor has 25600 steps/revolution, giving an accuracy of about $1.95 \times 10^{-4}$ mm/step. The motor position accuracy is within one step, i.e. $1.95 \times 10^{-4}$ mm, which is much lower than all other errors in the system, and is neglected in the present analysis. The error in the z-direction is determined by the location of the first position of the rake ( $= l_z$ ), and is within $\pm$ 0.5 mm. The error in the y-direction ( $= l_y$ ) is $\pm$ 0.005 inch ( $\approx \pm$ 0.13 mm ). This is the width of the ruler mark made on the connecting plate between the rake assembly and the translation stage. Therefore, the error in the grid coordinates is :

$$l_{yz} = \sqrt{l_y^2 + l_z^2} = \sqrt{0.13^2 + 0.5^2} \approx 0.51\ mm \approx 0.02\ inch \qquad (2.1)$$

The following inaccuracies were set during the assembly of the rake and remain constant during the runs as long as the rake was not opened. The error in the

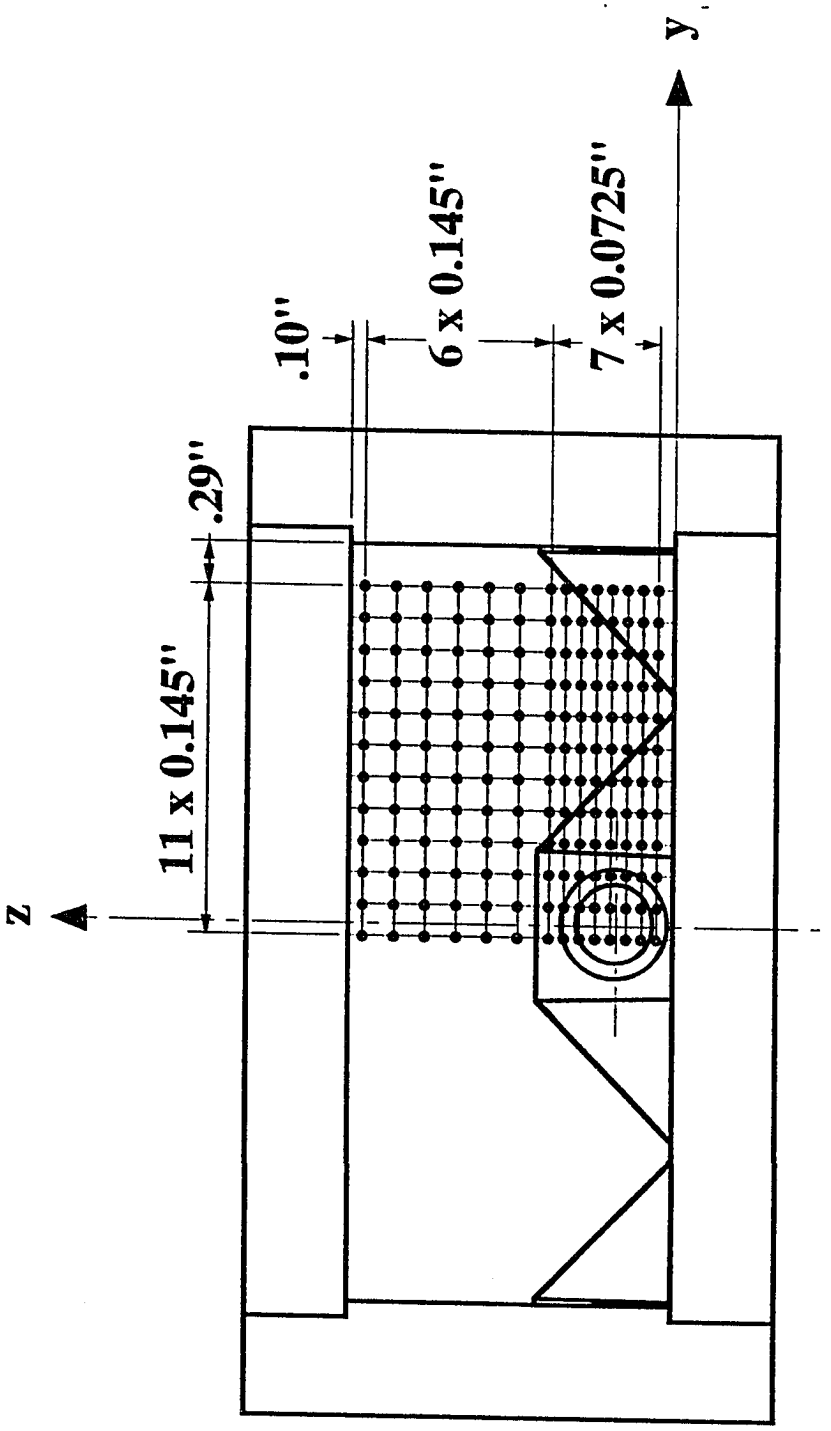


Total number of sampling points : 168

Fig. 2.6 The sampling grid for probe measurements

distance between the rake and the probes tips ( $= l_x$ ) was about $\pm$ 0.5 mm. Due to this error the probes tips were not in the same cross-section plane. The distance between two adjacent probes was determined by the distance between the grooves in which the probes were placed. These grooves were machined with a tolerance ( $= l_2$ ) of $\pm$ 0.01 inch ( $\approx \pm$ 0.25 mm ). The alignment of the probes — the tip of each probe — was within $\pm$ 0.5 mm from the normal; $l_3$ is the error in y-direction (spanwise); and, $l_4$ is the error in z-direction; each was $\pm$ 0.5 mm. An error of 0.5 mm corresponds to an angular error of 1.5°. Therefore the total error in the probes' tips location is :

$$l = \sqrt{l_x^2 + l_{yz}^2 + l_2^2 + l_3^2 + l_4^2} \approx 1\ mm. \tag{2.2}$$

Hence the "point" measured by the probes was actually a small volume in space and can be approximated by a sphere having a radius of 1 mm ( 0.04 inch ) .

### 2.4.3 Resolution of the Probes

The resolution of the probes was determined by the capture area of the probes. For the total pressure probe the inlet diameter of the probe was 0.030 inch ( $\approx$ 0.76 mm ). This dimension was greater than the Kolmogorov's scale. The Kolmogorov's scale can be inferred from Batchelor's scale calculated in Sec. 2.9.1. Since the Schmidt number was about one, the two scales were the same. Batchelor's scale, and hence Kolmogorov's scale is shown in Table 2.6, and is $\lambda_B = 2.25 \times 10^{-2}$ mm for air. This length scale was about 34 times smaller than the inlet diameter of the total pressure probe. The total temperature probe had an inlet diameter of 0.060 inch ( $\approx$ 1.5 mm ). Since the Prandtl number was about one, the temperature microscale was the same as Kolmogorov's scale estimated above, and the inlet diameter was greater than the temperature microscale.

## 2.5 Imaging System

The imaging system was composed of two sub-systems : the laser/optics system and the camera/image acquisition system.

### 2.5.1 The Laser and the Optics System

Illumination was obtained using a frequency doubled Nd:YAG laser[66], pulsed at 6 Hz with a pulse length of 10 ns. The laser and the optics layout is shown in Fig. 2.7. The output energy was about 200 mJ per pulse at 532 nm. The frequency of the 532 nm light was doubled to 266 nm in the ultra violet with 10% to 15% efficiency[46], using a temperature-phase-matched KD*P crystal mounted in a temperature stabilized dry cell. The ultra violet light was split from the residual green with a Brewster's angle prism and the plane of polarization was rotated to the vertical with a quartz zero-order half-wave plate for the vertical light sheet. For the horizontal light sheet the plane of polarization was rotated to the horizontal. The light sheet was formed by a pair of lenses : a plano-concave cylindrical lens with a focal length of 100 mm, and a plano-convex spherical lens with a focal length of 1 m. Optics are UV grade fused silica, coated for 266 nm . The theoretical (diffraction limited) light sheet thickness was about 50 $\mu m$ [46]. Typically the laser light sheet was about 5 cm wide and 0.5 mm thick at the waist. The spherical and cylindrical lenses were mounted on a moveable rail system that allowed the light sheet to be formed and moved at any position. The laser beam was brought to optics mounted on the rail by a periscope ( two 90° turns by two mirrors ).

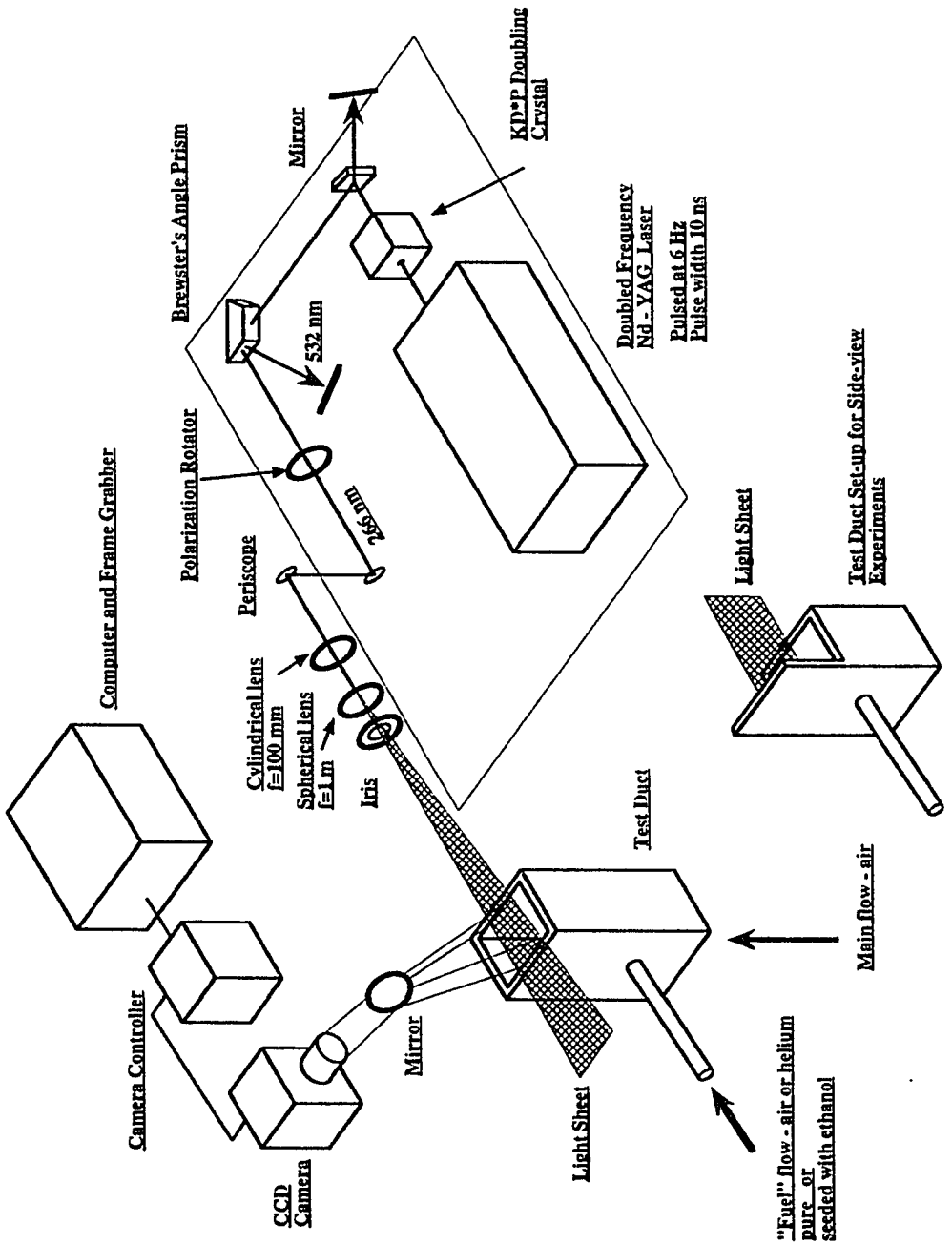


**Fig. 2.7 Mie scattering optical arrangement**

### 2.5.2 Camera and Image Acquisition System

The images were recorded by an intensified video (RS172) using a Photometrics AT200 CCD camera[67] through a UV-Nikkor with F/4.5 and 105 mm focal length camera lens. The CCD array contains 512 × 512 pixels, each pixel corresponds to $20\mu m \times 20\mu m$. The images were binned, with a binning factor of two. Therefore the images have only 256 × 256 pixels. Binning is a technique of combining charge from adjacent pixels during the readout process. Binning improves the signal-to-noise ratio and extends the dynamic range of the CCD imager at the expense of spatial resolution. Because binning reduces the number of pixels to be processed and digitized, readout speed is also increased, and the storage space on the computer disk and in the computer memory is reduced. The camera has a charge transfer efficiency (CTE) of 0.99999, where 1.0 is perfect. The quantum efficiency of the CCD was about 35% at the 266 nm light used in the present study. Quantum efficiency measures the sensor's efficiency in generating electronic charge from incident photons. At a given wavelength the creation of charge from incident light is intrinsically linear. The quantum efficiency and the system noise level ( discussed in Sec. 2.10.2.5 ) determine the sensitivity of the CCD imager. The camera system was interfaced to a personal computer equipped with a frame grabber for data acquisition and storage. The images were composed of 16-bit data (65536 gray levels) and were digitized at a rate of 40,000 pixels per second with a digitization noise of four electrons r.m.s. ( see item 1 on page 68 ). The camera was mounted on a rail system that allowed it to be moved to any desired location. The camera exposure time was set at 167 ms ( 1/6 sec ) to ensure the capture of the scattered light from a single laser pulse. This was done because of software limitations that prevented the triggering of the camera from the laser pulse. After the software was upgraded, this limitation was removed, and

triggering was possible. The computer required approximately four seconds to digitize an image and display it on the screen. Sequences of ten of these single shot images were acquired for all the cases. Details about images acquisition are presented in Sec. 2.6.2. A ten seconds exposure time was also employed for several sequences. The image thus acquired can be considered an average of sixty instantaneous images. For this exposure time, sequences of two to five average images were acquired.

## 2.6 Data Acquisition

The investigation required the development of two data acquisition systems : (1) flow field survey data acquisition system, and (2) image acquisition system. A description of each system is given below.

### 2.6.1 Flow Field Survey

The investigation required the design and development of an automated, personal computer based, data acquisition system. A special computer program, written in HT-BASIC[68], was developed and used to control the traverse stage. The program also controlled the Hewlett-Packard 3497A data acquisition unit[64], which acquired the data at a sampling rate of 50 Hz, and recorded the pressure transducers and the thermocouples output. First, the translation stage computer — the "compumotor"[69], was turned on, and allowed to reset. Then the computer program on the PC was started and took control over the compumotor and the analog-to-digital unit. The data acquisition algorithm shown in Fig. 2.8 was the basis for the computer code, and was used in all of the flow field surveys conducted. At each point in the flow field the data were recorded according to the order of the A-to-D channels. Ten readings per

probe were taken at each point in the flow field, in the main plenum chamber, and in the fuel plenum chamber. Subsequently, the average and the standard deviation for each probe reading were calculated.

### 2.6.2 Images Acquisition

A separate personal computer was used to acquire and store the data from the CCD camera. The PMIS software[67], was used for images acquisition and processing. The image acquisition plan was as follows :

1. one 10 ms image of grid pattern ( to establish coordinate location ).
2. one sequence of ten background images at 167 ms.
3. one sequence of ten background images at 10 s.
4. one sequence of ten reference images at 10 s in still air.
5. one sequence of ten reference images at 10 s in slow flow ( just to clean the dust from the air ).
6. one sequence of ten images at 167 ms of the main flow only.
7. one sequence of ten images at 10 s of the main flow only.
8. two sequences of ten images at 167 ms of air jet injected into the main flow.
9. one sequence of five images at 10 s of air jet injected into the main flow.
10. one sequence of five images at 167 ms of helium jet injected into the main flow.
11. two images at 10 s of helium jet injected into the main flow.

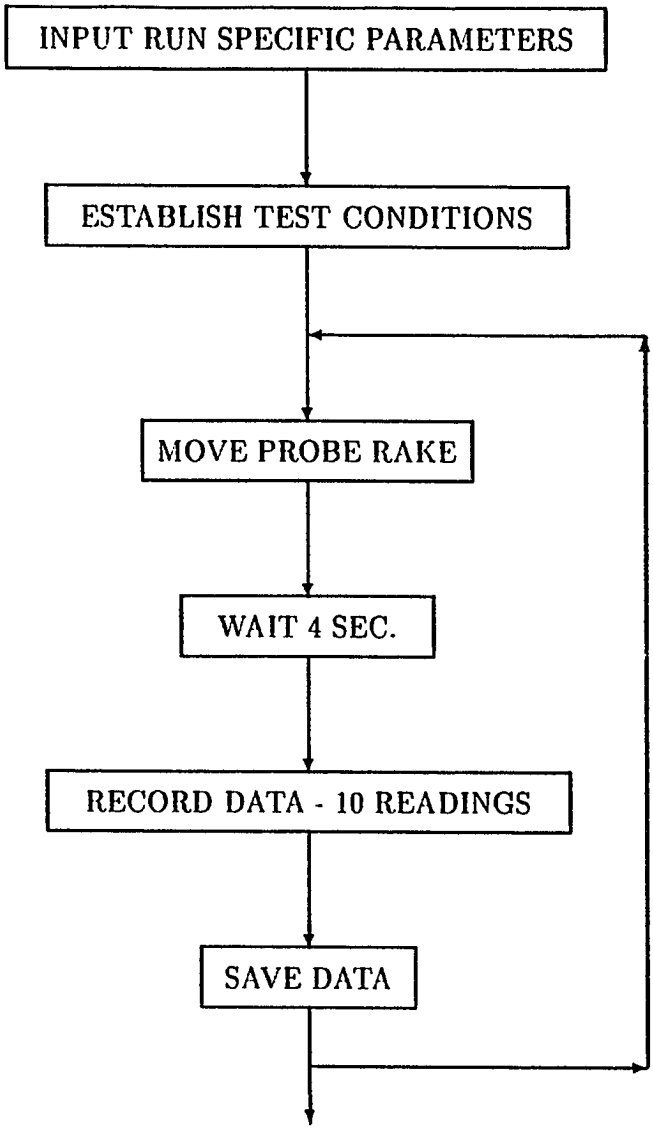


Fig. 2.8 Data acquisition algorithm

12. four sequences of ten images at 167 ms of ethanol seeded air jet injected into the main flow.

13. one sequence of five images at 167 ms of ethanol seeded helium jet injected into the main flow.

14. one sequence of two images at 10 s of air jet injected into the main flow with a shadow in one side of the light sheet.

15. one sequence of two images at 10 s of air jet injected into the main flow with a shadow in the other side of the light sheet.

16. one sequence of ten reference images at 10 s in slow flow ( just to clean the dust from the air ).

17. one sequence of ten reference images at 10 s in still air.

18. one sequence of ten background images at 10 s.

19. one sequence of ten background images at 167 ms.

20. one 10 ms image of grid pattern.

For the grid image, a grid made from graph paper was placed exactly in the field of view of the camera. The background images were taken in complete darkness. The reference images were taken with the light sheet at the model but without flow or with a very slow flow to blow away the dust in the air. The background, reference, and grid images were repeated at the end of the test to check if there were any changes during the run. The above plan was applied in all the experiments.

## 2.7 Experimental Conditions

### 2.7.1 Main Flow

The main flow was obtained from compressed dry air supplied through a 600 psia supply line. The water concentration in the main flow was estimated to be in the range of three to ten parts per million[46]. The Mach number at the nozzle exit was calculated to be two. The nominal stagnation pressure was 115. psia yielding a static pressure of 14.7 psia ( 101000 Pa ) at the nozzle exit. The ambient stagnation temperature, varied between 282 K and 298 K. During a run, the stagnation temperature dropped as much as 5 K. Based on a stagnation temperature of 290 K, the main flow velocity was 508 m/s and the mass flow rate was 3.78 kg/s. The Reynolds unit number was 101. $\times 10^6$ 1/m. The main flow conditions are summarized in Table 2.1.

### 2.7.2 Fuel Flow

Two kinds of "fuels" were injected : air or helium. The air was obtained from a 1000 psia supply line and the helium was supplied from compressed bottles. During the run the pressure was not steady. The measured pressure fluctuations are shown together with the nominal values. Table 2.1 summarizes the nominal fuel injection conditions. Tables 2.2 and 2.3 present the shear layer characteristics of the present flow. The convective velocity and Mach number, and the relative Mach number are defined in Sec. 1.2.2.

### 2.7.3 Ethanol Injection

The amount of ethanol injected was changed between the different runs from 7 cc/min up to 10 cc/min. During each run the amount of ethanol was maintained

Table 2.1 Main flow and fuel injection conditions

| Property | | Main flow | Helium jet | Air jet |
|---|---|---|---|---|
| Stagnation : | | | | |
| $P_0$ | kPa | $793 \pm 3$ | $434 \pm 21$ | $510 \pm 28$ |
| $T_0$ | K | 290 | 290 | 290 |
| $\rho_0$ | $Kg/m^3$ | 9.52 | 0.721 | 6.13 |
| Throat : | | | | |
| $P^*$ | kPa | $419 \pm 2$ | $211 \pm 10$ | $269 \pm 15$ |
| $T^*$ | K | 242 | 217 | 242 |
| $\rho^*$ | $Kg/m^3$ | 6.03 | 0.468 | 3.87 |
| Nozzle exit : | | | | |
| P | kPa | $101 \pm 1$ | $80 \pm 5$ | $115 \pm 6$ |
| T | K | 161 | 147 | 189 |
| $\rho$ | $kg/m^3$ | 2.193 | 0.263 | 2.123 |
| U | m/s | 508 | 1213 | 449 |
| a | m/s | 254 | 713 | 275 |
| M | | 2.00 | 1.70 | 1.63 |
| $\dot{m}$ | kg/s | 3.78 | 0.0128 | 0.0384 |
| $Re_d$ | | — | 199,000 | 540,000 |
| $Re \times 10^6$ | 1/m | 101 | 28 | 75 |

Table 2.2 Shear layer characteristics for helium injection

| Property | | Helium jet | Air - mainstream |
|---|---|---|---|
| | | Stream No. 1 | Stream No. 2 |
| $\gamma$ | | 1.67 | 1.40 |
| Velocity, U | m/s | 1213. | 508. |
| Sound velocity, a | m/s | 713. | 254. |
| $\overline{v} = U_1/U_2$ | | 2.38 | |
| $\overline{\rho} = \rho_1/\rho_2$ | | 0.120 | |
| $\overline{p} = p_1/p_2$ | | 0.792 | |
| $\overline{T} = T_1/T_2$ | | 0.913 | |
| $\overline{\mathcal{M}} = \mathcal{M}_1/\mathcal{M}_2$ | | 0.138 | |
| $\Delta U = U_1 - U_2$ | m/s | 705. | |
| $\mathrm{Re}_{d,\Delta U}$ | | 115,000 | |
| Convective Velocity, $U_C$ | m/s | 693. | |
| Convective Mach number, | $M_C$ | 0.73 | |
| Relative Mach number, | $M_R$ | 1.46 | |

Table 2.3 Shear layer characteristics for air injection

| Property | | Air - mainstream | Air jet |
|---|---|---|---|
| | | Stream No. 1 | Stream No. 2 |
| $\gamma$ | | 1.40 | 1.40 |
| Velocity, U | m/s | 508. | 449. |
| Sound velocity, a | m/s | 254. | 276. |
| $\overline{v} = U_2/U_1$ | | 0.882 | |
| $\overline{\rho} = \rho_2/\rho_1$ | | 0.968 | |
| $\overline{p} = p_2/p_1$ | | 1.138 | |
| $\overline{T} = T_2/T_1$ | | 1.174 | |
| $\overline{\mathcal{M}} = \mathcal{M}_2/\mathcal{M}_1$ | | 1.000 | |
| $\Delta U = U_1 - U_2$ | m/s | 61. | |
| $Re_{d,\Delta U}$ | | 73,000 | |
| Convective velocity, $U_C$ | m/s | 480. | |
| Convective Mach number, | $M_C$ | 0.11 | |
| Relative Mach number, | $M_R$ | 0.23 | |

constant. The ethanol was stored at room temperature of about 296 K which results in a density of 787 kg/$m^3$, giving a mass flow rate between $0.92 \times 10^{-4}$ kg/s and $1.31 \times 10^{-4}$ kg/s . Table 2.4 summarizes the partial pressures and the mass and molar fraction of the injected ethanol. The ethanol properties were taken from Wegener et al.[70].

Fig. 2.9 shows the saturation curve for ethanol, plotted with the ethanol vapor pressure as it expands through the supersonic nozzle. The state of the ethanol at the stagnation conditions is labelled 1. At these conditions the ethanol is fully evaporated. As it expands through the nozzle, it follows the isentropic curve shown. Wegener et al.[70] found that condensation of ethanol vapor in supersonic nozzle begins at super-saturation ratios of about 10–14, depending on the ethanol loading (partial pressures). Based on their results, for the ethanol loading in this study, the condensation will occur at a supersaturation ratio of about 12. Fig. 2.9 shows that this supersaturation ratio (state 2 on the plot) occurs at a temperature of about 230 K for air which corresponds to a Mach number greater than one. Thus the condensation begins just downstream of the sonic throat and ends by the time the flow reaches the nozzle exit. If this condensation ratio holds in helium too, then the ethanol condensation in helium begins at a temperature of 223 K (state 2 on the plot) which corresponds to a Mach number smaller than one. Thus the condensation in helium begins just upstream of the sonic throat and ends by the time the flow reaches the nozzle exit. Hence the tracer droplets are formed within the nozzle and are injected by the "fuel" jet into the main flow.

Table 2.4 Ethanol injection conditions

| Property | | In helium jet | | In air jet | |
|---|---|---|---|---|---|
| $\dot{m}$ | kg/s | $0.92 \times 10^{-4}$ | $1.31 \times 10^{-4}$ | $0.92 \times 10^{-4}$ | $1.31 \times 10^{-4}$ |
| X | | 0.00067 | 0.00097 | 0.00151 | 0.00215 |
| Y | | 0.0071 | 0.0100 | 0.0024 | 0.0034 |
| $\mathcal{M}_{i,gas}$ | kg/k mole | 4.003 | 4.003 | 28.97 | 28.97 |
| $\mathcal{M}_{mix}$ | kg/k mole | 4.30 | 4.42 | 29.0 | 29.0 |
| Stagnation (vapor) : | | | | | |
| $P_0$ (partial) | Pa | 291 | 421 | 770 | 1097 |
| $T_0$ | K | 290 | 290 | 290 | 290 |
| Throat (vapor) : | | | | | |
| $P^*$ (partial) | Pa | 141 | 205 | 406 | 578 |
| $T^*$ | K | 217 | 217 | 242 | 242 |
| Nozzle exit (condensed) : | | | | | |
| $\rho_{liquid}$ | $kg/m^3$ | 917.3 | | 879.3 | |
| T | K | 147 | | 189 | |

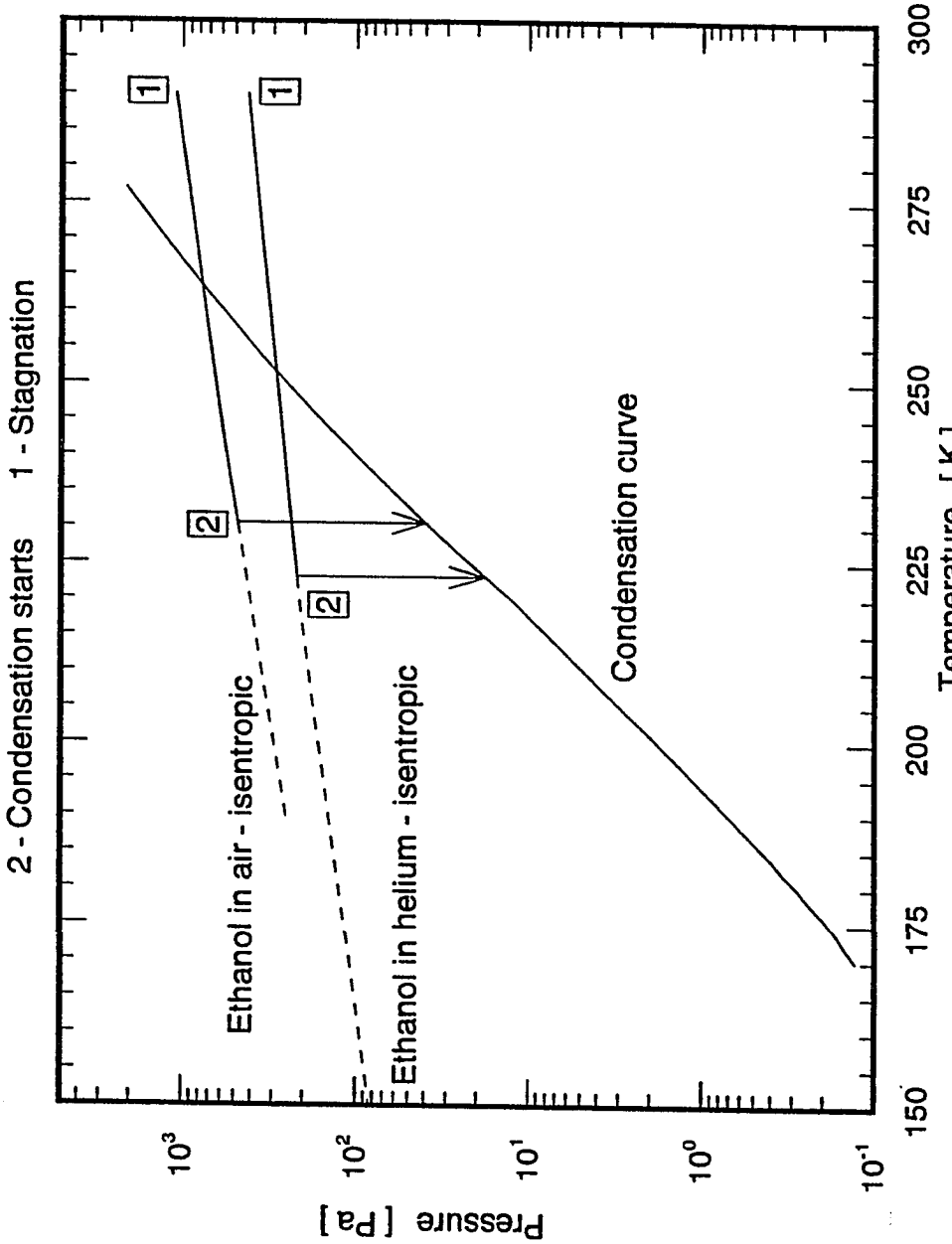


Fig. 2.9 Pressure - temperature diagram for ethanol condensation process

## 2.8 Flow Visualization

A planar Rayleigh/Mie scattering technique was employed in this study, which allowed direct visualization of fluid mixing in the supersonic flow. The mixing process was visualized by laser light sheet scattering from small ethanol droplets which condense in the injector. Satisfactory flow tracking capability of scattering particles is essential for reliable visualization. The aerodynamic behaviour of a particle depends on its inertia and the drag force; the light scattering behaviour depends on the particle shape, surface area and refractive index. The common parameter determining both aerodynamic and optical characteristics of the particle is its diameter. Both issues are addressed in the following sub-sections.

### 2.8.1 Theory

Rayleigh scattering is a technique that has been used for both flow visualization and quantitative density imaging for many years in low-speed flows, and recently in supersonic flows as well. From a quantum mechanical point of view, a gas molecule can absorb a photon from an incident electromagnetic wave. The absorbed photon causes an electron to be excited into an unstable state for a very short time ( less than psec )[71]. In elastic events, the electron then drops to its original state emitting a second photon of the same frequency as the incident one. This emission, known as the scattering process, is random in the sense that the photon can propagate with equal probability in any direction in the plane normal to the polarization vector of the incident E-field of the electromagnetic wave. Since the emitted photon is at the same frequency as the incident photon, the Rayleigh scattering is not specific to the molecules causing the scattering. Thus, this technique cannot be used for individual

species concentration measurements but only to measure total number density. It is also possible for the energy input due to the incident photon to be dissipated by collisions of the excited molecule with other molecules. In that situation the photon energy would have been absorbed and converted into thermal energy. The parameters controlling the scattering of planar electromagnetic radiation by isolated spherical particles are $d/\lambda$, the ratio of particle diameter to the incident radiation wavelength; n, the refractive index of the particle relative to the surroundings; and the polarization state of the incident radiation. The three scattering regimes are delineated as :

1. Rayleigh scattering for $d/\lambda \ll 1$
2. Lorenz-Mie scattering for $d/\lambda \approx 1$
3. Geometric optics for $d/\lambda \gg 1$

The differential cross-section for Rayleigh scattering from gas molecules at 90° to the plane of polarization may be expressed as[72]

$$\left(\frac{\partial\sigma}{\partial\Omega}\right)_{Ray} = \frac{4\pi^2(n_{STP,i}-1)^2}{N_{STP}^2\lambda^4} \tag{2.3}$$

where $n_{STP,i}$ and $N_{STP}$ are the refractive index and the number density at standard temperature and pressure ( STP ). In a mixture of gases, the Rayleigh scattering signal is a function of the mole fraction weighted average of the scattering cross sections of the individual gases[72]

$$\left(\frac{\partial\sigma}{\partial\Omega}\right)_{mix} = \sum_i X_i \left(\frac{\partial\sigma}{\partial\Omega}\right)_{Ray} \tag{2.4}$$

where $X_i$ is the mole fraction of constituent i. Rayleigh scattering is dependent on total flow density, and in general can not be used to identify species in a binary mixing field. However, in the case where the Rayleigh scattering cross section for one of the species is significantly different from that of the other, the technique can be used to

identify species gradients. The utility of the technique for identification of species in a mixture is dependent therefore upon weak changes in number density, and strong differences in refractive index between the species. In supersonic flows, however, due to the cooling of the gas as it expands through a nozzle, some gas constituents may condense and form clusters[73,74]. The Rayleigh scattering from clusters may interfere with the Rayleigh scattering signal due to air molecules, thus making the interpretation of the data difficult.

The differential cross-section for Rayleigh scattering of polarized light from a particle viewed at 90° to the plane of polarization is given by[75]

$$\left(\frac{\partial\sigma}{\partial\Omega}\right)_{particle} = \frac{16\pi^4}{\lambda^4}\left[\frac{n^2-1}{n^2+2}\left(\frac{d_p}{2}\right)^3\right]^2 \tag{2.5}$$

where n is the particle material relative refractive index, i.e. :

$$n = \frac{n_{particle}}{n_{medium}} \tag{2.6}$$

In terms of the volume $V_p$ of the small scatterer, the last equation becomes :

$$\left(\frac{\partial\sigma}{\partial\Omega}\right)_{particle} = \frac{9\pi^2 V_p^2}{\lambda^4}\left(\frac{n^2-1}{n^2+2}\right)^2 \tag{2.7}$$

Hirleman[71] mentions that for visible radiation, Rayleigh scattering approximations are valid for particles diameters of $d < 0.05\mu m$; and geometric optics approximations are valid for roughly $d > 5\mu m$. According to Siegel and Howell[75], an approximate size limit for Rayleigh scattering is that the ratio of particle radius to the wavelength is less than 0.05 . McCartney[76] mentions that Rayleigh scattering regime may be assumed for $d_p < 0.06\lambda$. According to Clemens and Mungal[77], for a particle diameter that is less than about ten times the wavelength of the light, the scattering can be considered Rayleigh scattering. The particles size estimation is done in Sec. 2.8.3.

### 2.8.2 Planar Rayleigh/Mie Scattering

The experiments were carried-out with two kinds of "fuels" injected into the main airstream : air and helium. The helium was used to simulate hydrogen injection. Air was used to make preliminary runs in order to minimize the helium consumption. Due to a large difference in the Rayleigh cross section (about 100 at 193 nm) between the injected helium and the mainstream air, in the molecular regime, one would expect a very low signal from the helium flow. Hence, the pure helium signal and the background signal are of comparable magnitude[78]. Outside the helium injection region and the boundary layer, Rayleigh signals were predominantly due to clusters which were formed as a result of cooling which takes place during the expansion process[79]. Shirinzadeh et al.[74] also pointed out that the Rayleigh signal due to clusters is a strong function of the local pressure and temperature of the flow. The largely differing scattering cross sections of air and helium together with the existing signal-to-noise ratio ( see the "binning technique" in Sec. 2.5.2 ), and by applying the technique described in Sec. 4.4.2.6, enable the helium jet in the Rayleigh scattering images to be identified. In order to identify the air injected into the main airstream the fog visualization technique is used, taking advantage of the large scattering cross sections of particles seeded into the flow. Tests were conducted where the helium was also seeded. In general, two fog visualization methods are employed[77] :

1. **Product formation method**

   This method is particularly useful because it directly marks the mixed fluid. The technique involves the seeding of the low speed stream with water or alcohol vapors. When the vapor laden relatively warm fluid mixes with the relatively cold high speed fluid, the water rapidly condenses, forming a fine fog. Because droplets are formed only where mixing occurs, and because the similarity to a

chemically reacting system, where two separate reactants meet within a mixing zone to form a product, this method is called the "product formation" method in analogy with combustion.

2. **Passive scalar method**

   In this method the droplets are allowed first to condense throughout the entire supersonic stream, and then to dilute by mixing with the low speed stream. Hence, this method provides a marker that is passive in the sense that it does not affect the velocity field.

Both methods are simple and safe to use.

### 2.8.3 Ethanol Condensation

In the present work the "fuel" was seeded with ethanol. First, water was considered as a seeding liquid. Its relatively low vapor pressure caused an incomplete evaporization upon reaching the injector's exit. For this reason it was changed to ethanol, which has a higher vapor pressure than the water. It also has the added benefit of low heat of vaporization, thus perturbing the flow less upon condensation. The mass fraction of ethanol seeded into the "fuel" flow was about 0.003 for air "fuel" and about 0.01 for helium "fuel" ( see Table 2.4 ). The numerical simulations of Squires and Eaton[80] demonstrate that mass loadings of less than 1% have negligible effect on turbulence quantities in isotropic turbulence, suggesting that in the present study the condensate fog does not influence the turbulence. Upstream of the injector nozzle throat the ethanol was in vapor form. As the flow expands through the nozzle, the ethanol condenses through homogeneous nucleation, where the nuclei consist of small molecular clusters of ethanol. High levels of supersaturation are

achieved because small molecular clusters ( smaller than the critical diameter ) are not stable and evaporate. Only clusters larger than the critical size are stable and continue to grow. Clusters of this size become more probable at higher supersaturation ratios. This ratio is defined as the ratio of the vapor pressure to the saturation pressure at the static temperature of the carrier gas. Wegener et al.[70] investigated the condensation of ethanol in supersonic nozzles and found that once sufficient numbers of stable cluster nuclei are formed, the condensation process takes place rapidly in about $50\mu s$, after which, virtually all of the vapor has condensed. There will always be some vapor present since there is a finite saturation pressure at the free stream conditions. The number density and the radii of ethanol droplets leaving the nozzle exit were measured by Clumpner[81], where the droplet number densities were found to be about $10^{12} - 10^{13}\ cm^{-3}$ with radii of about 50 - 100 $\AA$ ( diameter of 0.01 - 0.02 $\mu m$ ) and a Gaussian distribution with standard deviation of about $8\AA$ (0.0008 $\mu m$). Because the experimental conditions ($M_{exit} = 1.4$) in the above cited work were close to the present work ($M_{exit} = 1.63$), it is assumed that the ethanol droplets in this study are of comparable size. As pointed out, the wavelength of the light is 266 $nm$ ( 0.266 $\mu m$ ). If the particle diameter is less than about ten times the wavelength of light, then the scattering can be considered Rayleigh scattering, where the scattered light increases as the sixth power of particle diameter[77]. According to McCartney[76], Rayleigh scattering regime may be assumed for $d_p < 0.06\lambda$. In the present study, taking the larger diameter, $d_p/\lambda = 0.02/0.266 \sim 0.075$ which is less than 0.1, but higher then 0.06. This particle diameter is at the nozzle exit. Downstream from the nozzle exit the ethanol droplets grow due to coalescence, and the droplets diameter increases, favoring Mie scattering rather than Rayleigh scattering.

### 2.8.4 The Motion of Ethanol Droplets

The ethanol condensation takes place in the injector nozzle and ethanol droplets are carried out of the nozzle by the fuel jet. The jet mixes with the main air stream, and light scattering from the ethanol droplets signals the mixing region providing the droplets follow the jet flow. The question is how accurately these particles follow the fluid motion and represent the flow structures. This question can be answered by analyzing the ratio of the particle aerodynamic response time to the local flow time scale, known as the Stokes number. Direct numerical simulations conducted by Samimy and Lele[82], for a particle laden compressible mixing layer suggest that for correct visualization, the Stokes number should be less than 0.5 . In the present subsection the Stokes number for the present visualization is estimated.

If a spherical particle, of density $\rho_p$, velocity U, and diameter d, is projected into a quiescent fluid with viscosity $\mu$, and its drag can be considered Stokesian, then a characteristic stop time $t_p$ is given by Melling[83] as

$$t_p = \frac{\rho_p d^2}{18\mu}(1 + 2.7Kn) \tag{2.8}$$

where the term in parentheses is a correction factor for slip, due to free molecular flow and Kn is the Knudsen number based on particle diameter. If the ethanol droplets are assumed to be $0.02\mu m$ and injected into air or into helium, then this characteristic time, calculated from the above equation, is given in Table 2.5. The ratio of this stop time to an adequate fluid mechanical time scale, $t_f$, is the Stokes number, Sk=$t_p/t_f$. The fluid mechanical time scale is defined as :

$$t_f = \frac{\delta}{\Delta U} \tag{2.9}$$

where $\delta$ is the jet visual half thickness ( the radius of the jet ) and $\Delta U$ is the velocity difference across the jet, i.e., the jet centerline velocity minus the main stream velocity.

In a given flow $t_f$ is changing as the flow is evolving. Therefore the smallest $t_f$ should be used in the calculations, i.e., the time based on the jet exit characteristics. Table 2.5 summarizes the ethanol droplet characteristics. The formulas provided by White[84], pp.27–29, were used to estimate the mean-free-path and viscosities of the gases ( air and helium ). The ethanol properties were taken from Wegener et al.[70].

Table 2.5 Ethanol droplets characteristics

| Property | | In air jet | In helium jet |
|---|---|---|---|
| $\Delta U$ | m/s | 61 | 705 |
| $\delta_{jet}$ | m | $3.6 \times 10^{-3}$ | $3.6 \times 10^{-3}$ |
| $t_f$ | $\mu s$ | 59 | 5 |
| $\lambda_{mfp,gas}$ | m | $3.2 \times 10^{-8}$ | $9.2 \times 10^{-8}$ |
| Kn ( based on $d_p$=0.02 $\mu m$ ) | | 1.6 | 4.6 |
| $\mu_{gas}$ | Pa s | $1.27 \times 10^{-5}$ | $1.15 \times 10^{-5}$ |
| $\rho_p$ | kg/$m^3$ | 879.3 | 917.3 |
| $t_p$ | $\mu s$ | 0.0082 | 0.0238 |
| Sk=$t_p/t_f$ | | 0.00014 | 0.00476 |

Samimy and Lele[82] calculated the Stokes number using a fluid mechanical time based on vorticity thickness of the shear layer. Using the incompressible result that the visual thickness is about twice the vorticity thickness, the Stokes number based on the visual thickness should be less than 0.25 . This condition is clearly met in the present work for both jets for particles size corresponding to the injector exit. Downstream from the nozzle exit the ethanol droplets grow due to coalescence, and the diameters of the droplets increase, thus changing the characteristic stop time of

the particles, $t_p$. The particle coagulation is discussed in the Sec. 2.10.2.4. The effect of coagulation on the ethanol droplets is shown in Table 2.7. The diameter of the droplets can increase about twice the size at the jet exit plane. Even for particles 10 times bigger than the estimated size, the Stokes number is less than the limit set by Samimy and Lele[82]. It may be concluded that the visualization is correct in the sense that the particles faithfully follow the flow.

## 2.9 Resolution of the Visualization Tests

This section analyzes the experimental resolution of both spatial and temporal scales.

### 2.9.1 Spatial Resolution

The smallest imaged area was about 1.1 inch × 1.1 inch ( $\approx 780mm^2$ ) resulting in a discretized area of 109 $\mu m \times$ 109 $\mu m$ per pixel. The smallest scale in the flow is the Batchelor or mass diffusion scale, $\lambda_B$, which follows the relation : $\lambda_B \sim \delta Sc^{-1/2} Re_{\delta,\Delta U}^{-3/4}$, where $\delta$ is the local width of the shear layer ( the diameter of the jet ), $Re_{\delta,\Delta U}$ is the local Reynolds number based on the velocity difference of the shear flow and $\delta$, and Sc is the Schmidt number. Dowling and Dimotakis[85] suggest a constant of proportionality of 12.5 . Hence :

$$\lambda_B = 12.5 \times \delta \; Sc^{-1/2} \; Re_{\delta,\Delta U}^{-3/4} \tag{2.10}$$

As a means of quantifying the resolution of the experiment, the following ratio was estimated : $L/\lambda_B$, where L is the largest dimension of the examined volume ( here 109 $\mu m$ ) and $\lambda_B$ is defined above. If this ratio is greater than about one, then the amount of mixed fluid will be overpredicted since both mixed and pure fluids can

reside within the examined volume[21]. Table 2.6 shows the resolution of the present visualization experiments. The Schmidt numbers for each of the gas pairs ( helium-air and air-air ) were estimated from formulas provided in Bird et al.[86], pp.19–25 and pp.510–512.

Table 2.6 The resolution of the visualization experiments

| Property | | In air jet | In helium jet |
|---|---|---|---|
| L | m | $1.09 \times 10^{-4}$ | $1.09 \times 10^{-4}$ |
| $\delta_{jet}$ | m | $7.16 \times 10^{-3}$ | $7.16 \times 10^{-3}$ |
| $Re_{\delta,\Delta U}$ | | 73000 | 115000 |
| Sc | | 0.8 | 0.93 |
| $\lambda_B$ | m | $2.25 \times 10^{-5}$ | $1.5 \times 10^{-5}$ |
| $L/\lambda_B$ | | 5. | 7.3 |
| $\tau_B=\lambda_B/U$ | ns | 50. | 12. |

The experiment cannot resolve the spatial scale. For larger fields of view the spatial resolution was lower than the one mentioned in Table 2.6. Although the actual mixed fluid levels cannot be determined at the level of a diffusion length, the mixed fluid will be differentiated on gray scales between the minimum and maximum signals, which actually correspond to the average mixture fraction within each examined volume, and is composed of both pure and molecularly mixed fluid.

### 2.9.2 Temporal Resolution

The mean Batchelor-scale passage time is calculated based on the Batchelor's length scale and the jet exit velocity.

$$\tau_B = \frac{\lambda_B}{U} \tag{2.11}$$

This time scale is shown in Table 2.6. The width of the laser pulse is 10 ns, being less then the Batchelor-scale passage time. Hence the temporal scale may be considered resolved for air injection, but may not have been enough for helium injection.

## 2.10 Experimental Errors and Noise in Visualization Tests

Noise appears as random variation of the registered signal about an average value, either in time, or in space. These fluctuations obviously limit detectivity. It is therefore important to understand their origin, and to decrease their effects.

### 2.10.1 Noise Sources from the Test Facility

Problems during acquisition of the images included radio frequency noise from the laser and acoustical noise and vibrations from the facility. To minimize these effects the camera was wrapped first in aluminum foil and then in foam. The aluminum foil shielded the camera from the laser interference, while the foam damped the vibrations caused by the flow as it discharged to the laboratory. The rails on which the camera was mounted were secured with braces and weighted down with sand bags and weights, to reduce the mechanical vibrations transmitted to the camera. However, acoustical noise effects on the images could not be completely eliminated, and

from time to time, increased noise levels were experienced during data acquisition. Re-initialization of the camera (switching it off and then back on) eliminated the problem.

### 2.10.2 Noise Sources in Image Acquisition

Errors associated with the image acquisition are of five categories : marker shot noise, stray light, light sheet nonuniformity, fog nonuniformity, and camera noise.

#### 2.10.2.1 Marker shot noise

Marker shot noise is discussed by Rosensweig et al.[87] and is due to the fact that there is a finite number of markers within the probe volume and this number varies with time. The signal to marker shot noise ratio is :

$$SNR_{markershot} = \frac{N}{N_{rms}} = N^{1/2} \tag{2.12}$$

where $N_{rms}$ is the rms marker shot noise and N is the average number of markers within the measurement volume. For the present case, assuming a number density of $10^{12}$ $cm^{-3}$ ( corresponding to droplets of d $\approx$ 0.02 $\mu$m ), and using the volume imaged per pixel ( 0.109 $\times$ 0.109 $\times$ 0.5 $mm^3$ ), the expected signal-to-noise ratio is about 2000. Since this signal-to-noise ratio is very high it is not the dominant noise source.

#### 2.10.2.2 Stray light noise

Although every effort was made to eliminate stray light, it was impossible to completely eliminate this problem. In order to obtain an estimate of stray light levels, an image was acquired that had a small portion of the light sheet blocked, thus introducing a shadow in the image. After subtraction of the background image,

intensity levels on the order of 10% of the freestream value existed in the shadow region where zero intensity levels would be expected.

#### 2.10.2.3 Light sheet nonuniformity noise

The third source of error in the acquired images was due to laser light sheet nonuniformity. The method described in the image processing Sec. 4.4.2.3, greatly reduced these errors, although the correction was not always perfect.

#### 2.10.2.4 Fog nonuniformity noise

The fourth souce of error is fog nonuniformity. The ethanol droplets are formed within the injector nozzle and then injected into the main stream, where they grow due to coagulation ( coalescence ). The droplets which come out the nozzle are fairly uniform. For conditions very similar to the present study, Clumpner[81] found a Gaussian distribution of condensed ethanol droplets with a mean diameter of about 0.02 $\mu m$ and a standard deviation of 0.0008 $\mu m$. As the fog convects downstream the droplets size increases causing an augmentation in the light intensity. Thus the light intensity across an ethanol seeded side image changes due to the change of the droplets diameter. Fuchs[88] models the coagulation of aerosols by assuming the droplets can be described by Brownian motion superimposed on the bulk flow The droplets are assumed to coalesce upon every collision with other droplets, and the number density is expressed as :

$$N = \frac{N_0}{1 + K_0 N_0 t} \tag{2.13}$$

where N is the number density, $N_0$ is the initial number density, $K_0$ is the coagulation rate constant, and t is the time. The rate constant $K_0$ increases as the particle size decreases. A rough estimate of the effect of coagulation can be made by using the

values of $K_0$ tabulated in the book by Fuchs[88]. If the droplets exit the nozzle with d=0.02 $\mu m$ and $N_0 = 10^{12}\ cm^{-3}$, with a rate constant of $K_0 = 34 \times 10^{-10}\ cm^3/s$, as they travel from the nozzle exit about 1.5 inches downstream ( from the injector's exit to the end of the side view visualization plane ) they will have grown to about 0.021 $\mu m$ with a resulting increase of about 5% in the scattered light from one side to the other. Both turbulence and strong acoustic fields act to increase the coagulation rate beyond the predictions based on Brownian motion. Very high sound levels and high number densities typically augment the coagulation rate by less than an order of magnitude. In the present work, both strong acoustic fields and high number densities were encountered suggesting that this effect may be important. Taking the rate constant, $K_0$ to be one order of magnitude higher than the value given by Fuchs[88], i.e. $K_0 = 34 \times 10^{-9}\ cm^3/s$, the effect of coagulation on the ethanol droplets is given in Table 2.7.

For the side view visualization plane, the table shows an increase of about 57% in the particle diameter from the jet exit to the downstream edge of the field of view for the air jet. For the helium jet, the increase is only about 27% . Turbulence enhances coagulation by increasing the relative motion between particles. For particles that are small relative to the turbulent microscales, and move with the gas, the enhancement of coagulation due to turbulence is proportional to the third power of the particle diameter and the square root of the dissipation rate[89]. For the present conditions, the turbulence influence on droplet coagulation can be ignored.

In conclusion, these approximate estimations suggest that there is a non-negligible increase of droplets diameter across a side view resulting in a corresponding increase in the scattered light. About the same amount of light intensity increase across a side view was observed in the acquired images, and it proves, indirectly, that the ethanol

Table 2.7 Effect of coagulation on ethanol droplets characteristics

Rate constant of $K_0 = 34 \times 10^{-9}$ $cm^3/s$

| Distance from the injector exit | | | In air jet $U_{exit}$=449 m/s | | | In helium jet $U_{exit}$=1213 m/s | | | Comments |
|---|---|---|---|---|---|---|---|---|---|
| x | x/d | x/h | $t_f$ | N $\times 10^{11}$ | $d_p$ | $t_f$ | N $\times 10^{11}$ | $d_p$ | |
| m | | | $\mu$ s | $cm^{-3}$ | $\mu$ m | $\mu$ s | $cm^{-3}$ | $\mu$ m | |
| 0 | 0 | 0 | 0 | 10 | 0.02 | 0 | 10 | 0.02 | Jet exit plane |
| 0.0122 | 1.7 | 0.75 | 27 | 5.2 | 0.0248 | 10 | 7.5 | 0.0220 | No extension walls |
| 0.0381 | 5.3 | 2.3 | 85 | 2.6 | 0.0314 | 31 | 4.9 | 0.0254 | Side view edge |
| 0.0630 | 8.8 | 3.9 | 140 | 1.74 | 0.0359 | 52 | 3.6 | 0.0281 | 2″ extension walls |
| 0.1138 | 16 | 7 | 253 | 1.04 | 0.0425 | 94 | 2.4 | 0.0323 | 4″ extension walls |
| 0.1646 | 23 | 10 | 367 | 0.74 | 0.0476 | 136 | 1.78 | 0.0356 | 6″ extension walls |

droplets size are about the size that was initially assumed.

#### 2.10.2.5 CCD Camera Noise

The fifth source of error came from the CCD camera. First of all there are manufacturing non-uniformities, i.e. defects that locally affect the quality of the sensitive surface, e.g. isolated pixels with higher dark current than their neighbors (hot spot), or insensitive pixel (dark spot). The camera used in this study passed the manufacturer's quality tests, the number of defective pixel being within the manufacturer's tolerances. Image processing techniques (cosmetic corrections) can diminish these effects. Camera noise is comprised of three components : electronics, dark current,

and photonic.

1. The CCD is used with additional electronics that amplify the video signal and then digitize it for computer processing. The circuits themselves introduce noise. The preamplifier noise is generated by the on-chip output amplifier. This noise is very low, of the order of a few electrons, and is negligible. The only noise taken into consideration is due to the quantification error during signal digitization. For the 16 bit A-to-D converter used in the present work, and following the analysis of Buil[90], pp.45-46, the quantification noise is about four electrons. Therefore this noise is also negligible in the present application.

2. The dark current noise is the charge that accumulates from thermal generation at finite temperatures. It is called "dark" because it accumulates even with the shutter closed and the camera in complete darkness. This dark current is composed of a mean current and a thermal current noise. The mean thermal level is an offset which is simply added to the useful signal. This thermal signal may be removed from the data during the processing, by a simple subtraction. The thermal signal's value is spatially dependent. The thermal noise is the random component of the thermal signal that reduces the certainty about the true level of the signal. Because the camera is actively cooled ( to $-45°C$ ) this thermal level and thermal noise is very low, but is a particular concern in very low light applications not applicable in this experiment. Both preamplifier and dark noise remain constant at different light levels.

3. A noise that is extrinsic to the CCD is the so-called "photon noise". It originates in the quantum ( corpuscular ) nature of the light. The arrival of the photons follows a Poisson distribution. The value of this noise is equal to the square root

of the average number of the electrons that are collected during the integration ( = charge accumulation ) time, and is equal to the square root of the signal produced by the CCD ( the light level ). This noise is simply the uncertainty in the data. It is lower at low light levels, but comprises a higher proportion of the total signal. For high levels of light, as in the images taken with the flow on, the preamplifier noise and the dark noise are much lower than the photon noise, and the CCD is photon noise limited.

In conclusion, the CCD camera noise can be divided into two major components : the signal ( photonic ) noise and the readout noise. The readout noise includes all the noises that are not related to the signal, like thermal current, cosmetic defects, electronic noise. This readout noise can be estimated by measuring the fluctuation of the signal coming from a given pixel on a large number of successive images taken in complete darkness. At the begining of each run, a sequence of ten images taken in complete darkness ( so-called background images — see Sec. 2.6.2 ) was recorded and then analyzed to obtain the fluctuations r.m.s. and to estimate the readout noise. The readout noise was about 1% of the signal level. Such a level shows that the camera noise is controlled by the signal intensity level ( photonic noise ), and is indicative of the high quality of the CCD. Indeed, the signal-to-noise ratio of a perfect sensor is linked only to the statistical fluctuations of the number of photons received per unit of time[90]. A signal-to-noise ratio ( SNR ) in the range of 40-50 existed in the seeded images at typical laser light sheet intensities.

# Chapter 3

# NUMERICAL COMPUTATIONS

A numerical study which closely tracked the experimental effort, was undertaken to enhance the understanding of the experimental data, and to point out trends for improving the mixing enhancement techniques.

## 3.1 Computer Code

The computer code used in this study was one of the SPARK family of codes developed at the NASA Langley Research Center, Hampton, VA, USA. The particular SPARK code employed was the low storage version of the SPARK3D code which solves the full three-dimensional unsteady Navier-Stokes equations together with appropriate species continuity equations. A chemical source term may also be added to include the effects of finite-rate chemistry, however, this feature was turned off because the purpose of the computation was to simulate the cold flow experiments. A Baldwin and Lomax[91] algebraic eddy-viscosity turbulence model was included with the code. Eklund et al.[92] implemented the Eggers[93] mixing length model for the jet region of the flow. The code was advanced in time using a compact, spatially fourth-order accurate, symmetric, predictor-corrector algorithm until steady-state convergence was obtained. The code has been used to predict reacting and non-reacting flows of

different scramjet combustor injection schemes by Drummond[94], Eklund et al.[92,95], Riggins et al.[24–26], Northam et al.[23], Waitz[32], Donohue et al.[29].

Three cases were simulated in this study to allow direct comparison with the experiments, and these are as follows :

1. Simulation of the Mach 2 main air flow with the jet off, to study the ramp's influence on the flow.

2. Simulation of an air jet injected at Mach 1.63 from a circular nozzle into the Mach 2 main air flow.

3. Simulation of an helium jet injected at Mach 1.7 from a circular nozzle into the Mach 2 main air flow.

## 3.2 Governing Equations

The governing equations solved by the SPARK code are presented below. For three-dimensional flows, the continuity, momentum, energy and species equations can be expressed in the strong conservation form in the Cartesian coordinates as[99]

$$\frac{\partial \mathbf{U}}{\partial t} + \frac{\partial \mathbf{E}}{\partial x} + \frac{\partial \mathbf{F}}{\partial y} + \frac{\partial \mathbf{G}}{\partial z} = \mathbf{H} \tag{3.1}$$

For $i = 1, \ldots, (N_S - 1)$, the vectors of the conserved variables are as follows :

$$\mathbf{U} = \begin{pmatrix} \rho \\ \rho u \\ \rho v \\ \rho w \\ \rho \varepsilon \\ \rho Y_1 \\ \vdots \\ \rho Y_{N_S} \end{pmatrix} \tag{3.2}$$

$$\mathbf{E} = \begin{pmatrix} \rho u \\ \rho u^2 - \sigma_x \\ \rho uv - \tau_{xy} \\ \rho uw - \tau_{xz} \\ (\rho \varepsilon - \sigma_x)u - \tau_{xy}v - \tau_{xz}w + q_x \\ \rho Y_1(u + \tilde{u}_1) \\ \vdots \\ \rho Y_{N_S}(u + \tilde{u}_{N_S}) \end{pmatrix} \tag{3.3}$$

$$\mathbf{F} = \begin{pmatrix} \rho v \\ \rho uv - \tau_{xy} \\ \rho v^2 - \sigma_y \\ \rho vw - \tau_{yz} \\ (\rho \varepsilon - \sigma_y)v - \tau_{xy}u - \tau_{yz}w + q_y \\ \rho Y_1(v + \tilde{v}_1) \\ \vdots \\ \rho Y_{N_S}(v + \tilde{v}_{N_S}) \end{pmatrix} \tag{3.4}$$

$$\mathbf{G} = \begin{pmatrix} \rho w \\ \rho uw - \tau_{xz} \\ \rho vw - \tau_{yz} \\ \rho w^2 - \sigma_z \\ (\rho\varepsilon - \sigma_z)w - \tau_{xz}u - \tau_{yz}v + q_z \\ \rho Y_1(w + \tilde{w}_1) \\ \vdots \\ \rho Y_{N_S}(w + \tilde{w}_{N_S}) \end{pmatrix} \tag{3.5}$$

$$\mathbf{H} = \begin{pmatrix} 0 \\ \rho \sum_{i=1}^{N_S} Y_i b_{ix} \\ \rho \sum_{i=1}^{N_S} Y_i b_{iy} \\ \rho \sum_{i=1}^{N_S} Y_i b_{iz} \\ \rho \sum_{i=1}^{N_S} Y_i \mathbf{b}_i(\mathbf{u} + \tilde{\mathbf{u}}_i) \\ \dot{\omega}_1 \\ \vdots \\ \dot{\omega}_{N_S} \end{pmatrix} \tag{3.6}$$

where :

$$\sigma_x = -p + 2\mu\frac{\partial u}{\partial x} + \lambda\nabla\cdot\mathbf{u} \tag{3.7}$$

$$\sigma_y = -p + 2\mu\frac{\partial v}{\partial x} + \lambda\nabla\cdot\mathbf{u} \tag{3.8}$$

$$\sigma_z = -p + 2\mu\frac{\partial w}{\partial x} + \lambda\nabla\cdot\mathbf{u} \tag{3.9}$$

$$\tau_{xy} = \mu\left(\frac{\partial u}{\partial y} + \frac{\partial v}{\partial x}\right) \tag{3.10}$$

$$\tau_{yz} = \mu\left(\frac{\partial v}{\partial z} + \frac{\partial w}{\partial y}\right) \tag{3.11}$$

$$\tau_{xz} = \mu\left(\frac{\partial u}{\partial z} + \frac{\partial w}{\partial x}\right) \tag{3.12}$$

$$q_x = -\kappa\frac{\partial T}{\partial x} + \rho\sum_{i=1}^{N_S} h_i Y_i \tilde{u}_i + R_u T \sum_{i=1}^{N_s}\sum_{j=1}^{N_s} \frac{X_j D_i^T}{\mathcal{M}_i \mathcal{D}_{ij}}(\tilde{u}_i - \tilde{u}_j) \tag{3.13}$$

$$q_y = -\kappa\frac{\partial T}{\partial y} + \rho\sum_{i=1}^{N_S} h_i Y_i \tilde{v}_i + R_u T \sum_{i=1}^{N_s}\sum_{j=1}^{N_s} \frac{X_j D_i^T}{\mathcal{M}_i \mathcal{D}_{ij}}(\tilde{v}_i - \tilde{v}_j) \tag{3.14}$$

$$q_z = -\kappa\frac{\partial T}{\partial z} + \rho\sum_{i=1}^{N_S} h_i Y_i \tilde{w}_i + R_u T \sum_{i=1}^{N_s}\sum_{j=1}^{N_s} \frac{X_j D_i^T}{\mathcal{M}_i \mathcal{D}_{ij}}(\tilde{w}_i - \tilde{w}_j) \tag{3.15}$$

$$\varepsilon = \sum_{i=1}^{N_S} h_i Y_i - \frac{p}{\rho} + \frac{u^2 + v^2 + w^2}{2} \tag{3.16}$$

$$p = \rho R_u T \sum_{i=1}^{N_S} \frac{Y_i}{\mathcal{M}_i} \tag{3.17}$$

$$h_i = h_i^R + \int_{T^R}^{T} C_{p_i}\, dT \tag{3.18}$$

$$\frac{C_{p_i}}{R_i} = A_i + B_i T + C_i T^2 + D_i T^3 + E_i T^4 \tag{3.19}$$

Only $(N_S - 1)$ species equations were considered in the formulation since the mass fraction of the species which was left out was prescribed by satisfying the constraint equation

$$\sum_{i=1}^{N_S} Y_i = 1 \tag{3.20}$$

which was obtained from mass conservation. Coefficients in the specific heat at constant pressure expression were taken from McBride et al.[96]. Knowing the specific heat of each species, the enthalpy of each species can be found, and then the sum of the internal and kinetic energy is computed as

$$\varepsilon = \sum_{i=1}^{N_S} h_i Y_i - \frac{p}{\rho} + \frac{u^2 + v^2 + w^2}{2} \tag{3.21}$$

The individual species viscosities are computed from Sutherland's law :

$$\frac{\mu}{\mu_0} = \left(\frac{T}{T_0}\right)^{3/2} \frac{T_0 + S}{T + S} \tag{3.22}$$

where $\mu_0$ and $T_0$ are reference values and S is the Sutherland's constant. All three values are tabulated for the species used in this study [84,97]. The species thermal

conductivities are also computed from Sutherland's law :

$$\frac{\kappa}{\kappa_0} = \left(\frac{T}{T_0}\right)^{3/2} \frac{T_0 + S}{T + S} \tag{3.23}$$

but with different values of the reference values $\kappa_0$ and $T_0$, and the Sutherland's constant S . Additional data on different properties was obtained from Arp[98].

The multicomponent diffusion equation for the diffusion velocity of the $i^{th}$ species is expressed as

$$\begin{aligned} \nabla X_i \;=\; & \sum_{j=1}^{N_S} \left(\frac{X_i X_j}{\mathcal{D}_{ij}}\right) (\tilde{\mathrm{u}}_\mathrm{j} - \tilde{\mathrm{u}}_\mathrm{i}) + \left(\frac{\rho}{p}\right) \sum_{j=1}^{N_S} Y_i Y_j (\mathrm{b_i} - \mathrm{b_j}) + (Y_i - X_i) \left(\frac{\nabla p}{p}\right) + \\ & \sum_{j=1}^{N_S} \left(\frac{X_i X_j}{\rho \mathcal{D}_{ij}}\right) \left(\frac{D_j^T}{Y_j} - \frac{D_i^T}{Y_i}\right) \left(\frac{\nabla T}{T}\right) \end{aligned} \tag{3.24}$$

where

$$\tilde{\mathrm{u}}_\mathrm{i} = \tilde{u}_i \hat{\mathrm{i}} + \tilde{v}_i \hat{\mathrm{j}} + \tilde{w}_i \hat{\mathrm{k}} \tag{3.25}$$

In the diffusion equation, it is assumed that the body force vector per unit mass is negligible ($\mathrm{b_i} = 0.0, i = 1, \ldots N_S$) . In addition, the thermal diffusion coefficient, $D_i^T$, is considered to be negligible in comparison with the binary diffusion coefficient, $\mathcal{D}_{ij}$. The above equation was applied to only ($N_S - 1$) species. The diffusion velocity for the species that was left out was prescribed by satisfying the constraint equation

$$\sum_{i=1}^{N_S} Y_i \tilde{\mathrm{u}}_\mathrm{i} = 0 \tag{3.26}$$

The governing equations are expressed in terms of the generalized coordinate transformation, and are then solved in the computational domain[99–101].

## 3.3 Turbulence Modeling

The flow considered in this study was turbulent with separated regions. This type of flow is very difficult to model reliably even with the most sophisticated turbulence

models. While the turbulent fluctuations are not resolved, their effect upon the mean flow is modeled by solving the Reynolds-averaged Navier-Stokes equations. These equations include additional terms : the Reynolds stresses, heat flux and mass flux terms, that represent the effect of the turbulent fluctuations upon the mean flow. The turbulent stresses are calculated through the eddy viscosity ( Boussinesq ) approximation that relates the turbulent stresses to the mean rate of strain by a coefficient, called the eddy viscosity coefficient. This approximation assumes that the transport of fluid properties due to the motion of turbulent eddies is analogous to the effect due to molecular motion. Turbulence is then modeled as an increase in the transport coefficients, and the Reynolds-averaged equations become similar to the Navier-Stokes equations, except for the modifications to the transport coefficients. The effective transport coefficients take the form

$$\mu = \mu_l + \mu_t \tag{3.27}$$

$$k = C_p \frac{\mu_l}{Pr_l} + C_p \frac{\mu_t}{Pr_t} \tag{3.28}$$

$$\rho \mathcal{D} = \frac{\mu_l}{Sc_l} + \frac{\mu_t}{Sc_t} \tag{3.29}$$

The eddy viscosity coefficient, $\mu_t$, is evaluated as

$$\mu_t = c \rho U L \tag{3.30}$$

where c is a constant, U is a velocity scale and L is a length scale. However, U and L are properties of the flow rather than properties of the fluid. In this study two algebraic models were considered, namely the Baldwin-Lomax model and the Eggers model, so that the velocity and length scales were evaluated from the mean flow. The Baldwin-Lomax model[91] is extensively used for wall bounded flows. In this model, the velocity scale is based on the vorticity distribution and the length scale on the

distance from the wall. The Baldwin-Lomax treatment of the wall boundaries is combined with a turbulence model for the jet based on the Eggers length model[93] mixing. This approach was used by Eklund et al.[92] and by Chitsomboon et al.[102] to model the turbulence of a jet in a supersonic mainflow. The velocity scale is defined as the velocity in the jet's core with the constant c=0.0164 as given by Eggers[93]. The length scale is the average of the half-width of the jet in the spanwise and normal directions. The concentration of the injectant was used to determine the half-width. Smooth transitions are enforced at the boundary of the jet and at the edge of the wall boundary layer. In all calculations, the turbulent Schmidt and Prandtl numbers were set to constant values of 0.5 and 0.9 respectively, and the turbulent viscosity was limited to 1000 times the laminar viscosity[92].

## 3.4 Numerical Technique

The original code, developed by Drummond et al.[99,100], solved the two-dimensional set of equations. This code was subsequently modified, by Carpenter[101], to solve the three-dimensional set of equations while making efficient use of memory. This low memory version of the SPARK code provides two algorithms for solving the Navier-Stokes equations. The first algorithm is the original unsplit explicit technique of MacCormack which is a two-step predictor-corrector scheme. The algorithm is second-order accurate in both space and time. The second algorithm is the steady state Cross-MacCormack algorithm developed by Carpenter[101]. This algorithm is derived by replacing the one-sided difference operators in MacCormack's predictor-corrector scheme with compact difference operators. The algorithm, while formally still second-order accurate in space and time, attains fourth-order spatial accuracy

at steady state. To illustrate, consider a central difference approximation to the 2-D differential equation

$$\mathbf{U}_t + \mathbf{E}_x + \mathbf{F}_y = 0. \tag{3.31}$$

With the central-difference operators $\overline{\delta}$ and $\delta_2$ defined as

$$\overline{\delta_x}\mathbf{E}_{i,j} = \mathbf{E}_{i+1,j} - \mathbf{E}_{i-1,j} \tag{3.32}$$

$$\delta_{2x}\mathbf{E}_{i,j} = \mathbf{E}_{i+1,j} - 2\mathbf{E}_{i,j} + \mathbf{E}_{i-1,j} \tag{3.33}$$

one can write

$$\mathbf{E}_x = \frac{\overline{\delta_x}}{2\Delta x}\mathbf{E} - \frac{\Delta x^2}{3!}\mathbf{E}_{xxx} + O(\Delta x^4). \tag{3.34}$$

Transfering the second term on the RHS to LHS and rearanging, one obtains

$$(1 + \frac{\delta_{2x}}{3!})\mathbf{E}_x = \frac{\overline{\delta_x}\mathbf{E}}{2\Delta x} + O(\Delta x^4) \tag{3.35}$$

or

$$\mathbf{E}_x = \frac{\overline{\delta_x}}{2\Delta x}\mathbf{E}/(1 + \frac{\delta_{2x}}{3!}) + O(\Delta x^4). \tag{3.36}$$

Similarly,

$$\mathbf{F}_y = \frac{\overline{\delta_y}}{2\Delta y}\mathbf{F}/(1 + \frac{\delta_{2y}}{3!}) + O(\Delta y^4). \tag{3.37}$$

Substituting Eqs.( 3.36) and ( 3.37) into Eq. ( 3.31) yields

$$(1 + \frac{\delta_{2x}}{3!})(1 + \frac{\delta_{2y}}{3!})\mathbf{U}_t = -(1 + \frac{\delta_{2y}}{3!})\frac{\overline{\delta_x}}{2\Delta x}\mathbf{E} - (1 + \frac{\delta_{2x}}{3!})\frac{\overline{\delta_y}}{2\Delta y}\mathbf{F} + O(\Delta x^4, \Delta y^4). \tag{3.38}$$

Omitting the implicit differencing on the left hand side of the equation, which requires tridiagonal matrix inversion, then is obtained

$$\mathbf{U}_t = -(1 + \frac{\delta_{2y}}{3!})\frac{\overline{\delta_x}}{2\Delta x}\mathbf{E} - (1 + \frac{\delta_{2x}}{3!})\frac{\overline{\delta_y}}{2\Delta y}\mathbf{F} + O(\Delta x^2, \Delta y^2). \tag{3.39}$$

The algorithm given by Eq. ( 3.39), while formally second-order accurate, attains fourth-order spatial accuracy at steady state. Similarly, the Cross-MacCormack algorithm applied to Eq. ( 3.31) is implemented as

$$\Delta \mathbf{U}_{i,j} = -\frac{\Delta t}{\Delta x}\left[(1+\frac{\delta_{2y}}{3!})\mathbf{E}_{i+1,j} - \mathbf{E}_{i,j}\right] - \frac{\Delta t}{\Delta y}\left[(1+\frac{\delta_{2x}}{3!})\mathbf{F}_{i,j+1} - \mathbf{F}_{i,j}\right]$$

$$\Delta \mathbf{U}^{*}_{i,j} = -\frac{\Delta t}{\Delta x}\left[\mathbf{E}^{*}_{i,j} - (1+\frac{\delta_{2y}}{3!})\mathbf{E}^{*}_{i-1,j}\right] - \frac{\Delta t}{\Delta y}\left[\mathbf{F}^{*}_{i,j} - (1+\frac{\delta_{2x}}{3!})\mathbf{F}^{*}_{i,j-1}\right]$$

$$\mathbf{U}^{n+1}_{i,j} = \mathbf{U}^{n}_{i,j} + \frac{1}{2}\left[\Delta \mathbf{U}_{i,j} + \Delta \mathbf{U}^{*}_{i,j}\right]. \qquad (3.40)$$

For both algorithms only three planes of data need to be stored simultaneously. These planes correspond to the forward predictor and backward corrector planes around the grid point evaluated. The low storage version of the code generally requires about five time less storage than the full SPARK3D code, and is about 20% slower. Fourth-order artificial viscosity, based on gradients of pressure and temperature, is included in the solution algorithm to suppress numerical oscillations in the vicinity of shock waves.

## 3.5 Computational Grids

The grid used in the calculations was generated externaly to the SPARK code and is shown in Figs. 3.1–3.3. The grid is a body fitted grid, hence the ramps can be modeled accurately. The entire domain, including the ramps, was gridded and then the injector ramp was formed by blanking out a region of the domain. The blanking was performed within the code by setting the velocity equal to zero at all points within the ramp, and applying appropiate boundary conditions on the walls of the ramp and the injection plane. The grid consists of a number of separate zones in which the nodes were clustered at one or more of the zonal edges so that large flow

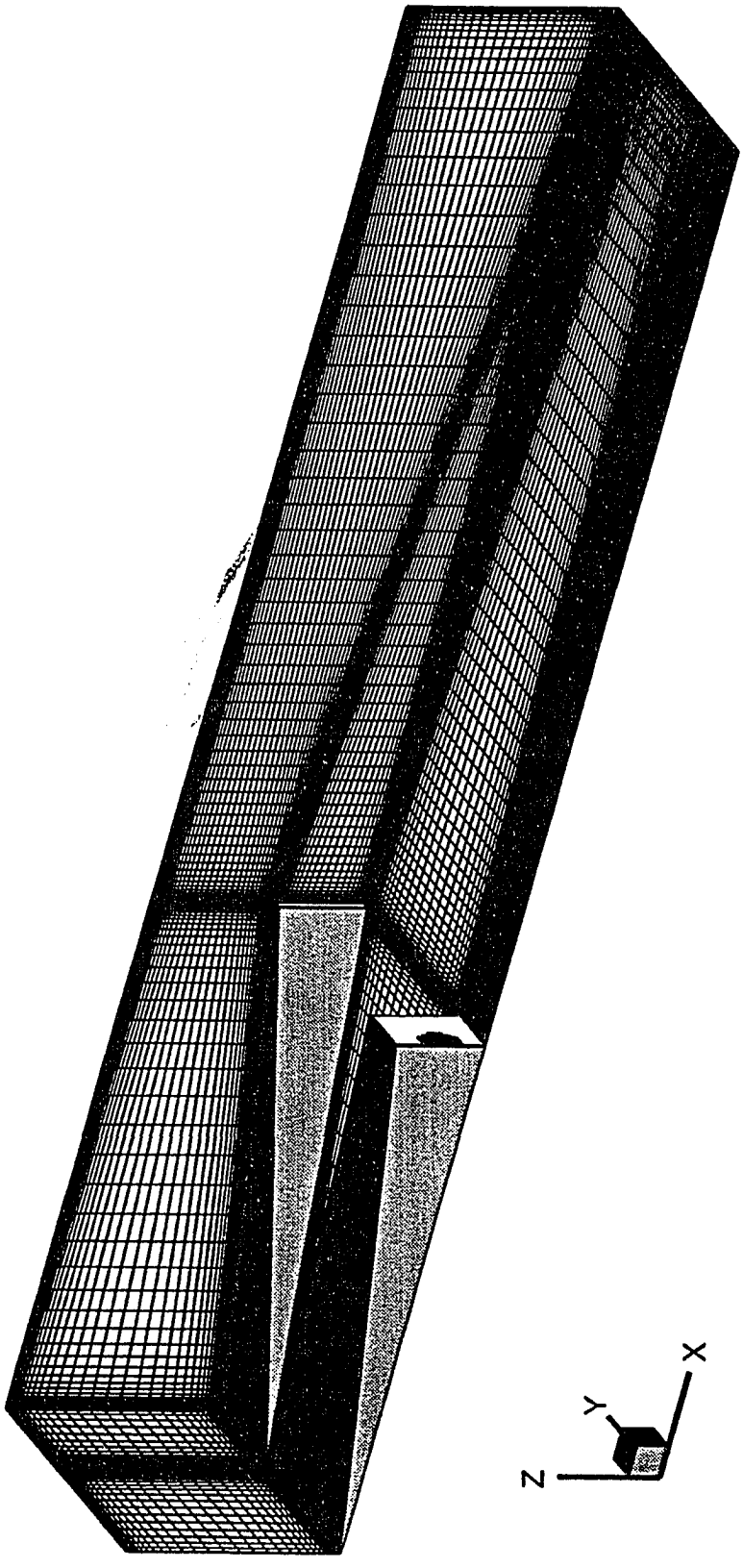


Fig. 3.1 Perspective view of the computational grid

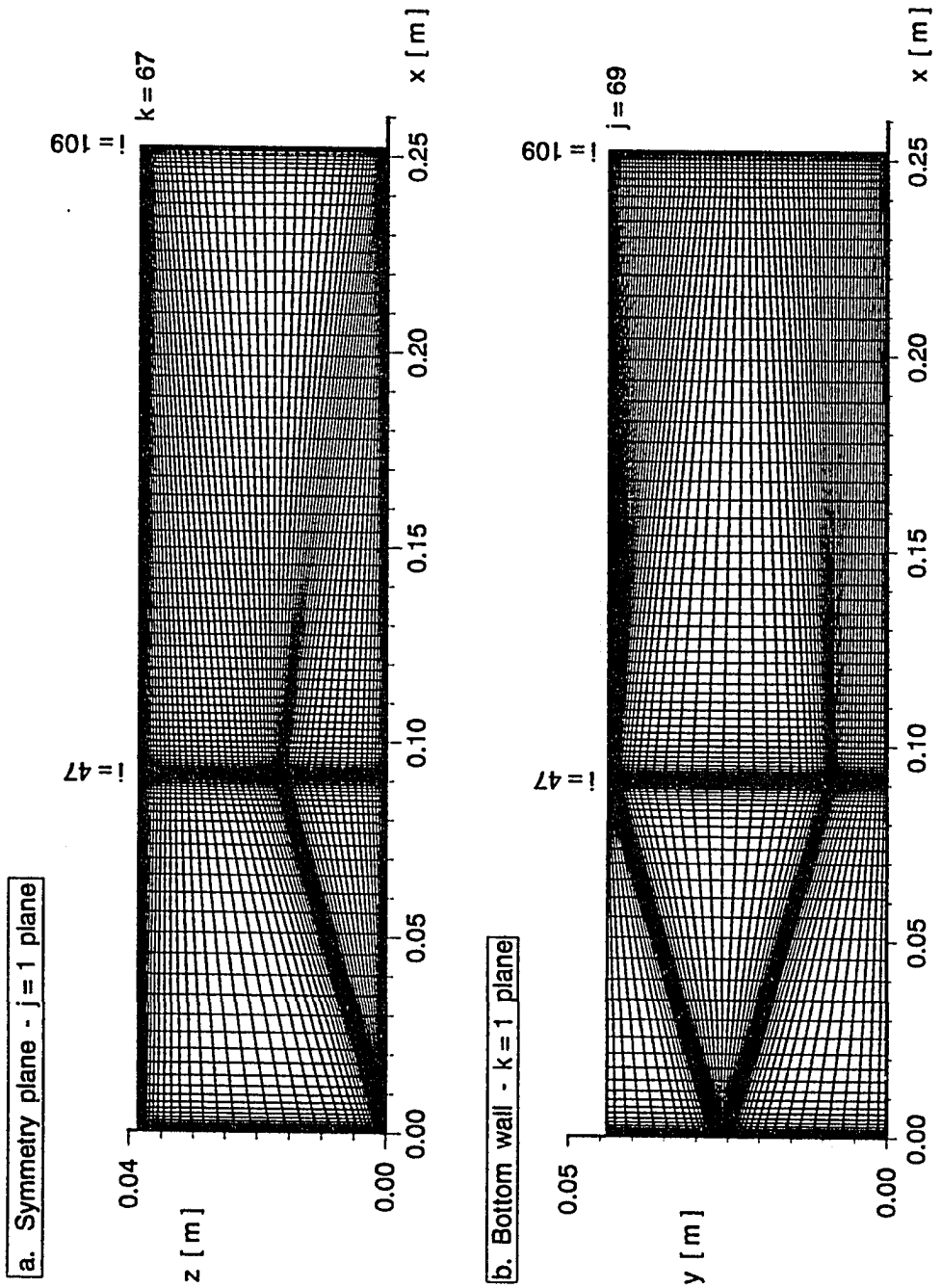


Fig. 3.2 Longitudinal planes of the computational grid

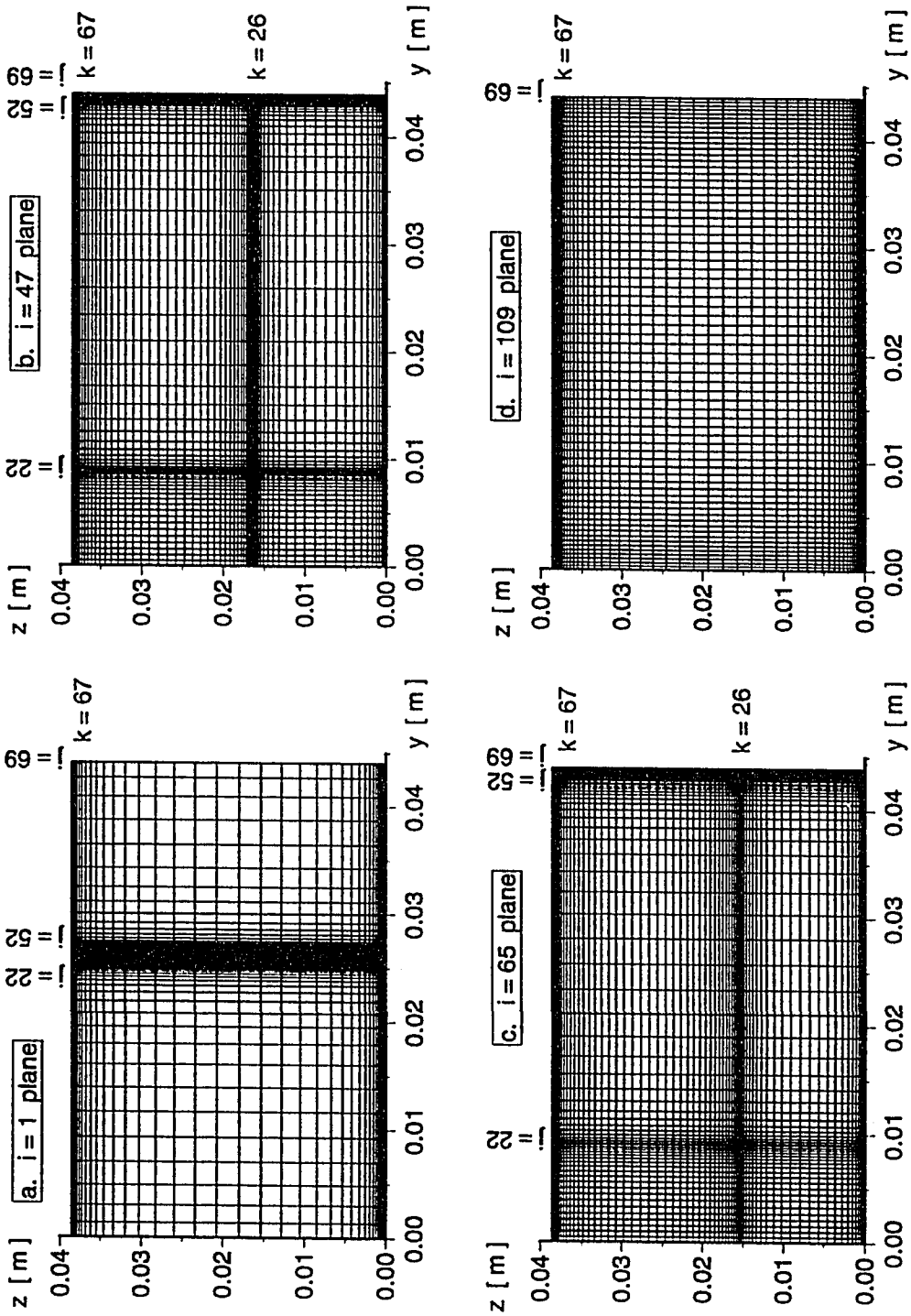


Fig. 3.3 Transverse planes of the computational grid

gradients near the boundaries and the planes defining the injector could be resolved without excessive computational expense. The functions for grid stretching, were taken from Anderson et al.[103], pp.247–251. Details of the zonal boundaries and stretching parameters are given in Tables 3.1 – 3.3. The dimension of the grid is 109 points in x, 69 in y, and 67 in z-direction, a total of 503,907 points. Table 3.4 shows a comparison between the grid used in the present study and grids used in other works done on swept-ramp injectors.

## 3.6 Boundary Conditions

The inflow boundary conditions were determined from the reservoir conditions, assuming slug flow, and were chosen to match those of the experimental studies. The velocity, pressure, temperature, and concentrations were specified. Using the fact that the experimental duct is symmetric, only half of the duct was modeled, and the symmetry conditions were applied at the center plane. Along solid walls, the no-slip and no-penetration conditions were imposed, together with assumptions of a zero normal pressure gradient and a zero normal total-temperature gradient (adiabatic walls). The bottom wall, top wall, and ramp surfaces were treated in this manner. However, the side wall was treated as an inviscid wall by setting only the normal velocity equal to zero, because the grid resolution on this wall could not resolve the boundary layer, causing instabilities in the solution. This treatment was not expected to appreciably affect the accuracy of the solution in the vicinity of the jets. The flow variables at the exit plane boundary were extrapolated from the interior assuming a zero gradient at the exit plane.

Table 3.1 Zonal boundaries and stretching parameters for x-direction

| x-direction grid nodes | Length mm. | $\beta$ | $\alpha$ | Comments |
|---|---|---|---|---|
| 1 - 47 | 91.06 | 1.009 | 0.5 | ramp region |
| 47 - 65 | 16.00 | 1.03 | 0.5 | |
| 65 - 91 | 102.62 | 1.25 | 0.5 | |
| 91 - 109 | 42.41 | 1.02 | 0.0 | |

Table 3.2 Zonal boundaries and stretching parameters for y-direction

| y-direction | Inlet plane | | | Injection plane | | | Exit plane | | |
|---|---|---|---|---|---|---|---|---|---|
| grid nodes | Length mm. | $\beta$ | $\alpha$ | Length mm. | $\beta$ | $\alpha$ | Length mm. | $\beta$ | $\alpha$ |
| 1 - 12 | 20.86 | 1.435 | 0.5 | 4. | 1.93 | 0.5 | | | |
| 12 - 22 | 4.1 | 1.05 | 0.0 | 4.9 | 1.0945 | 0.0 | | | |
| 22 - 52 | 1.92 | uniform | — | 34.04 | 1.0255 | 0.5 | | | |
| 52 - 62 | 4.1 | 1.05 | 0.0 | | | | | | |
| 62 - 69 | 12.92 | 1.395 | 0.5 | | | | | | |
| 52 - 69 | | | | 0.96 | 1.02 | 0.0 | | | |
| 1 - 69 | | | | | | | 43.9 | 1.25 | 0.5 |

Table 3.3 Zonal boundaries and stretching parameters for z-direction

| z-direction | Inlet plane | | | Injection plane | | | i = 91 plane | | |
|---|---|---|---|---|---|---|---|---|---|
| | | | | | | | Exit plane | | |
| grid nodes | Length | $\beta$ | $\alpha$ | Length | $\beta$ | $\alpha$ | Length | $\beta$ | $\alpha$ |
| | mm. | | | mm. | | | mm. | | |
| 1 - 26 | 0.20 | 1.0015 | 0.0 | 16.256 | 1.0445 | 0.5 | | | |
| 26 - 67 | 38.40 | 1.00605 | 0.5 | 22.352 | 1.045 | 0.5 | | | |
| 1 - 67 | | | | | | | 38.60 | 1.0067 | 0.5 |
| | | | | | | | 38.60 | 1.0044 | 0.5 |

Table 3.4 Grids comparison

| | | Present study | Eklund et al.[95] | Riggins et al.[24] | Waitz[32] |
|---|---|---|---|---|---|
| Type | | Body fitted | Body fitted | Cartesian | Cartesian |
| x | mm. | 252.1 | 419.1 | 140. | 500. |
| $N_x$ | | 109 | 151 | 87 | 100 |
| y | mm. | 43.9 | 21.2 | 44. | 25.4 |
| $N_y$ | | 69 | 43 | 61 | 27 |
| z | mm. | 38.6 | 38.1 | 38. | 88.9 |
| $N_z$ | | 67 | 79 | 61 | 45 |
| $N_{tot}$ | | 503907 | 512947 | 323727 | 121500 |
| Average cell volume | $mm^3$ | 0.848 | 0.660 | 0.723 | 9.292 |

## 3.7 Iteration Technique

First, the computations were started without fuel injection at the ramp base ( downstream-facing step ) by setting the flow quantities in the domain equal to their values at the inflow plane. However, behind the ramp a linear profile in velocity was assumed. Initially, the turbulent model was turned off, and a laminar flow was computed. The solution was advanced in time using a local time step calculated by combining the convective and the diffusive time scales. The Courant number and the artificial viscosity coefficient were initially set equal to 0.1 and 1.5, respectively. After 33,000 iterations with approximately 6.8 cpu seconds per time step ( on a CRAY Y-MP computer ), the fuel jet was turned on by setting the appropriate conditions on the plane surface of the downstream-facing ramp base. After 8000 iterations of laminar flow, the turbulence model was turned on. The Courant number and the artificial viscosity coefficient were gradually changed to 0.5 and 0.5 respectively. For this case approximately 8.8 cpu seconds per time step were required to advance the computations on a CRAY Y-MP computer.

The residual is defined as the maximum change in the non-dimensional density between successive iterations, and is expressed as :

$$\frac{\rho_t - \rho_{t-\Delta t}}{\rho_t} \tag{3.41}$$

where $\rho_t$ means the density at time step "t". The computations were considered converged when the residual was below 0.5 % . In addition, the flowfield variables were monitored to ensure steady-state was achieved.

# Chapter 4

# DATA REDUCTION AND ANALYSIS PROCEDURES

This chapter describes the procedures to reduce the flow field survey data and the image processing procedures. Also, the experimental and computational data analysis procedures are described.

## 4.1 Matrix of Experimental Cases

This section is devoted to presenting a tabulation of the test cases studied both by visualization and flow field probe survey. Table 4.1 displays the visualization experiments cases and Table 4.2 shows the flow field survey cases. The cases that were tested are marked by an "X". A total of nine different cases were tested.

## 4.2 Reduction of Flow Field Survey Data

The raw data ( $p_{total}$, $p_{cone}$, $T_0$ ) were reduced to obtain fundamental variables ( M, $\rho$, p, T ). The reduction procedure relied on several assumptions and approximations which had no uniform validity throughout the flow field. Assuming inviscid flow

Table 4.1 Visualization-Experiments Matrix

| No. | Nozzle inserts | Main Flow | Injectant | Cross-section views 0″ x/d=1.7 x/h=.75 | 2″ x/d=8.8 x/h=3.9 | 4″ x/d=16. x/h=7. | 6″ x/d=23. x/h=10. | Side views |
|---|---|---|---|---|---|---|---|---|
| 1 | Circular nozzle | OFF | Ethanol seeded air | X | X | | | X |
| | | | Helium | X | X | | | X |
| | | ON | Ethanol seeded air | X | X | X | X | X |
| | | | Ethanol seeded helium | X | X | X | X | X |
| | | | Helium | X | X | X | X | X |
| 2 | Nozzle with three steps | OFF | Ethanol seeded air | X | X | | | X |
| | | | Helium | X | X | | | X |
| | | ON | Ethanol seeded air | X | X | X | X | X |
| | | | Ethanol seeded helium | X | X | X | X | X |
| | | | Helium | X | X | X | X | X |
| 3 | Nozzle with vortex generators in x orientation | OFF | Ethanol seeded air | X | X | | | X |
| | | | Helium | X | X | | | X |
| | | ON | Ethanol seeded air | X | X | X | X | X |
| | | | Ethanol seeded helium | X | X | X | X | X |
| | | | Helium | X | X | X | X | X |
| 4 | Nozzle with vortex generators in cross orientation | OFF | Ethanol seeded air | X | X | | | X |
| | | | Helium | X | X | | | X |
| | | ON | Ethanol seeded air | X | X | X | X | X |
| | | | Ethanol seeded helium | X | X | X | X | X |
| | | | Helium | X | X | X | X | X |
| 5 | Tapered nozzle with horizontal throat slot | OFF | Ethanol seeded air | X | X | | | X |
| | | | Helium | X | X | | | X |
| | | ON | Ethanol seeded air | X | X | X | X | X |
| | | | Ethanol seeded helium | X | X | X | X | X |
| | | | Helium | X | X | X | X | X |
| 6 | Tapered nozzle with vertical throat slot | OFF | Ethanol seeded air | X | X | | | X |
| | | | Helium | X | X | | | X |
| | | ON | Ethanol seeded air | X | X | X | X | X |
| | | | Ethanol seeded helium | X | X | X | X | X |
| | | | Helium | X | X | X | X | X |
| 7 | Elliptical nozzle with horizontal major axis | OFF | Ethanol seeded air | X | X | | | X |
| | | | Helium | X | X | | | X |
| | | ON | Ethanol seeded air | X | X | X | X | X |
| | | | Ethanol seeded helium | X | X | X | X | X |
| | | | Helium | X | X | X | X | X |
| 8 | Elliptical nozzle with vertical major axis | OFF | Ethanol seeded air | X | X | | | X |
| | | | Helium | X | X | | | X |
| | | ON | Ethanol seeded air | X | X | X | X | X |
| | | | Ethanol seeded helium | X | X | X | X | X |
| | | | Helium | X | X | X | X | X |
| 9 | Trapezoidal nozzle | OFF | Ethanol seeded air | X | X | | | X |
| | | | Helium | X | X | | | X |
| | | On | Ethanol seeded air | X | X | X | X | X |
| | | | Ethanol seeded helium | X | X | X | X | X |
| | | | Helium | X | X | X | X | X |

Table 4.2 Probes-Experiments Matrix

| No. | Nozzle inserts | Cross-sections 0″ x/d=1.7 x/h=.75 | 2″ x/d=8.8 x/h=3.9 | 4″ x/d=16. x/h=7. | 6″ x/d=23. x/h=10. | Flow conditions |
|---|---|---|---|---|---|---|
| 1 | Circular nozzle | X | X | X | X | |
| 2 | Nozzle with three steps | X | X | X | X | Jet |
| 3 | Nozzle with vortex generators in x orientation | X | X | X | X | |
| 4 | Nozzle with vortex generators in cross orientation | X | X | X | X | and |
| 5 | Tapered nozzle with horizontal throat slot | X | X | X | X | |
| 6 | Tapered nozzle with vertical throat slot | X | X | X | X | main |
| 7 | Elliptical nozzle with horizontal major axis | X | X | X | X | |
| 8 | Elliptical nozzle with vertical major axis | X | X | X | X | flow |
| 9 | Trapezoidal nozzle | X | X | X | X | |
| 10 | Not applicable | X | X | X | X | Main flow only - jet off |

about the cone of the static pressure probe, with a conical shock of uniform strength attached to the tip of the cone, results in a conical flow pattern [ Shapiro[104], pp.653–654 ]. This flow is tabulated for zero angle of attack[105,106]. For a given gas, i.e. given $\gamma$ and gas constant R, the following relation is obtained :

$$\frac{p_\infty}{p_{cone}} = func(M_\infty, \theta_{cone}) \tag{4.1}$$

For a known $\theta_{cone}$, the above relation becomes :

$$p_\infty = F(M_\infty + measured\ quantity) \tag{4.2}$$

For the total pressure ( Pitot ) probe the following assumptions are made :

1. The shock wave which stands ahead of the mouth of the tube, is locally normal to the stagnation streamline.

2. The flow of the stagnation line is brought to rest isentropically in the subsonic region aft of the shock.

3. The ratio of specific heats, $\gamma$, is a constant.

These assumptions result in the Rayleigh supersonic Pitot-tube formula which is given as follows [ Shapiro[104], pp.153–154 ] :

$$\frac{p_\infty}{p_{total}} = \frac{\left[\frac{2\gamma}{\gamma+1}M_\infty^2 - \frac{\gamma-1}{\gamma+1}\right]^{\frac{1}{\gamma-1}}}{\left[\frac{\gamma+1}{2}M_\infty^2\right]^{\frac{\gamma}{\gamma-1}}} \tag{4.3}$$

For a given gas, i.e. given $\gamma$, the above relation may be expressed as :

$$p_\infty = G(M_\infty + measured\ quantity) \tag{4.4}$$

The intersection of F and G defines the unique values of $p_\infty$ and $M_\infty$ which satisfy the measured quantities. The procedure to reduce the data was based on a root-bisection

iteration in $M_\infty$ on the difference $F - G$ . At each iteration step, the conical flow solution was obtained from three points interpolation in the tables given by Sims[105] for zero angle of attack. The procedure was calibrated in a straight duct flow.

## 4.3 Presentation of the Flow Survey Data

Each run consisted of measuring a two-dimensional plane. The four measured planes are shown in Fig. 4.1a. The x-distance shown in the figure was measured from the injector exit centerline. The survey was completed over half duct only. The sampling grid is shown in Fig. 2.6. It consisted of 168 points within the region of interest. Each probe ( Pitot, static pressure, and total temperature ) was passed through the same point. Passing each of the probes through the same point in space required extension of the survey beyond the bounds of the grid. Further, since it was necessary that the measurements from each of the probes be acquired at the same physical location in space, the spacing of the grid in the spanwise direction ( y-direction ) had to be evenly divisible into the spacing between the probes themselves. The rake was stopped at each grid point as shown in the algorithm of Sec. 2.6.1. The raw data was reduced as described in the preceding section, and then it was mirrored about the symmetry plane. After being mirrored the data was contoured with Tecplot[107], a graphic software package.

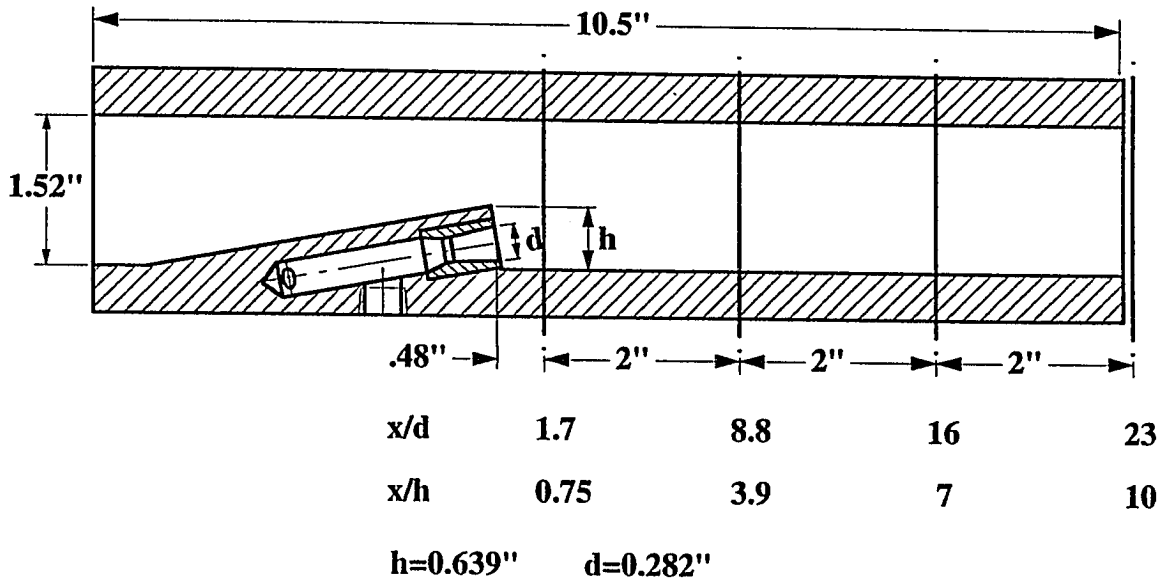


a. Cross-section visualization and probes measurements planes

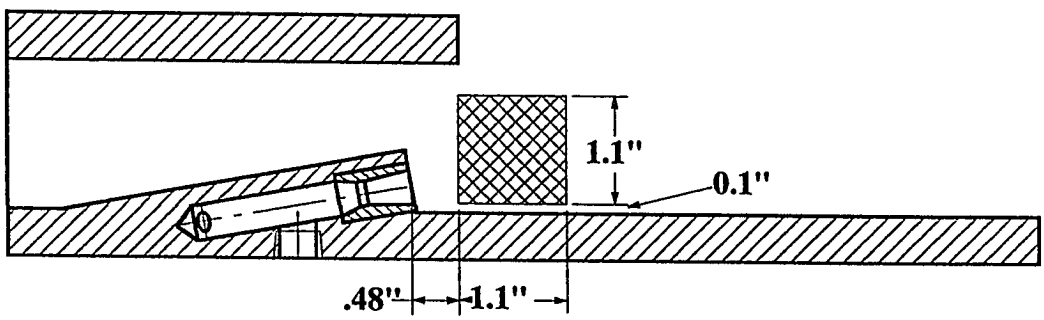


b. Side-view visualization plane

Fig. 4.1 Flow field survey planes

## 4.4 Image Processing

Image processing was used to enhance and analyze digital images. Image acquisition and processing systems typically consist of the following components :

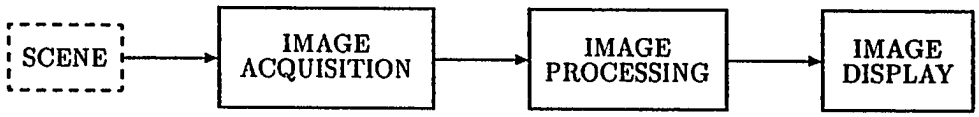


Image acquisition devices convert a continuous ( analog ) scene into a numerical representation ( a digital image ) of that scene so that it may be processed by a computer. Image processing is then employed to perform two tasks : one is to produce improved digital images ( image enhancement ), and the second is to generate quantitative data about the objects within the image ( image analysis ). Finally, the image display component provides a means to output the resultant image on a screen or on a hardcopy.

This section describes the image processing procedures that assist in interpretation and in extracting useful information from the CCD images. Image processing was carried out on a SUN workstation using the PV-WAVE, an image processing software package by Precision Visuals, Inc.[108], and KBVision, an image processing software by Amerinex Artificial Intelligence,Inc.[109].

### 4.4.1 Image Processing Terminology

A digitized image is represented by a two-dimensional array, I(x,y), where x and y denote the spatial coordinates, and the value I(x,y) is the brightness or intensity function. If I(m,n) is used, m represents the x-direction index and n, similarly, is the y-direction index, and M and N denote the maximum value of m and n respectively.

The smallest unit that is addressable in an image is defined as a picture element or *pixel.* The digital value of each pixel represents its intensity value. Images of this form are known as *sampled* or *raster* images, because they consist of discrete grid samples. The resolution, or the spatial sampling, determines the intervals at which the scene is sampled to acquire a good approximation of that scene. The greater the resolution, the greater the detail. In this study, the resolution of the images was 256 × 256 pixels. Brightness quantization imposes a limit on the number of discrete grey levels that a pixel value may be assigned. The acquisition system used 16 bits per pixel, thus yielding 65536 different grey levels for each pixel. During the image processing the pixel values were scaled down to 8 bits per pixel, thereby allowing each pixel to have up to 256 different values at any one time. On this scale, zero value represents black, and 255 represents white.

### 4.4.2 Image Enhancement

Image enhancement is necessary because of the degradation of the image data, usually introduced during the image acquisition process. The CCD is affected by different noise sources which are superimposed on the image, and are filtered-out by different image enhancement techniques known as "filters". The optical system can also deform the image ( geometric distortion — as in the cross-section images ). Image processing helps to compensate for these deformations and to restore the original geometry. The image enhancement techniques are primarily a series of "image in — image out" processes, during which the visual appearance of the image is modified and improved. The following paragraphs describe the corrections and enhancements applied to the images.

#### 4.4.2.1 Cosmetic corrections

A CCD image is rarely completely free from artifacts such as defective pixels and bright spots. The laboratory air contained a large number of dust particles which were highlighted by the laser light sheet, and thus seen as bright spots in the background and reference images taken in still air ( no flow ). Since the light sheet did not change intensity level abruptly from one pixel to another in an image, any small region of considerably higher intensity value than the surrounding pixels in the average reference images was identified as a dust particle. Dust particles typically occupied only one pixel. Occasionally they would occupy two to four pixels. The closest non-dust pixel value was used to replace the bad (dust) pixels.

#### 4.4.2.2 Thermal current and background illumination

To remove undesirable background illumination levels and thermal currents, a sequence of ten background images was acquired with no flow, the light sheet blocked from reaching the model, and the CCD in complete darkness. An average background image was computed, dust particles removed, and then this average background image was subtracted from all images. As mentioned before, the thermal current and the background illumination are spatially varying and the thermal noise is random in nature. Thus, subtracting an average background image from an instanteneous image did not remove all the thermal-current and background-illumination effects, but the residuals were minimal.

#### 4.4.2.3 Flatfielding

The laser light sheet was non-uniform, therefore variations in the CCD output, which were due to this non-uniformity, may inadvertently could be interpreted as

variations in flow characteristics. In addition, the relative sensitivity of the individual elements that form the CCD detector mosaic was not uniform, adjacent pixels not reacting in the same way to identical incident photon flux. Correction of these non-uniformities was obtained by dividing the acquired image ( after subtracting the background image ) by another image ( a reference image ) made on a uniform field of view — a *flat-field.* This reference image was acquired with the light sheet at the model, but with the flow off, thus having an uniform density and temperature background. An average reference image was computed from a sequence of ten reference images acquired this way, and with the dust particles removed. Then, the average background image was subtracted from this average reference image, thus obtaining the reference image for flatfielding the acquired images. If I(x,y) is the image to be corrected for non-uniformity, F(x,y) is the flat-field, and B(x,y) is the average background image, the processed image will be E(x,y) :

$$E(x,y) = \overline{FB}\frac{I(x,y) - B(x,y)}{F(x,y) - B(x,y)} \tag{4.5}$$

The value of $\overline{FB}$ is equal to the average intensity of the flat-field minus the background, i.e. : average$(F - B)$. The distribution of light intensity in the light sheet varied from one laser shot to another, therefore, flatfielding an instanteneous image with a reference image averaged over many shots did not remove all the effects of the nonuniformity of the light sheet, but the residual effects were minimal.

#### 4.4.2.4 Geometric corrections

The cross-sectional view images were also corrected for distortion due to the camera and mirror angles. First a grid image was acquired with a grid made of graph paper placed in the field of view of the CCD under conditions identical to those of

the image to be processed, i.e., the same setting of the CCD and the optics. This grid had a perspective distortion because the camera was looking sidewise through a flat mirror and not perpendicular to the grid plane. The correction was accomplished by introducing a correspondence between the acquired grid and a reference perfect grid with approximately the same size as the acquired grid. The correspondence was obtained interactively by selecting a point in the recorded image grid and then pointing to the corresponding point in the perfect grid image for the number of points specified — usually four points. The transformation thus obtained was then applied to any appropriate image. The transformed image looked as it would have appeared in a perpendicular imaging arrangement.

#### 4.4.2.5 Filtering

The Rayleigh scattering images ( pure helium injection into the main air stream ) were very noisy. In order to separate the useful information from the noise, a non-linear filter was used. The chosen filter was the median filter. A matrix ( known as *convolution mask* ) was moved in the image. The amplitude of the point situated in the center of the mask was replaced by the median value of the sampling points located under the mask. The median value was determined by sorting the sampling points according to increasing intensity. The median value was then equal to the intensity of the point at the center of this sorted sample. The two remarkable properties of this filter are : ( a ) it evens out any pixel with abnormal intensity with respect to its neighborhood, which is often the sign of noise, and ( b ) the details of the image are well preserved. A mask of $7 \times 7$ was used in filtering the Rayleigh scattering images.

#### 4.4.2.6 Histogram equalization

In the Rayleigh scattering images ( pure helium injection into the main air stream ) the pure helium signal and the background signal were of comparable magnitude, and it was difficult to distinguish the helium signal above the background noise level. A technique that optimizes the image contrast was used. It is known as *histogram equalization.* In the Rayleigh scattering images, most pixels reside in a few small intensity subranges near zero ( black ) level. By spreading the distribution so that each range of pixel values contained an approximately equal number of members, the information content of the display was maximized. This technique results in a contrast enhancement that allowed the helium signal to appear clearly in these images.

### 4.4.3 Image Analysis

Since all the images were acquired under identical flow conditions, the changes observed in the images were due to the different nozzle inserts and the interaction between the main flow and the injectant carrying ethanol droplets. By analyzing the intensity contours, quantitative information about mixing and jet penetration was obtained. In addition, analysis of the instantaneous images provided information about the structural behavior of the jet/mainstream interface region and qualitative characteristics of the mixing. Quantitative information, like geometric properties of objects in an image, was obtained by image analysis, consisting of three main phases : image segmentation, object recognition, and quantitative analysis. Images consisted of shades of grey, but extraction of geometric properties from a grey scale was difficult. Therefore the grey-shades images were transformed, through image segmentation techniques, into a binary format, specifically into foreground and background. After the binary images had been produced, object recognition techniques

were employed to locate and distinguish a particular object ( the foreground ) from the background or other objects. Once an object had been identified, several geometric properties could be computed. The image analysis was performed on the composite images. In the following sub-sections the compositing technique, as well as the image analysis schemes are described. The image processing procedures were implemented by Leonard[110] in a program named BlobTool, within the KBVisual[109] software package.

#### 4.4.3.1 Compositing

A variety of structures were observed over the ensemble of images acquired in each case. Because it is possible to support almost any hypothesis concerning the mixing process by preferentially considering only those images displaying the desired features, a more objective criterion for the analysis of predominant structure size and orientation is necessary. For this reason composite images were analyzed rather than instantaneous ones. Compositing images is a technique that is often used with CCD's [ Buil[90], pp.283–287 ]. Instead of taking a long exposure image, shorter exposure images are taken, and then summed to reach the equivalent long exposure image. Short exposure images have the potential for imaging the turbulence, while long exposure images average in time and smooth out the turbulent structures, thus loosing temporal changes. The addition creates a composite image made-up of a number of different images. The composite is therefore an average image with less noise than any individual image. The images are first stacked and centered with respect to each other so that they are exactly superimposed. The resulting composite image shows a decrease in noise because the noise is uncorrelated from one image to another. Since noise is a random fluctuation of the signal around an average value,

its effect on the image is reduced as the number of images in the composite increases. On the other hand, the useful ( repetitive ) signals add up. Here, ten images were composited resulting in an increase in the signal-to-noise ratio by a factor of $\sqrt{10}$ with respect to a unique image. The long exposure image is not equivalent to the composite image. For example, suppose that a given flow structure produces a signal just slightly less than the quantification unit, in integration time $t_{exp}$. This flow structure is undetectable. However, by exposing ten times as long ( exposure time $= 10 \times t_{exp}$ ), it comes out clearly. Compositing ten images with exposure time $t_{exp}$ gives a composite image in which the flow structure does not appear because it does not appear in the images taken individually. In practice, the fluctuating character of the noise and some statistical principles interact so that the flow structure will be slightly discernible after compositing [ Buil[90], pp.283-287 ], but in no way comparable with the result of one long exposure. In the present study the flow structures in the seeded images have high intensity levels and are very turbulent. Therefore, the compositing method was chosen to process them so that on one hand the turbulent structures could be observed, and on the other hand the average image was also obtained. For unseeded helium flow, a long ( ten seconds ) exposure time was also employed because the signal from these images was very faint. The image thus acquired can be considered an average of sixty instantaneous images.

#### 4.4.3.2 Image segmentation

The purpose of image segmentation is to divide the image into meaningful regions to allow extraction of quantitative information from the image. As pointed-out by Leonard[110], the most commonly used point-dependent approach for image segmentation is *thresholding*. Five different thresholding methods are implemented in the

BlobTool, and they are :

1. User defined threshold. The user can choose any arbitrary threshold value based on a subjective evaluation of the image. If the threshold is too high, information is lost, if it is too low, an increase in background clutter is observed.

2. Otsu's method.

3. Moment preserving method.

4. Entropy analysis method.

5. Minimum error method.

Methods 2 – 5 are "automatic" methods in the sense that the threshold value is not defined by the user but is calculated by the algorithm itself. A discussion and a comparison of these threshold methods is provided by Leonard[110]. The "automatic" thresholding methods were the first to be employed. They thresholded the images at different threshold values. Since the purpose of this study was to compare the images to each other, a constant threshold value was desired. Before thresholding, the images were scaled to eight bits representation, i.e. from zero (black) to 255 (white). On this scale, a threshold value of 55 was selected after other values were considered. It was found that the automatic methods ( Otsu's and moment preserving, but not the entropy method ) usually calculated the threshold value between 50 and 60 most of the times. The entropy method gave values higher than 100 most of the times. It was also found that threshold values between 30 and 80 do not drastically change the object properties calculated after the thresholding. Threshold values lower than 10 resulted in a quasi-circular object with very little details on the perimeter. Threshold values greater than 100 resulted in a shape loss — the thresholded image was composed of

separated blobs instead of one contiguous blob. For intermediate values 10 – 30 and 80 – 100, drastic changes in the geometric quantities were observed. Therefore an average value of 55 was selected.

#### 4.4.3.3 Object recognition

After the image was thresholded, ( labeling the background of the image zero and the foreground one ), the image recognition process was applied. This means that an algorithm to detect objects in an image was run. There are several algorithms that can perform this task,one of them, namely LAF ( Line Adjacency Fill ) algorithm was implemented in the BlobTool program[110].

#### 4.4.3.4 Quantitative analysis

After the object has been detected in the image, several geometric properties can be computed. The *area* of an object is calculated by counting all the pixels that belong to the object. Similarly, the *perimeter* is computed through counting the "perimeter" pixels — object pixels adjacent to background pixels. After the area and the perimeter of an object are determined the *roundness* or the *compactness* can be computed as

$$\frac{(perimeter)^2}{4\pi(area)} \tag{4.6}$$

For reference, the circle has a compactness of one.

Many geometric properties can be determined from the moments of an objects. In shape analysis, moments assist in defining the direction and orientation, center of area, and eccentricity of an object, and its displacement within the image. The area center $\overline{m}$ position is the sum of all the coordinates in the object divided by the total

area of the object. The center's $\overline{n}$ position is similarly defined.

$$\overline{m} = \frac{1}{area} \sum_{m=0}^{M-1} \sum_{n=0}^{N-1} I(m,n) \times m \tag{4.7}$$

$$\overline{n} = \frac{1}{area} \sum_{m=0}^{M-1} \sum_{n=0}^{N-1} I(m,n) \times n \tag{4.8}$$

where I(m,n) is zero, if background and one, if an object. The moments of an object may be affected by shift or change in scale of the image, therefore, moments are made shift invariant by defining the ij th moment, $M_{ij}$, as

$$M_{ij} = \sum_{m=0}^{M-1} \sum_{n=0}^{N-1} (m - \overline{m})^i (n - \overline{n})^j I(m,n) \tag{4.9}$$

where i,j=0,1,2 . The orientation, $\theta$, of an object is the angle associated with the axis of least moment of inertia and is given by

$$\theta = \frac{1}{2} tan^{-1} \left( \frac{2M_{11}}{M_{20} - M_{02}} \right) \tag{4.10}$$

where $M_{11}$ is the xy moment about the center, $\overline{m}$, $\overline{n}$, $M_{02}$ is the second moment about the horizontal line through the center and $M_{20}$ is the second moment about the vertical line through the center of the object. The eccentricity of an object is given by

$$\frac{(M_{20} - M_{02})^2 + 4M_{11}}{area} \tag{4.11}$$

For each perimeter pixel, its distance to the center of the area was calculated, and the maximum and the minimum distances were determined, their ratio being an additional eccentricity criterion for the object.

## 4.5 Analysis of Experimental and Computational Data

This section describes the methods used to analyze the injector's performance subject to various nozzle inserts. Three areas were addressed : mixing performance, loss analysis, and jet penetration. These performance parameters were interpreted in terms of scales much greater than those on which molecular mixing took place. Furthermore, only the mean flow field was considered, and the temporal aspects were addressed based on their manifestation in the mean. These goals result from the limited scope of the study as discussed in Sec. 1.3.

### 4.5.1 Mixedness Measure

An understanding of the effectiveness of an injection scheme requires detailed knowledge of the level to which the injectant is mixed with the surrounding air as a function of distance downstream from the plane of injection.

#### 4.5.1.1 Mixedness measure from experiments

To quantify mixing, measurement of species concentration is the most direct method. Since this measurement was not performed in this study, mixing will be inferred from other quantities obtained from the visualization tests. Mixing is a two-step process. The first step, stretching, is a necessary precursor to the second step, diffusion, because it is through gradient intensification that diffusive effects become important. This suggests that an appropiately defined stretching parameter can be used to characterize mixing. In this study two geometric properties were used to characterize the mixing : the area and the perimeter of the thresholded images.

An additional factor, the compactness [ = $(perimeter)^2$ / ($4\ \pi$ area ) ] was used to characterize the effectiveness of the various nozzle inserts. Higher compactness values mean longer and more convoluted interfaces that facilitate the molecular-scale mixing through diffusion.

#### 4.5.1.2 Mixedness measure from numerical computations

The numerical results allow determination of the fraction of the total injectant mass flux which was present in various concentrations at each axial station : $Y_{inj}$ vs. $\overline{x}$ . This measure will be displayed on contour plots to provide qualitative and quantitative means for comparison with the experiments. A bulk measure of the extent to which the injectant has mixed with the mainstream is the decay of the maximum injectant mass fraction downstream of the injection plane : $Y_{inj,max}$ vs. $\overline{x}$ .

### 4.5.2 Loss Analysis

Any mixing augmentation scheme will increase the irreversible losses, decrease the axial momentum and eventually decrease the engine thrust so that it is important to grade the various injectors on a loss basis. The losses associated with mixing augmentation schemes can be classified into three categories : thermodynamic losses directly associated with mixing, losses which are associated with phenomena that enhance the mixing, and losses associated with phenomena that do not enhance mixing. The loss directly associated with mixing is measured by the entropy rise due to pure diffusion of dissimilar molecular species. This entropy rise cannot be avoided, and since it results directly from mixing, it is acceptable. The losses which are associated with phenomena that enhance mixing are acceptable as well if they are efficacious. These losses originate from the fuel preconditioning inside the nozzle inserts, and from the

flow losses incured by the swept-ramp. Flow losses for a ramp configuration include shock, friction and pressure drag on the face of the ramp, vorticity generation, base pressure drag, and flow recirculation[26]. The shock causes the pressure rise which is fundamental in generating the vortical roll-up off the ramp. Its strength determines the pressure rise, the vorticity field strength, and vorticity generation losses. All the other ramp losses are undesirable. The flow losses incurred by placing a ramp in a supersonic airstream must not negate the benefit which is obtained by the mixing enhancement. The losses that do not enhance mixing are related to shocks generated by the combustor walls ( here by the duct walls ), wall friction, shock wave – boundary layer interaction, and shock-shock interactions. An efficient injection scheme would limit all these losses, especially those that are caused directly by the existence of the scheme. However, due to the non-linear, coupled nature of this flow field, separate losses are difficult to distinguish.

In this study the entropy was calculated based on the numerical simulation data according to the following equation

$$S = \sum_{i=1}^{N_S} n_i \left( \int_{T_{ref}}^{T} \hat{C}_{p,i} \frac{dT}{T} - R_u \ln \frac{p}{p_{ref}} + s_{i,ref} \right) - R_u \sum_{i=1}^{N_S} n_i \ln X_i \qquad (4.12)$$

where subscript "*ref*" stands for a reference thermodynamic state. Dividing by $R_u$ and by the total number of moles in the system, the following equation was obtained

$$\frac{s}{R_u} = \sum_{i=1}^{N_S} X_i \left( \int_{T_{ref}}^{T} \frac{\hat{C}_{p,i}}{R_u} \frac{dT}{T} - \ln \frac{p}{p_{ref}} + \frac{s_{i,ref}}{R_u} \right) - \sum_{i=1}^{N_S} X_i \ln X_i \qquad (4.13)$$

The second summation on the RHS of the last equation represents the entropy generated by the diffusive mixing. Since the mole fractions $X_i$ are always less than one, this term will always be positive. The magnitude of this term depends only on the mole numbers and is independent of the kind of the gases involved in the process. The increase in entropy occurs because the individual gases occupy a larger volume

after mixing than before.

### 4.5.3 Jet Penetration

Strong penetration of the fuel jet into the main airstream is required to reduce the adverse heating effects at the combustor wall. The lift-off height of the jet as a function of downstrem distance was obtained from calculating the centroid of the thresholded images as described in Sec. 4.4.3.4. This measure characterizes the bulk behavior of the injectant. This lift-off height was also calculated from the numerical results by calculating the height ( $\overline{z_i}$ ) of the injectant ( air or helium ) mass flux center, calculated as :

$$\overline{z_i} = \frac{\sum_{j=1}^{N_y} \sum_{k=1}^{N_z} \dot{m}_{inj}(j,k)\overline{z}(j,k)}{\sum_{j=1}^{N_y} \sum_{k=1}^{N_z} \dot{m}_{inj}(j,k)} \tag{4.14}$$

where : $\dot{m}_{inj}(j,k) = \dot{m}(j,k)Y_{inj}(j,k)$, and $N_y$ and $N_z$ are the number of grid points in y-direction and in z-direction respectively.

# Chapter 5

# RESULTS AND DISCUSSION

This chapter contains a detailed presentation of the data obtained both experimentally and computationally. The discussion provides a complete description of the flow field and injector performance characteristics.

## 5.1 Flow Field Survey Results

The experimental flow field survey results are displayed in detail in Figs. 5.1 through 5.10. These figures show the data obtained from the flow survey rake. The iterative procedure discussed in Sec. 4.2 was used to reduce the raw data to variables such as Mach number, static pressure, and static temperature. The results of this reduction procedure are presented for each tested case in the above mentioned figures. The errors associated both with the measurements and the data reduction techniques allow little confidence locally in these solutions. There are some areas where the flow angularity have produced erroneous local values. It should be stressed that the data were averaged in time and the unsteady component of the flow field was not resolved. First, the main flow only ( jet off ) was surveyed and then the jet was turned on and the combined flows were surveyed.

### 5.1.1 Main Flow – Jet Off

The flow field survey data of the main flow only ( jet off ) is presented in Fig. 5.1,a–d. For $\overline{x} = 0.75$, Fig. 5.1a, a subsonic region was observed in the base region of the ramp. High static temperatures and low static pressures were measured in this region. Two vortex cores were observed, having low Mach numbers, low total pressure, and high static temperature. On the side walls of the duct were two vortices generated by the side ramps. These two vortices were higher then the vortices generated by the middle ramp. For $\overline{x} \geq 3.9$ this subsonic region did not exist anymore. For $\overline{x} = 3.9$ the Mach number, total pressure, and temperature contours displayed a "mushroom" like form. This form disappeared downstream of this cross-section, the ramp's wake becoming quasi-axisymmetric. High Mach numbers and total pressure were observed between the ramps, indicating very low losses for the flow between the ramps. For $\overline{x} = 0.75$ and $\overline{x} = 3.9$ most of the flow field had a $P_{total}/P_{plenum}$ of 0.9 or higher. The lower total pressure was confined within the ramp's wake. For $\overline{x} = 10$, most of the flow field had $P_{total}/P_{plenum}$ of 0.8 or less, indicating that there were losses in the flow.

### 5.1.2 Main Flow and Injection

The survey data of this flow field is presented in Figs. 5.2 to 5.10. For $\overline{x} = 0.75$ the subsonic region downstream from the ramp's base still existed, however it was broken by the injectant into two subregions — above the injection port and below the injection port. The side vortices observed in the previous case were not affected by the injection. The fuel plenum chamber pressure was about 0.6 of the main flow plenum pressure ( see Table 2.1 ), therefore the isobar $P_{total}/P_{plenum} = 0.6$ and less can be considered as contouring the jet.

The flow field of the circular nozzle insert — the baseline case, is shown in Fig. 5.2. The global behavior was very similar to the previous case with the jet off. In the present case there was a greater loss in the total pressure at $\overline{x} = 0.75$. Further downstream, the results show that the jet had very little influence on the main flow. The flow field of the nozzle with three steps is displayed in Fig. 5.3. The flow field is similar to the baseline case. The flow field of the nozzle insert with vortex generators was surveyed with the tabs in "X" orientation as well as in cross orientation. The "X" case is shown in Fig. 5.4 and the cross case is shown in Fig. 5.5. The flow in both cases was very similar and only very minor differences could be observed within the experimental resolution. Figs. 5.6 and 5.7 display the flow field of the tapered-slot nozzle with the slot in horizontal position and in the vertical position, respectively. The tapered-slot nozzle displays the most noticeable changes when the throat slot was rotated from the horizontal to the vertical : Figs. 5.6b vs. 5.7b, 5.6c vs. 5.7c, and 5.6d vs. 5.7d. The jet from the nozzle with the horizontal throat slot spread more vertically, and the jet from the vertical throat slot spread more laterally staying lower than the former. The elliptical nozzle insert flow field is shown in Figs. 5.8 and 5.9 for the horizontal major axis and vertical major axis, respectively. Within the experimental resolution only minor differences could be observed. Both cases are very similar to the circular nozzle case. The trapezoidal nozzle flow field is shown in Fig. 5.10. The flow for $\overline{x} \geq 3.9$ is very similar to the baseline case.

In conclusion, all the nozzle inserts display similar behavior, except the tapered-slot insert with the vertical slot which spread more sidewise than the others. The main flow was very dominant — switching the jet on showed very little difference at $\overline{x} = 7$ and $\overline{x} = 10$ in comparison with the jet off case.

## 5.2 Flow Field Visualization Results

The Mie-scattering planar imaging technique produced two-dimensional images containing intensity information that characterizes the visualized flowfield. Length scales in centimeters were drawn on each image. Also, the ramp and the injector insert were displayed in the background to facilitate the understanding of the images. For the side views, the flow was from left to right, and the length scales shown were measured from the bottom wall and from the injector exit. For the transverse views, the flow was towards the observer, and the length scales were measured from the bottom wall and from the centerline.

Since all the images were acquired under the same flow conditions, the changes observed were caused by the different nozzle inserts and the interaction between the main flow and the injectant that carried the ethanol droplets. By analyzing the intensity contours, quantitative information about mixing and jet penetration was obtained. In addition, analysis of the instantaneous images provided information about the structural behavior of the jet/mainstream interface region and qualitative characteristics of the mixing.

### 5.2.1 Jet Flow – Main Flow Off

The jet flow field only ( main flow off ) is shown in Figs. 5.11 through 5.14. Fig. 5.11 displays instantaneous images of transverse views of ethanol-seeded air jets at $\overline{x} = 0.75$ for the nine configurations tested. Each nozzle insert produced a jet with a unique shape. The circular nozzle and the nozzle with three steps created a circular cross-section jet. The trapezoidal insert created a trapezoidal jet. The jet from the nozzle with the vortex generators was deformed by the tabs, each tab

creating a small indent in the jet cross-section. For the tapered-slot nozzle the jet spread more to the minor axis of the slot. For the horizontal slot position the jet spread vertically, touching the bottom wall very close to the injector exit ( $\overline{x} = 0.75$ ) — an undesired behavior from the heat transfer point of view. The jet from the vertical slot injector spread laterally. The elliptical nozzle produced a jet with an elliptical cross-section. The same cross-section shape was observed when helium was injected instead of ethanol-seeded air ( Fig. 5.12 ). Fig. 5.13 displays instantaneous images of transverse views of ethanol-seeded air at $\overline{x} = 3.9$. The jets still display the characteristic cross-section shape as in the previous cross-section, but the areas increased due to entrainment, and jets have lifted relative to the nozzle exit plane. Fig. 5.14 shows side view images of ethanol-seeded air jets. Both large-scale and small-scale structures are visible in all the images.

### 5.2.2 Main Flow and Injection

The combined flow field — main flow and injection — is presented by instantaneous side and transverse views, and by composite views.

#### 5.2.2.1 Side views

Select instanteneous side view images of the ethanol-seeded air along the centerline plane of all the injectors are presented in Fig. 5.15. Large scale structures are visible in all the images. Smaller scale structures are also visible and appear to dominate the interfacial regions. An interesting feature is the black hole in the left side of the images, where the jet is very close to the injector's exit. The signal was lost because the re-evaporation of the ethanol downstream the Mach disk of the barrel shock, caused by the sudden compression (an increase in both temperature and

static pressure). Fig. 5.16 presents instantaneous images of ethanol-seeded helium jets. Both large and small scale structures were observed in this case too. The black hole caused by the re-evaporation of the ethanol is not seen in this case because the jet is almost pressure-matched to the surrounding pressure, and therefore the shock compression does not cause ethanol vaporization. Side views of instantaneous images of Rayleigh scattering ( helium injection ) are shown in Fig. 5.17. The images display the same global features as the ethanol-seeded images. Also, an oblique shock can be observed in these images. This oblique shock turns the flow that passed the expansion fan which emanates from the ramp base corner, in a direction which is nearly parallel to the jet. The small-scale structures are not visible in this case because the images were smoothed by a median filter to improve the quality of the images ( see Sec. 4.4.2.5 ). Also the contrast of these images was enhanced by applying the technique described in Sec. 4.4.2.6.

#### 5.2.2.2 Instantaneous transverse views

Instantaneous cross-section images of ethanol-seeded air jets of all the nozzle inserts are shown in Figs. 5.18 to 5.26. In Fig. 5.18 the injector nozzle geometry influence is immediately apparent. The jets shapes are similar to the previous case with the main flow off. However, in the present case the cross-section shows a torus shape caused by the re-evaporation of the ethanol, because of the barrel shock compression. This phenomenon is also observed in the side view images, as discussed above in Sec. 5.2.2.1.

In Fig. 5.19, the downstream distance is $\overline{x} = 3.9$, and all the images show the jets forming a "horseshoe" shape caused by the two streamwise vortices generated by the ramp, that lift and almost split the jet in two "blobs". Downstream, $\overline{x} = 7$

and $\overline{x} = 10$, ( Figs. 5.20 and 5.21 ), the jet flow becomes almost independent of the injection geometry and displays a quasi-axisymmetric pattern. Both large-scale and small-scale structures are visible in all these images. Figs. 5.22 through 5.25 present ethanol-seeded helium jets. These images display the same flow features as the ethanol-seeded air jets. As already mentioned, the helium jets are almost pressure-matched to the surrounding, therefore the ethanol does not re-evaporate at $\overline{x} = 0.75$, and the images display a solid cross-section. Fig. 5.26 shows helium injection into the main air stream ( Rayleigh scattering ). In spite of the poor quality the same behavior as in the case of Mie scattering could be observed.

#### 5.2.2.3 Composite transverse views

Ten images were composited resulting in an average image with less noise than any individual image ( see Sec. 4.4.3.1 ). The composite image was thresholded, thus dividing it into two distinct regions : the background and the foreground which was the ethanol seeded region. After the image was thresholded, several geometric properties could be computed that provided quantitative information about mixing. In this study, two geometric properties were used to characterize mixing : the area and the perimeter of the thresholded images. An additional factor, named compactness [ = $(perimeter)^2$ / (4 $\pi$ area ) ] was used to characterize the effectiveness of the various nozzle inserts. Higher compactness values mean longer and more convoluted interfaces that facilitate the molecular-scale mixing through diffusion. The z-centroid of the thresholded image was also calculated, providing a means of characterizing the jet penetration.

Figs. 5.27 to 5.30 show composite images of ethanol-seeded air jets. Figs. 5.31 to 5.34 show composite images of ethanol-seeded helium jets. The contour representing

the threshold value is also plotted on the images. The normalized cross-section area of the jets is displayed in Fig. 5.35a. The area increases monotonically downstream, up to $\overline{x} = 7$. Beyond this point the area remains constant for all the inserts with the exception of the tapered-slot nozzle with vertical slot, that continues to grow. The normalized perimeter shown in Fig. 5.35b, increases at a higher rate for $\overline{x} < 3.9$ than for $\overline{x} \geq 3.9$. Because the perimeter increases while the area remains constant for the last two planes, it may be concluded that the interface is more convoluted in the last plane than in the plane upstream. This can be seen also in Fig. 5.35c, where the compactness factor displays an increase from $\overline{x} = 7$ to $\overline{x} = 10$, indicating an increase in mixing. The compactness factor increases rapidly for $\overline{x} < 3.9$ due to rapid stretching of the jet by the vorticity in the region close to the ramp. This stretching increases the perimeter length, while the area which is proportional to the mass entrainment, grows slowly, thus obtaining a very high compactness factor. For $\overline{x} \geq 3.9$, the area starts growing fast and the interface growth slows-down, causing a decrease in the compactness factor. The z-centroid, displayed in Fig. 5.35d, shows a monotonic increase with the downstream distance at an angle of about 5°. The tapered-slot nozzle with the vertical slot has a lower penetration because it spreads more sidewise than vertically, thus having a lower center of area. Because the tapered-slot nozzle with vertical slot throat spreads more sidewise than the other inserts, the field of view for cross-sections $\overline{x} = 7$ and $\overline{x} = 10$ ( Fig. 5.29h, and Fig. 5.30h ) is smaller than the extent of this jet, introducing errors in the calculation of the area, perimeter, and compactness factor. The calculated area and perimeter length for this nozzle are smaller than the actual values.

## 5.3 Numerical Simulation Results

The numerical simulation results are displayed in Figs. 5.36 through 5.56. The data were time-averaged and the unsteady component of the flow field was not resolved. First, the main flow only ( jet off ) is displayed and then the combined flows, jet and main flow are displayed. Two kinds of "fuel" were simulated : air, and helium. This allowed observation of the jet/main-flow interaction and the influence of the "fuel" on the flow. For comparison purposes the numerical data have been plotted in the same form and in the same transverse planes as the experimental data plots.

### 5.3.1 Main Flow – Jet Off

The main flow field data ( jet off ) are presented in Figs. 5.36 through 5.42. Fig. 5.36,a–g shows calculated contours of flow variables, as well as velocity vectors, in the symmetry plane of the duct. The oblique shock wave formed by the ramp compression corner hits the upper wall and is reflected, hitting the ramp about 8 mm before the base. No additional oblique shock reflection is possible, thus obtaining a Mach reflection. Shortly after that, the flow encounters an expansion fan which turns the flow from the top wall of the ramp towards the base, accelerating the flow and decreasing the static pressure. Downstream from the base of the ramp, a subsonic recirculation region exists, having low static pressure and density, and high static temperature. This subsonic region has the form of a "bubble". Between this subsonic region and the expansion fan which emanates from the ramp corner, there is a curved shock wave which actually decelerates the flow to subsonic speeds and encapsulates the subsonic bubble. Further downstream, the expansion fan reflects from the upper wall of the duct and interacts with the curved shock which encloses the recirculation

bubble. This interaction, and further downstream interactions, are smeared out by viscous effects, and become difficult to identify. Fig. 5.37 displays contours at $\overline{x} = 0$ ( ramp base ). The ramp is drawn on these plots for orientation purposes. High pressure exists above the top wall of the ramp and low pressure between the ramps causing the flow to turn around the corners of the ramp, generating strong vorticity. Axial vorticity contours ( normalized by the freestream velocity and the height of the ramp ) are displayed, showing that strong vorticity is present in the flow and that it is concentrated in two counter-rotating vortices emanating from the corners of the ramp. The vortices cores have low Mach number, low static and total pressures and density, and high static temperature. Figs. 5.38 to 5.41 show the calculated contours for $\overline{x} = 0.75$, 3.9, 7, and 10. Fig. 5.42 shows a closeup of the velocity vectors and a Mach=1 contour near the ramp base. The ramp wake extends down to $\overline{x} \approx 4$ and a "tongue" of subsonic flow emanates from the ramp corner and penetrates the flow as far as $\overline{x} \approx 2.5$ ( h=0.639″$\approx$ 1.6 cm ).

### 5.3.2 Main Flow and Injection

The results of the combined flow with the circular nozzle are presented in Figs. 5.43 through 5.49 for air injection, and in Figs. 5.50 through 5.56 for helium injection. In these figures, the mass fraction of the "fuel" is also displayed, showing the jet spreading and penetration. No major differences were observed between the case of air injection and the case of helium injection, even though the velocity of the jet changed from 449 m/s ( air ) to 1213 m/s ( helium ). Both are very similar to each other and to the case with the jet off, showing that the main flow was very dominant, and the jet had very little influence. The velocity vectors plots indicate that the induced velocity entrains freestream fluid into the center of the injectant plume, creating the

"mushroom" shape which is observed in all other contours. Figs. 5.49 and 5.56 show a closeup of the velocity vectors and the Mach=1 contour near the ramp base. The ramp wake extends down to $\overline{x} \approx 4$ and a "tongue" of subsonic flow emanates from the ramp corner and penetrates the flow down to $\overline{x} \approx 2.5$, the jet discharging inside this subsonic region.

## 5.4 Discussion

The discussion is intended to provide a complete description of the characteristics of the flow field and injector performance. The interpretations are based largely upon the form of the flow field represented in the experiments and computations, where phenomena were not completely resolved either temporally or spatially. The spatial resolution provided by the computational grid ( 4623 points ) was considerably better than that of the experiments ( 168 points ). A utility of the numerical simulation is that it allows presentation of "fuel" mass fraction and of derived quantities such as vorticity which could not be obtained experimentally.

### 5.4.1 Comparison Between Experimental and Numerical Data

The comparison between the experimental and the numerical data is affected by the inherent difficulties in reducing the experimentally obtained rake data to base flow variables. Another source of error in the experimental data is the location of the probes ( see Sec. 2.4.2 ). This problem introduces errors in the location of the flow features. Also, due to the experimental grid resolution, which is significantly lower than that of the numerical grid, the experimental flow field gradients will appear broader than the gradients in the numerical simulations. Similarly, the sources of

error in the numerical solutions, in order of importance, are the turbulence model, grid resolution, the omission of the boundary layer on the side wall, and the fidelity of the modeled ramp base and circular geometry at the exit of the jet. The comparison between the experimental and the numerical data is based upon the form of the flow field ( pressure, temperature and Mach number contours ). This comparison shows a very good agreement at $\overline{x} = 0.75$, 3.9, and 7. For $\overline{x} = 10$ the numerical contours are located at higher z-coordinates than the experimental contours. Figs. 5.57a and 5.57b present the static pressure, measured and calculated, along the centerline plane of the top and bottom walls of the duct. The comparison shows good agreement regarding the position of the prominent flow features, i.e., expansion fan and shocks. The calculated wall pressure is in general higher than the measured pressure.

The effect of the jet stretching by the vortical flow field is shown in Fig. 5.58 which displays the computed location of the injectant's maximum mass fraction $Y_{inj,max}$. Fig. 5.58a shows the normal distance $\overline{z}$, and Fig. 5.58b shows the spanwise distance $\overline{y}$. Both the air and the helium jets display identical behavior. The $Y_{inj,max}$ is located on the centerline down to $\overline{x} \approx 1.5$, and then it moves sidewise to a maximum distance of $\overline{y} \approx 0.6$ due to stretching by the strong vortical field. The jet does not interact with the vortical flow until $\overline{x} \approx 1.5$ because it is enclosed in the subsonic "bubble" of the ramp wake. This also is corroborated by the visualization results — at $\overline{x} = 0.75$ the jets' cross-section mantains the shape and the size of the jet's exit cross-section, meaning that the jets do not interact significantly with the vortical flow field. At $\overline{x} \approx 3$ the subsonic "tongue" ( see Figs. 5.49 and 5.56 ) disappears and the $Y_{inj,max}$ reaches the maximum spanwise distance. The same behavior was observed in the visualization images. At $\overline{x} = 3.9$ the images show a "horseshoe" shape with the maximum intensity ( ethanol content ) found off centerline ( see Figs. 5.19 and 5.23 ).

The effect of the vortical flow was also inferred from the compactness factor displayed in Fig. 5.35c. The compactness factor increases very rapidly for $\overline{x} < 3.9$ due to rapid stretching of the jet fluid by the applied vorticity field in the region close to the ramp, where the bulk stirring takes place. Downstream, from $\overline{x} = 7$ to $\overline{x} = 10$, the compactness factor increases at a slower rate indicating a slower rate of mixing. The compactness factor behavior is in agreement with the behavior of the maximum mass fraction, $Y_{inj,max}$, as displayed in Fig. 5.58b. This behavior is consistent with the above description of the flow field.

Two more quantities are used to characterize the extent to which mixing has occured : the magnitude of the vorticity vector and the helicity. An integral measure of vorticity production within the flow is presented in Fig. 5.59a. The vorticity production is caused mainly by fluid migration from the high pressure region on the upper surface of the ramp to the low pressure region in the trough between the ramps, and is termed "ramp-generated vorticity". It increases gradually from the beginning of the ramp and reaches a maximum at $\overline{x} \approx 3$, where it begins to decay at a very slow rate. The helicity density is defined as the scalar product of the velocity vector and the vorticity vector :

$$H = \mathbf{u} \cdot \vec{\omega} \tag{5.1}$$

The helicity density was mass-averaged across each i=constant plane, and is presented in Fig. 5.59b. High values of helicity density reflect high values of speed and vorticity when the relative angle between them is small. The sign of the helicity density is determined by the sign of the cosine of the angle between the velocity and vorticity vectors. Therefore, the sign of the helicity density indicates the direction of swirl of the vortex relative to the velocity vector. Since in the present case the helicity density was mass-averaged across the transverse planes, the result is indicative of vorticity

transport by convection in the flow field. Fig. 5.59b shows that significant changes in the calculated helicity take place between the ramp base, $\overline{x} = 0$ and $\overline{x} \approx 3$. This change means that the major stirring (by the ramp vortices) occurs in this region, which is consistent with the aforementioned flow-field description.

Fig. 5.60 displays a combination of experimental and numerical data to facilitate the flow-field description. In the range of $0 < \overline{x} < 1.5$ the jet does not interact with the main flow – $Y_{inj,max}$ is one and the cross-section shape of the jet is the same as the cross-section of the nozzle. In the near-field mixing region, $1.5 < \overline{x} < 4$, where the main stirring takes place, the jet is stretched by the ramp-generated vortices, and is distorted into a"horseshoe" shape. Fresh air from the main flow is injected into the jet core, and the $Y_{inj,max}$ decays rapidly. The region $4 < \overline{x} < 7$ is a transition region between the near-field and the far-field mixing. In this region the vortices bring fuel from the upper part of the jet into the core, refilling the core with fuel. The jet cross-section becomes quasi-circular. In the far-field mixing region, $7 < \overline{x}$, the $Y_{inj,max}$ and the cross-section area of the jet level-off. The micro-mixing takes place in this region.

In conclusion, good overall agreement between the experimental data and the calculations was observed for this complex, highly three-dimensional flow field. Gaining confidence in the numerical solutions, additional derived quantities were obtained from the numerical simulations and were used to characterize this injection scheme.

### 5.4.2 Mixing

A measure of the mixing rate that has been used in previous investigations is the downstream decay of the maximum injectant mass fraction[57]. Fig. 5.61a shows the calculated decay of the injectant maximum mass fraction. The decay of $Y_{max}$ is a

sensitive indicator of the dominant mixing mechanism. Fig. 5.61a reveals that down to $\overline{x} \approx 1.5$ for air and $\overline{x} \approx 1$ for helium, $Y_{max}$ is equal to one, showing that the jet does not interact with the main flow in this region. Downstream of this region, the vortices generated by the ramp drive freestream air into the jet. This is responsible for the rapid initial drop in $Y_{max}$ ( and for producing the "horseshoe" shape as seen in the visualization results ). Mixing in this region of the flow field is strongly affected by the coupling of the jet flow to the pair of ramp generated vortices. As the jet entrains surrounding air and grows, the strength of the vortices decreases. As a result, the rate of decay of the $Y_{max}$ decreases too, as seen in Fig. 5.61a. This happens at $\overline{x} \approx 5$, which corresponds to x/d $\approx$ 11. In this region, the rate of decay of $Y_{max}$ is governed by the rate of small-scale mixing. Downstream from $\overline{x} \approx 7$ ( x/d $\approx$ 16 ), the decay of $Y_{max}$ levels-off. The cross-section area of the jet also levels-off at the same cross-section as $Y_{max}$ ( see Fig. 5.60 ). In this region the flow field is insensitive to the initial injector configuration, displaying a quasi-axisymmetric shape. This observation is consistent with the experimental flow field description presented in the previous sections. The decay of the maximum injectant mass fraction can also be presented on a log-log plot to give a useful indication of the rate of injectant mixing downstream of the injector exit plane. Previously, it has been found by Thomas et al.[57] that, far downstream of the injector, the data generally falls along a straight line in such a plot. The decay of the maximum injectant mass fraction can be written as :

$$Y_{max} \propto \left(\frac{Y}{d}\right)^{-n} \tag{5.2}$$

where $-n$ is the slope of the line fitted to the far-field mixing data. Taking the logarithmic differential of Eq. ( 5.2) gives

$$\frac{dY_{max}}{Y_{max}} = -n\frac{d(x/d)}{x/d} \tag{5.3}$$

The decay rate of $Y_{max}$ is dependent on both the local value of $Y_{max}$ and the location downstream of the injector. The relative change of $Y_{max}$ is proportional to the relative change in the normalized distance downstream of the injector. Thus, 1% change in x/d location produces a $n$% change in $Y_{max}$. A higher value of n indicates a faster relative rate of injectant far-field mixing. Therefore, the value of $n$ indicates the rate of mixing. Fig. 5.61 shows a log-log plot of the calculated decay of the maximum mass fraction of the injectant versus $x/d$. The slope of the calculated curves is very close to $-0.8$, which is the rate obtained by Thomas et al.[57] for different injection schemes. The helium jet displays a higher rate of decay of the maximum mass fraction than the air jet. The mixing efficiency, defined in Sec. 1.2.6, is presented in Fig. 5.62. The helium jet displays a greater efficiency than the air jet, a behavior which is consistent with the higher rate of decay of the maximum mass-fraction. Actually, the plot displays the effect of the molecular weight of the injectant — the lighter "fuel" has a higher mixing efficiency. The hydrogen, the actual fuel, will have a greater mixing efficiency under the same flow conditions.

The effect of the injector geometry was indirectly inferred from the compactness factor displayed in Fig. 5.35c. At $\overline{x} = 10$, the compactness ratio is fairly insensitive to the injector geometry. Only the insert with the vortex generators in cross orientation displays some advantage over other inserts.

It is of interest to cast the mixing performance in light of pertinent fuel/air mass flux ratios for scramjet applications and to consider the freestream area required relative to the area of the injector exit plane, if the fuel were to be homogeneously mixed to a desired mass fraction for a given set of conditions. The equivalence ratio, $\phi$, is expressed as

$$\phi = \frac{\overline{\dot{m}}}{\overline{\dot{m}}_{stoic}} \tag{5.4}$$

where the subscript "*stoic*" refers to stoichiometric, and the injectant to freestream mass flux ratio, $\overline{\dot{m}}$, is given by

$$\overline{\dot{m}} = \frac{\rho_{inj} U_{inj} A_{inj}}{\rho_\infty U_\infty A_\infty} = \overline{\rho}\,\overline{v}\,\overline{A} \tag{5.5}$$

Using the ideal gas equation of state for both the injectant and the freestream, the last equation can be expressed as

$$\overline{\dot{m}} = \frac{\overline{p}\,\overline{\mathcal{M}}\,\overline{v}\,\overline{A}}{\overline{T}} \tag{5.6}$$

Therefore, the area required to provide a desired equivalence ratio for a given set of injectant and freestream conditions is

$$\overline{A} = \frac{\phi\,\overline{\dot{m}}\,\overline{T}}{\overline{p}\,\overline{\mathcal{M}}\,\overline{v}} \tag{5.7}$$

For the following typical scramjet operating conditions : $\phi = 1$, $\overline{\dot{m}} = 0.03$, $\overline{\mathcal{M}} = 2/29$, $\overline{p} = 1$, $\overline{v} = 1$, and $\overline{T} = 1/6$, this area ratio is : $\overline{A} = 0.07$, which means that the injectant must be homogeneously mixed into an area approximately 14 times larger than the area of the injection exit plane.

### 5.4.3 Penetration

The jet penetration calculated from the visualization data is displayed in Fig. 5.63a. This figure actually displays the z-coordinate of the center of the area that contains ethanol droplets, originating from the injector, and characterizes the bulk behavior of the injectant. The calculation of this quantity was described in Sec. 4.4.3.4. Fig. 5.63b shows the z-coordinate of the maximum mass fraction of the injectant, and Fig. 5.63c shows the z-coordinate of the injectant mass centroid, obtained from the numerical simulations. The calculation of the last value was described in Sec. 4.5.3. The area-centroid and the mass-centroid are not the same. While the penetration based on the

mass center shows an average angle of 10°, the penetration based on the area center shows an average angle of only 5°, which means that within the cross-section area occupied by the injectant, the injectant was not homogeneously dispersed. There exist regions that are fuel rich and others fuel lean. The fuel rich regions were located around a line which maintained the initial injection angle, a behavior that also can be seen in the figures which display the calculated mass fraction contours of the injectant. These contours show a "kidney" shape, especially for $\overline{x} = 7$ and $\overline{x} = 10$, with the high mass fraction located in the upper part of the "kidney".

### 5.4.4 Losses

The losses incurred by the fluid as a result of interaction with the ramp and the jet are an important measure of the injector performance. Rise in the total mass-averaged entropy of the fluid through the computational domain is shown in Fig. 5.64. The entropy was calculated according to the procedure described in Sec. 4.5.2. The entropy increases monotonically for all the cases investigated, i.e., jet-off, air injection, and helium injection. For the helium injection the entropy due to mixing is also displayed. The entropy rise prior to the injection plane is caused by the ramp-generated shock system and subsequent non-isentropic flow in the boundary layer. Subtracting the entropy at $\overline{x} = 0$ from the entropy rise between $\overline{x} = 0$ and $\overline{x} = 10$ gives the entropy change caused by irreversibilities downstream from the injection plane. The entropy due to mixing is about 1/3 of the total entropy change downstream of the injection plane. The helium shows higher entropy levels than the air downstream of the injection plane, implying more mixing. This is consistent with the previous findings of higher mixing rate and mixing efficiency.

Another calculation of losses was made based on the rake data. Fig. 5.65a shows the average total pressure measured in the probe experiment, and Fig. 5.65b shows the increase of entropy calculated from the total pressure. All the injector inserts display a similar behavior and have virtually the same total pressure loss ( and entropy increase ), therefore, the average total pressure was fairly insensitive to the injector geometry. As can be inferred from the curve representing the jet off case, most of the total pressure losses are caused by the ramp. The normalized entropy calculated from the experimental data has a similar level to the entropy calculated from the computational data ( Fig. 5.64 ).

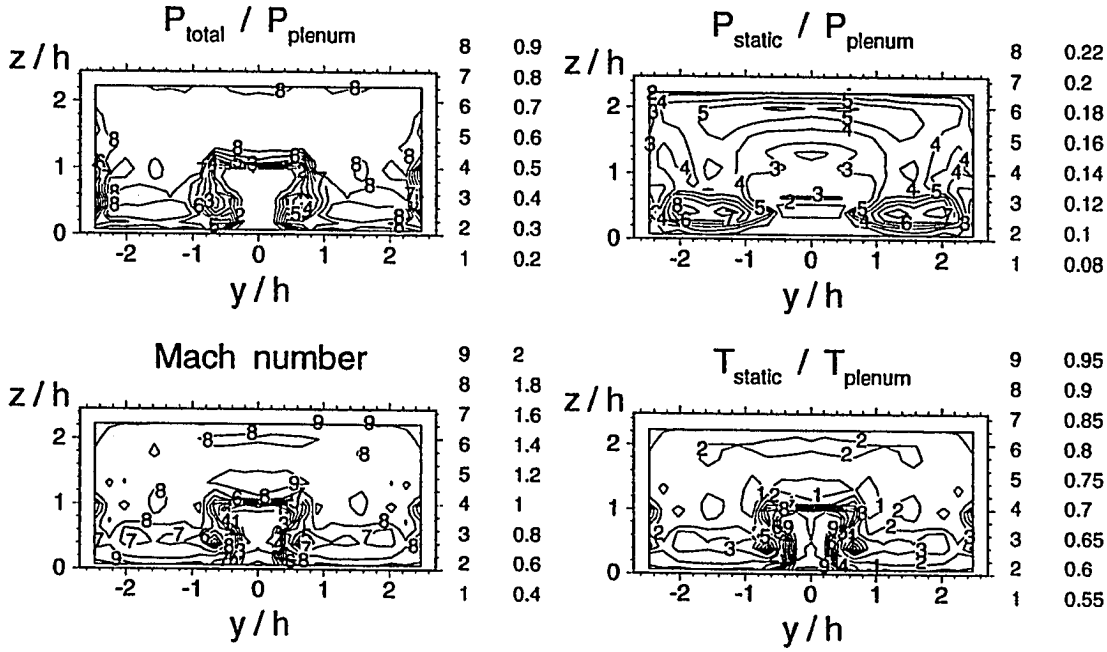


a. Cross - section at x / d = 1.7 , x / h = 0.75

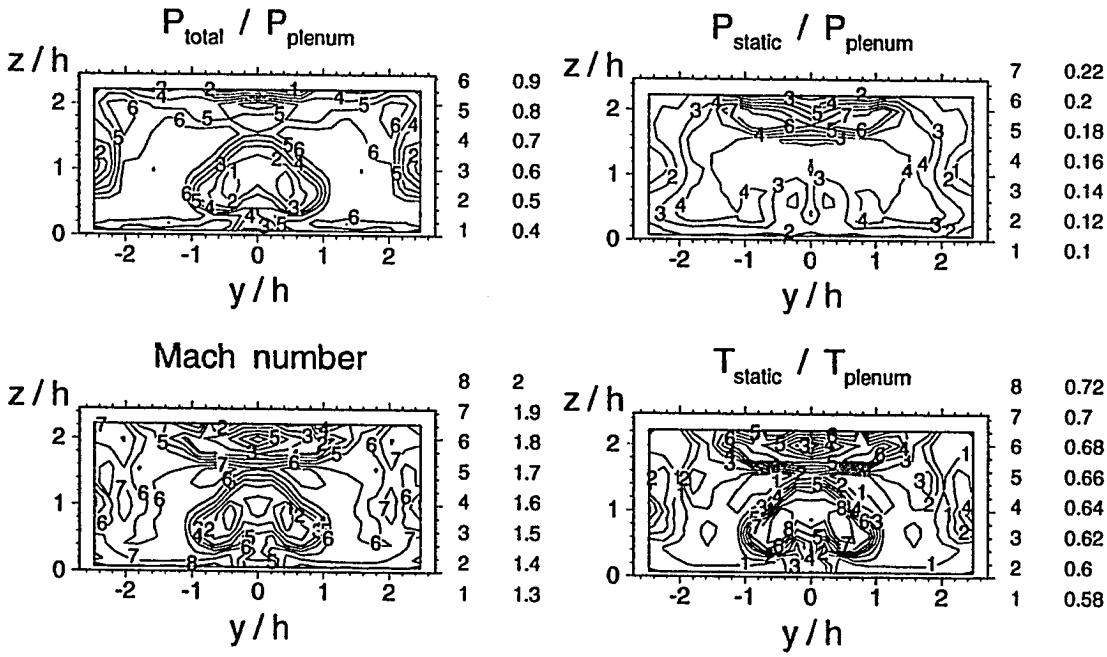


b. Cross - section at x / d = 8.8 , x / h = 3.9

Fig. 5.1 Experimental contours, main flow only, no injection

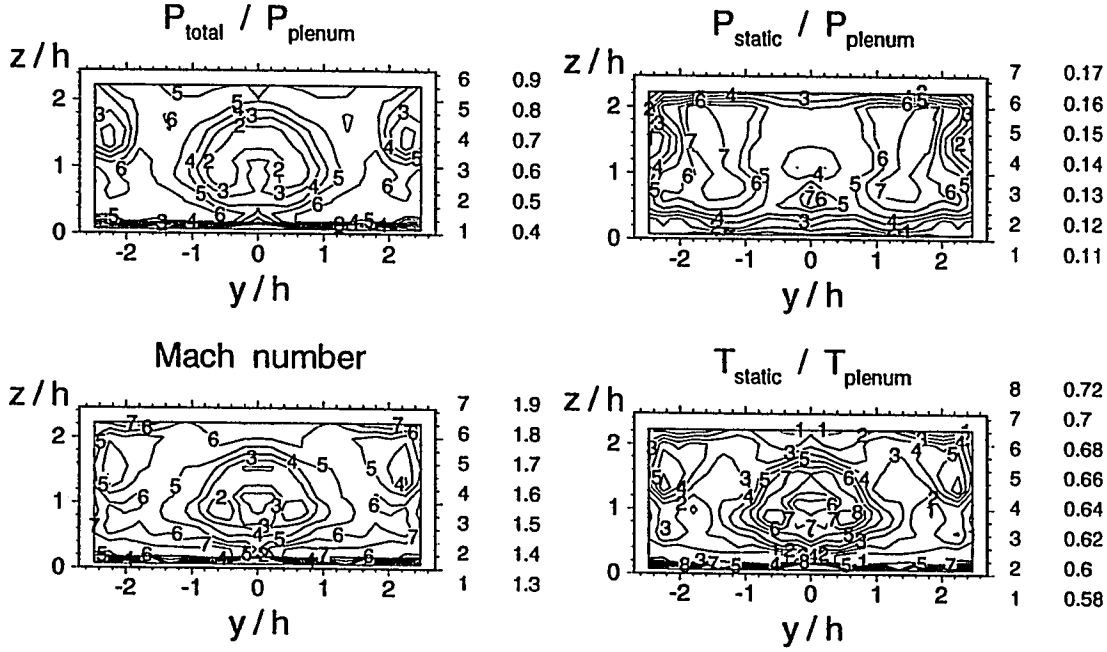


c. Cross - section at x / d = 16., x / h = 7.

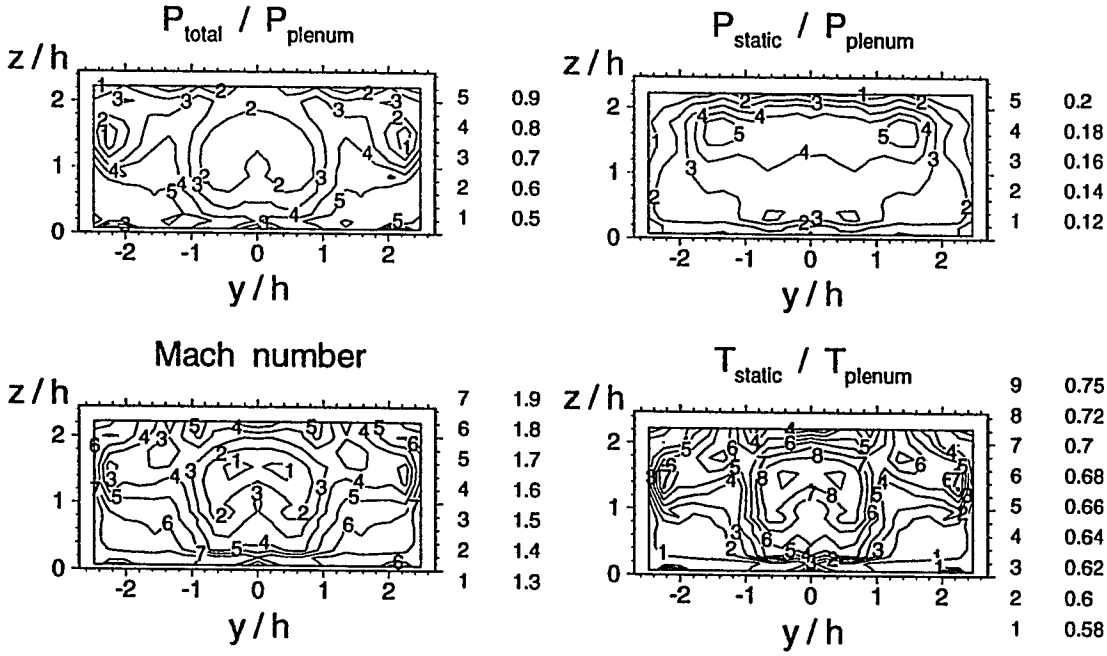


d. Cross - section at x / d = 23., x / h = 10.

Fig. 5.1 ( contd. ) Experimental contours, main flow only , no injection

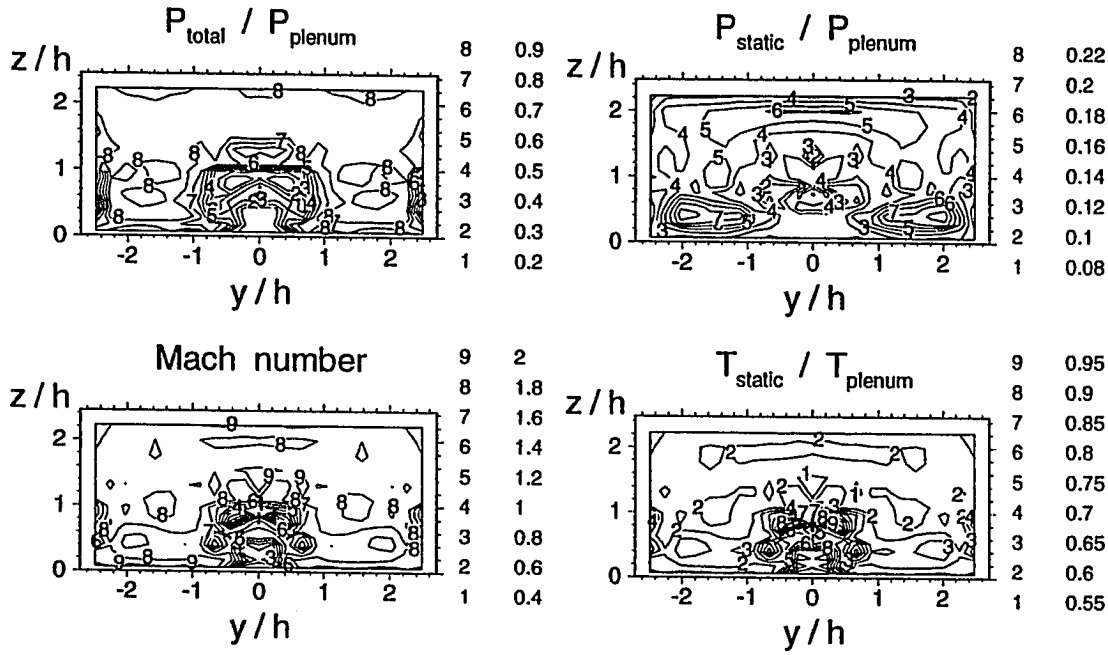


a. Cross - section at x / d = 1.7 , x / h = 0.75

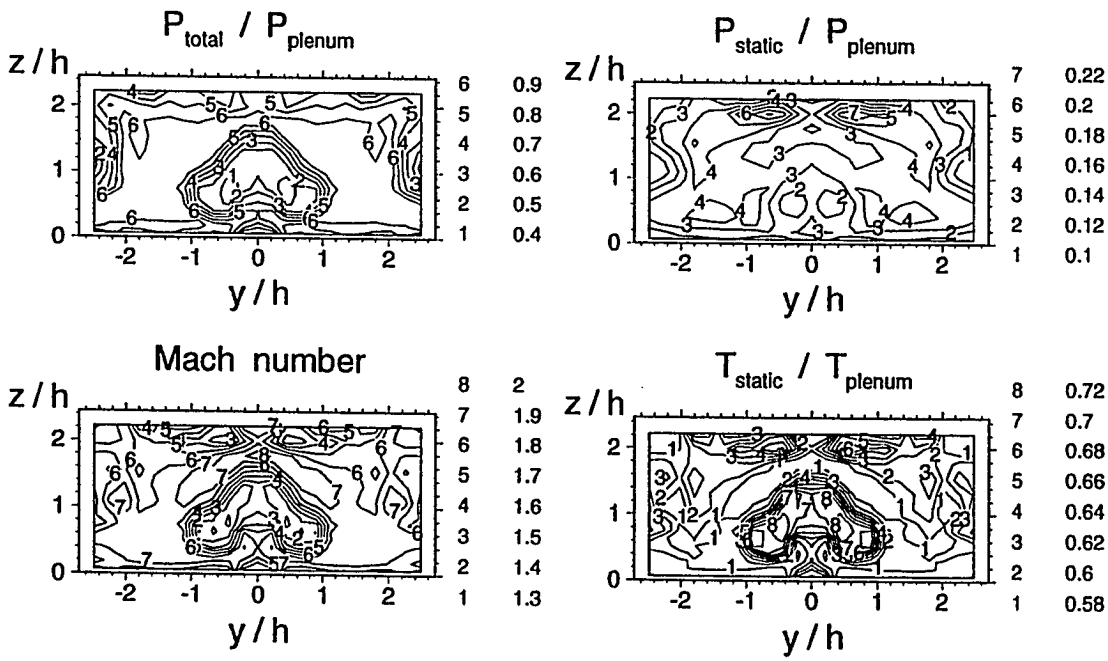


b. Cross - section at x / d = 8.8 , x / h = 3.9

Fig. 5.2 Experimental contours, circular nozzle insert

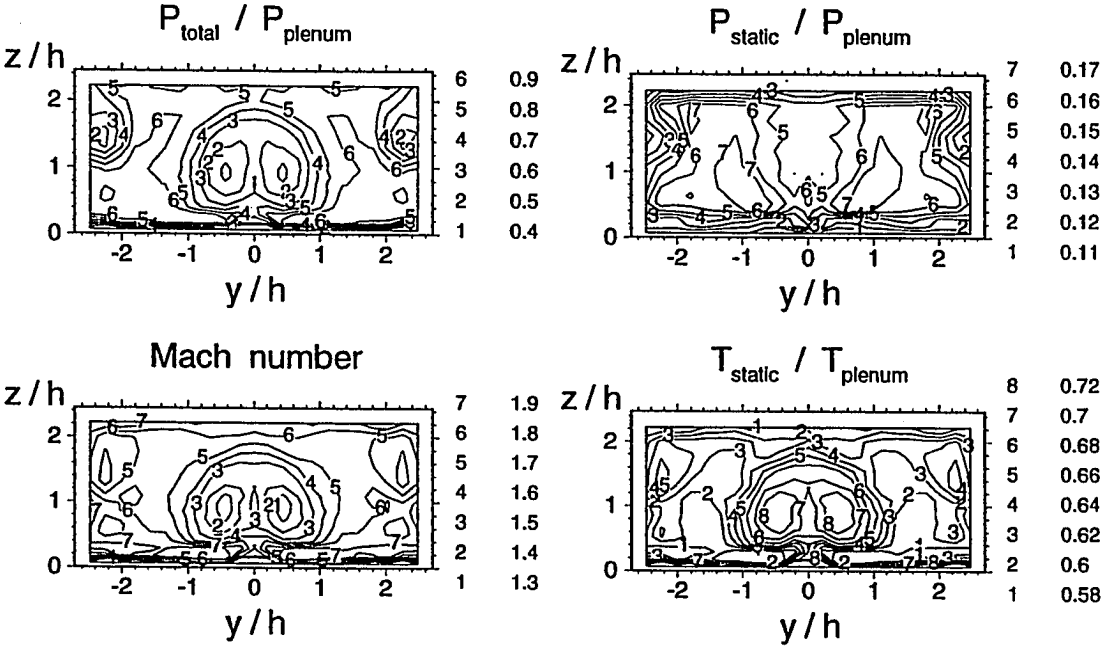


c. Cross - section at x / d = 16., x / h = 7.

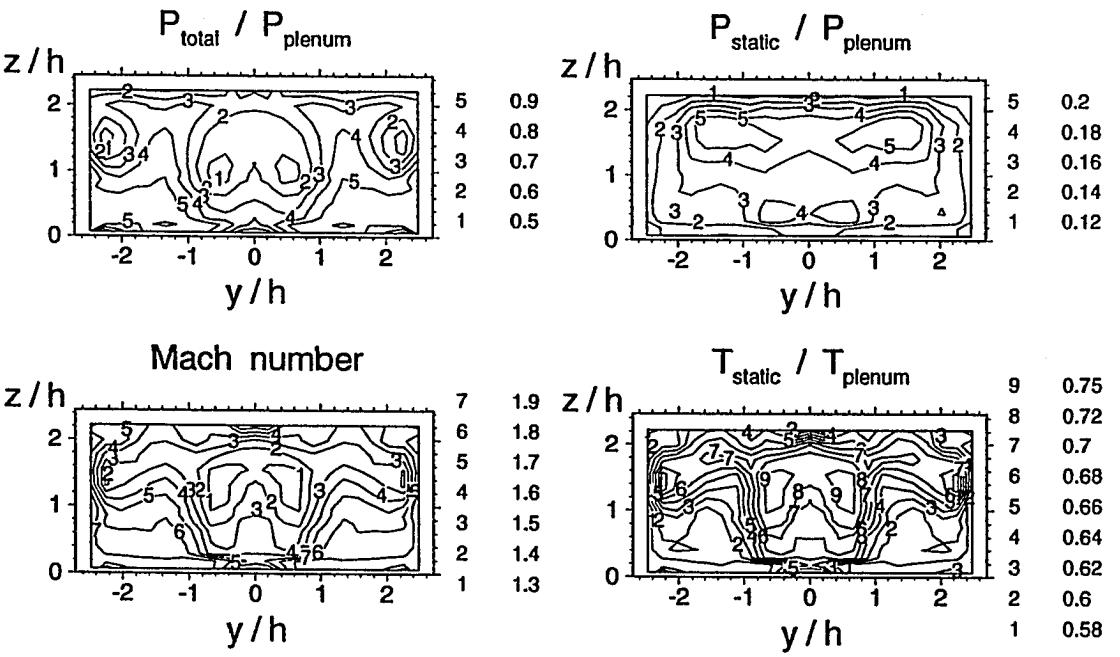


d. Cross - section at x / d = 23., x / h = 10.

Fig. 5.2 ( contd. ) Experimental contours, circular nozzle insert

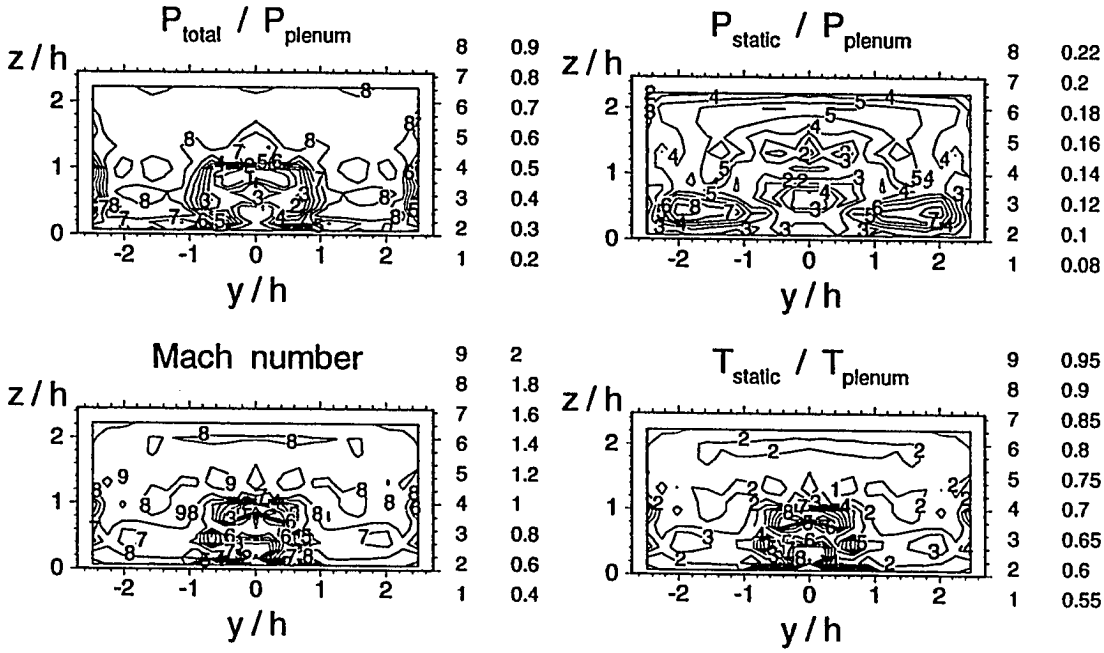


a. Cross - section at x / d = 1.7 , x / h = 0.75

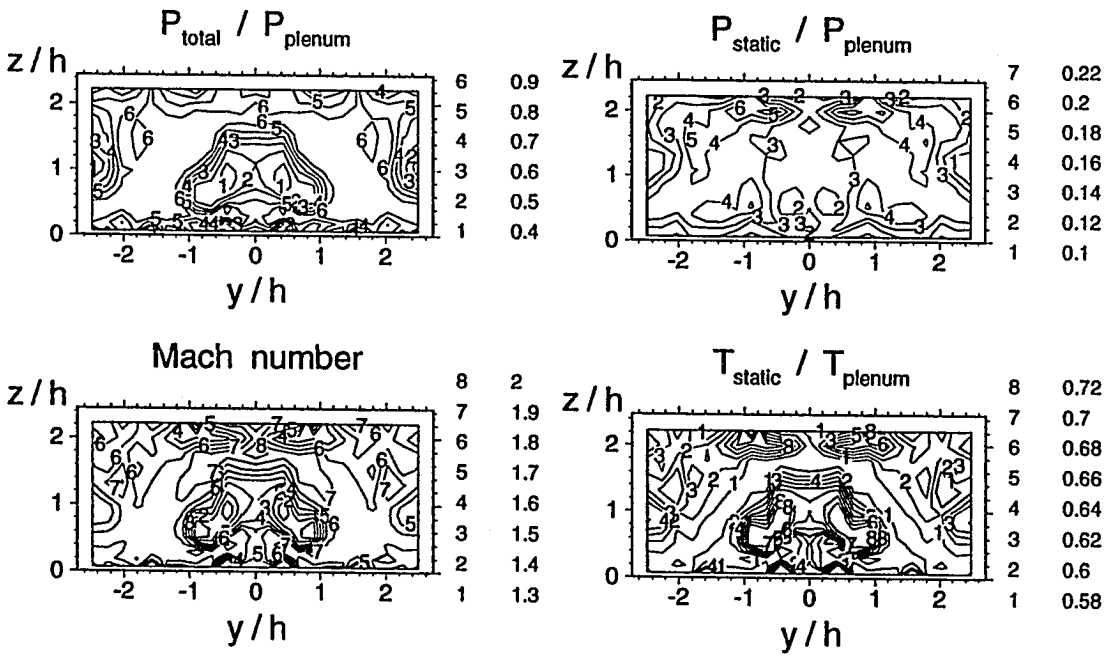


b. Cross - section at x / d = 8.8 , x / h = 3.9

Fig. 5.3 Experimental contours, nozzle with three steps

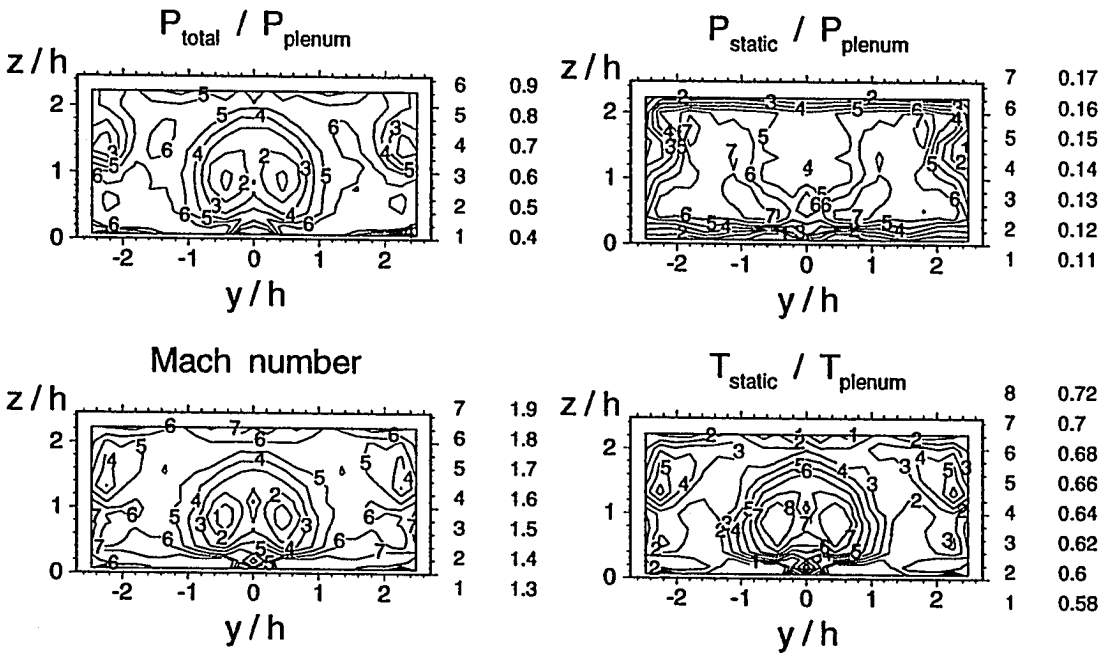


c. Cross - section at x / d = 16., x / h = 7.

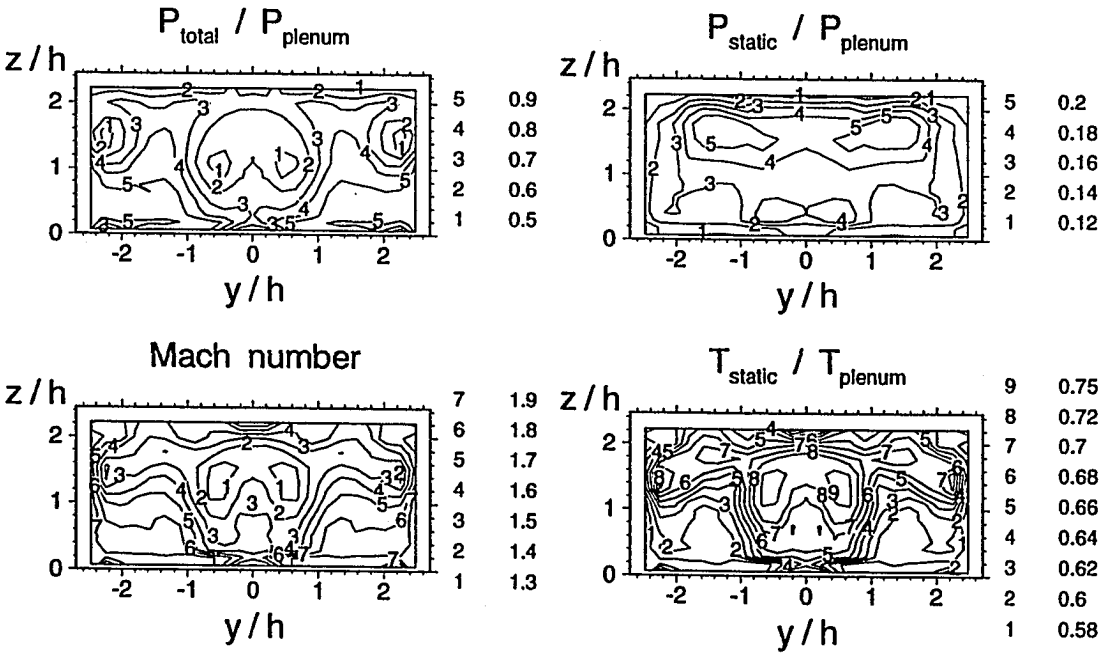


d. Cross - section at x / d = 23., x / h = 10.

Fig. 5.3 ( contd. ) Experimental contours, nozzle with three steps

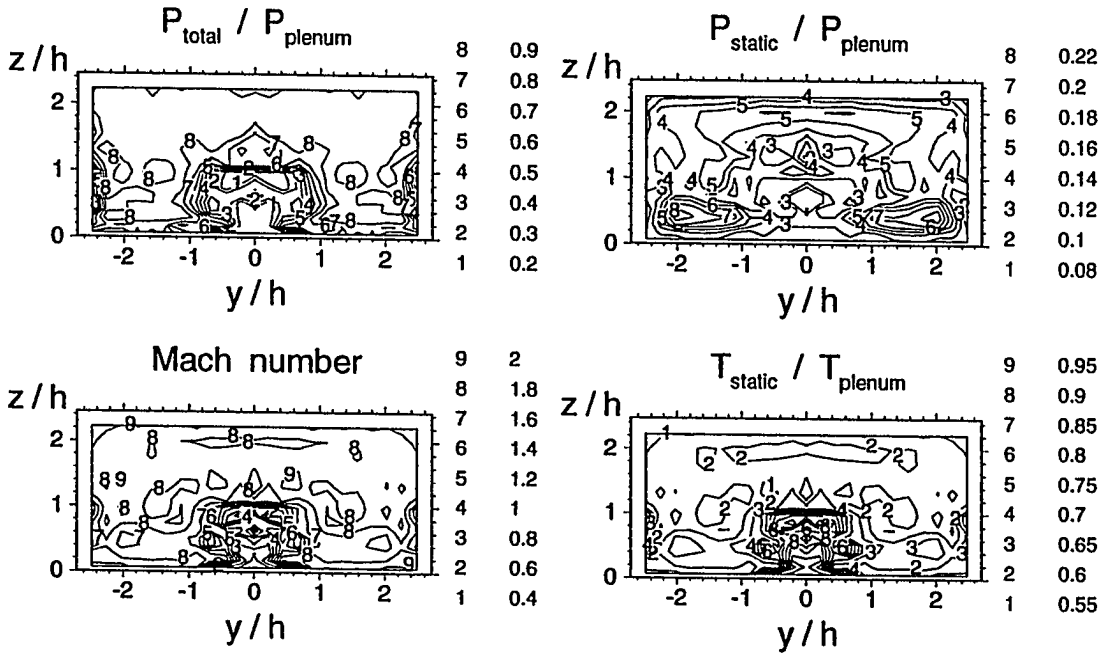


a. Cross - section at x / d = 1.7 , x / h = 0.75

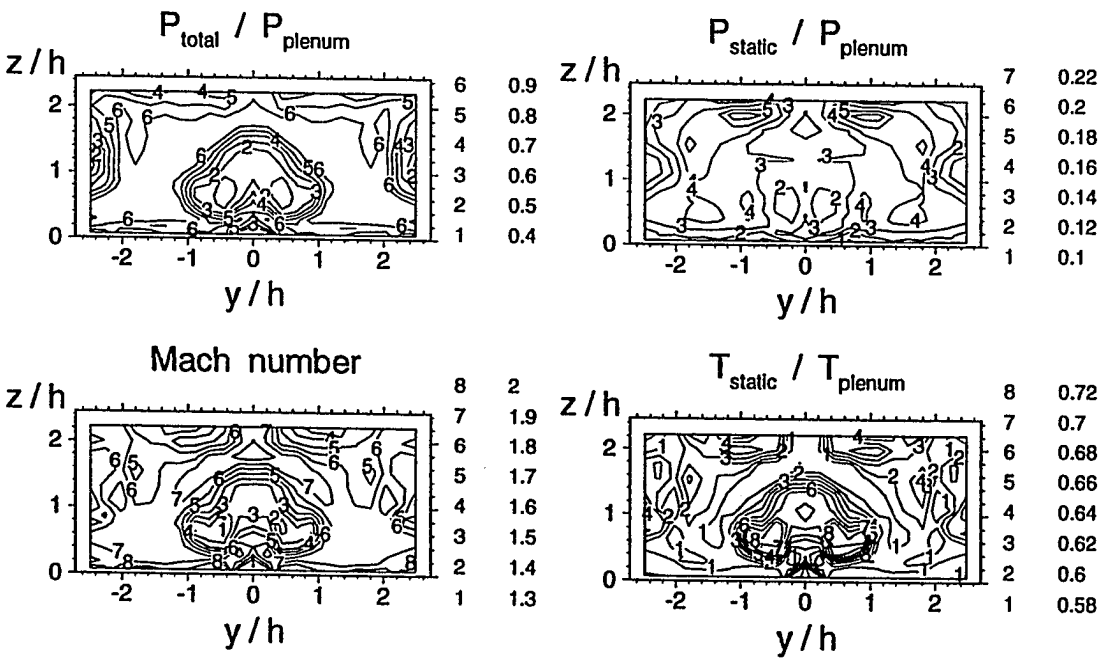


b. Cross - section at x / d = 8.8 , x / h = 3.9

Fig. 5.4 Experimental contours, nozzle with vortex generators , "X"

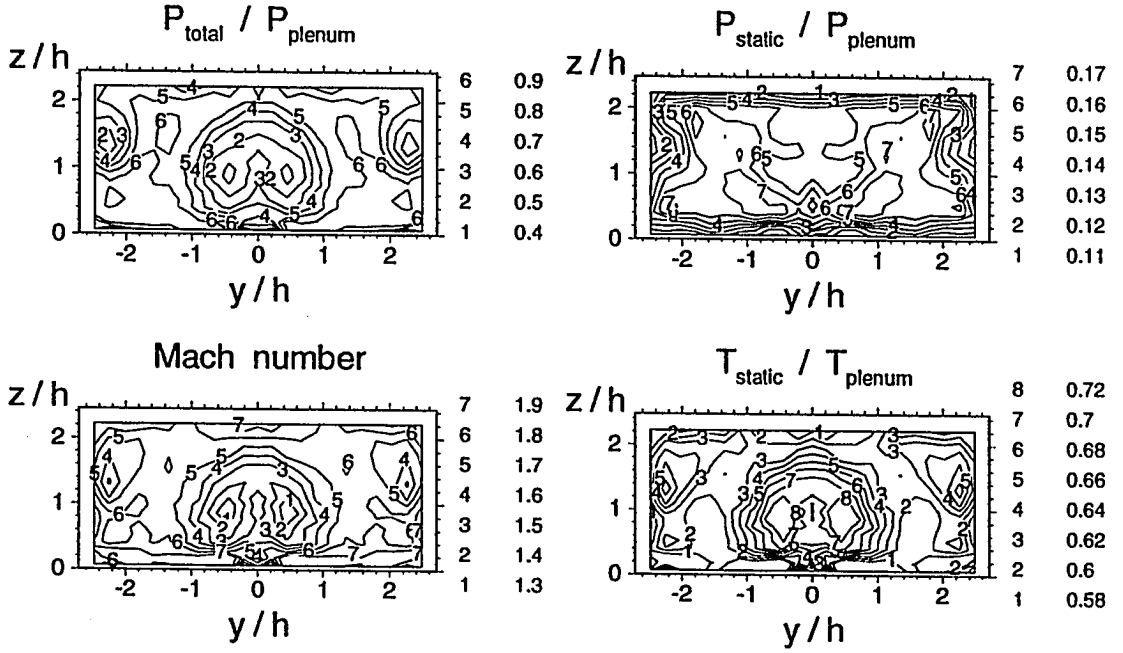


c. Cross - section at x / d = 16. , x / h = 7.

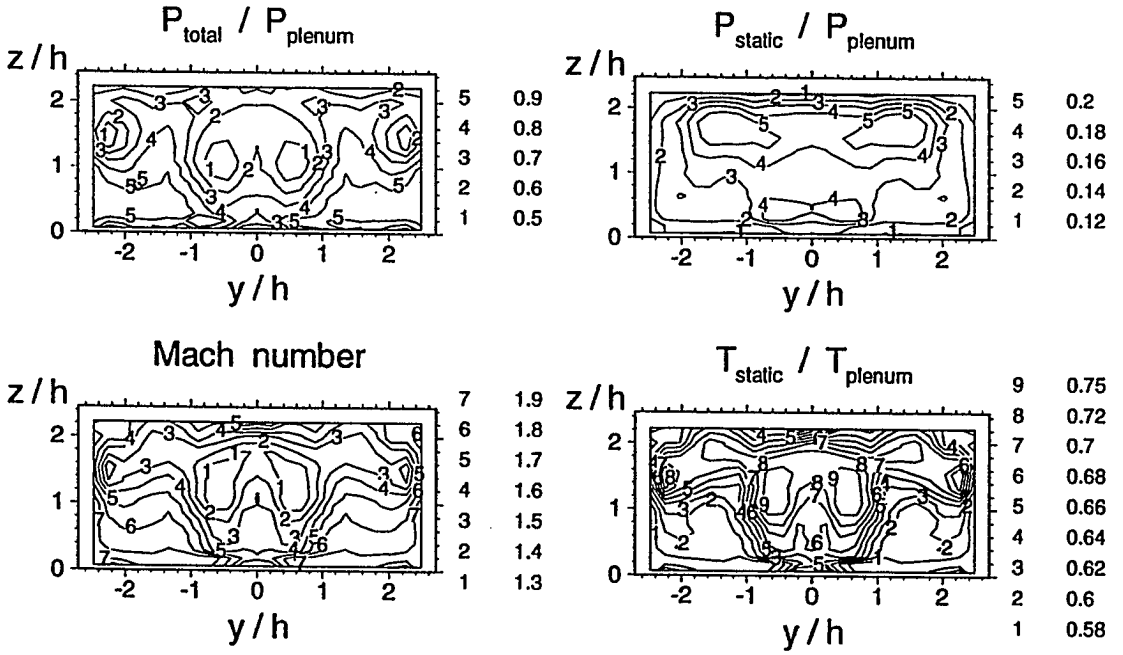


d. Cross - section at x / d = 23. , x / h = 10.

Fig. 5.4 ( contd. ) Experimental contours, nozzle with vortex generators , "X"

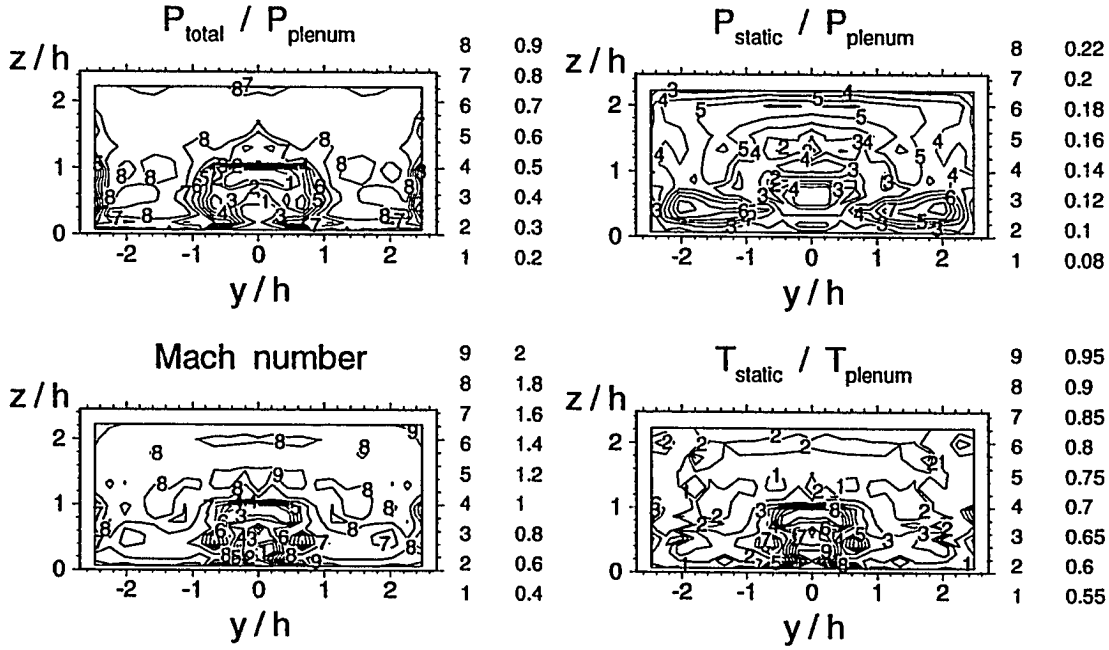


a. Cross - section at x / d = 1.7 , x / h = 0.75

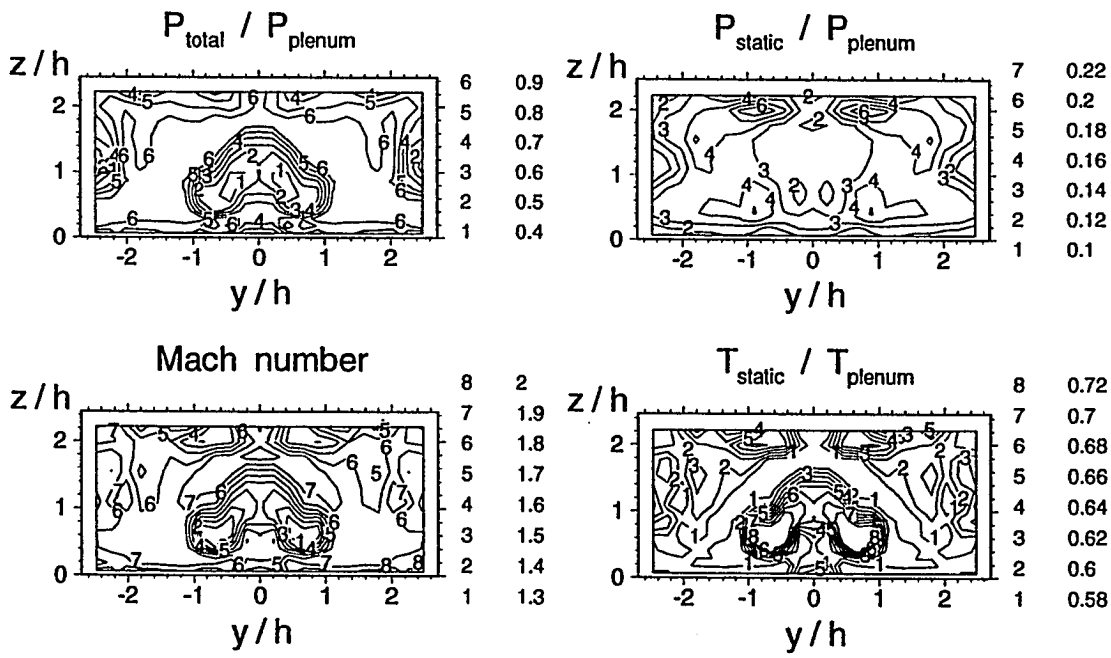


b. Cross - section at x / d = 8.8 , x / h = 3.9

Fig. 5.5 Experimental contours, nozzle with vortex generators , "+"

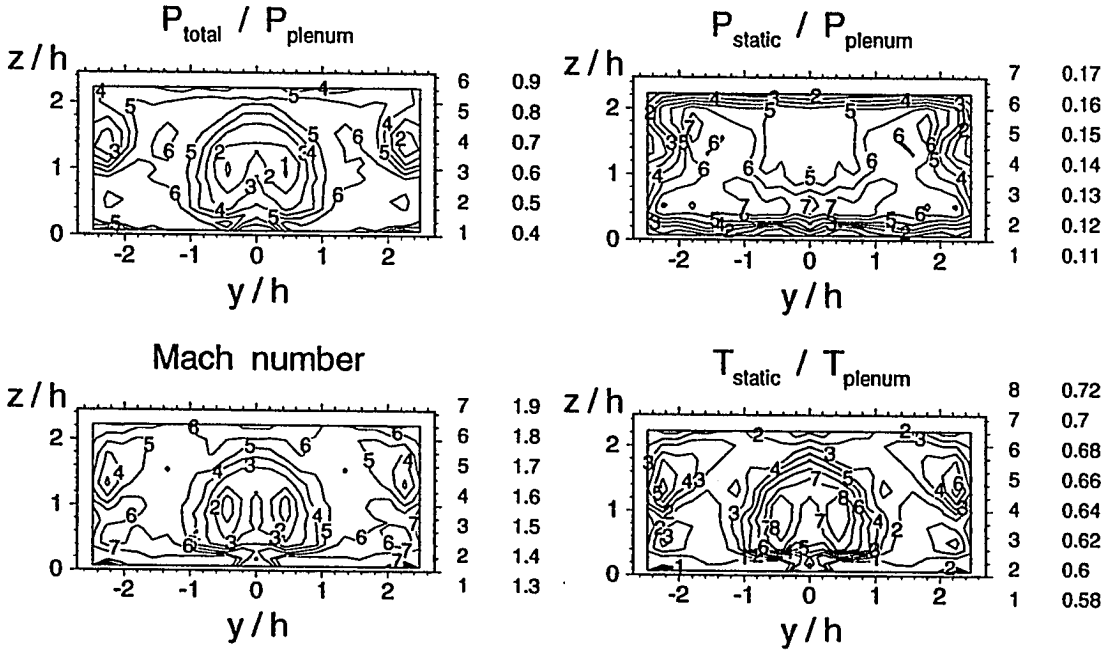


c. Cross - section at x / d = 16., x / h = 7.

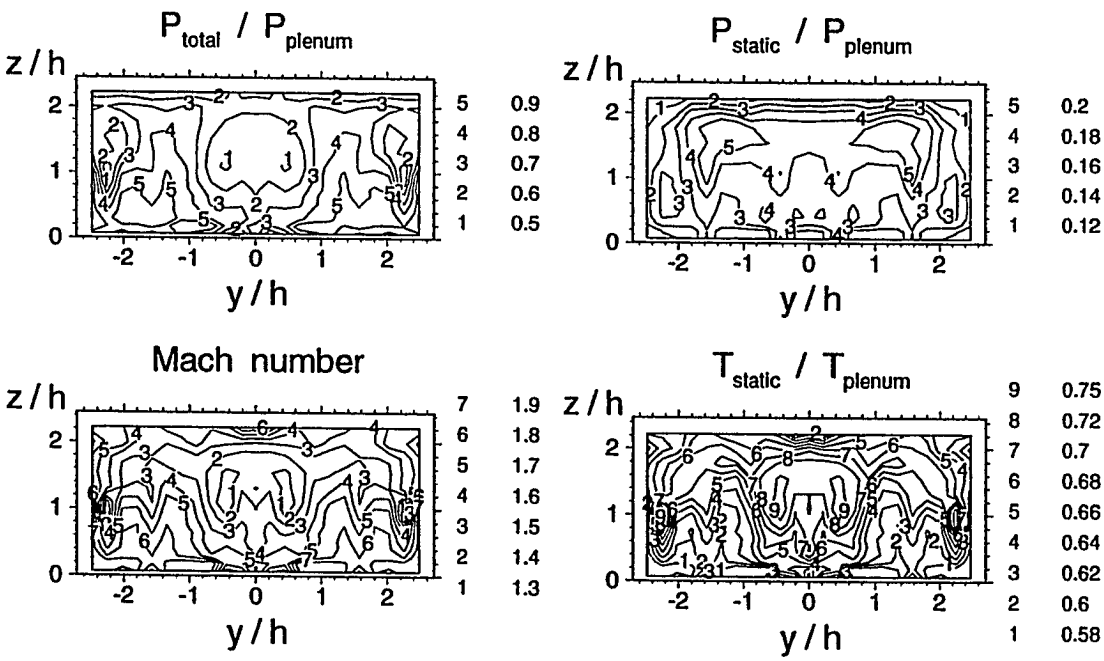


d. Cross - section at x / d = 23., x / h = 10.

Fig. 5.5 ( contd. ) Experimental contours, nozzle with vortex generators , "+"

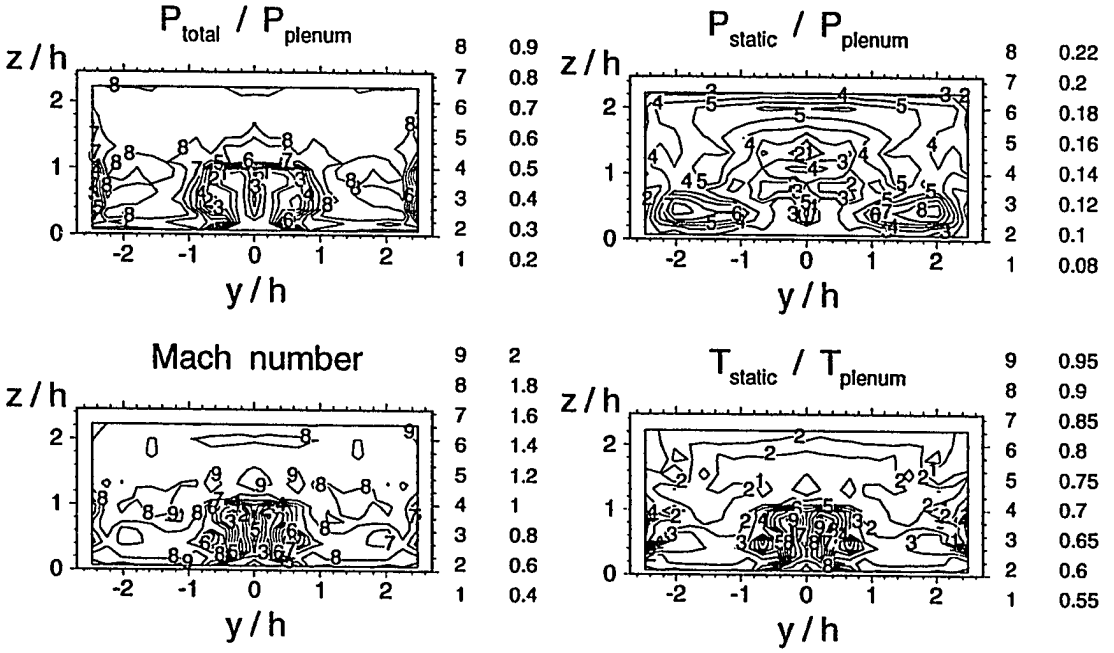


a. Cross - section at $x/d = 1.7$, $x/h = 0.75$

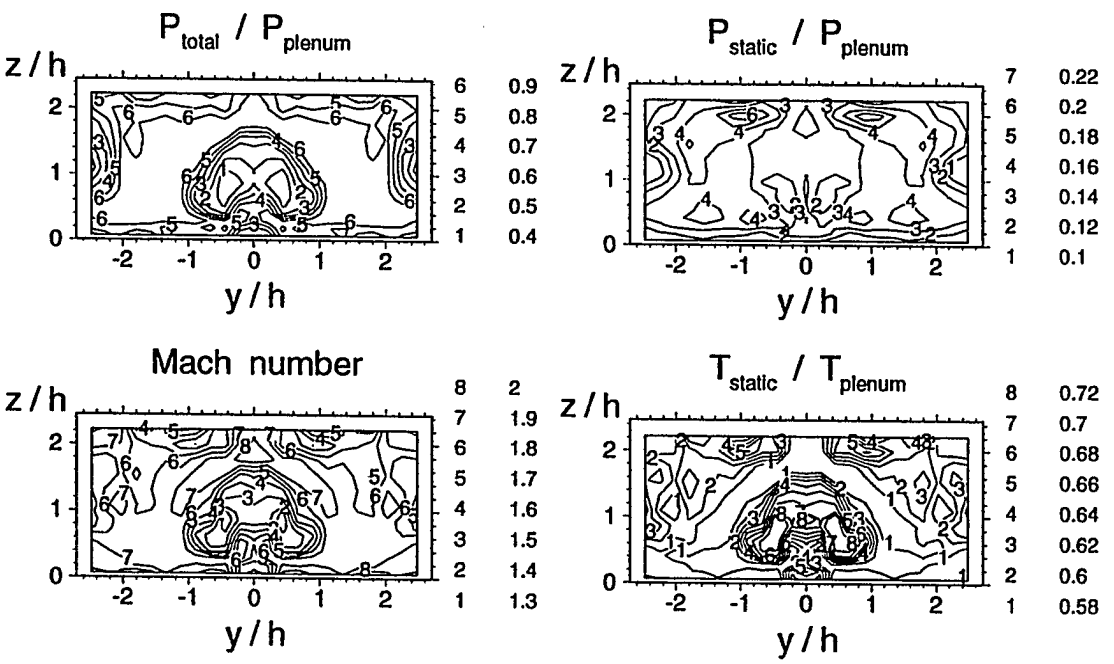


b. Cross - section at $x/d = 8.8$, $x/h = 3.9$

Fig. 5.6 Experimental contours, tapered-slot nozzle, horizontal slot

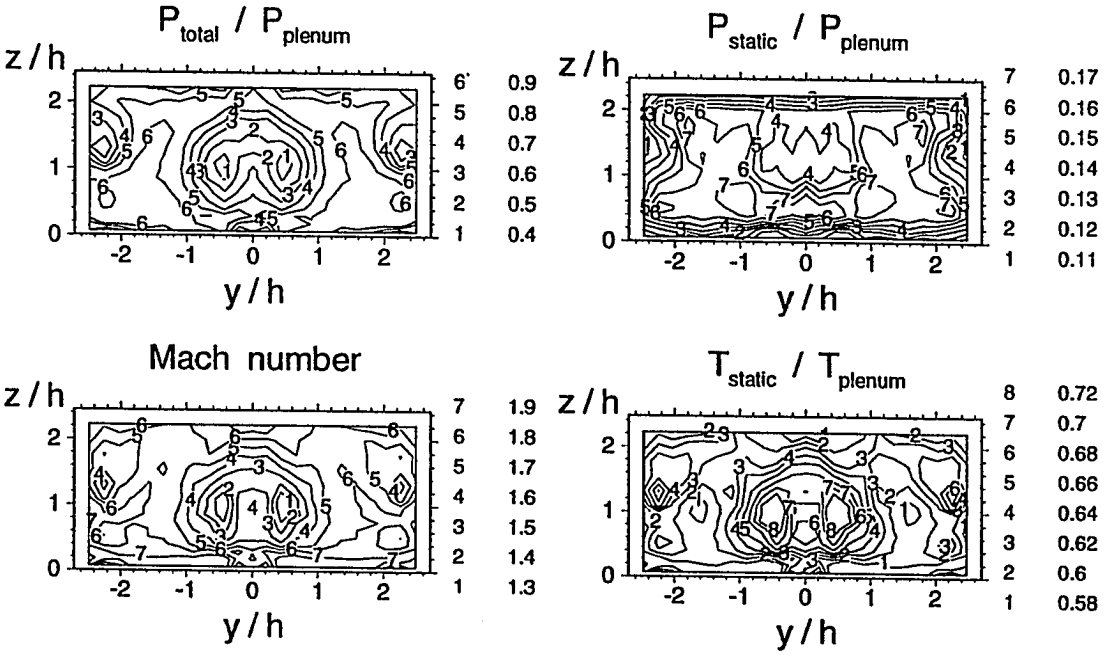


c. Cross - section at x / d = 16., x / h = 7.

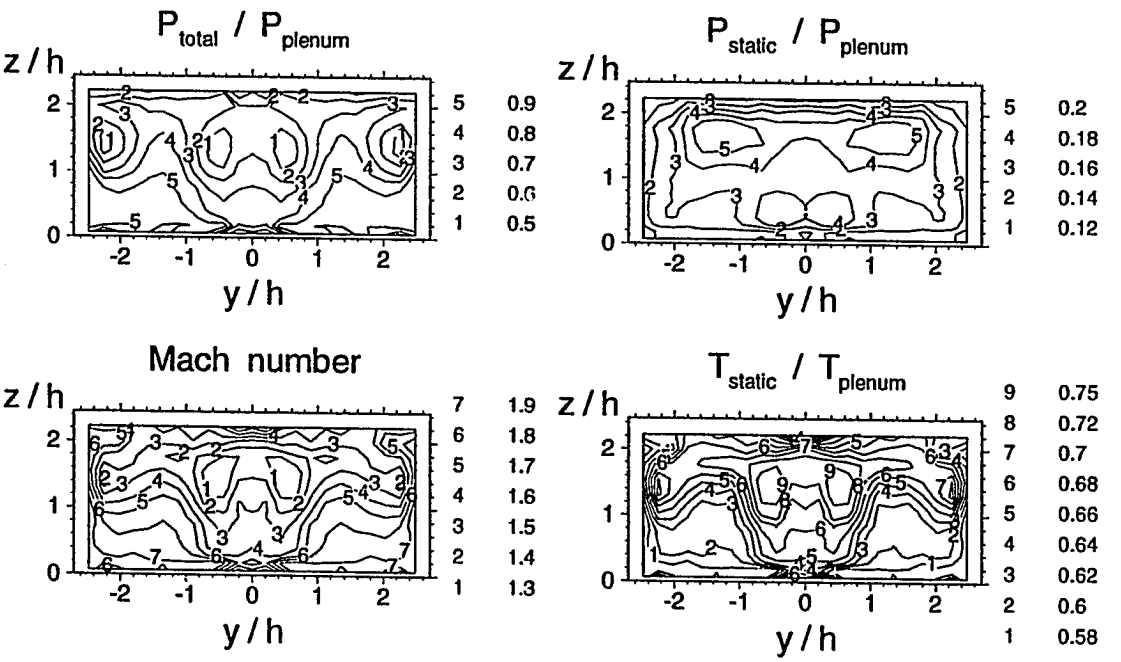


d. Cross - section at x / d = 23., x / h = 10.

Fig. 5.6 ( contd. ) Experimental contours, tapered-slot nozzle, horizontal slot

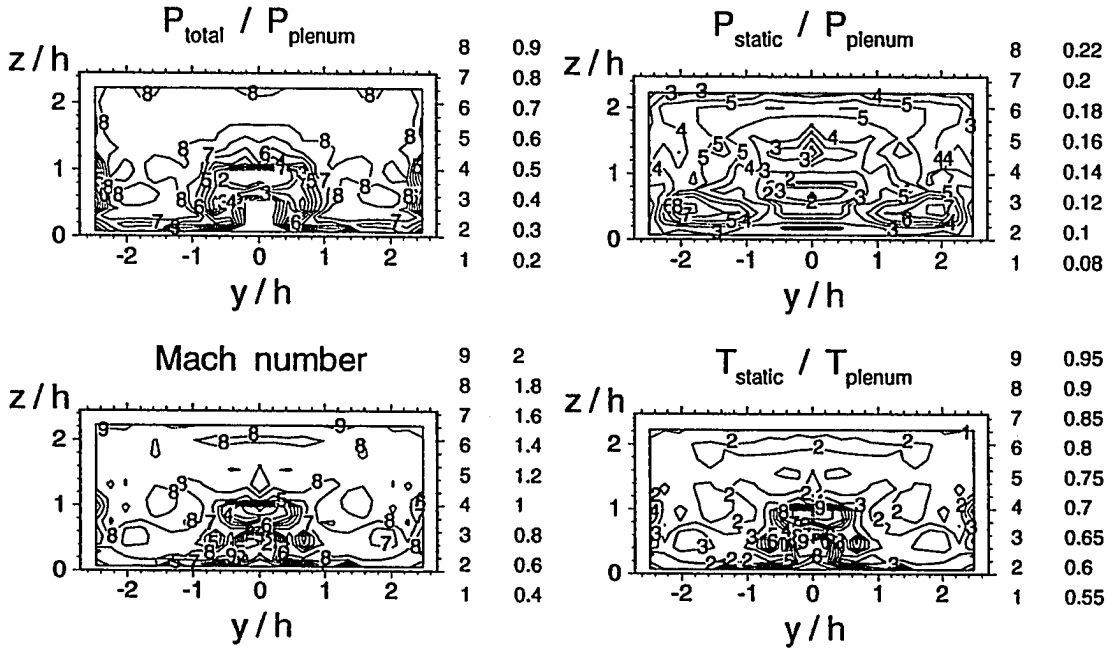


a. Cross - section at x / d = 1.7 , x / h = 0.75

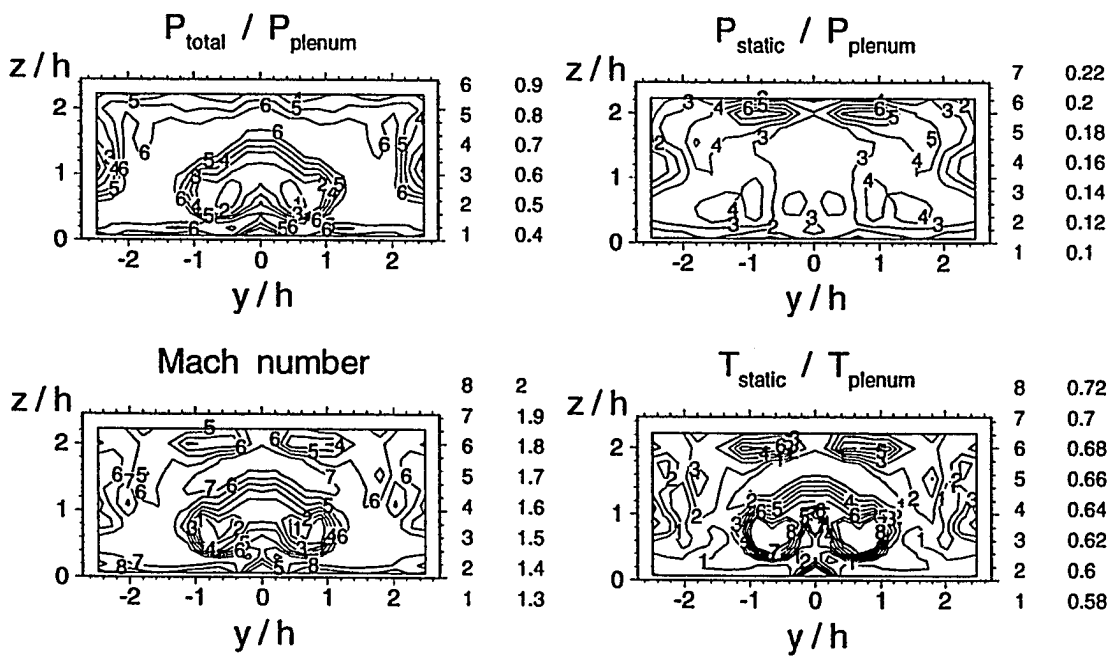


b. Cross - section at x / d = 8.8 , x / h = 3.9

Fig. 5.7 Experimental contours, tapered-slot nozzle, vertical slot

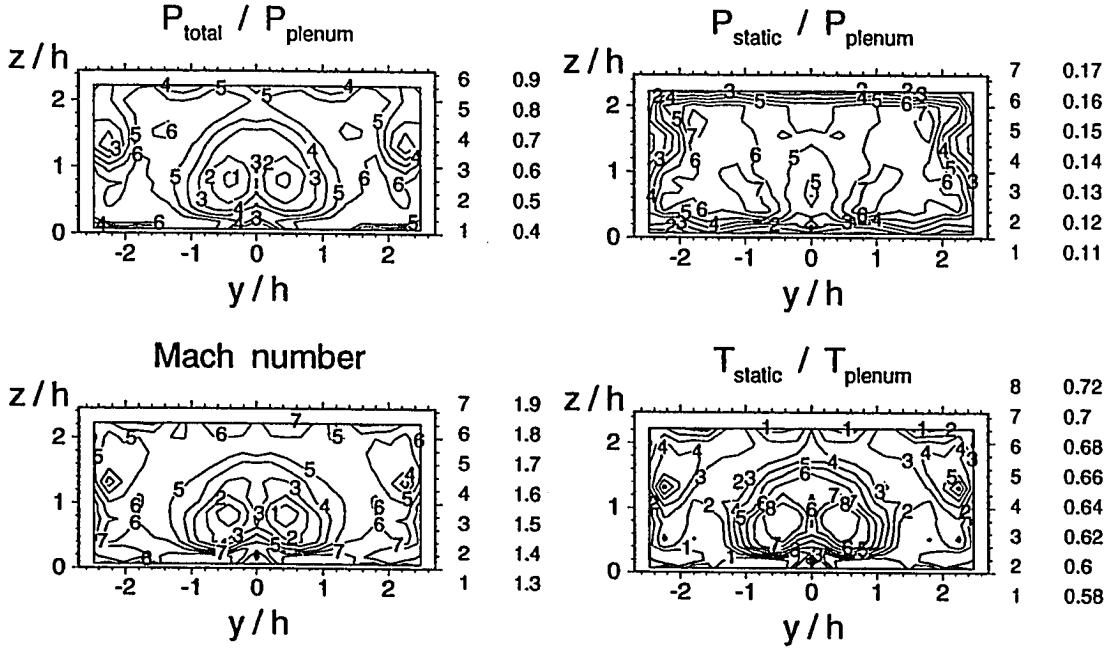


c. Cross - section at x / d = 16., x / h = 7.

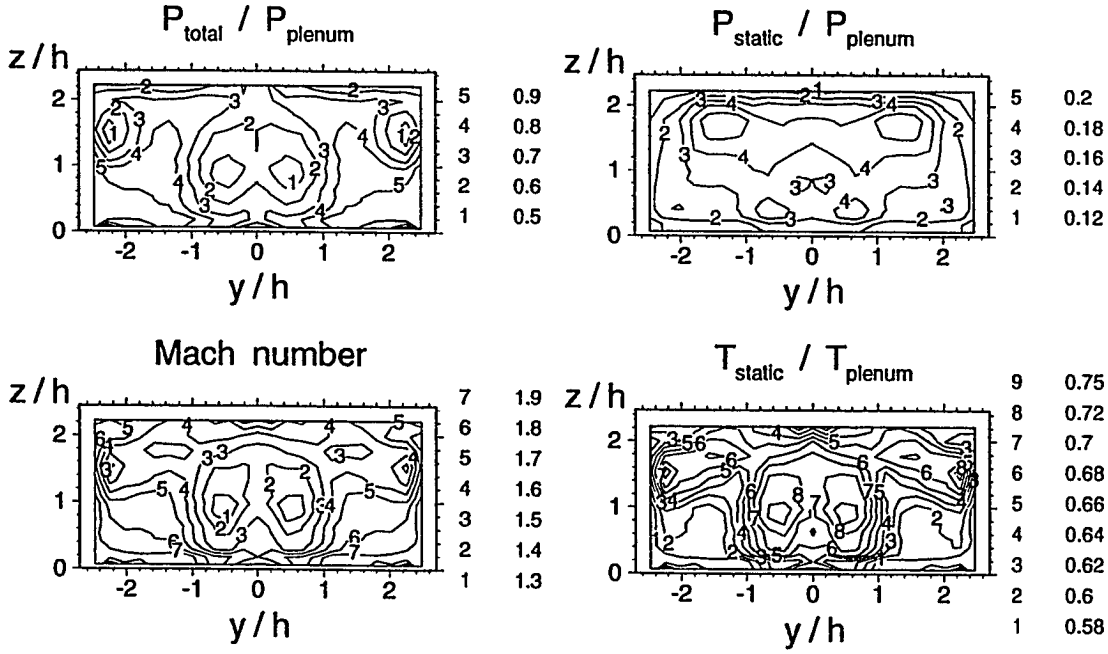


d. Cross - section at x / d = 23., x / h = 10.

Fig. 5.7 ( contd. ) Experimental contours, tapered-slot nozzle, vertical slot

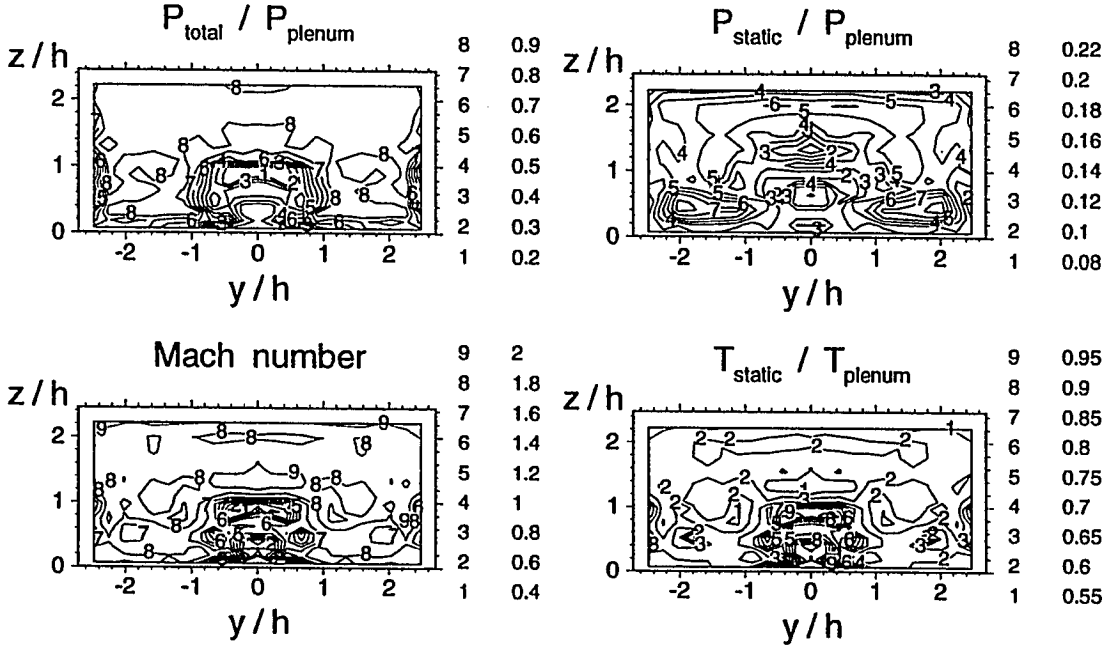


a. Cross - section at x / d = 1.7 , x / h = 0.75

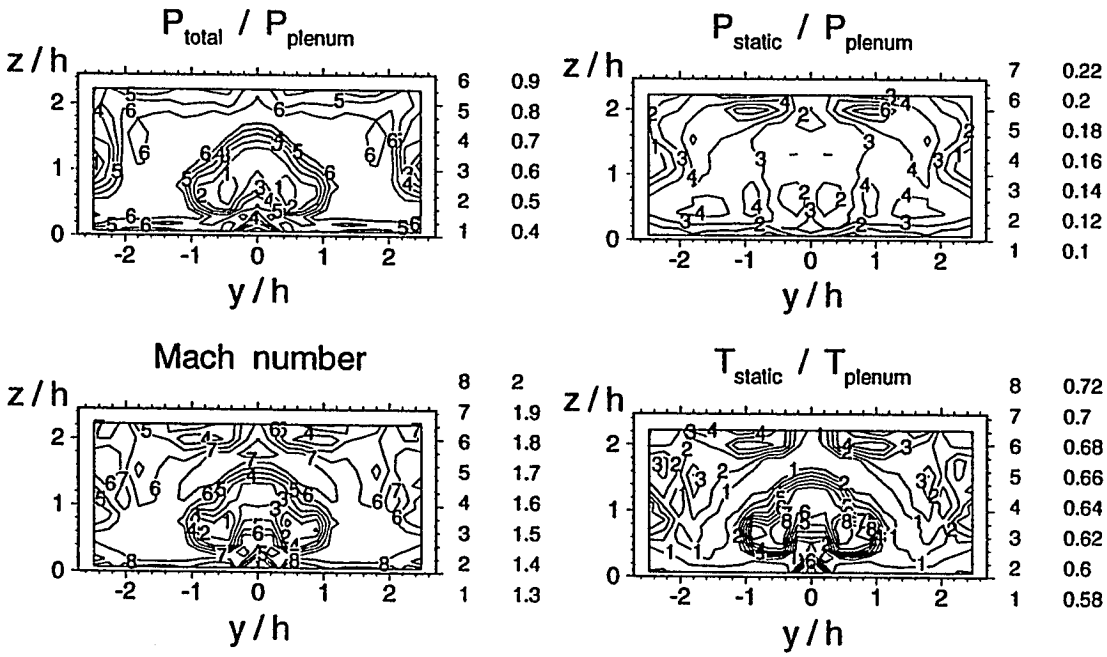


b. Cross - section at x / d = 8.8 , x / h = 3.9

Fig. 5.8 Experimental contours, elliptical nozzle, horizontal major axis

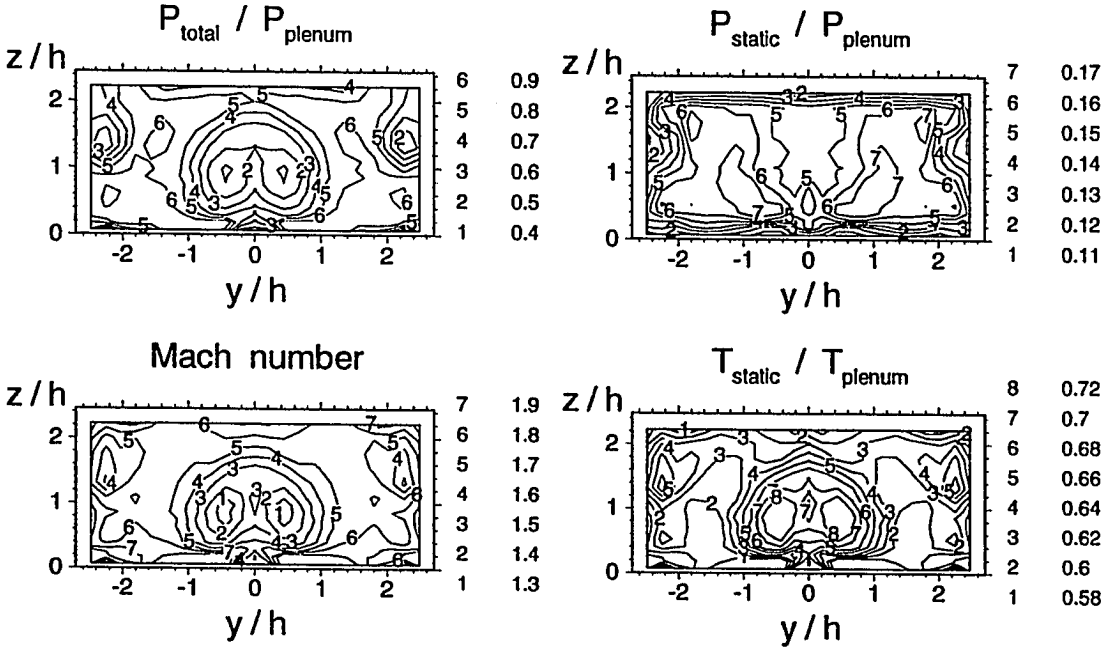


c. Cross - section at x / d = 16., x / h = 7.

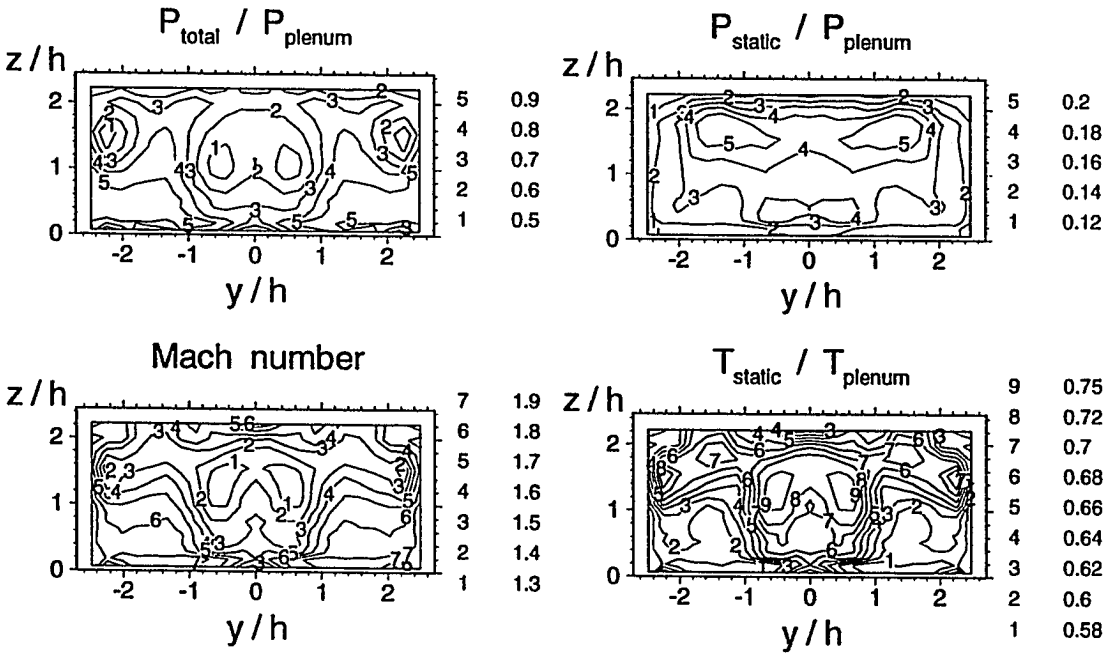


d. Cross - section at x / d = 23., x / h = 10.

Fig. 5.8 ( contd.) Experimental contours, elliptical nozzle, horizontal major axis

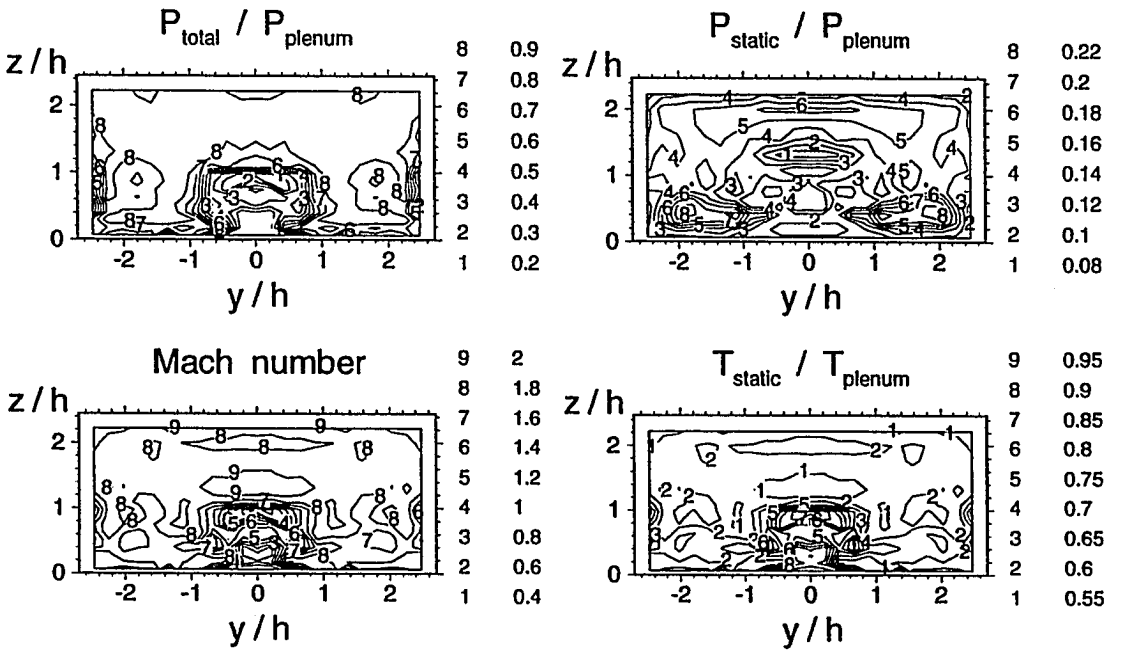


a. Cross - section at x / d = 1.7 , x / h = 0.75

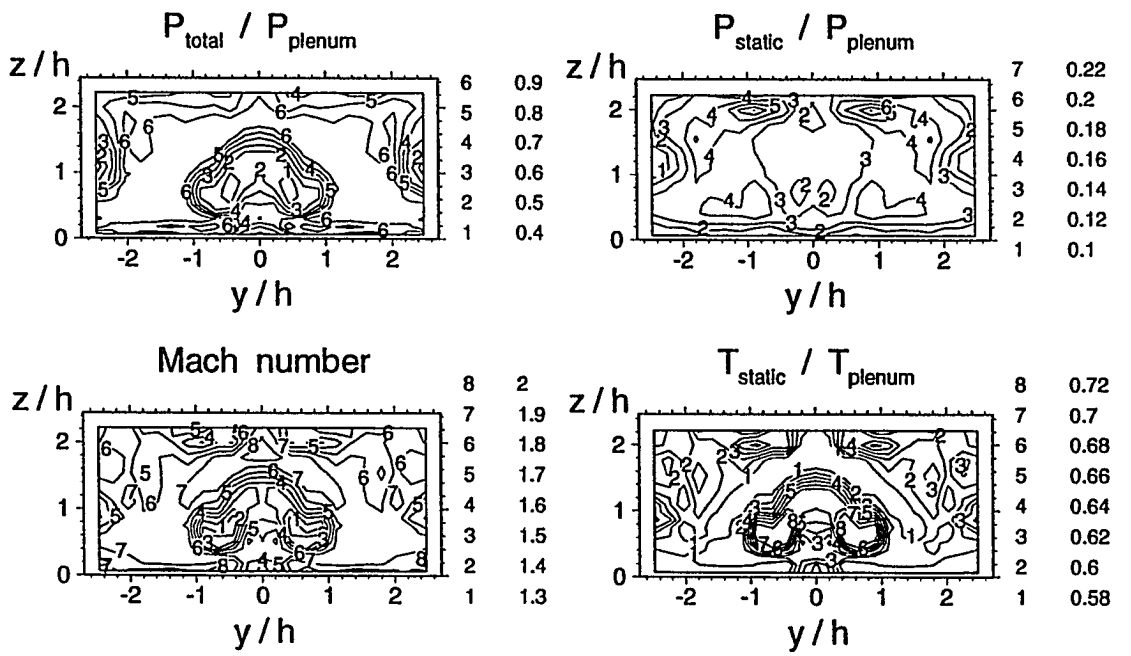


b. Cross - section at x / d = 8.8 , x / h = 3.9

Fig. 5.9 Experimental contours, elliptical nozzle, vertical major axis

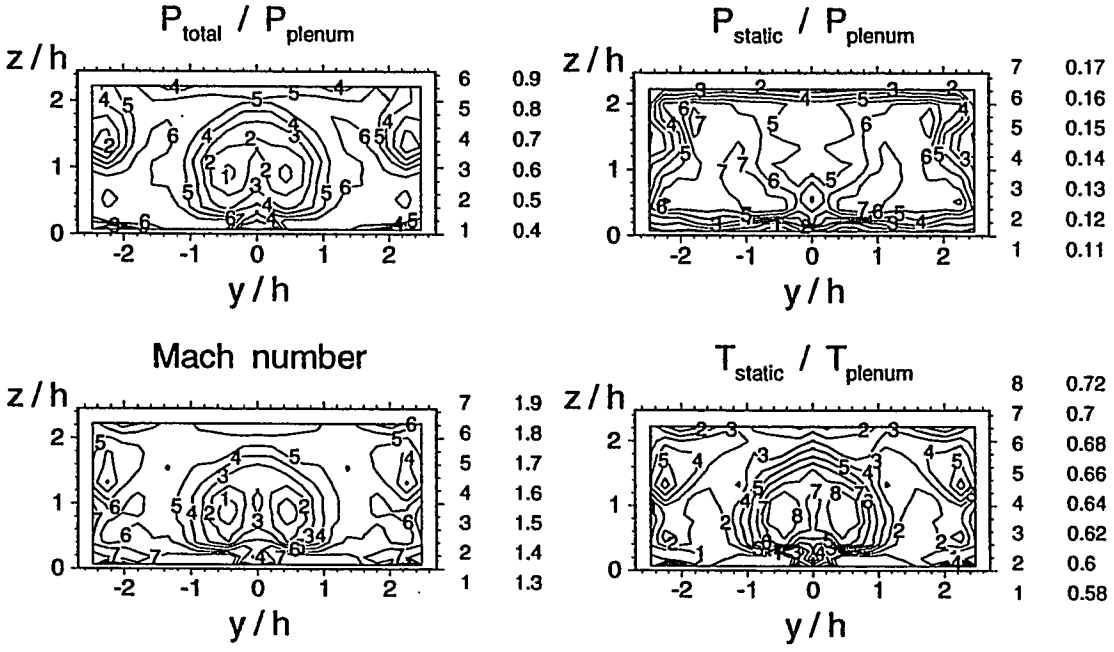


c. Cross - section at x / d = 16., x / h = 7.

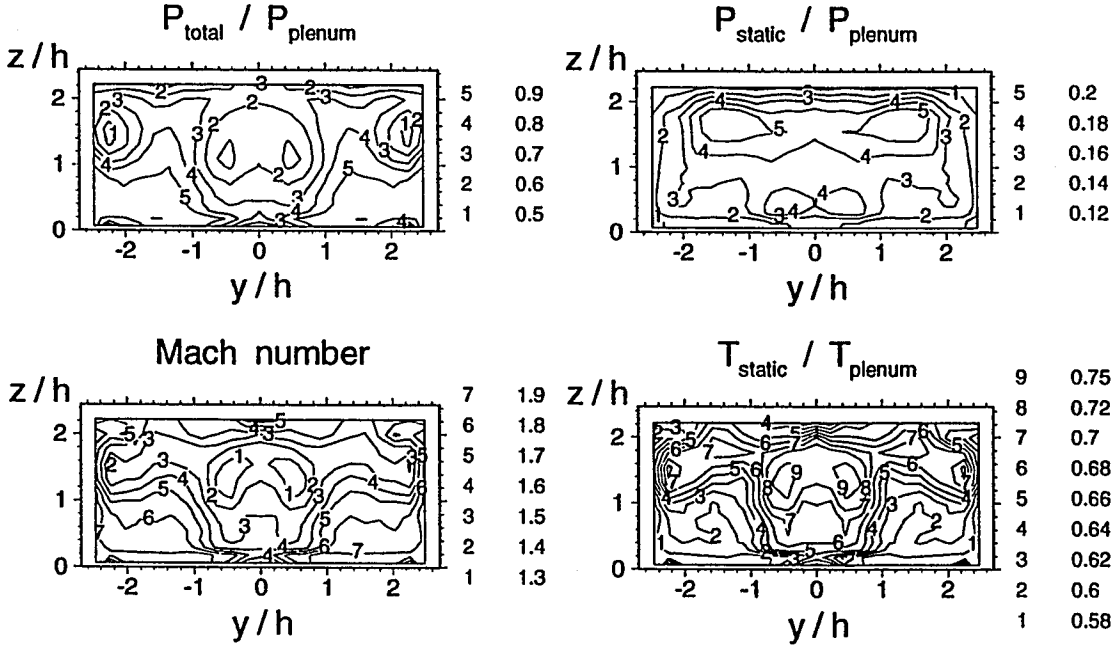


d. Cross - section at x / d = 23., x / h = 10.

Fig. 5.9 ( contd.) Experimental contours, elliptical nozzle, vertical major axis

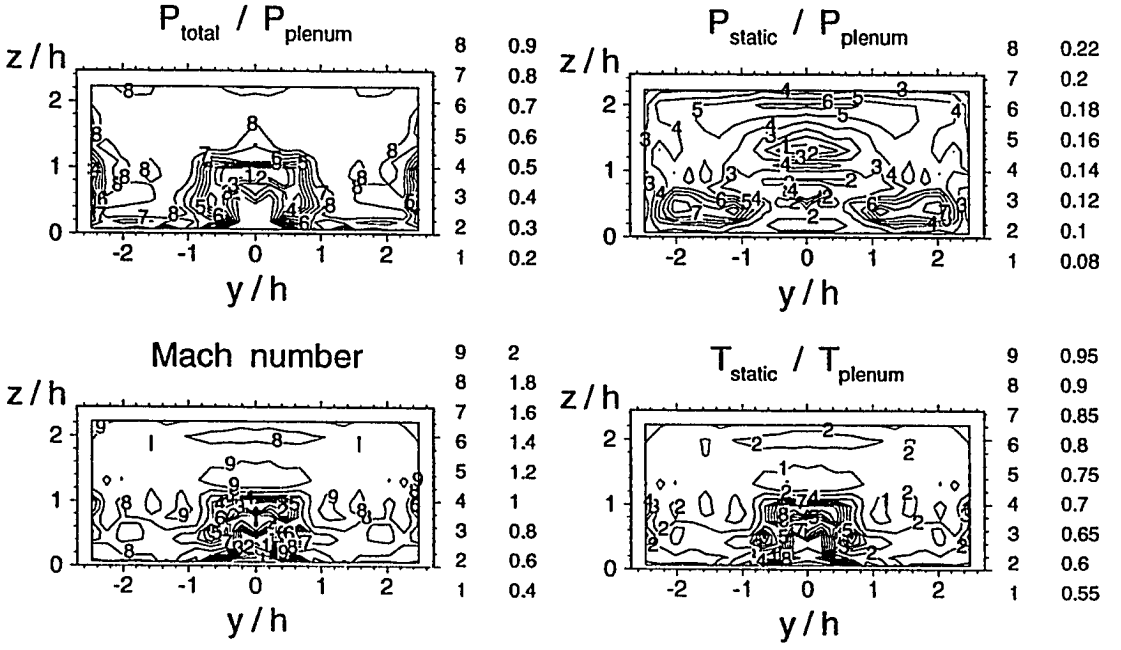


a. Cross - section at $x/d = 1.7$, $x/h = 0.75$

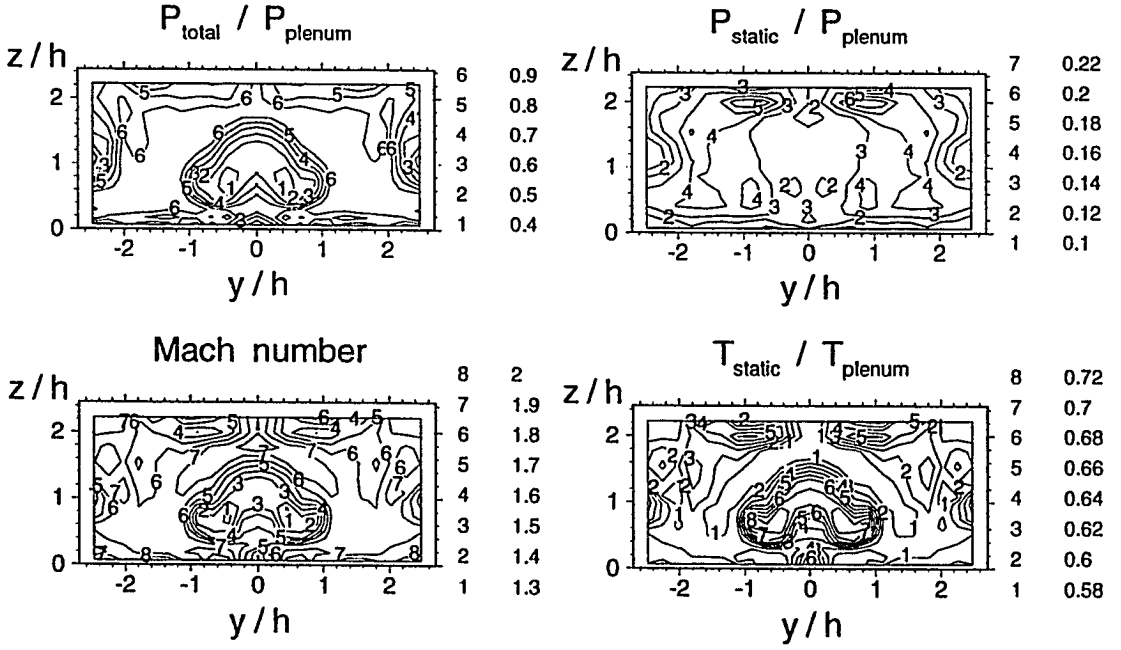


b. Cross - section at $x/d = 8.8$, $x/h = 3.9$

Fig. 5.10 Experimental contours, trapezoidal nozzle

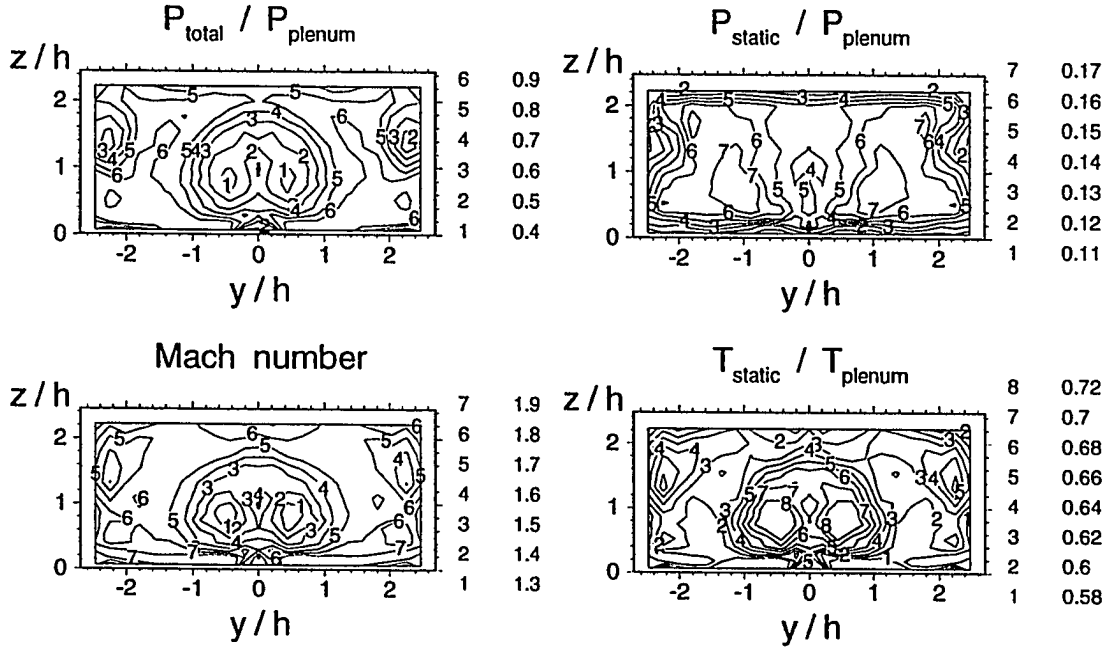


c. Cross - section at x / d = 16. , x / h = 7.

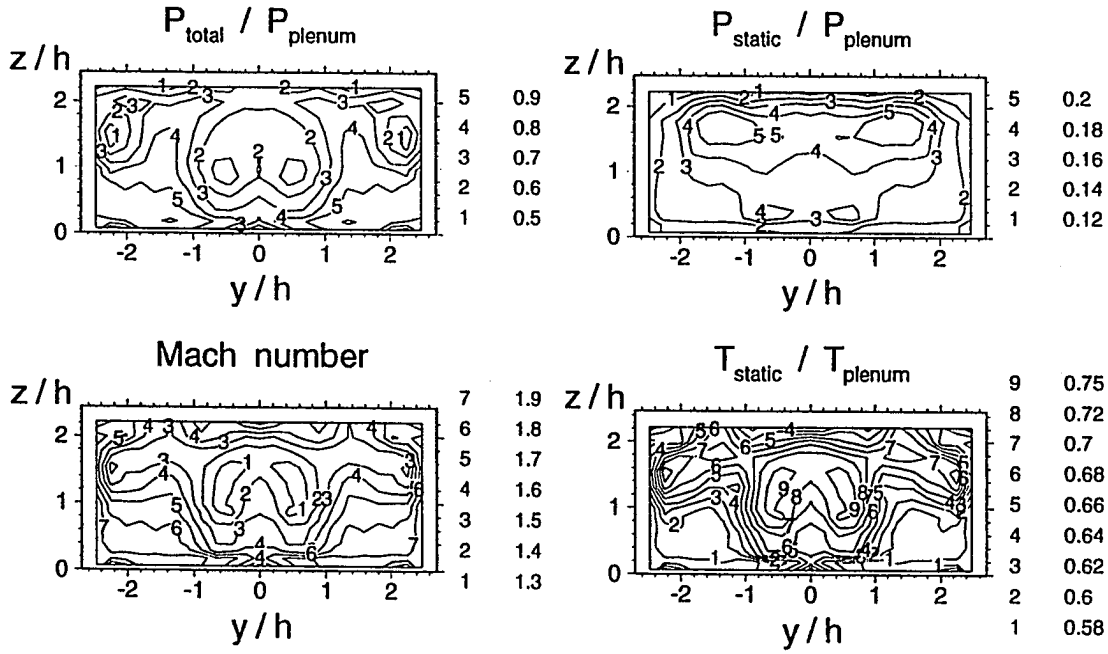


d. Cross - section at x / d = 23. , x / h = 10.

Fig. 5.10 ( contd. ) Experimental contours, trapezoidal nozzle

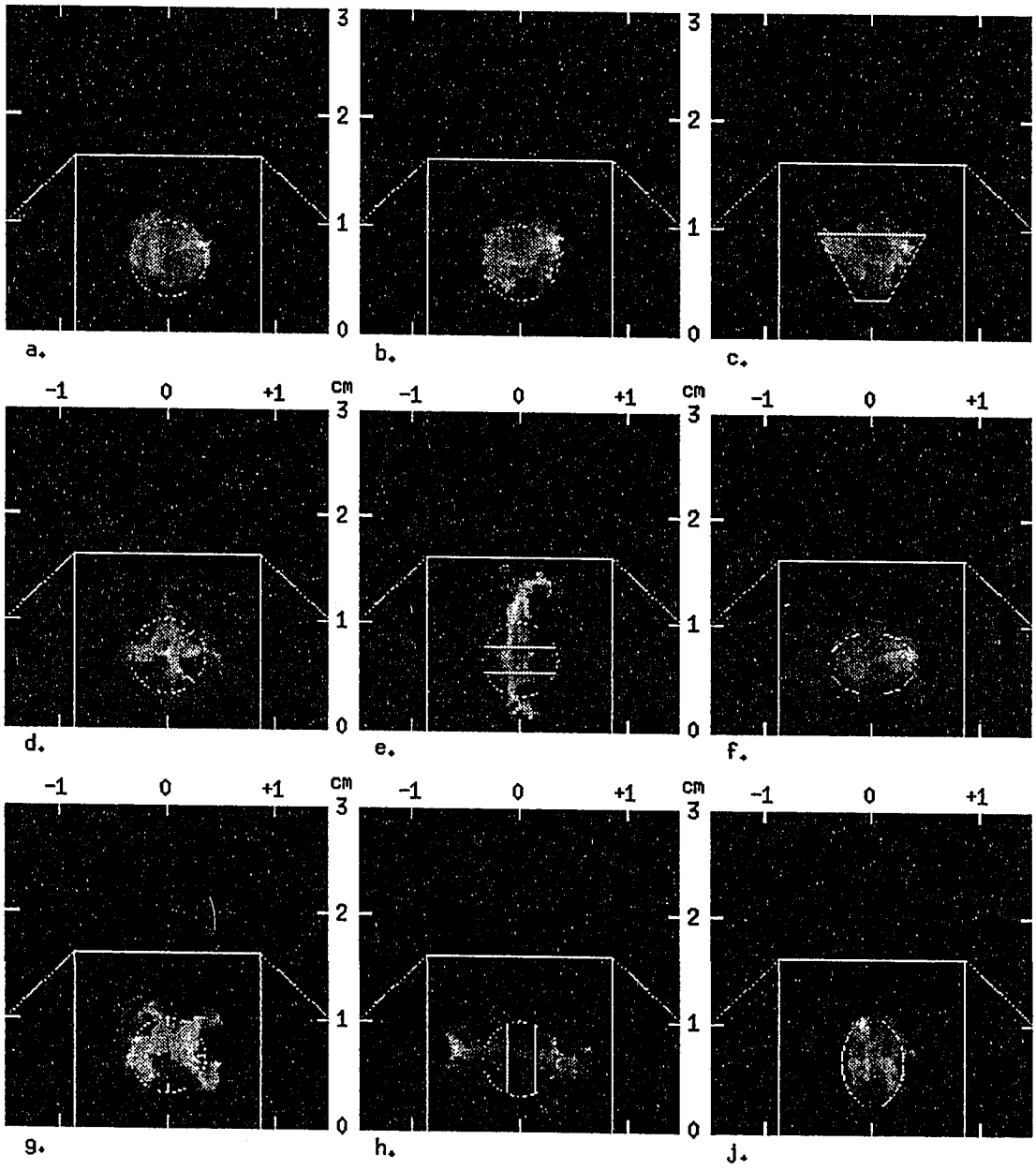


Fig. 5.11 Instantaneous images of ethanol-seeded air injection into still air at x/h=0.75

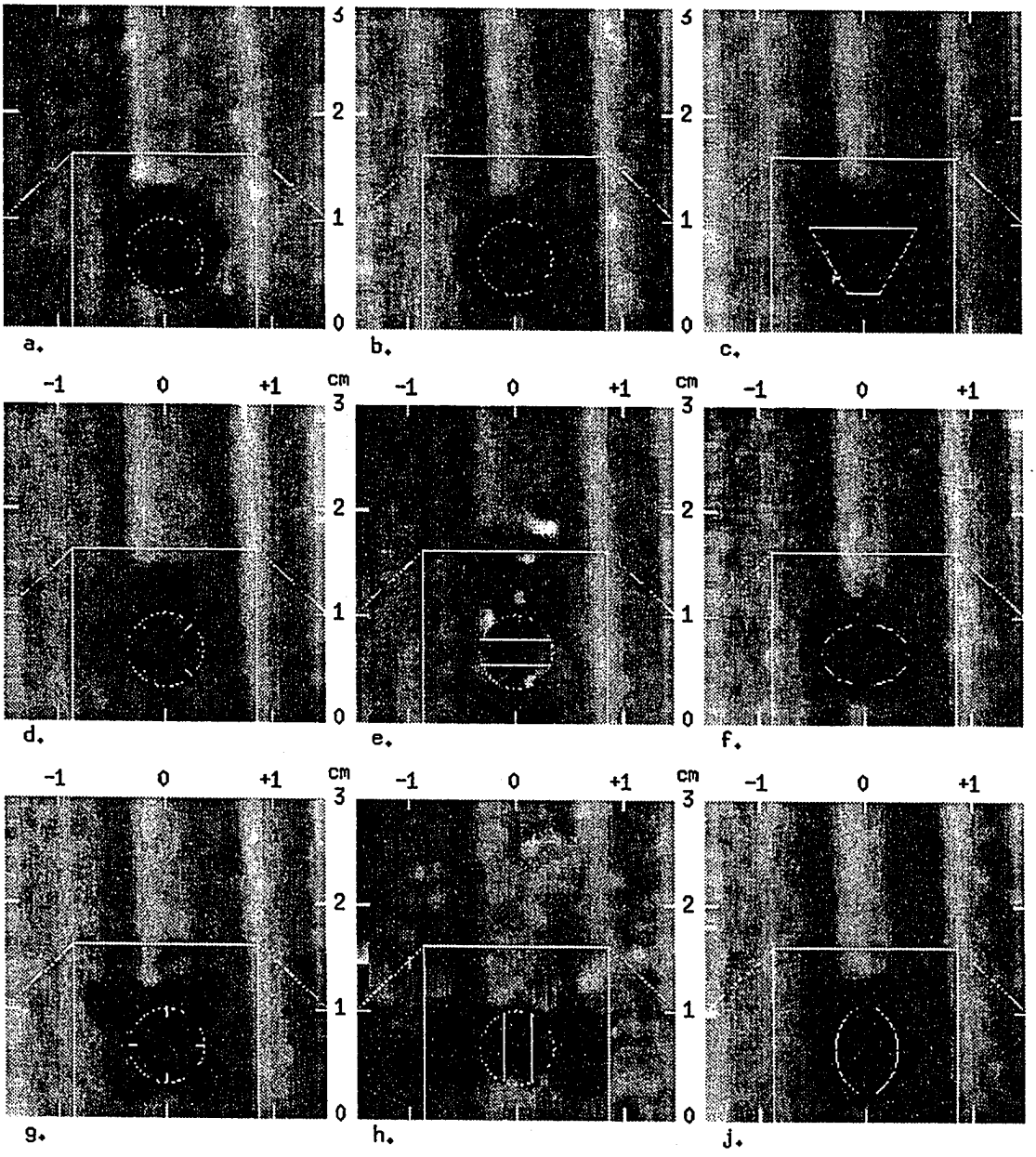


Fig. 5.12 Instantaneous images of helium injection into still air at x/h=0.75

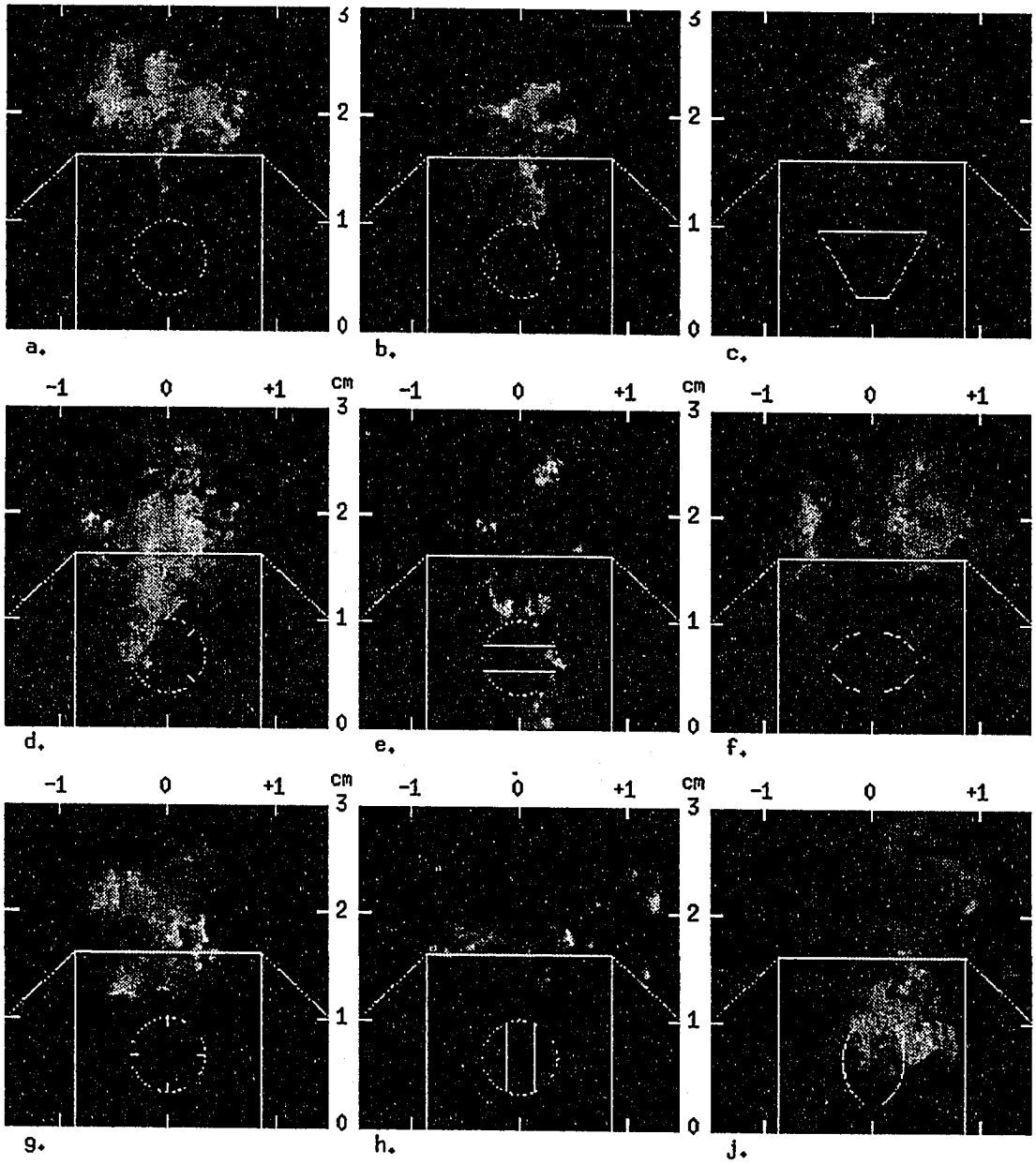


Fig. 5.13 Instantaneous images of ethanol-seeded air injection into still air at x/h=3.9

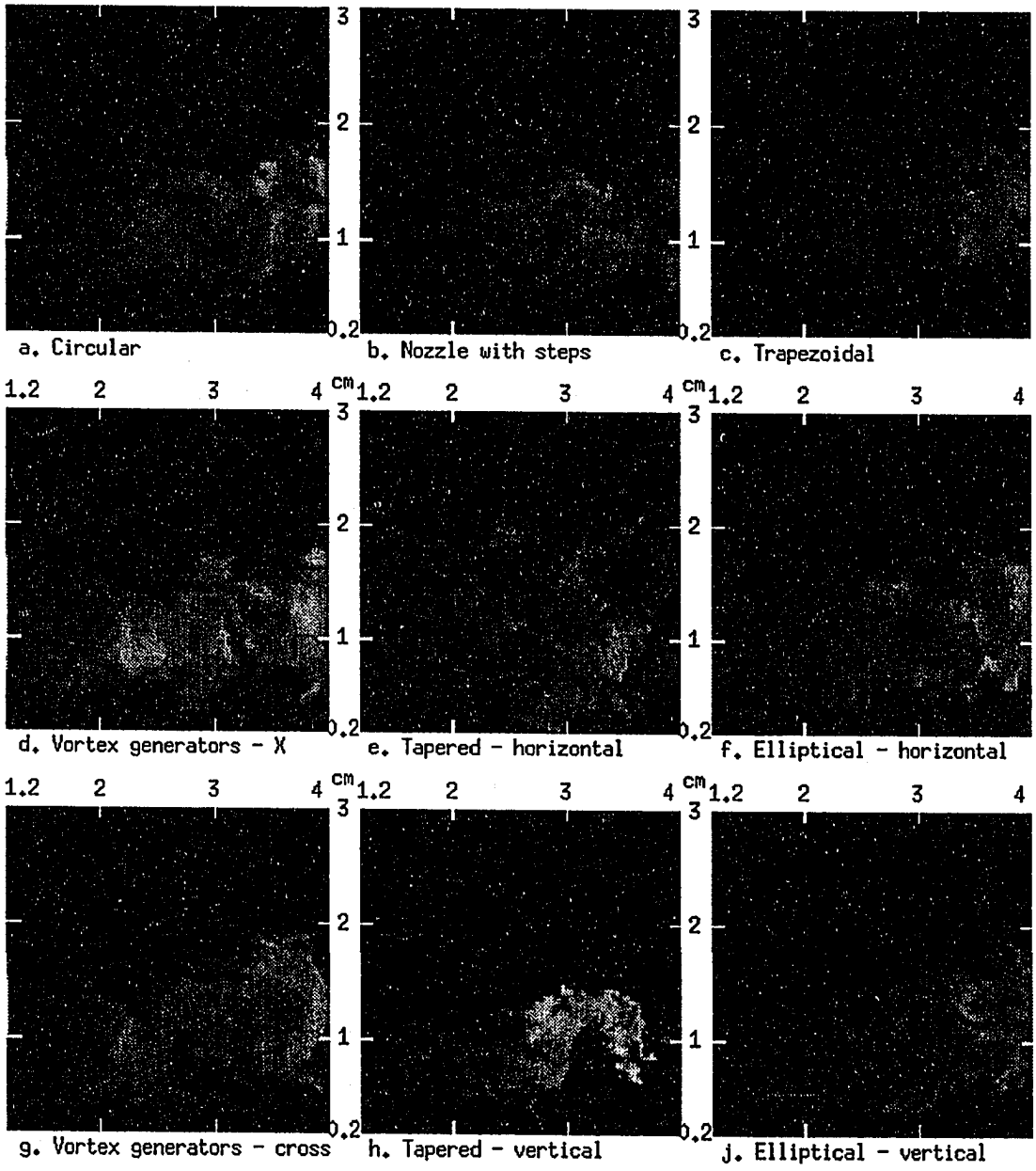


Fig. 5.14 Instantaneous side-view images of ethanol-seeded air jet only, no main flow

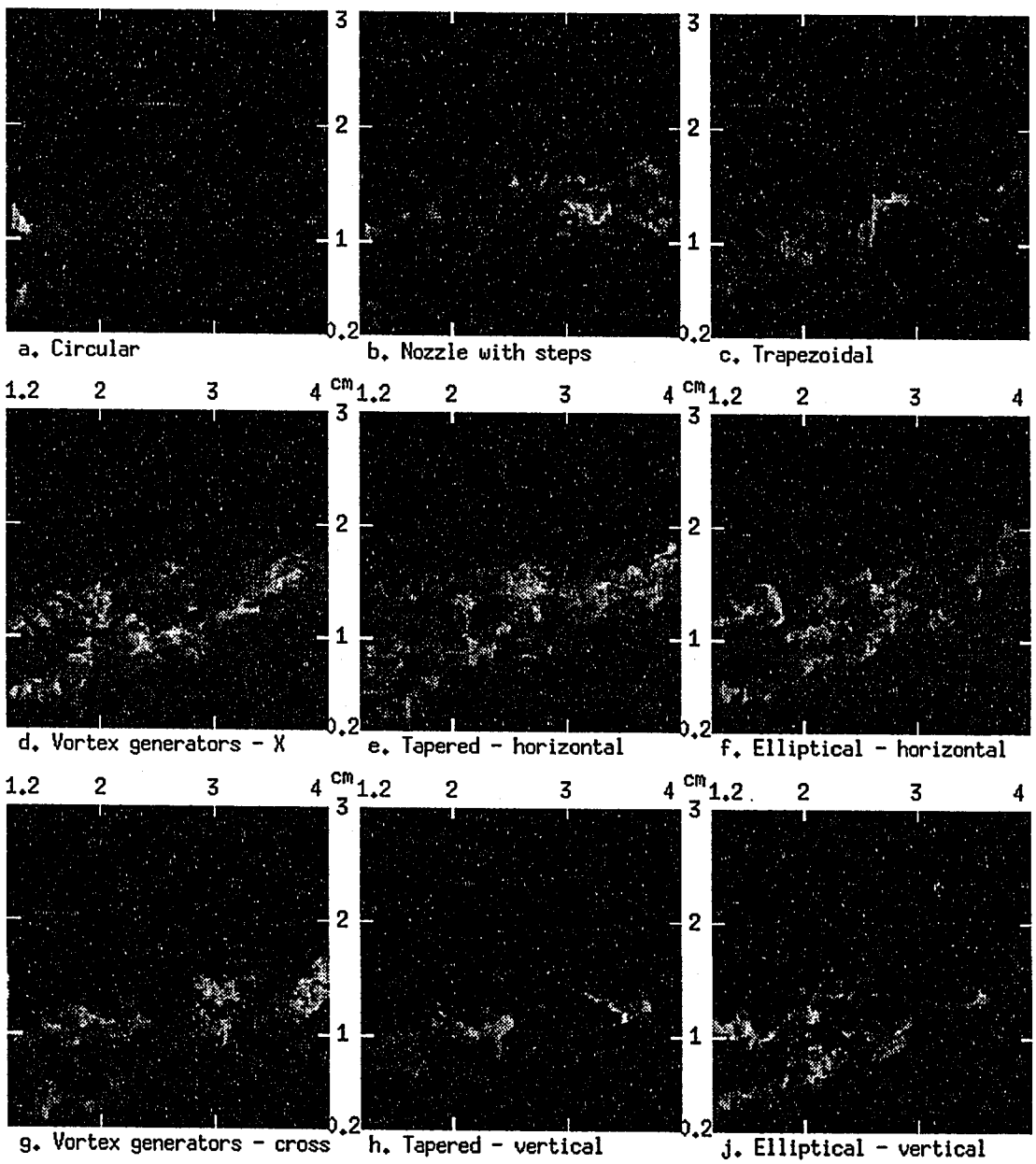


Fig. 5.15 Instantaneous side-view images of ethanol-seeded air jet

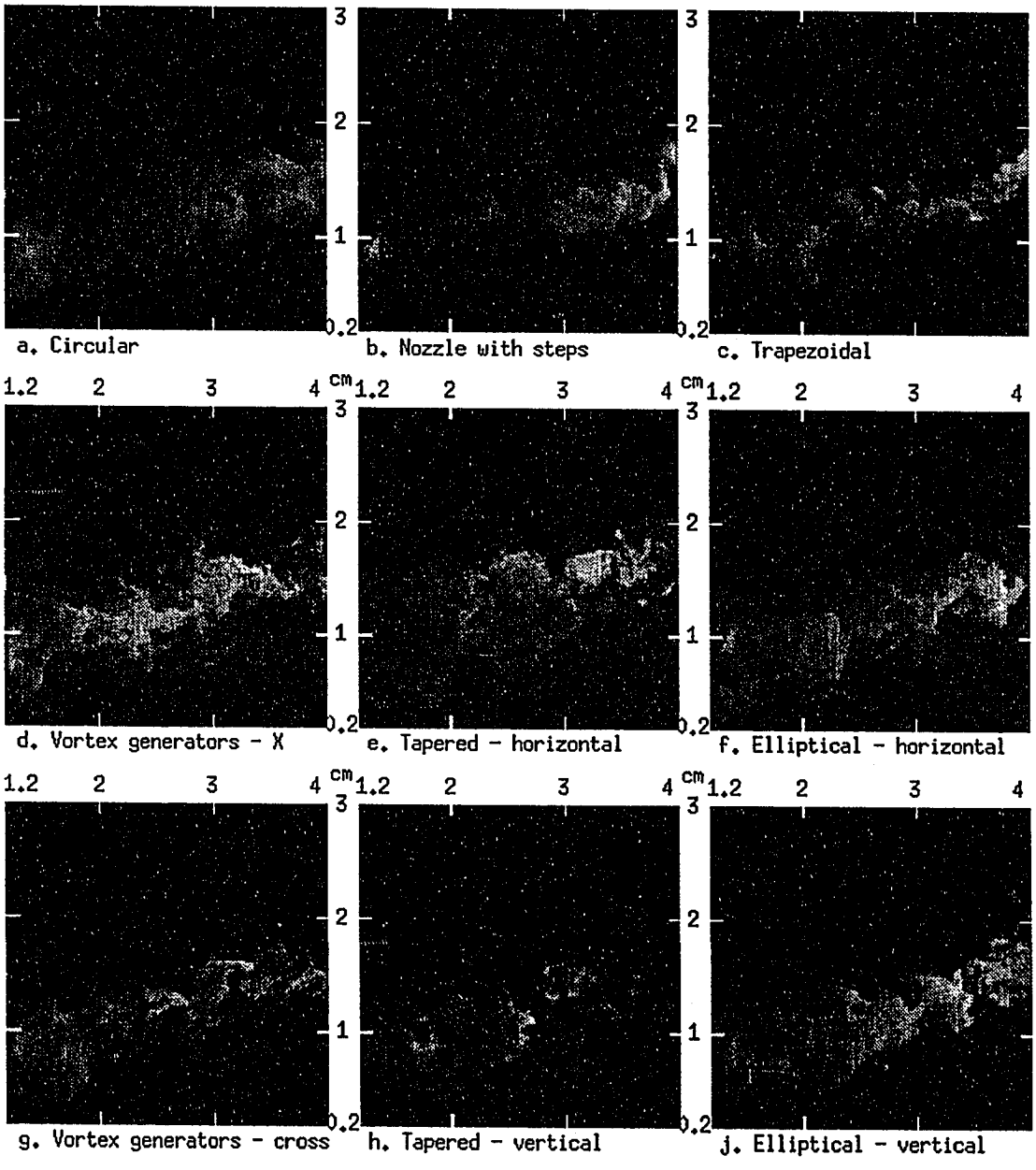


Fig. 5.16 Instantaneous side-view images of ethanol-seeded helium jet

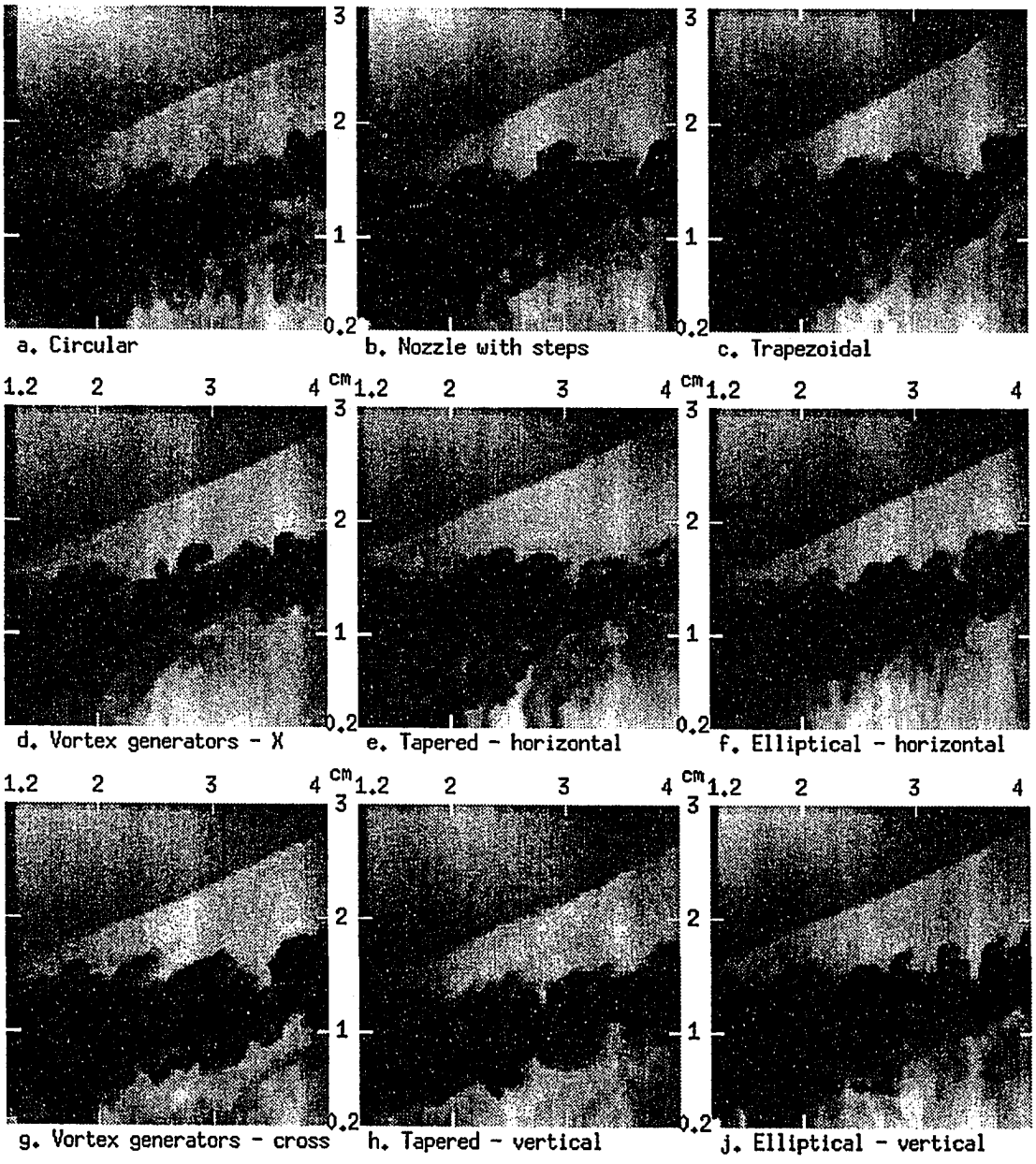


Fig. 5.17 Instantaneous side-view images of helium jet (Rayleigh signal)

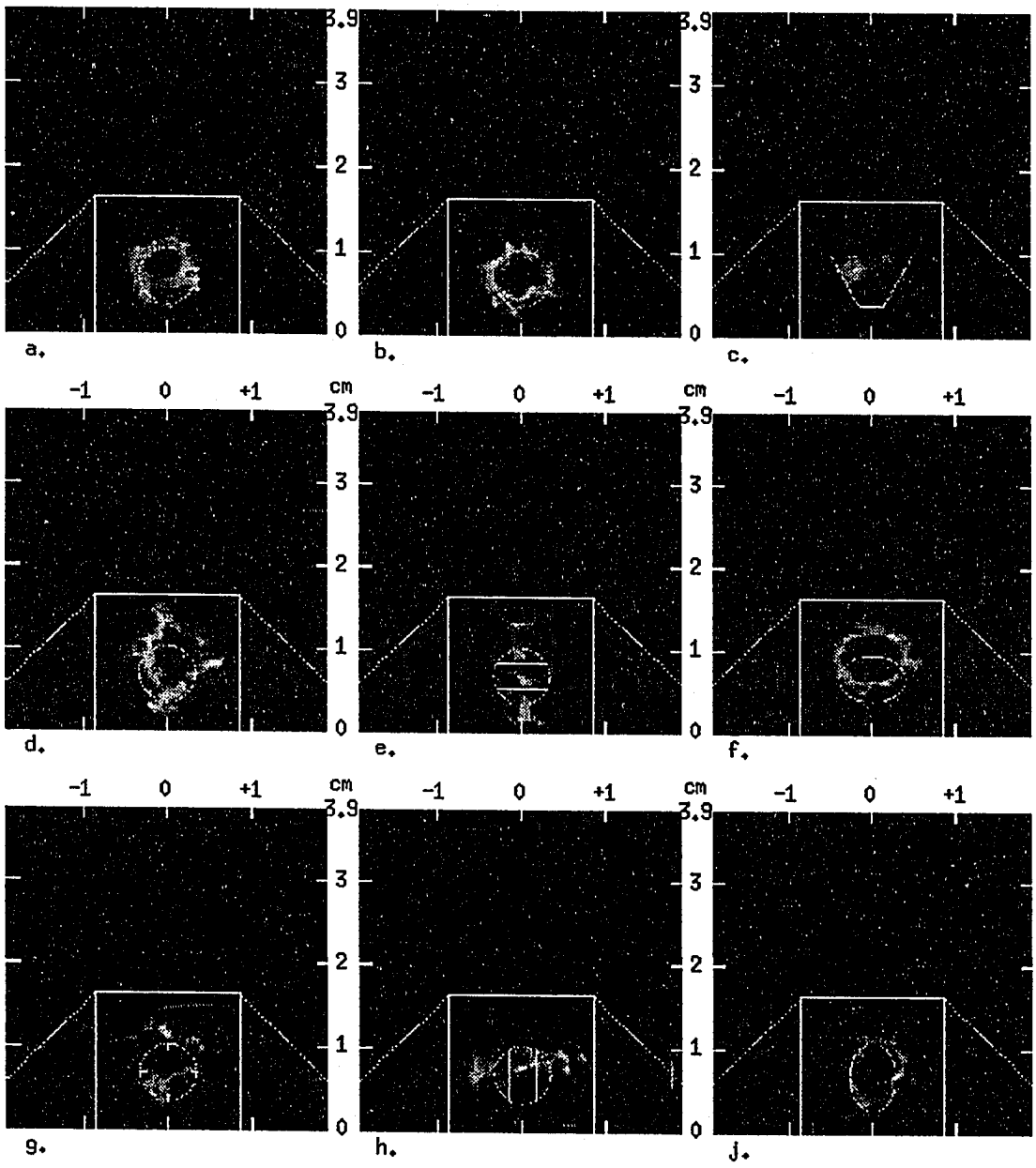


Fig. 5.18 Instantaneous transverse images of ethanol-seeded air injection at x/h=0.75

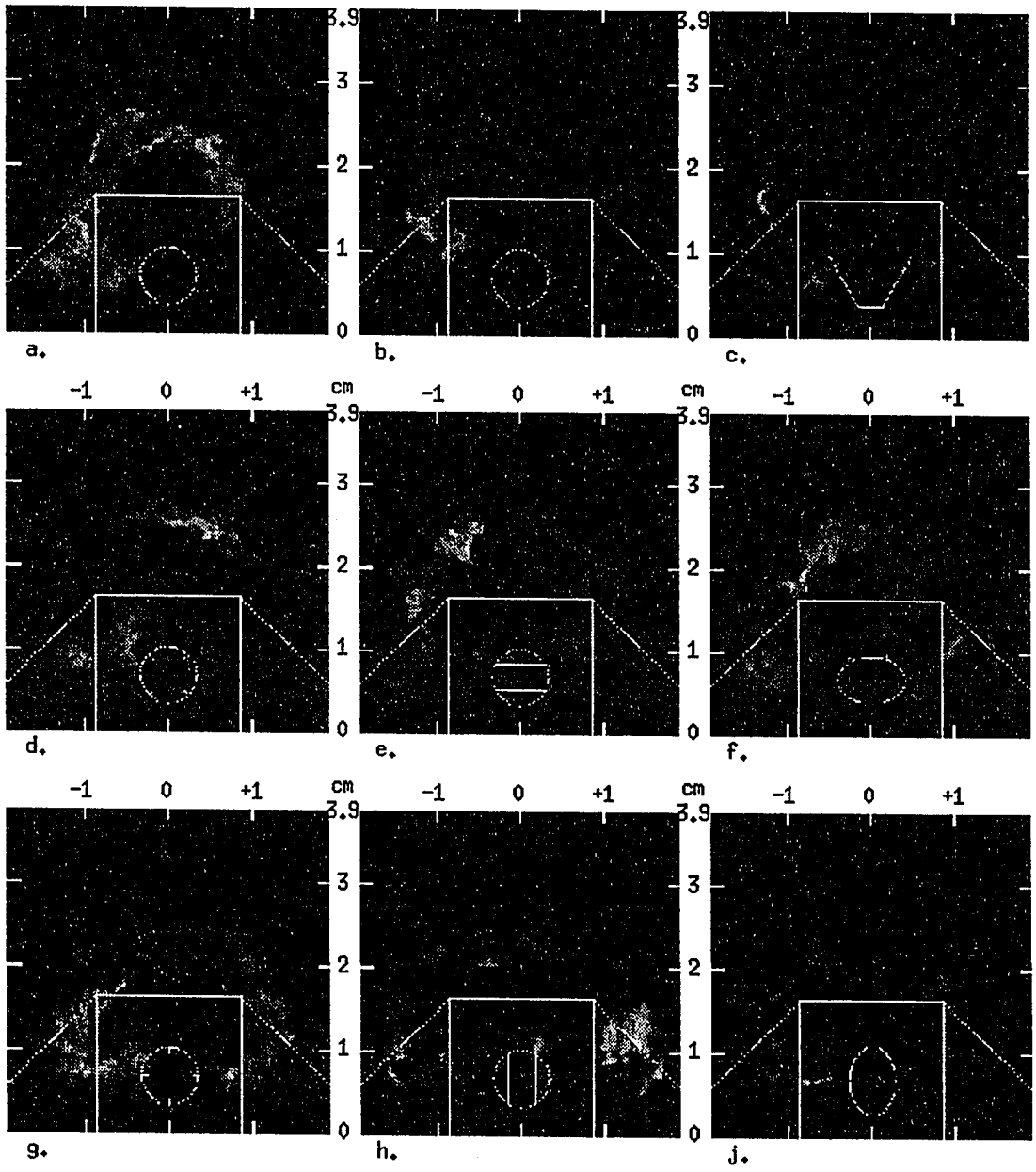


Fig. 5.19 Instantaneous transverse images of ethanol-seeded air injection at x/h=3.9

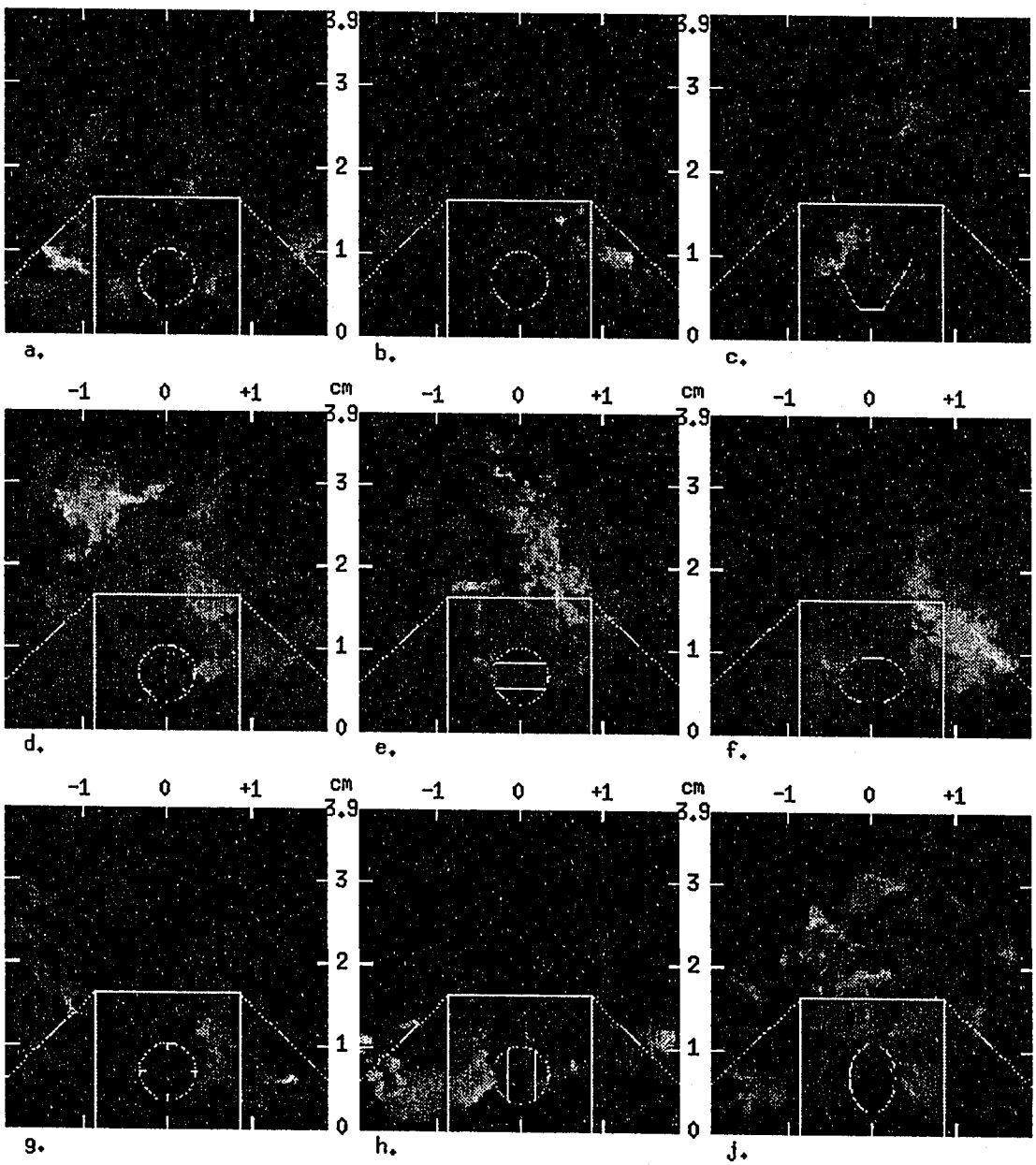


Fig. 5.20 Instantaneous transverse images of ethanol-seeded air injection at x/h=7.

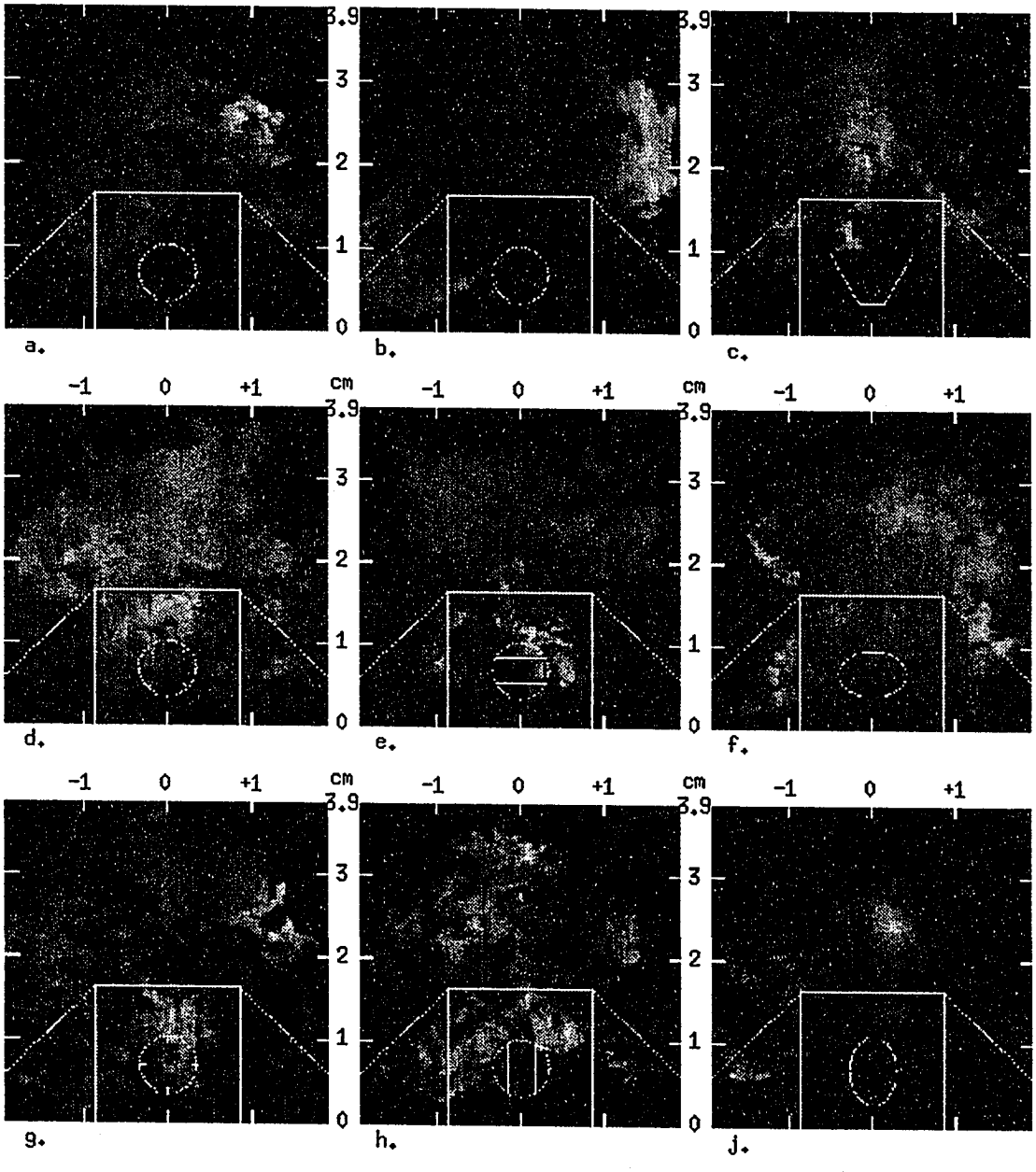


Fig. 5.21 Instantaneous transverse images of ethanol-seeded air injection at x/h=10.

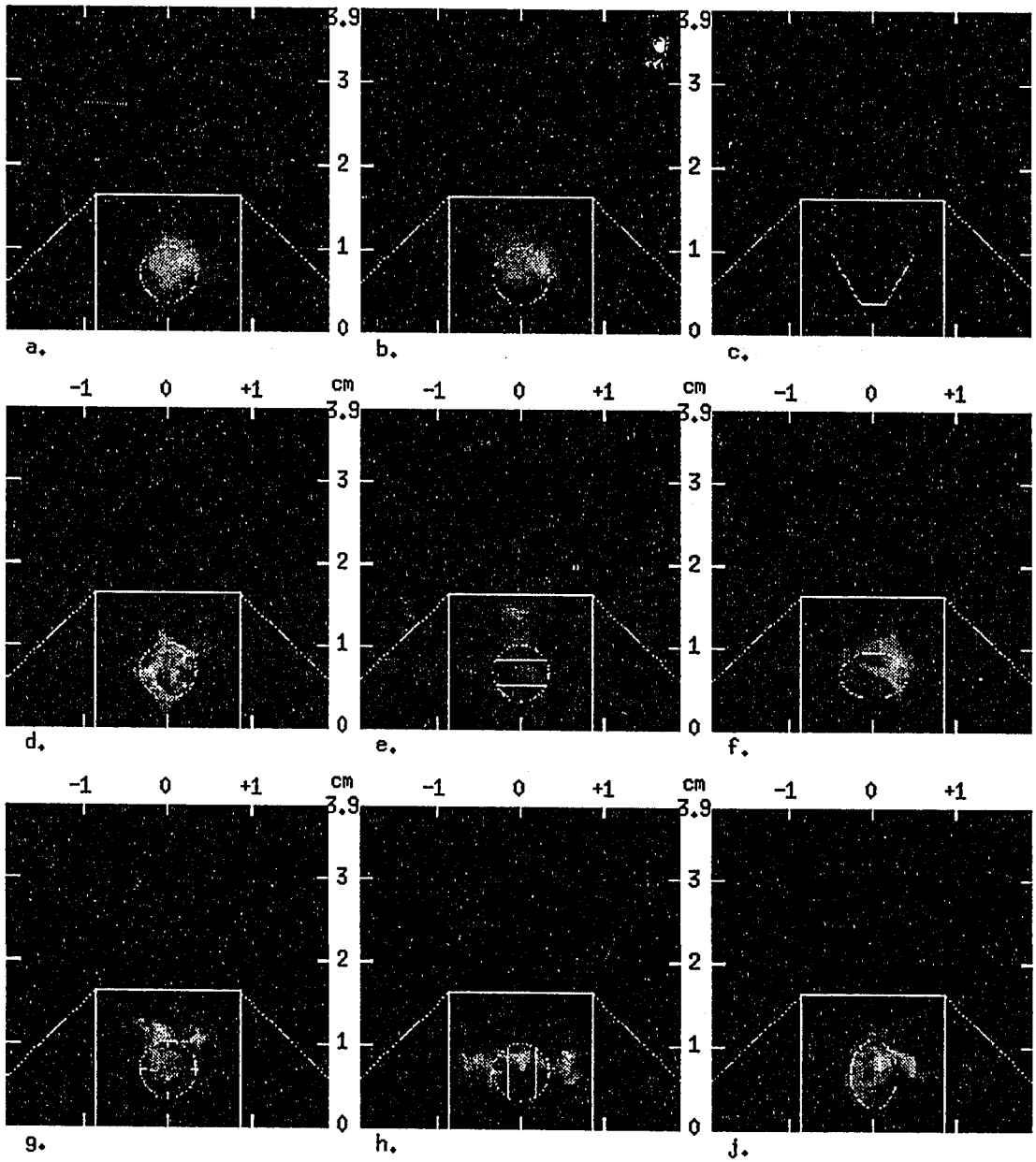


Fig. 5.22 Instantaneous transverse images of ethanol-seeded helium injection at x/h=0.75

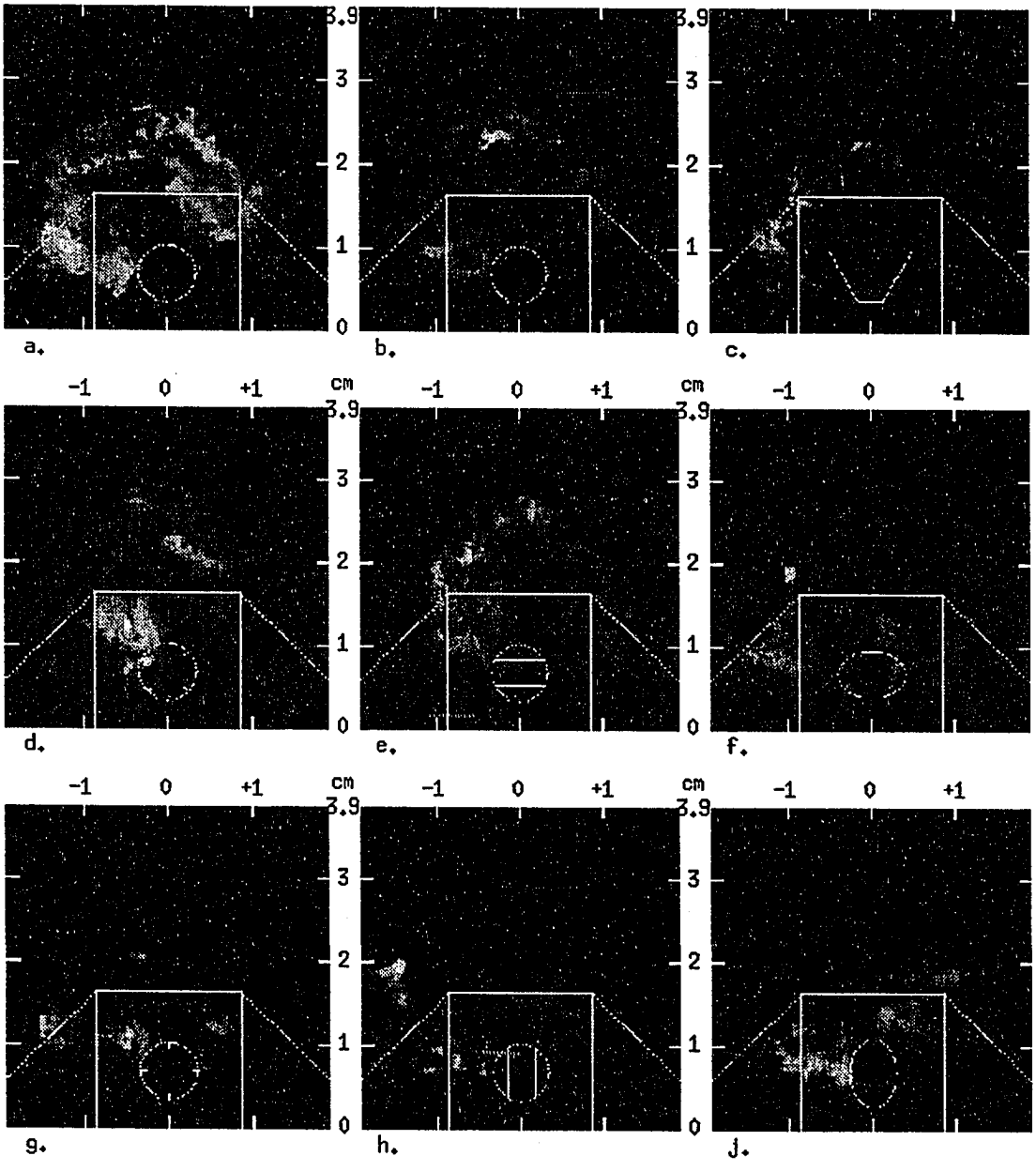


Fig. 5.23 Instantaneous transverse images of ethanol-seeded helium injection at x/h=3.9

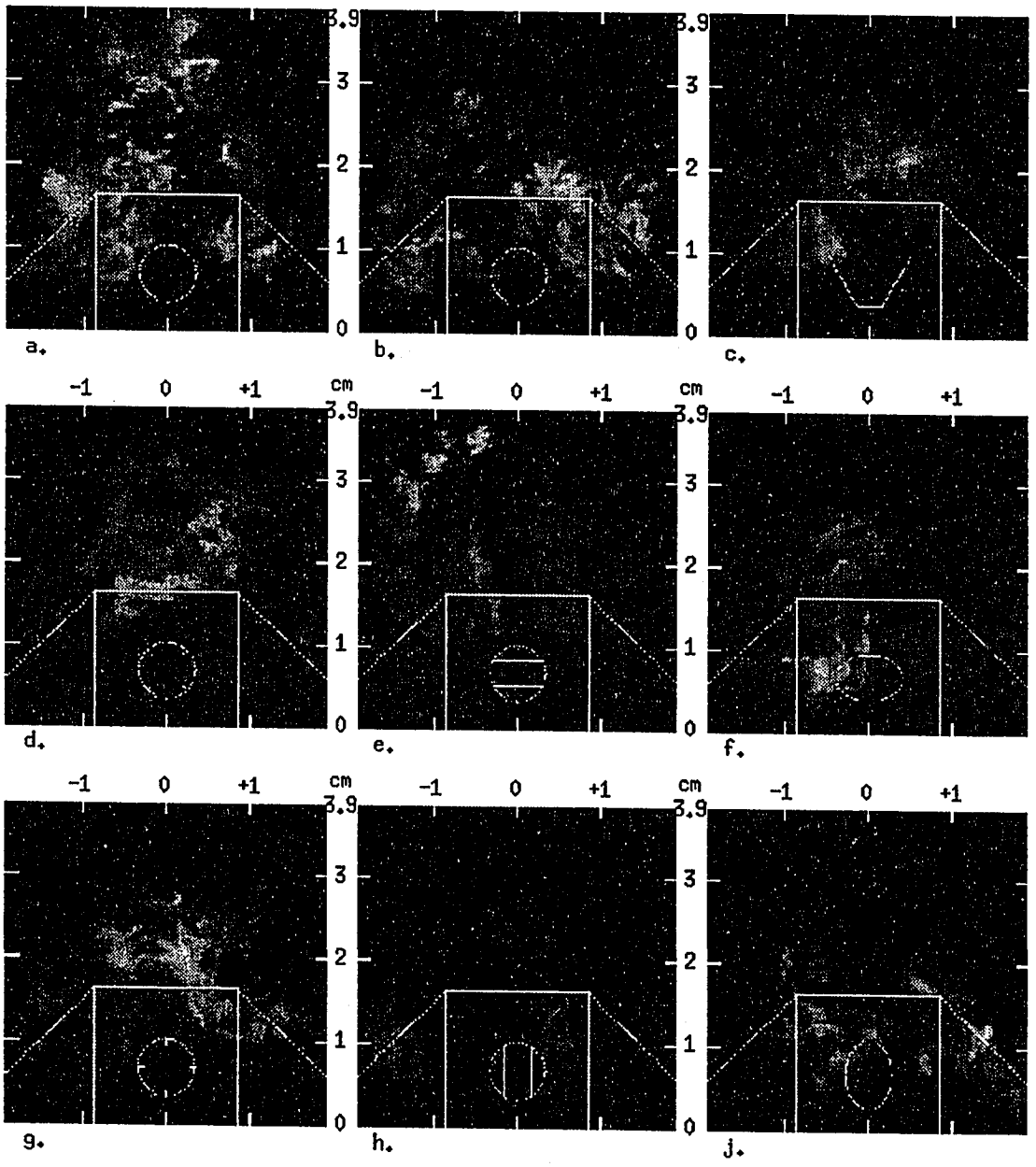


Fig. 5.24 Instantaneous transverse images of ethanol-seeded helium injection at x/h=7.

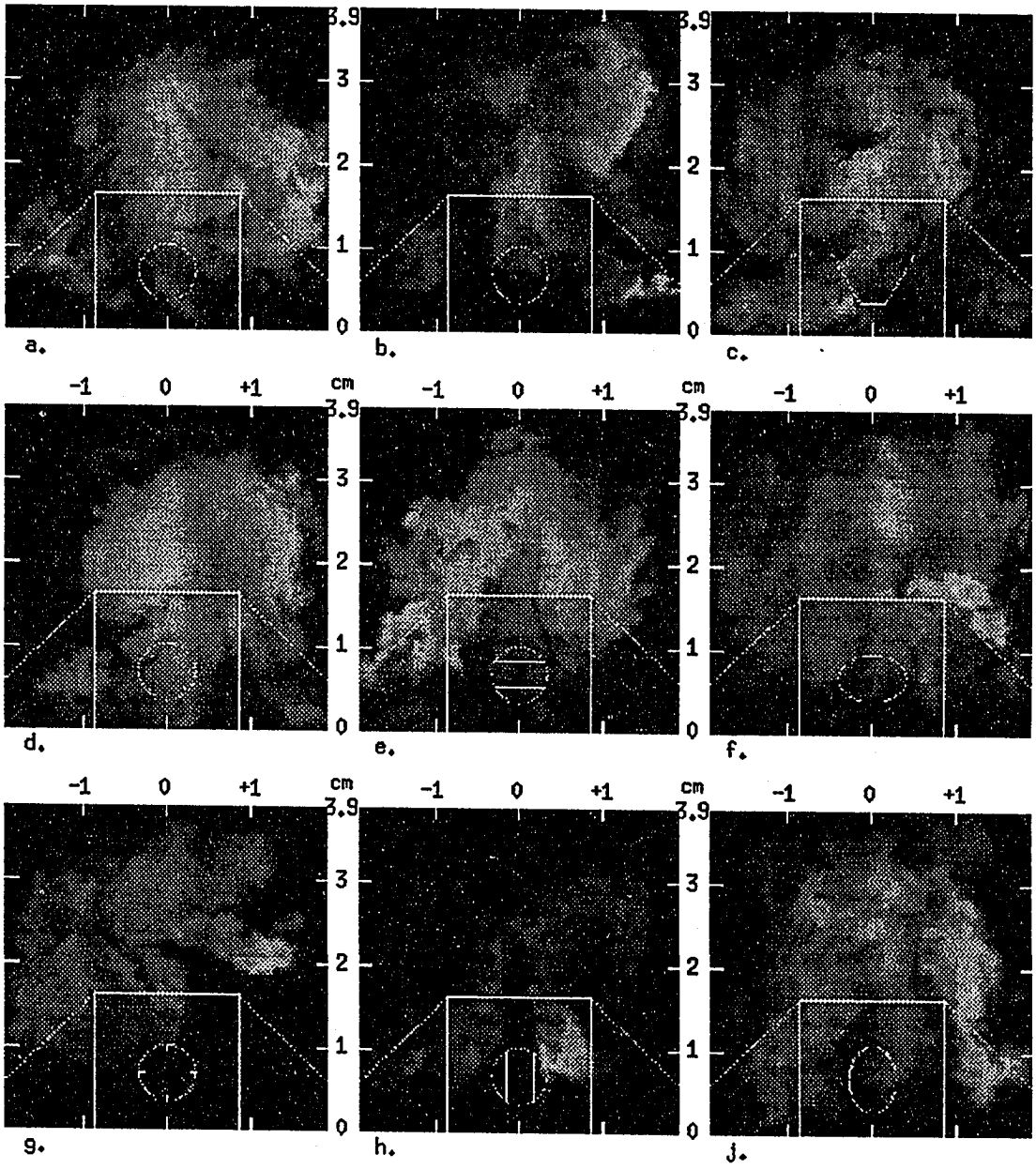


Fig. 5.25 Instantaneous transverse images of ethanol-seeded helium injection at x/h=10.

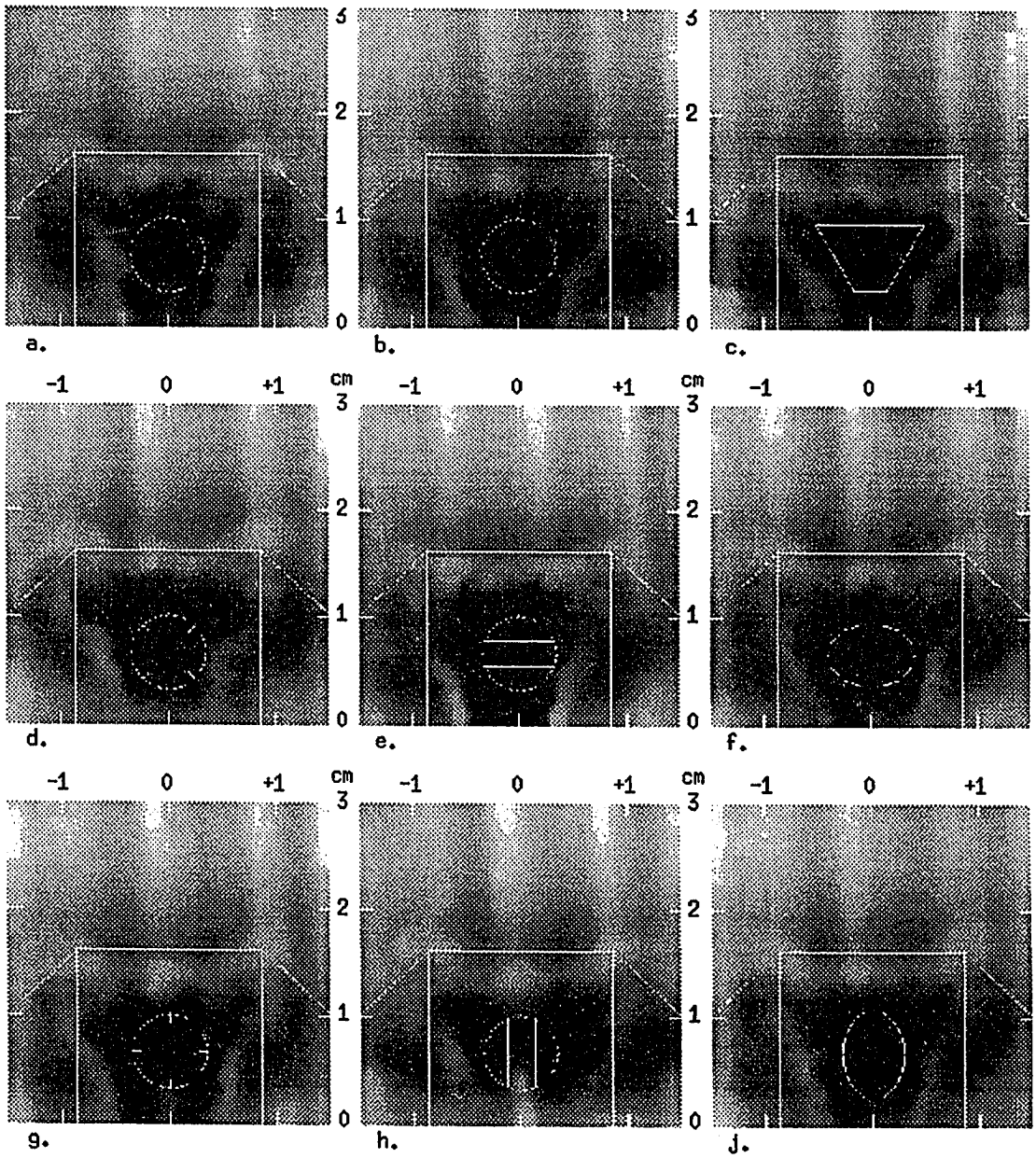


Fig. 5.26 Instantaneous transverse images of helium injection at x/h=0.75

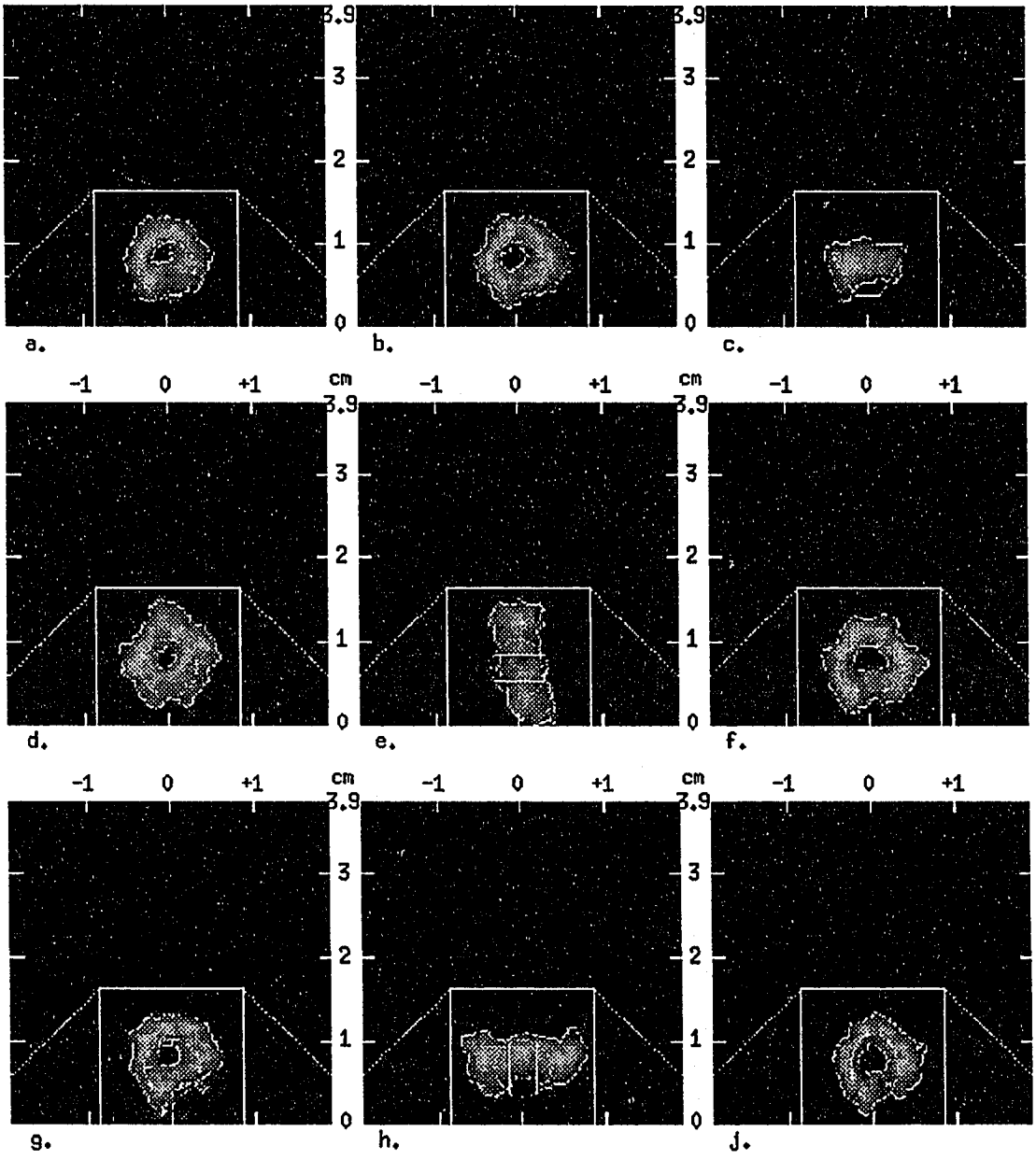


Fig. 5.27 Composite transverse images of ethanol-seeded air injection at x/h=0.75

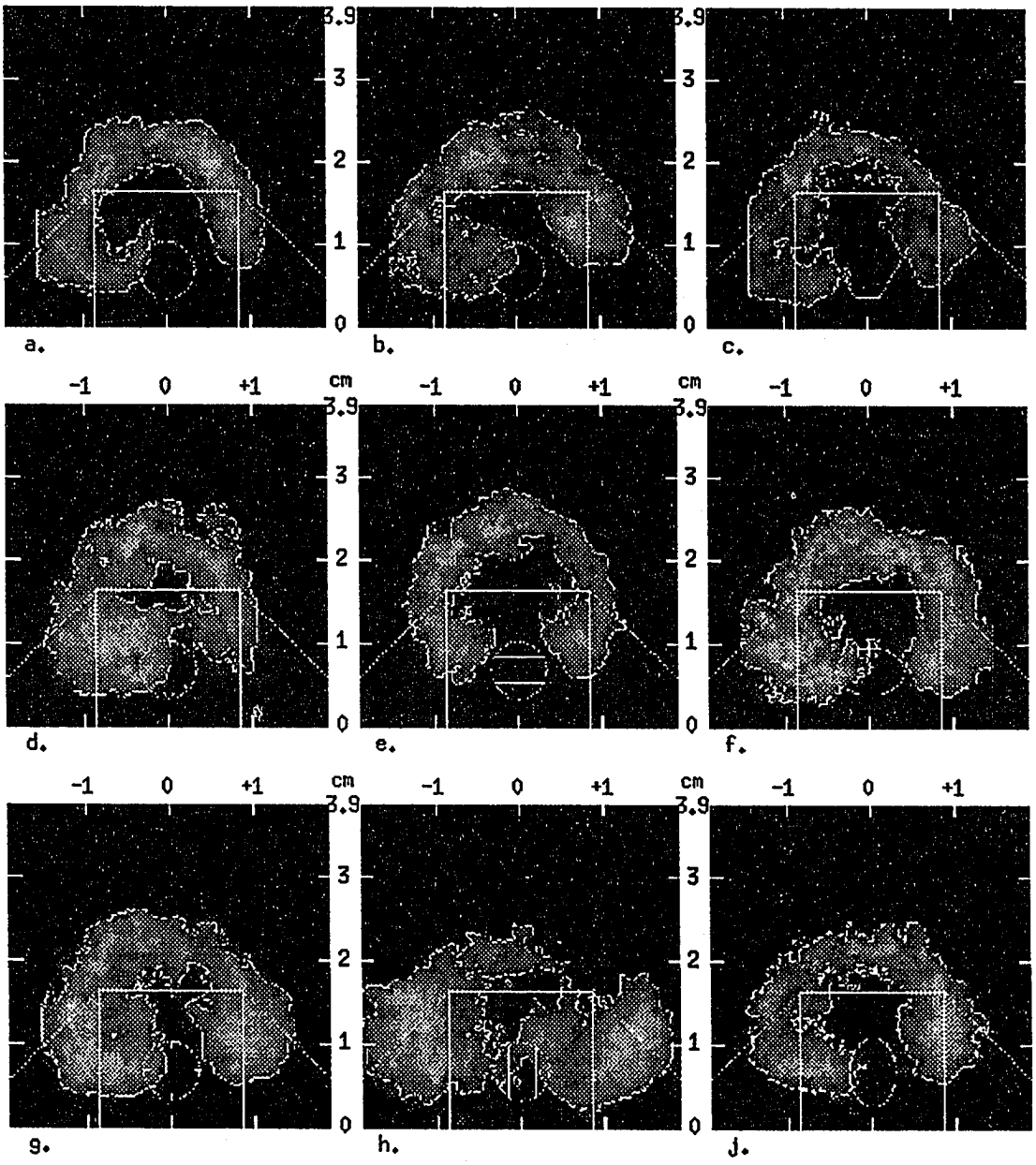


Fig. 5.28 Composite transverse images of ethanol-seeded air injection at x/h=3.9

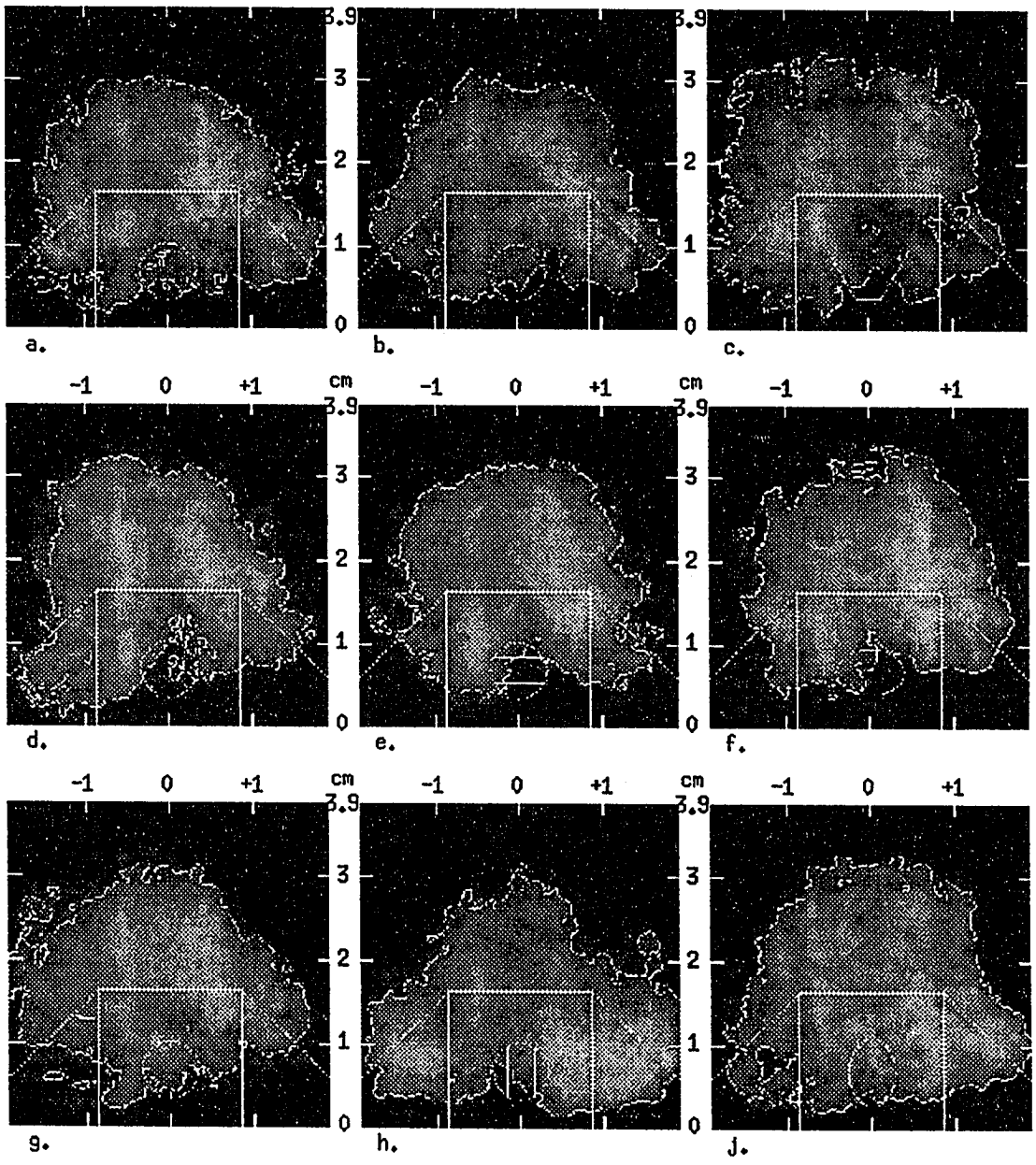


Fig. 5.29 Composite transverse images of ethanol-seeded air injection at x/h=7.

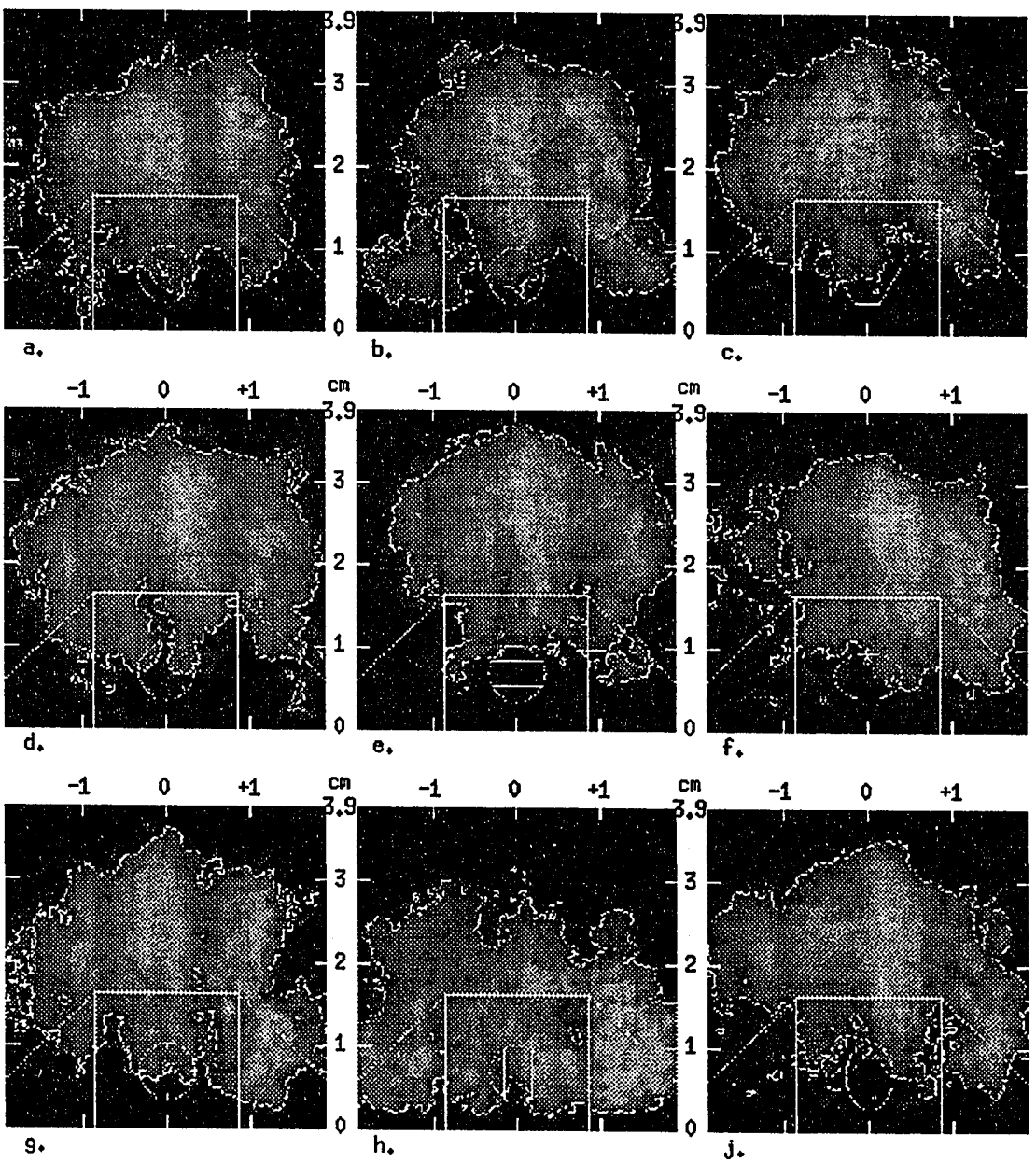


Fig. 5.30 Composite transverse images of ethanol-seeded air injection at x/h=10.

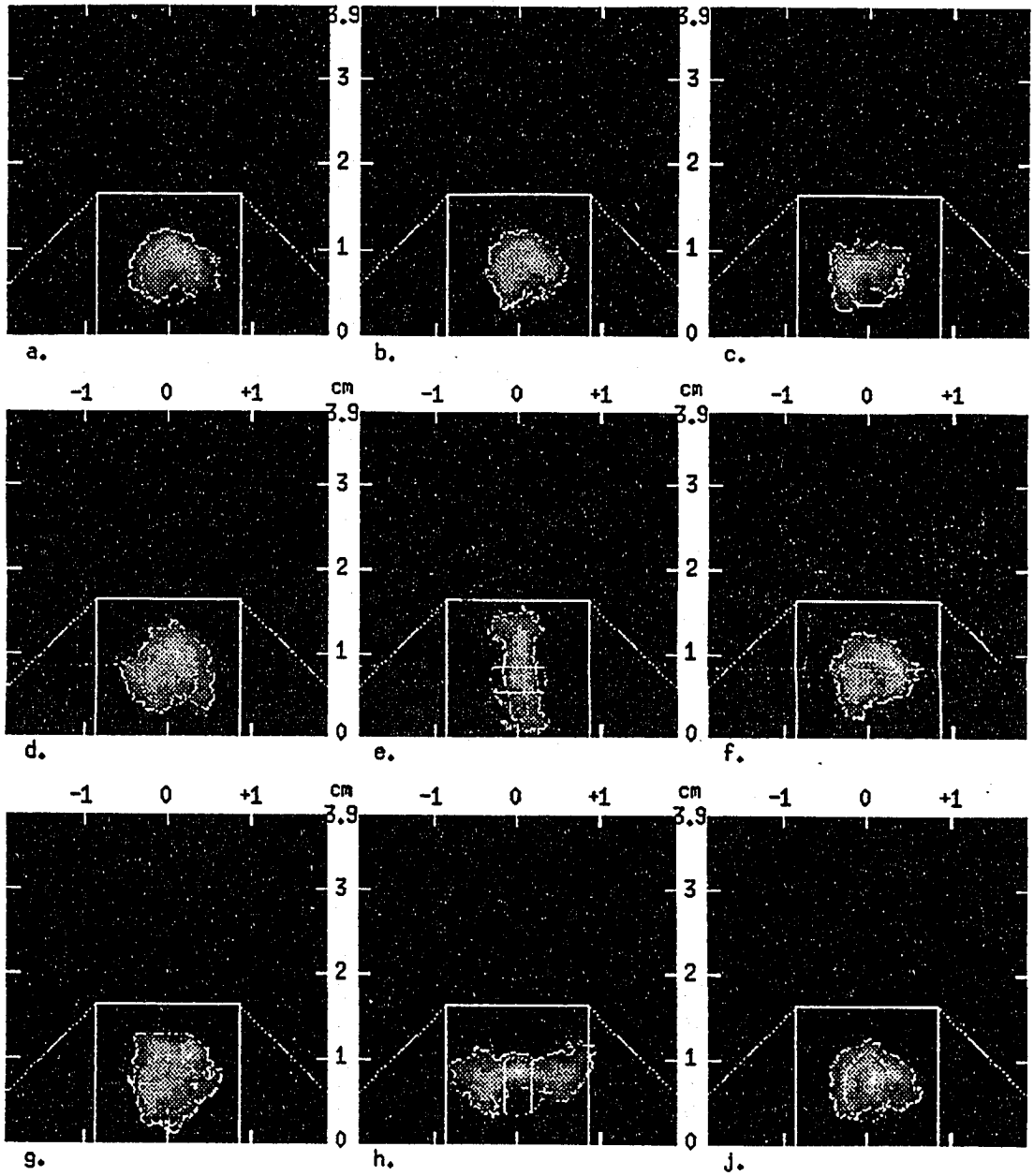


Fig. 5.31 Composite transverse images of ethanol-seeded helium injection at x/h=0.75

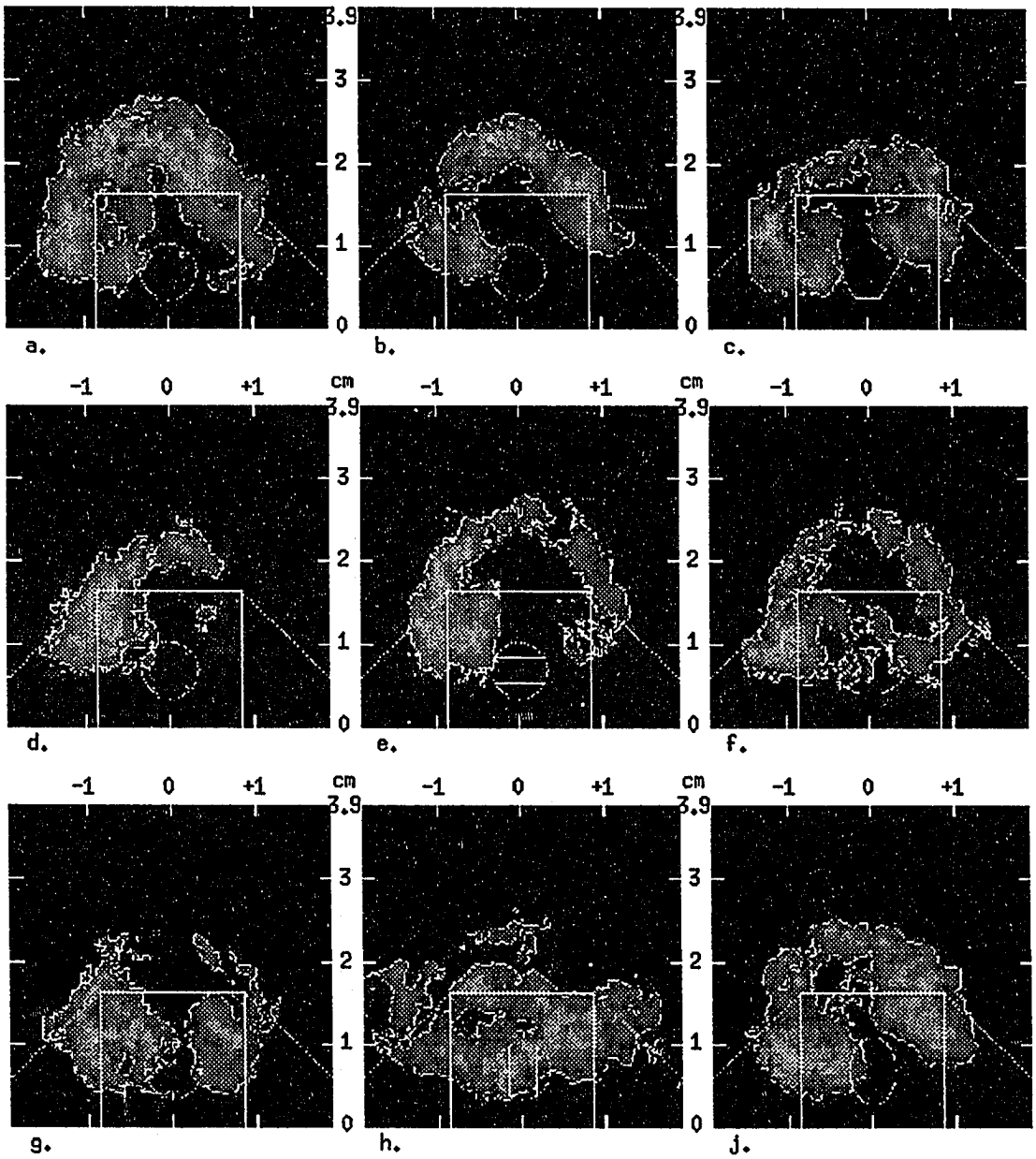


Fig. 5.32 Composite transverse images of ethanol-seeded helium injection at x/h=3.9

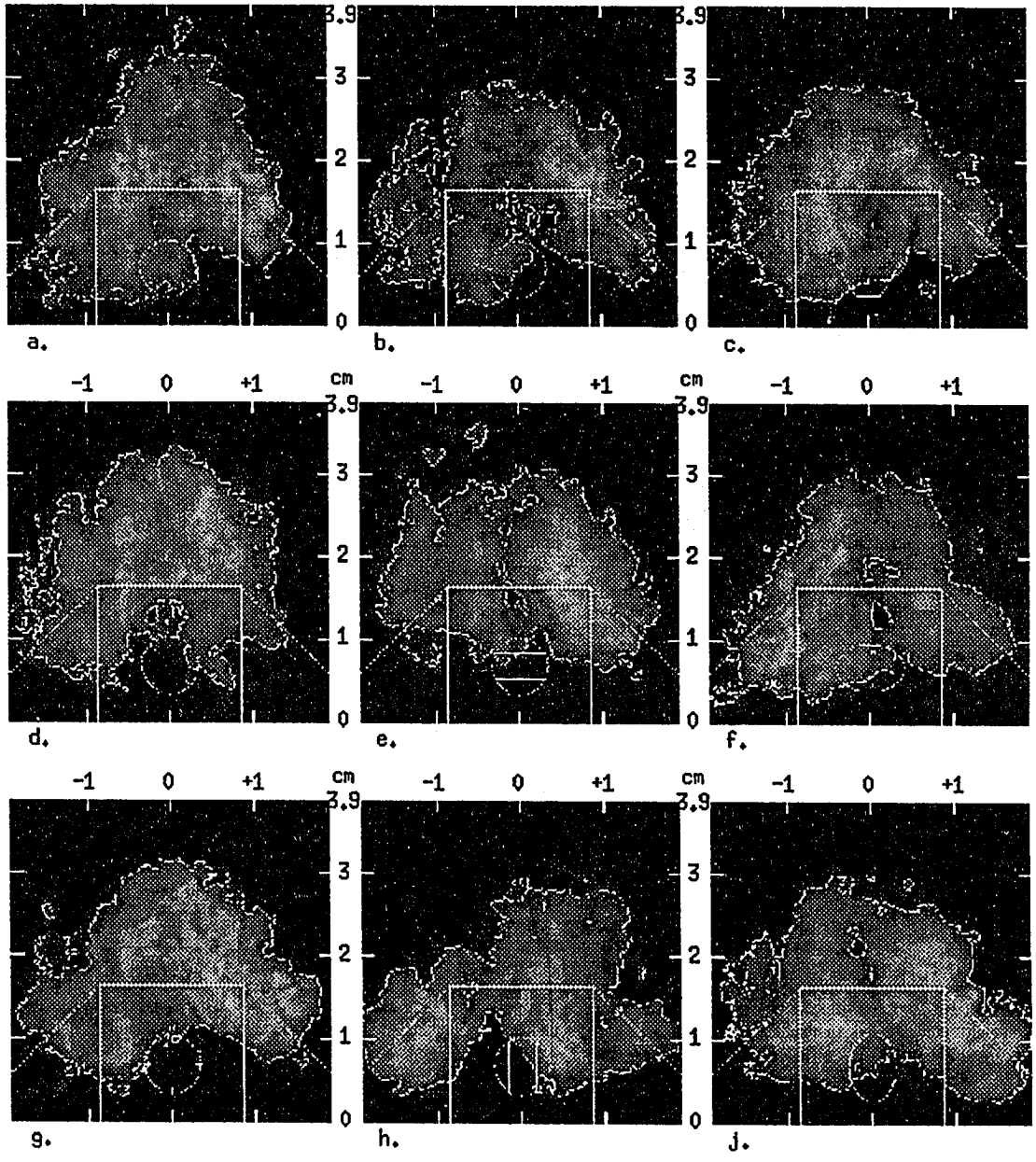


Fig. 5.33 Composite transverse images of ethanol-seeded helium injection at x/h=7.

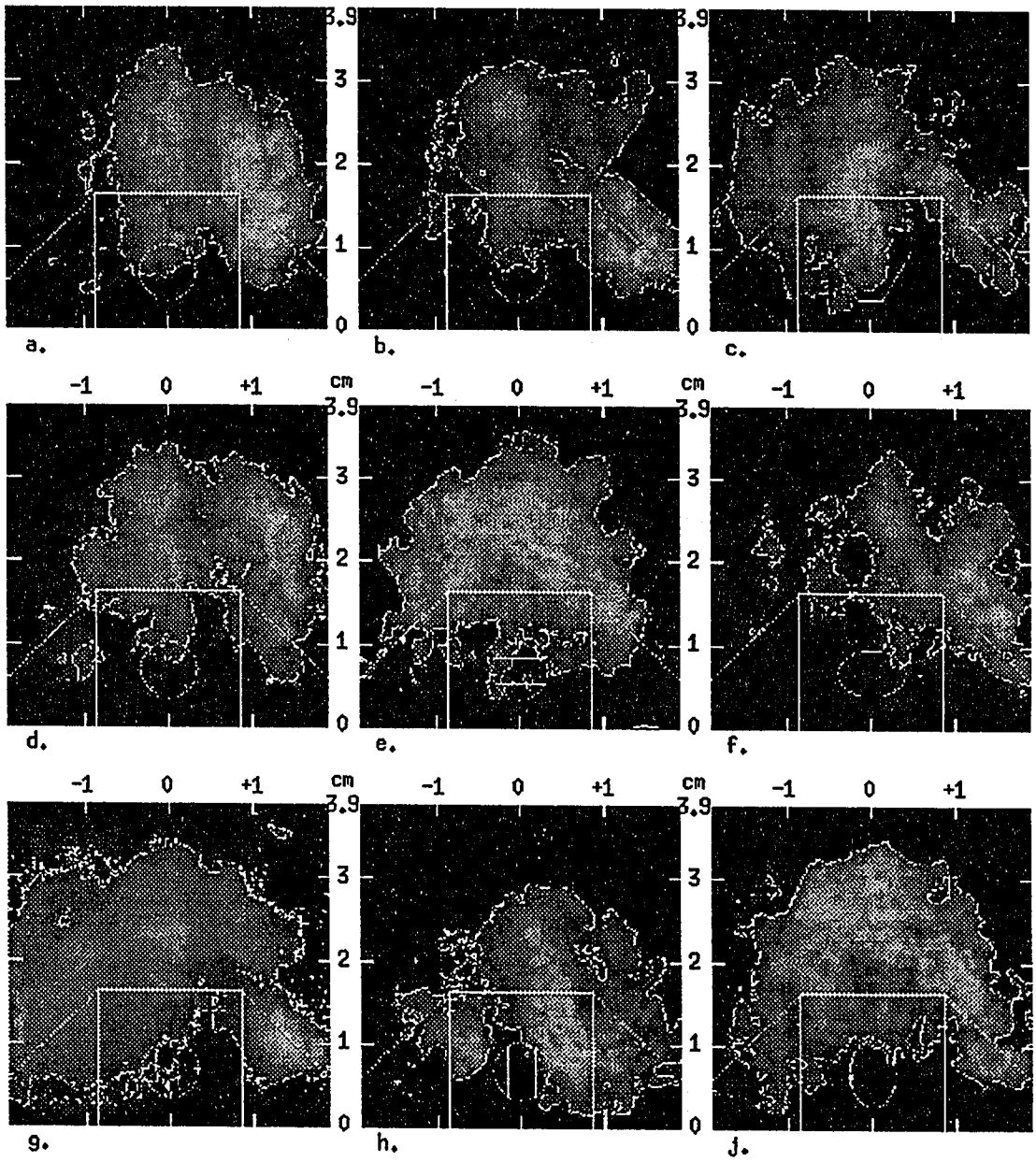


Fig. 5.34 Composite transverse images of ethanol-seeded helium injection at x/h=10.

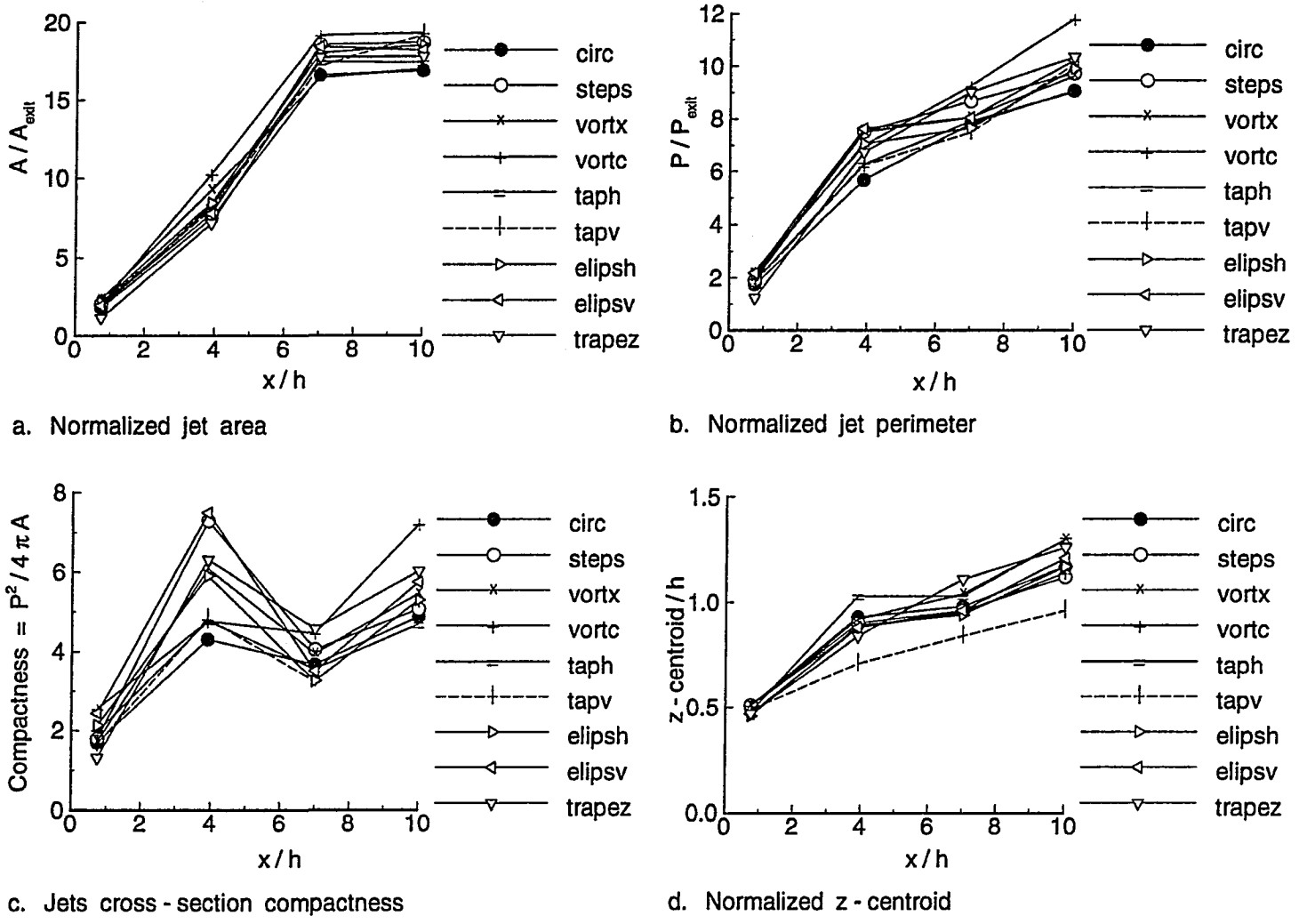


Fig. 5.35 Jets mixing characteristics from visualization tests

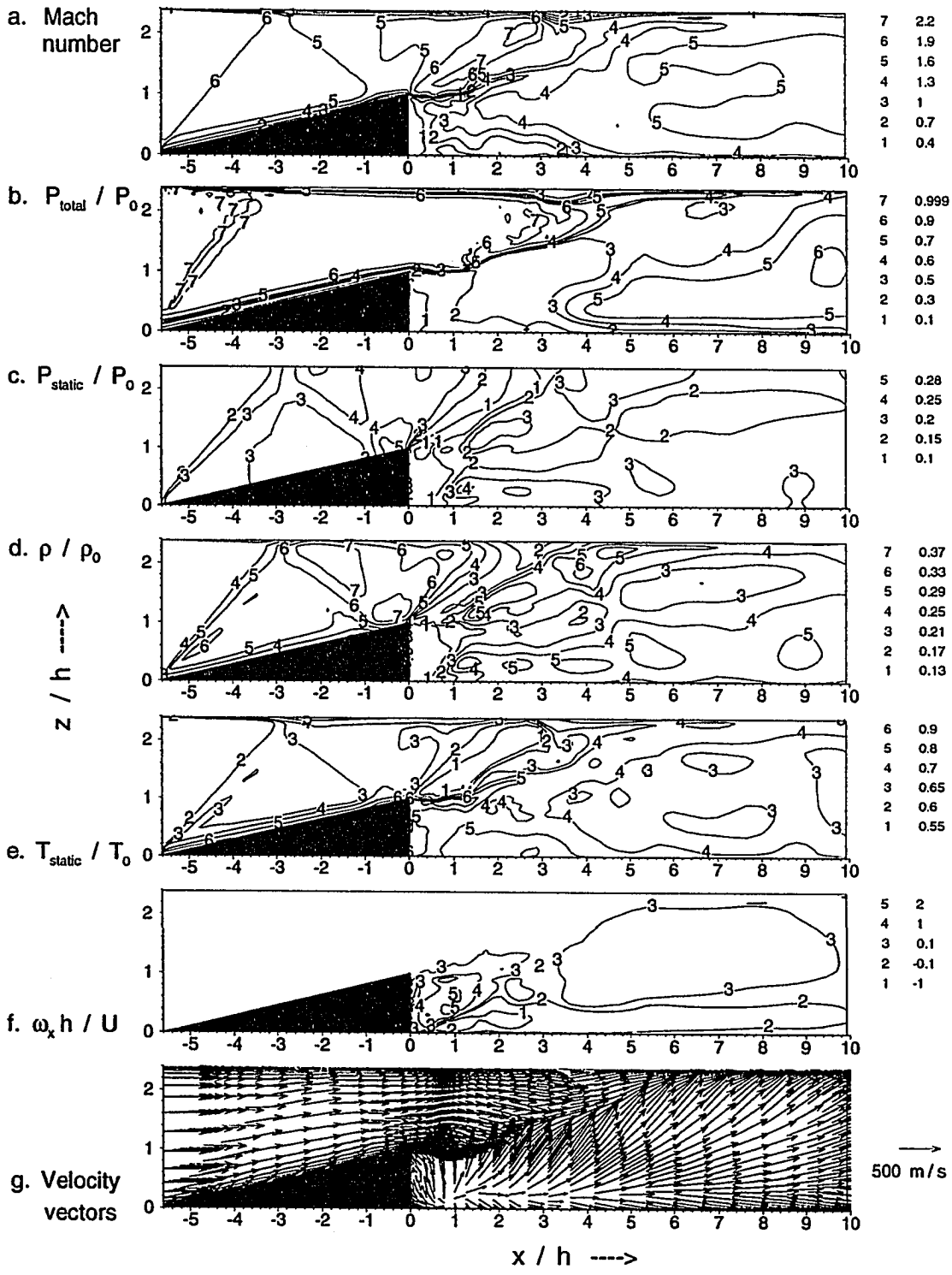


Fig. 5.36 Numerical simulation data of the main flow only in the symmetry plane

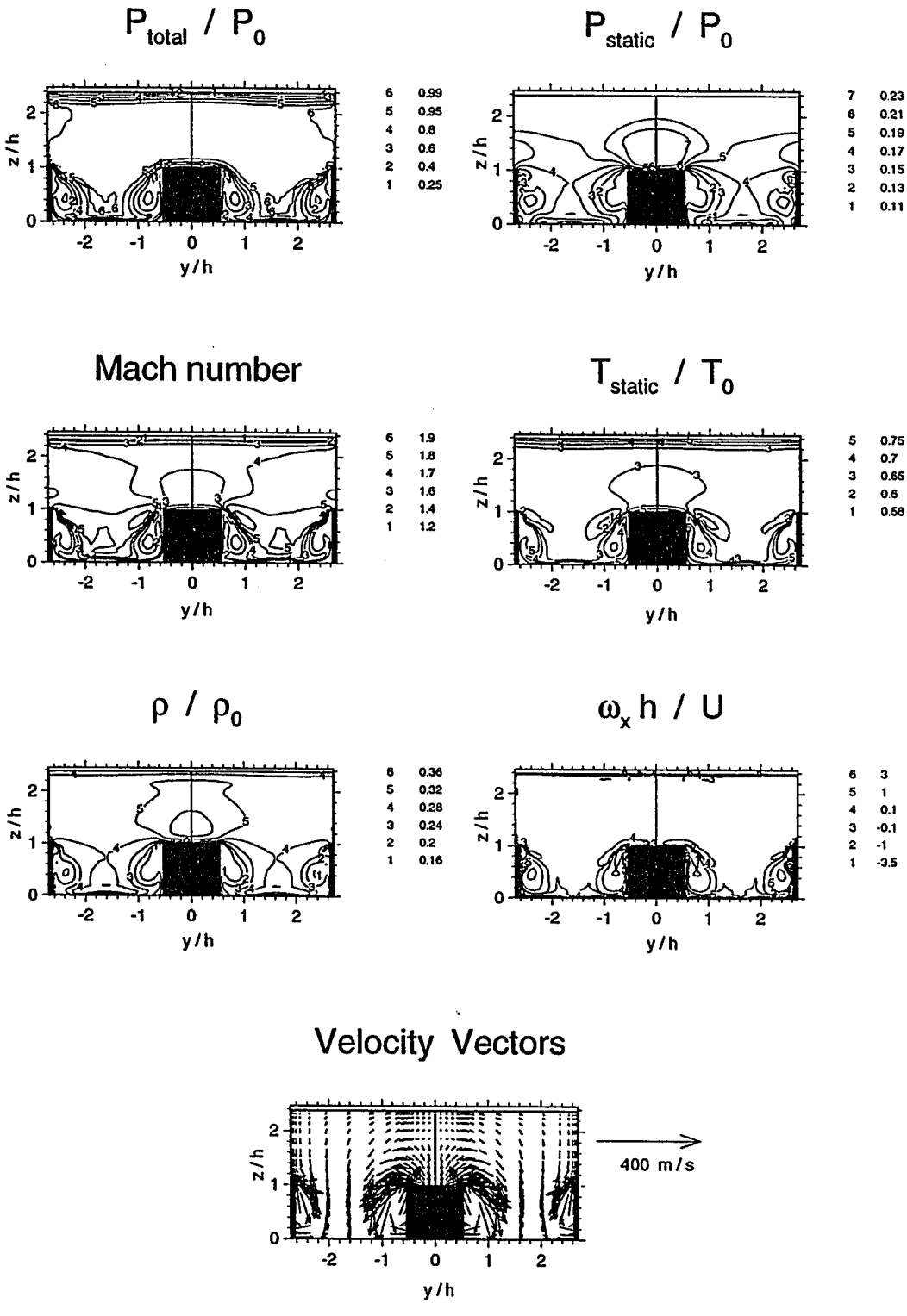


Fig. 5.37 Numerical simulation data of the main flow only at x / h = 0.

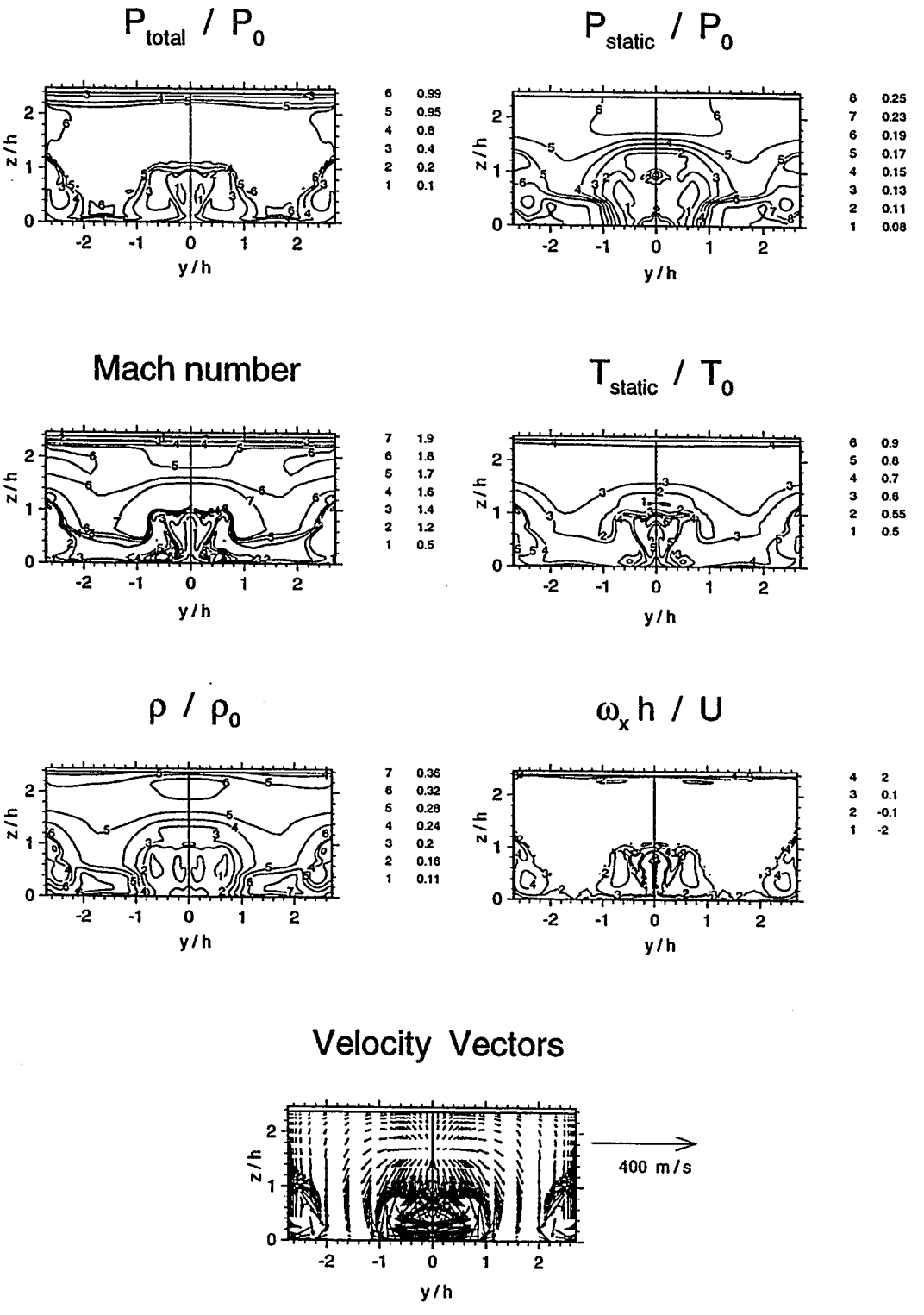


Fig. 5.38 Numerical simulation data of the main flow only at x / h = 0.75

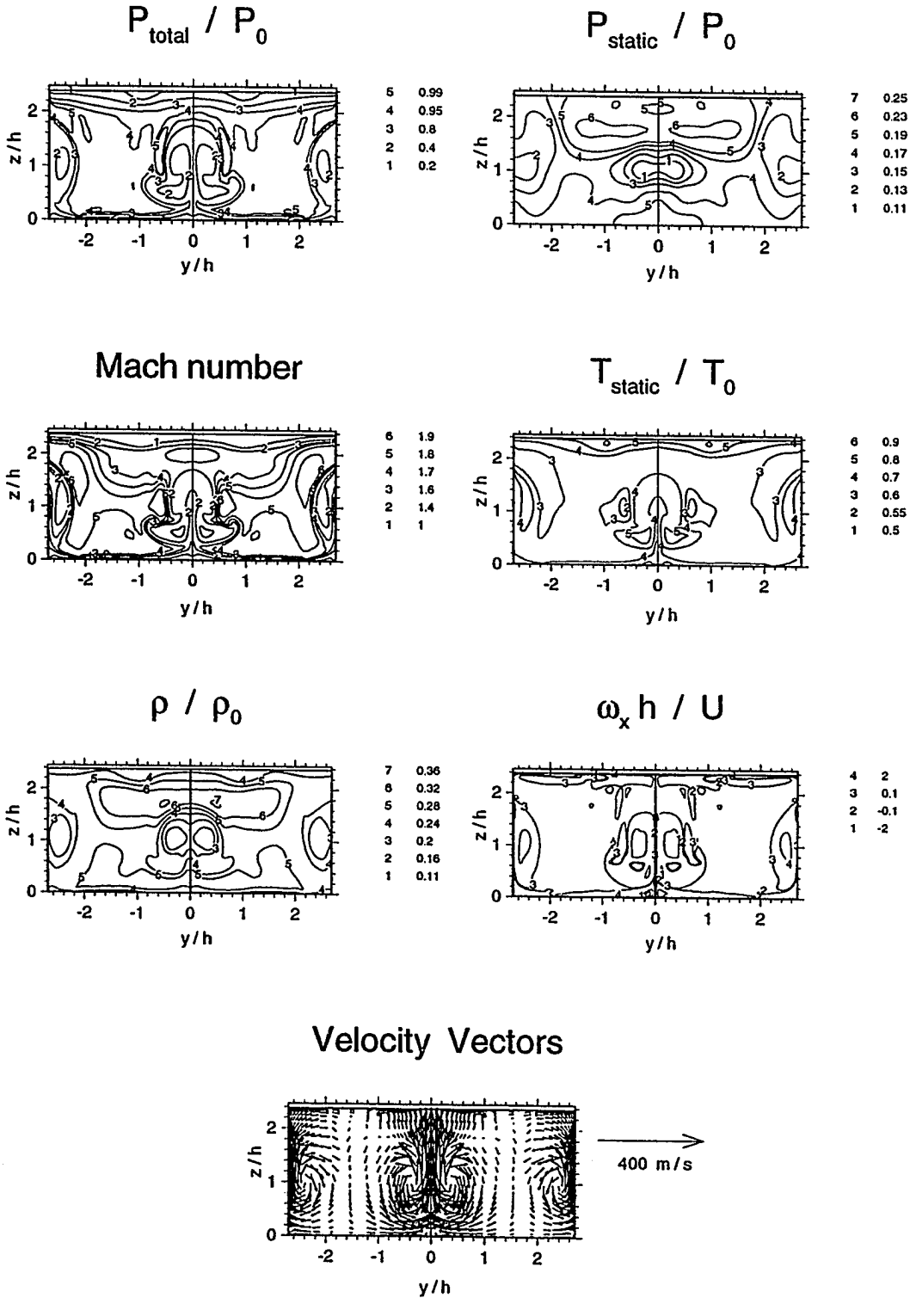


Fig. 5.39 Numerical simulation data of the main flow only at x/h = 3.9

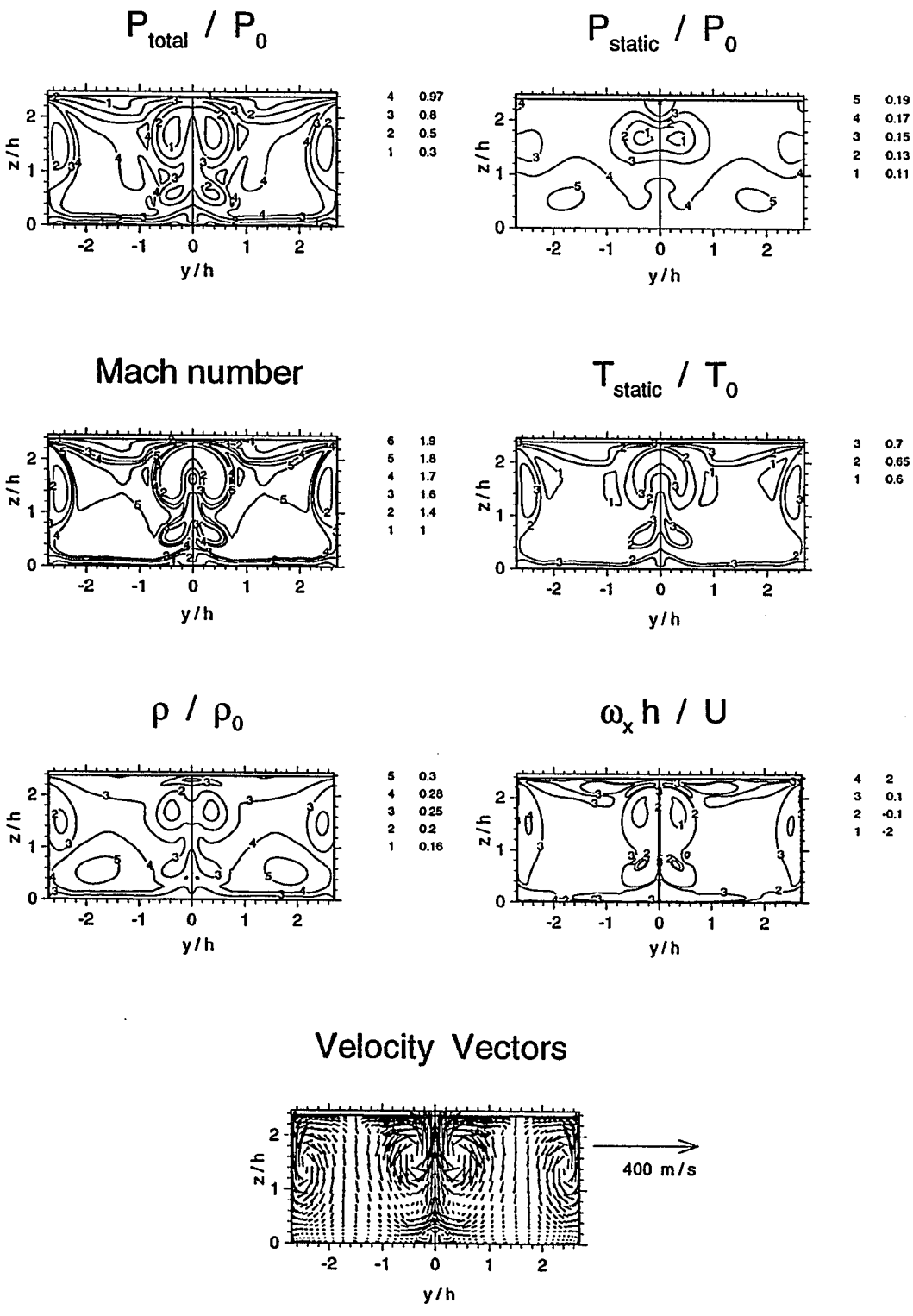


Fig. 5.40 Numerical simulation data of the main flow only at x / h = 7.

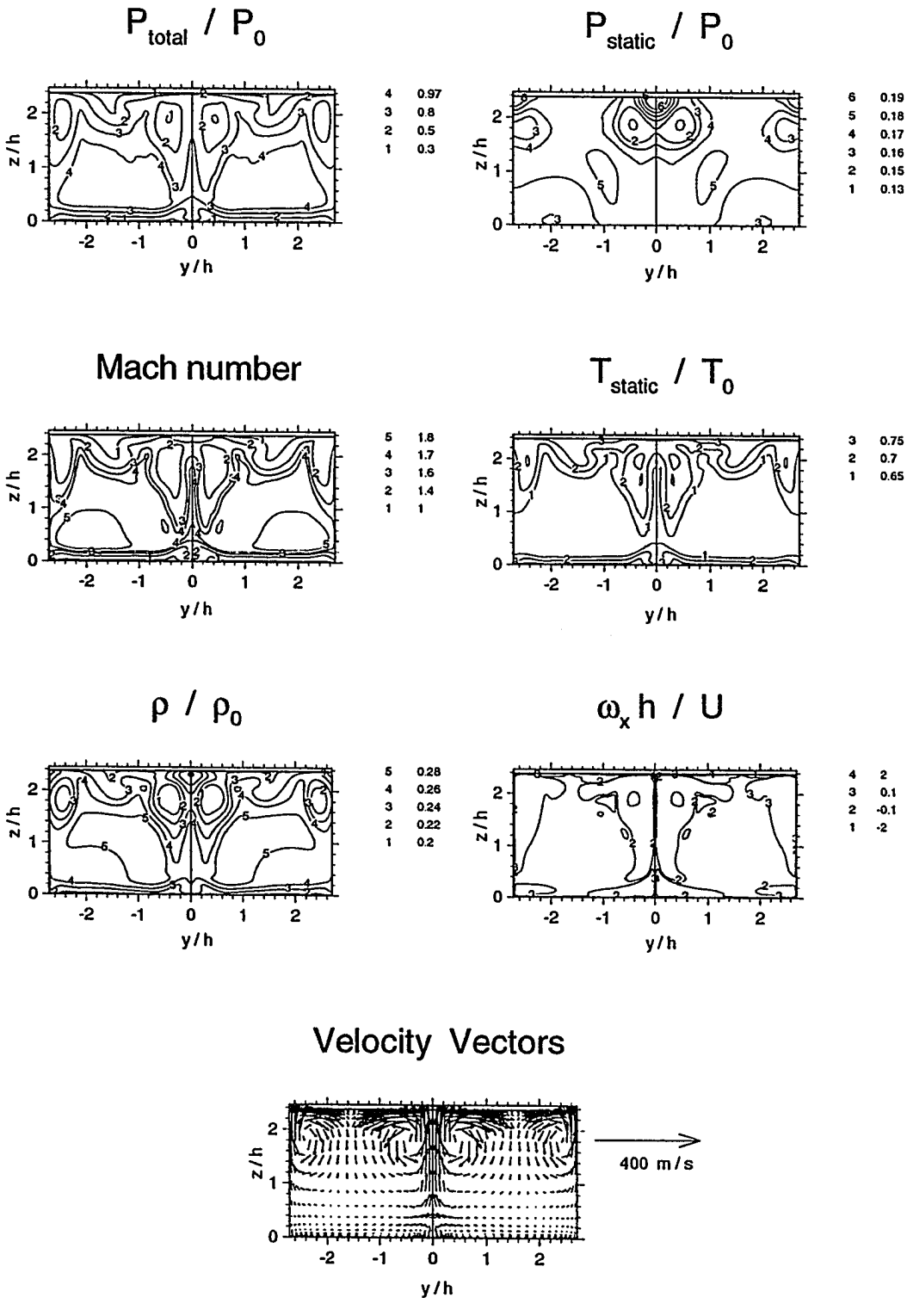


Fig. 5.41 Numerical simulation data of the main flow only at x / h = 10.

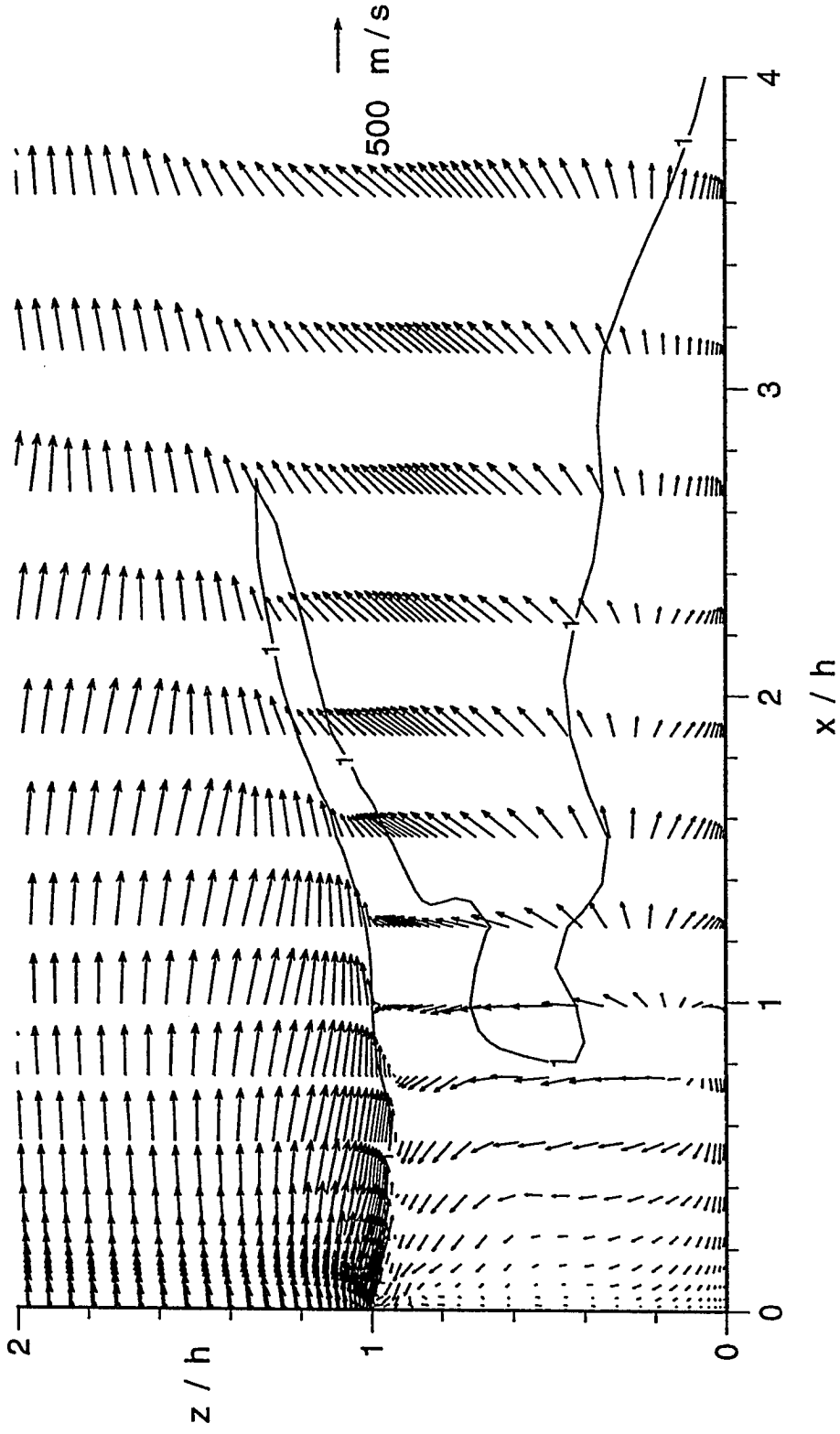


Fig. 5.42 Closeup of the velocity field and M = 1 contour near the ramp base
Main flow only, no injection

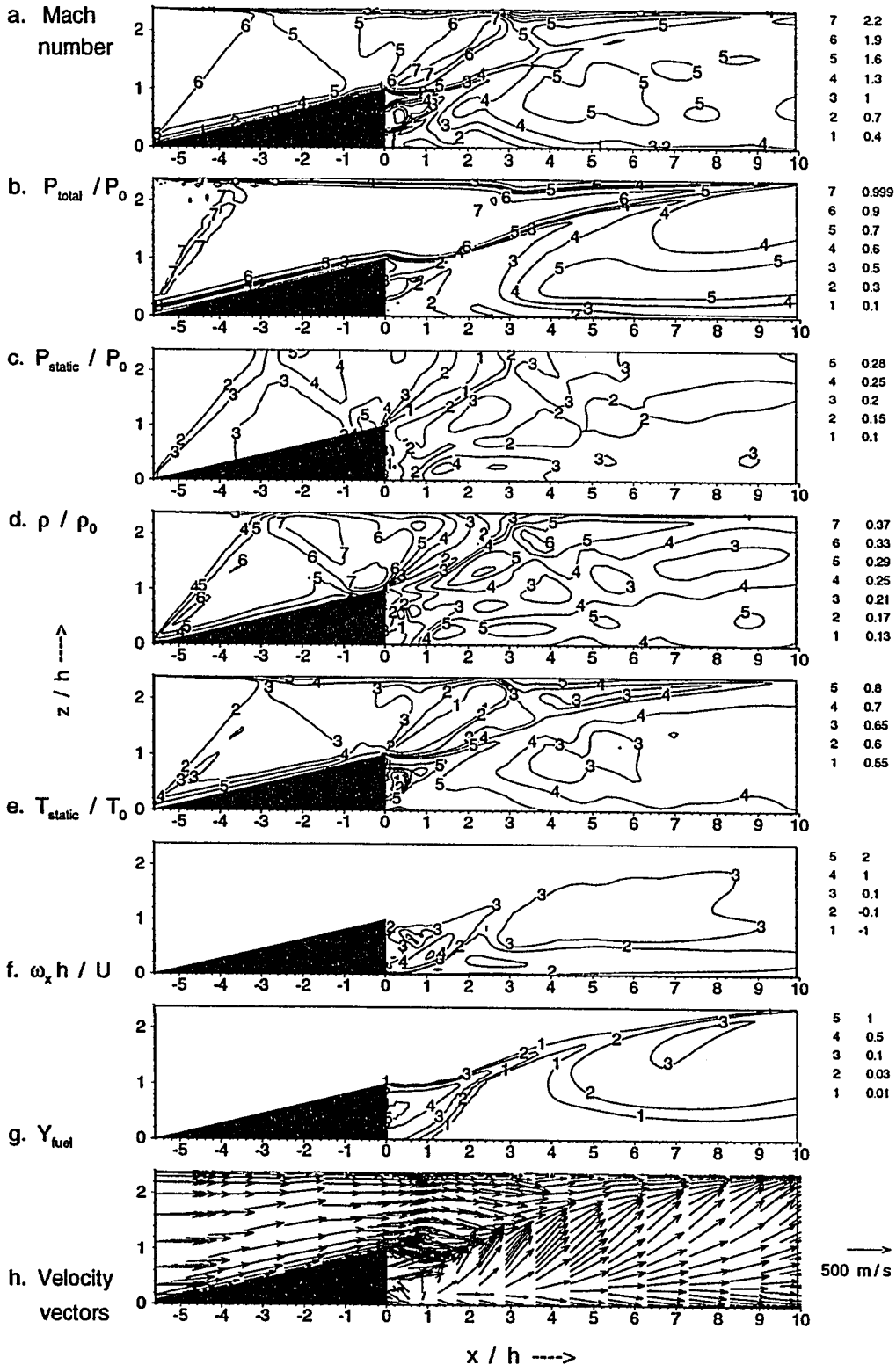


Fig. 5.43 Numerical simulation data of the main flow and air injection in the symmetry plane

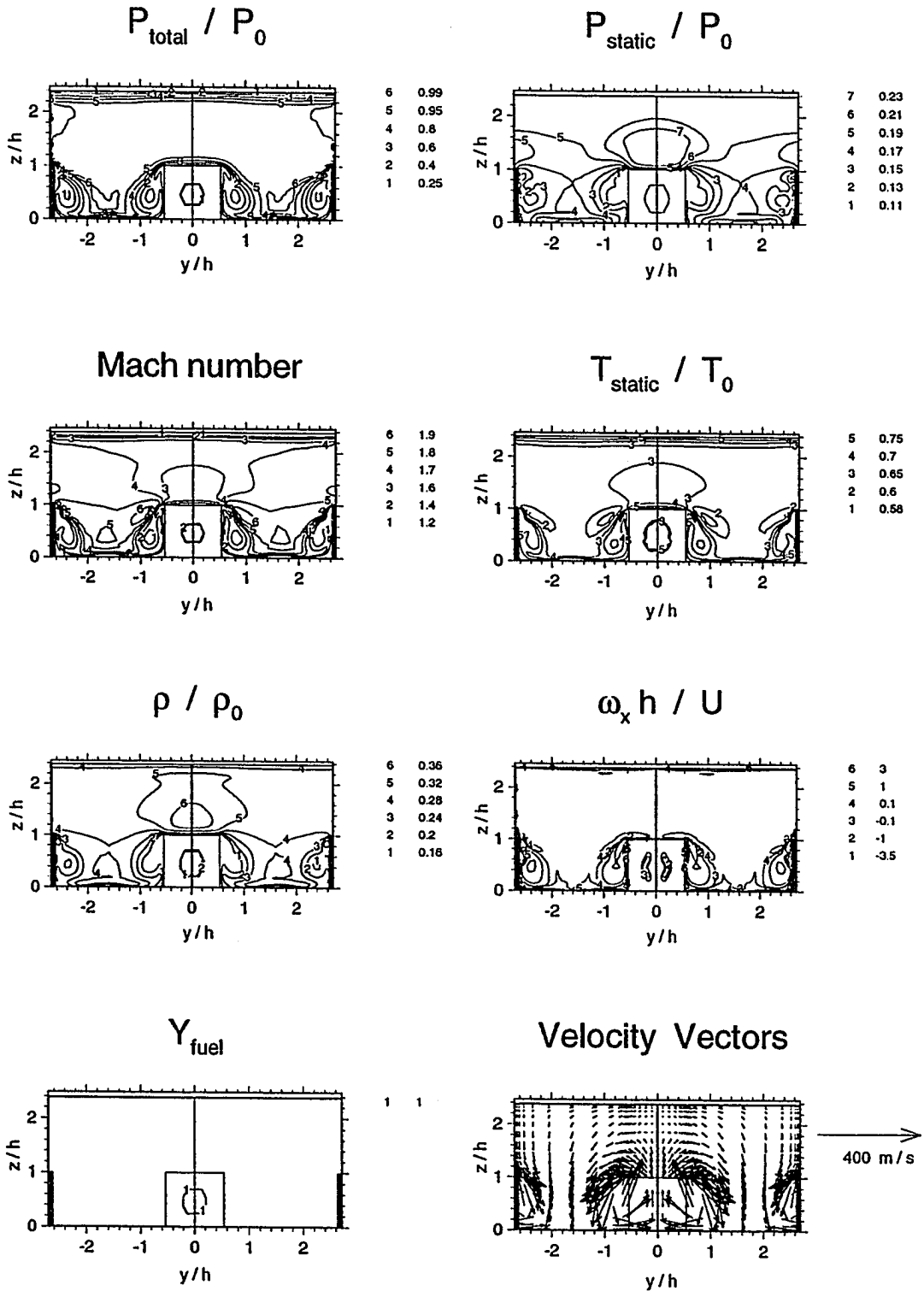


Fig. 5.44 Numerical simulation data of the main flow and air injection at x/h=0.

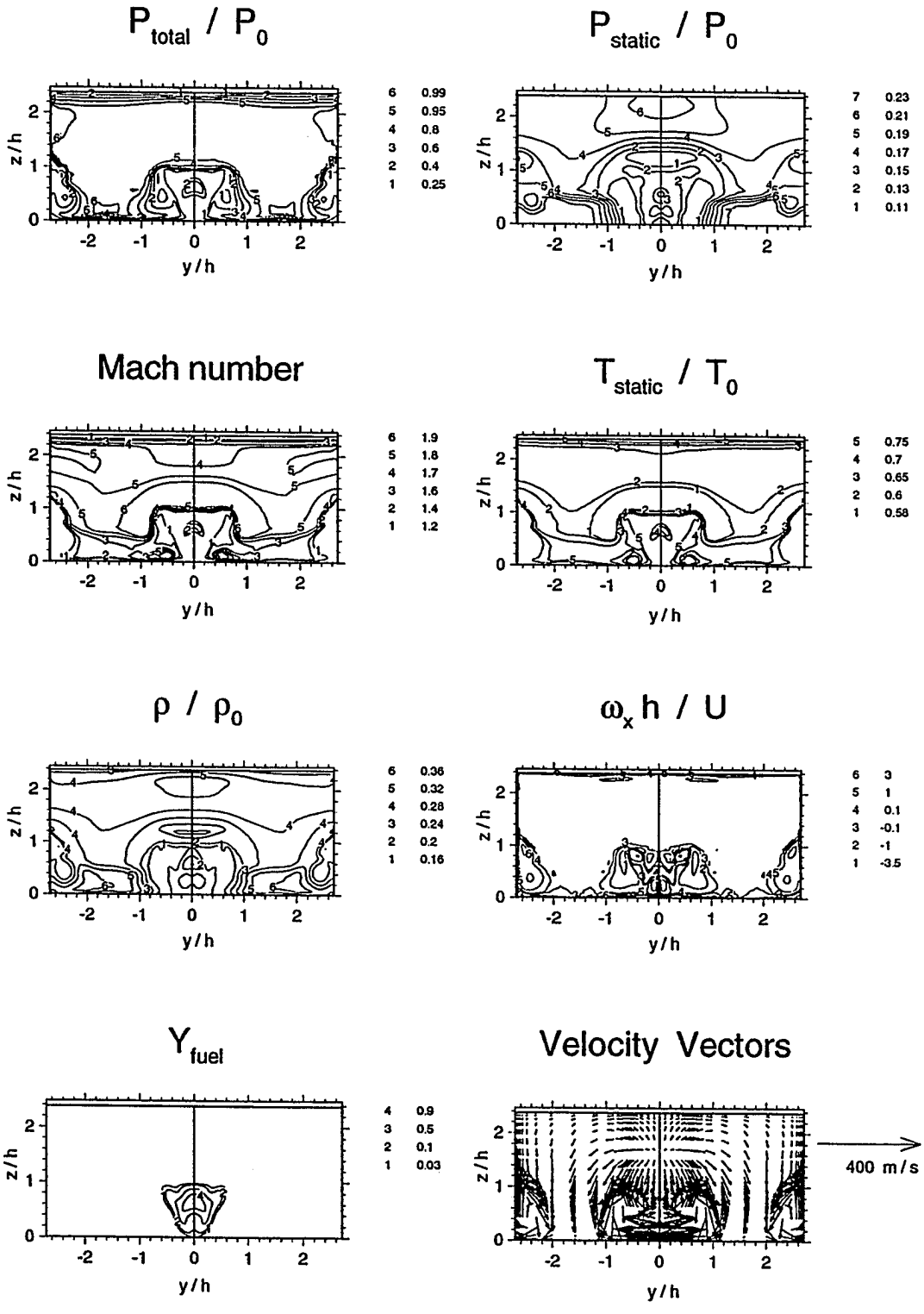


Fig. 5.45 Numerical simulation data of the main flow and air injection at x/h = 0.75

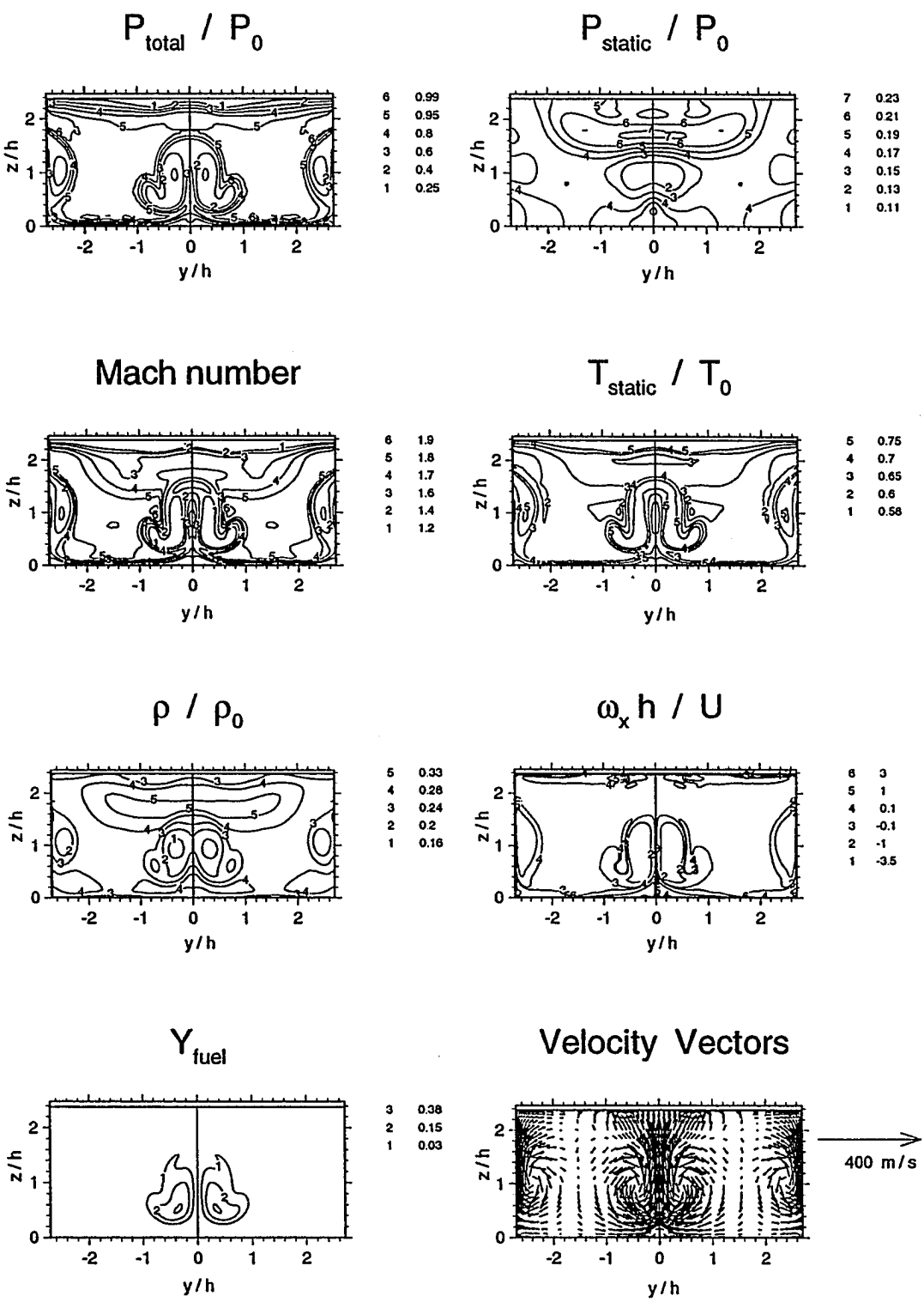


Fig. 5.46 Numerical simulation data of the main flow and air injection at x/h = 3.9

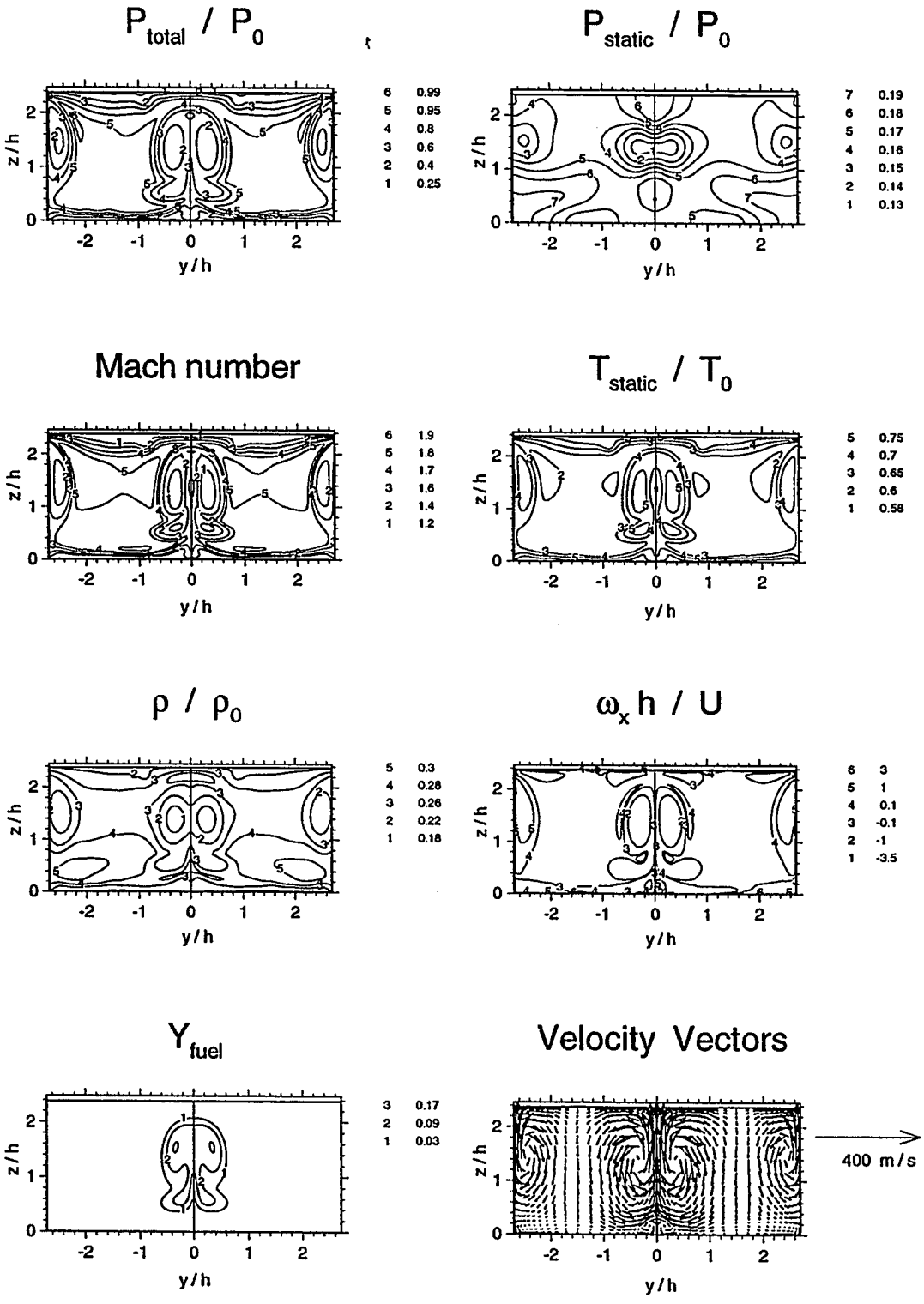


Fig. 5.47 Numerical simulation data of the main flow and air injection at x / h = 7.

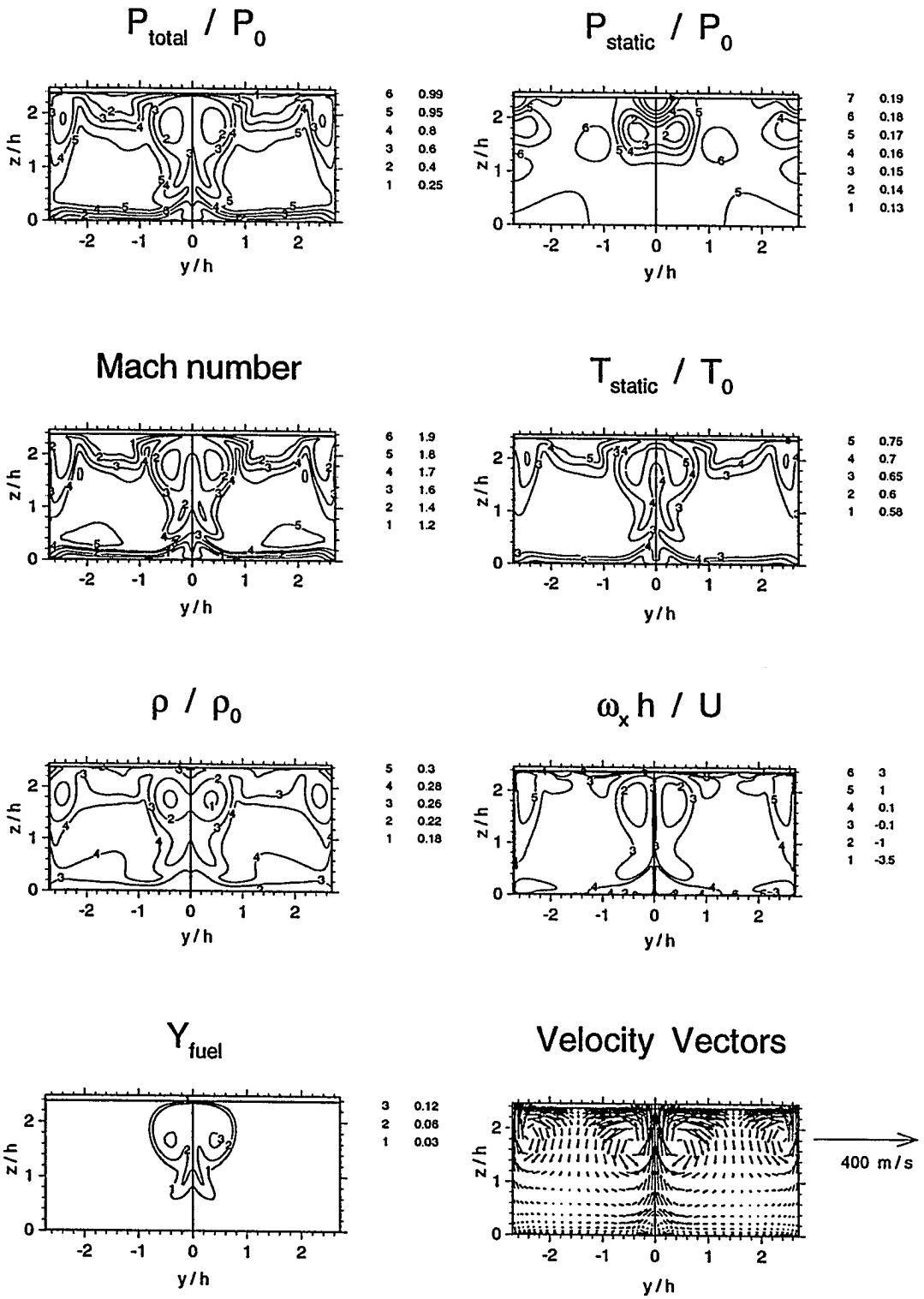


Fig. 5.48 Numerical simulation data of the main flow and air injection at x/h = 10.

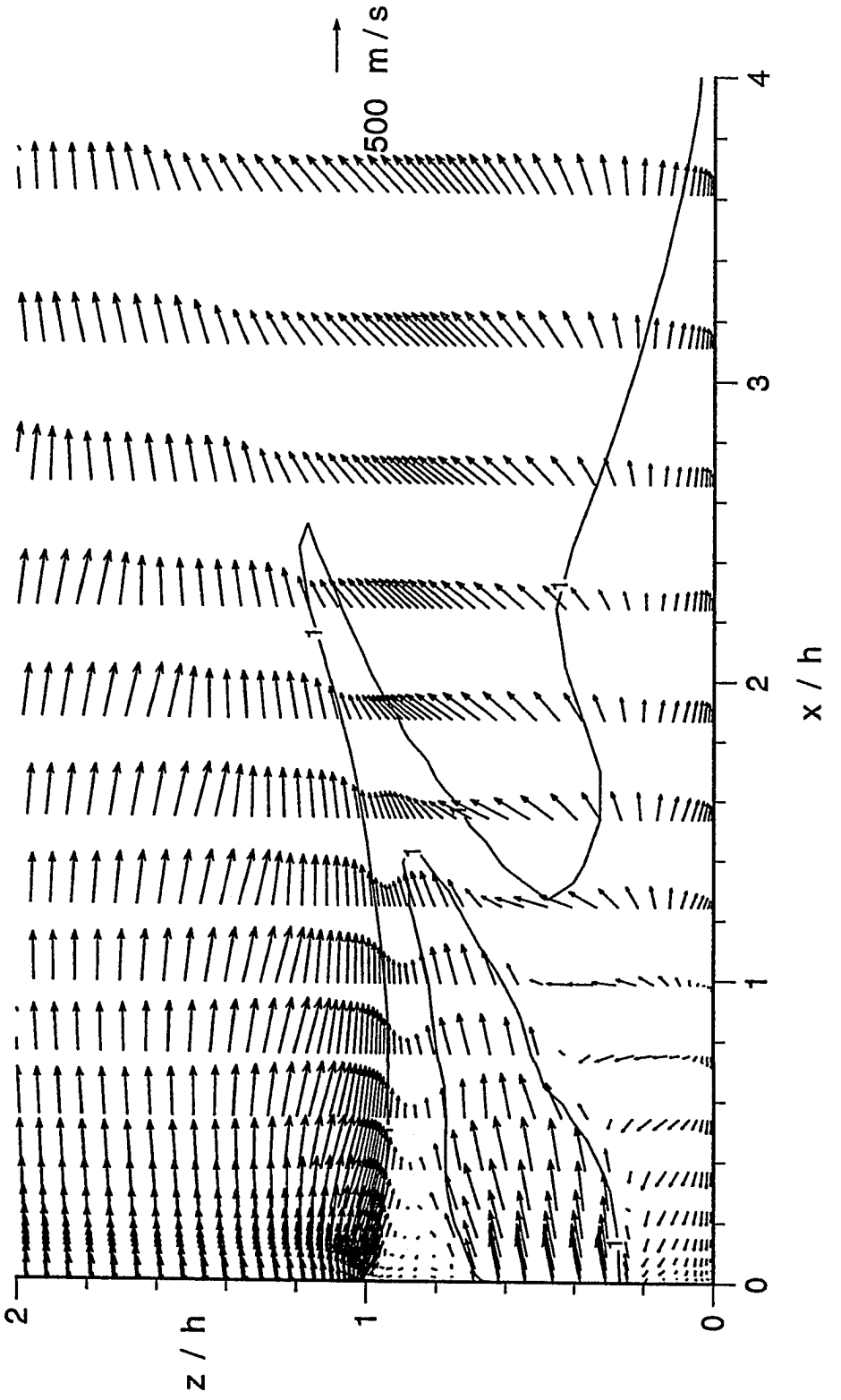


Fig. 5.49 Closeup of the velocity field and M = 1 contour near the ramp base
Main flow and air injection

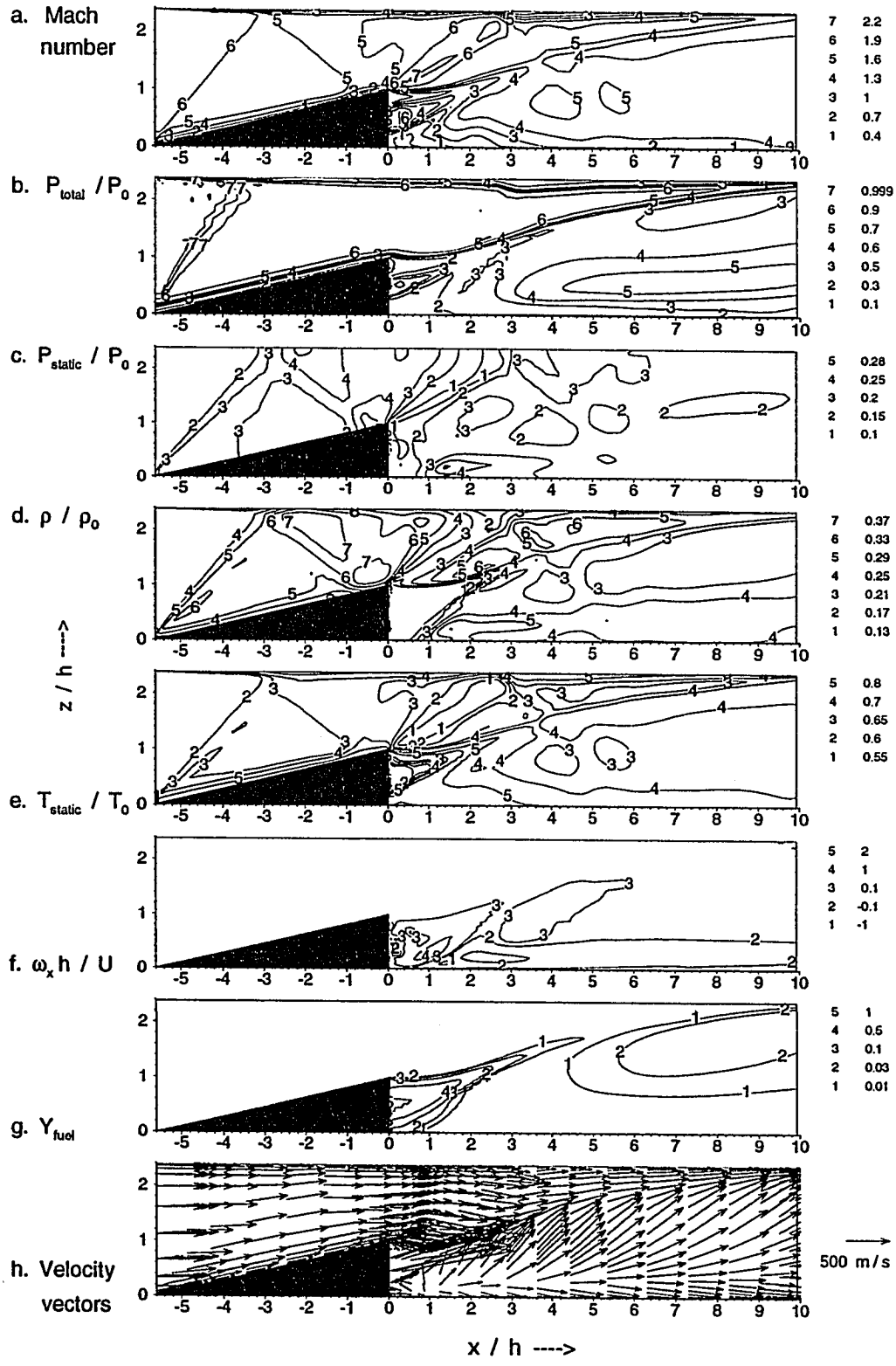


Fig. 5.50 Numerical simulation data of the main flow and helium injection in the symmetry plane

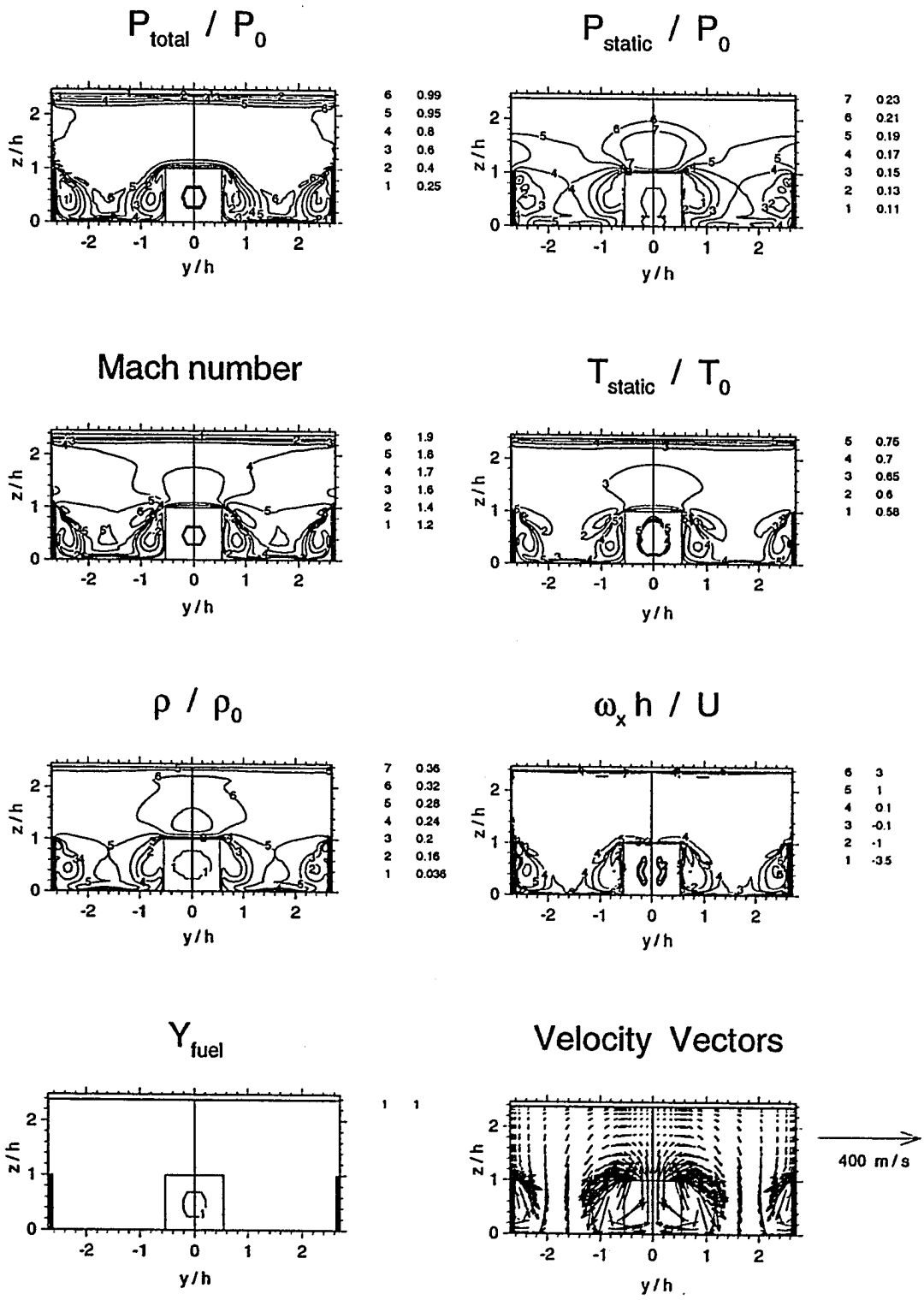


Fig. 5.51 Numerical simulation data of the main flow and helium injection at x/h = 0.

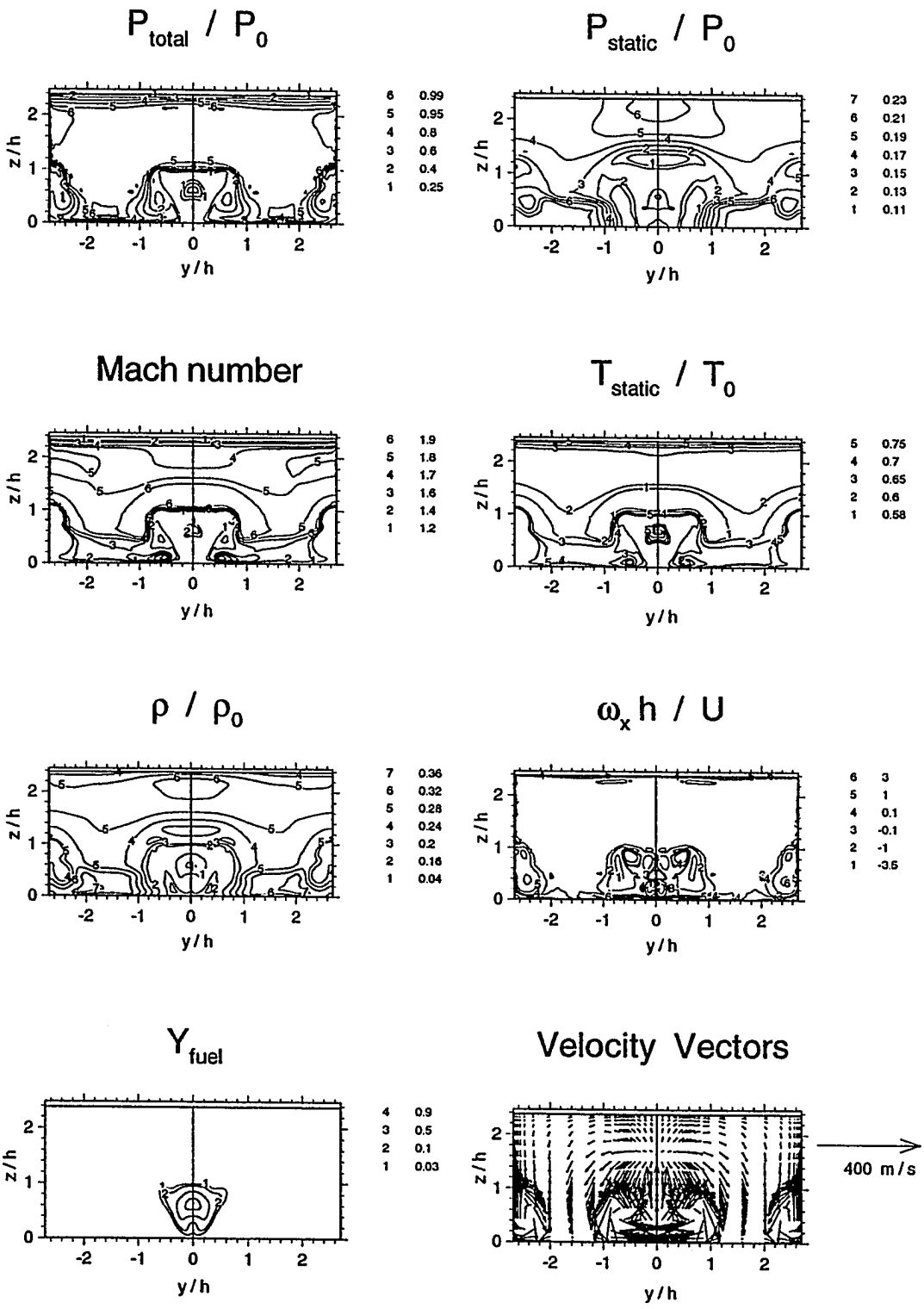


Fig. 5.52 Numerical simulation data of the main flow and helium injection at x/h = 0.75

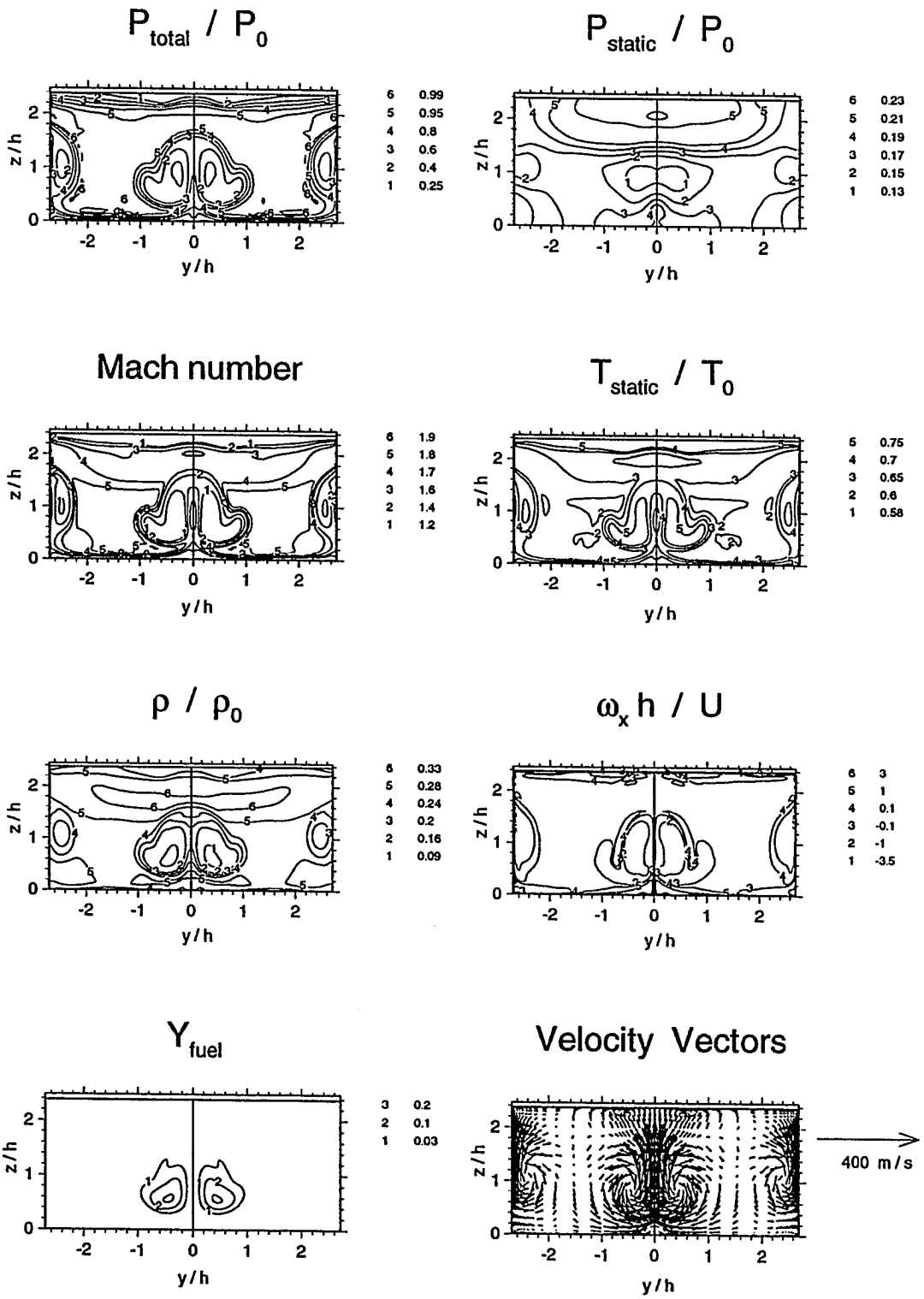


Fig. 5.53 Numerical simulation data of the main flow and helium injection at x/h=3.9

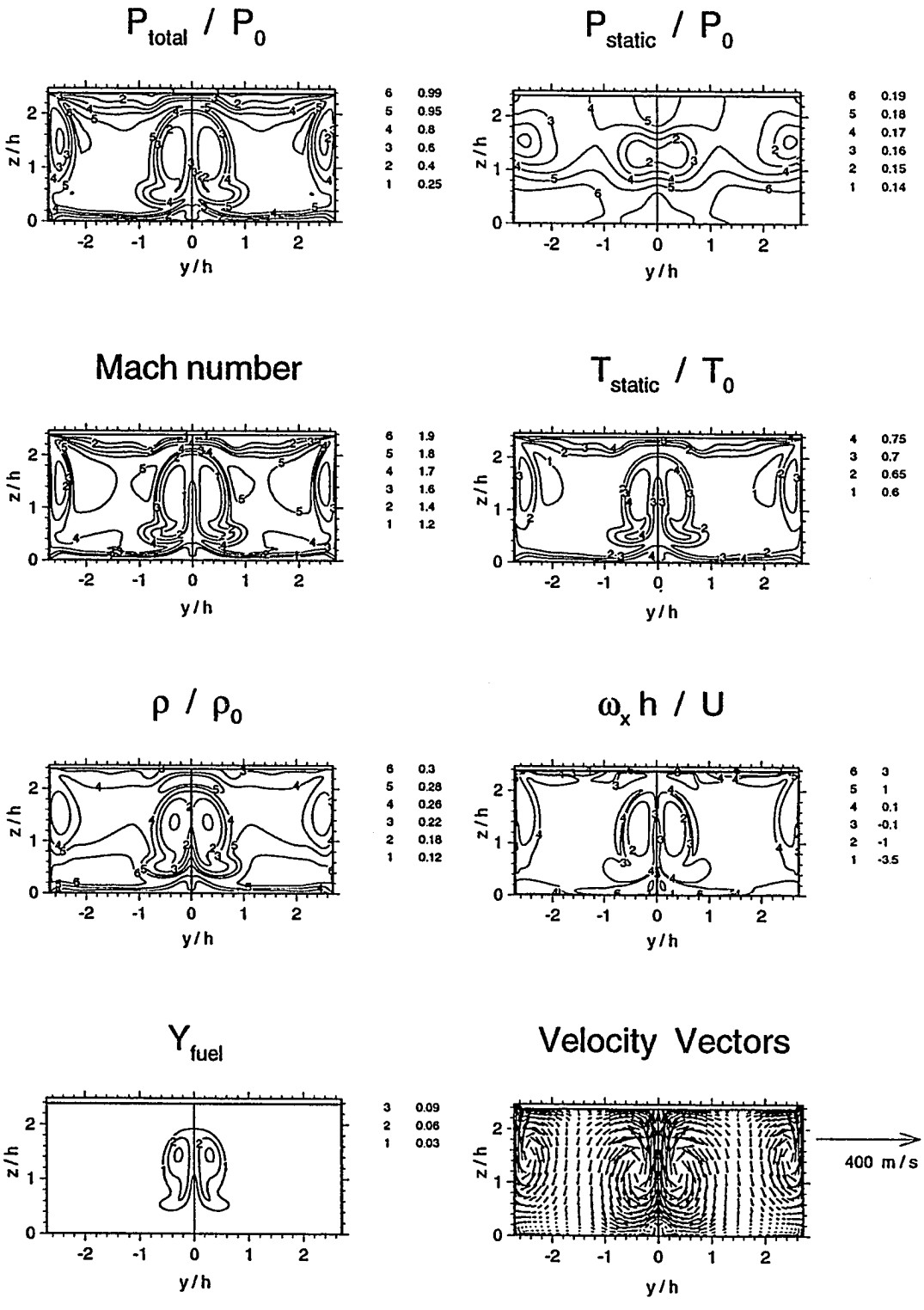


Fig. 5.54 Numerical simulation data of the main flow and helium injection at x/h = 7.

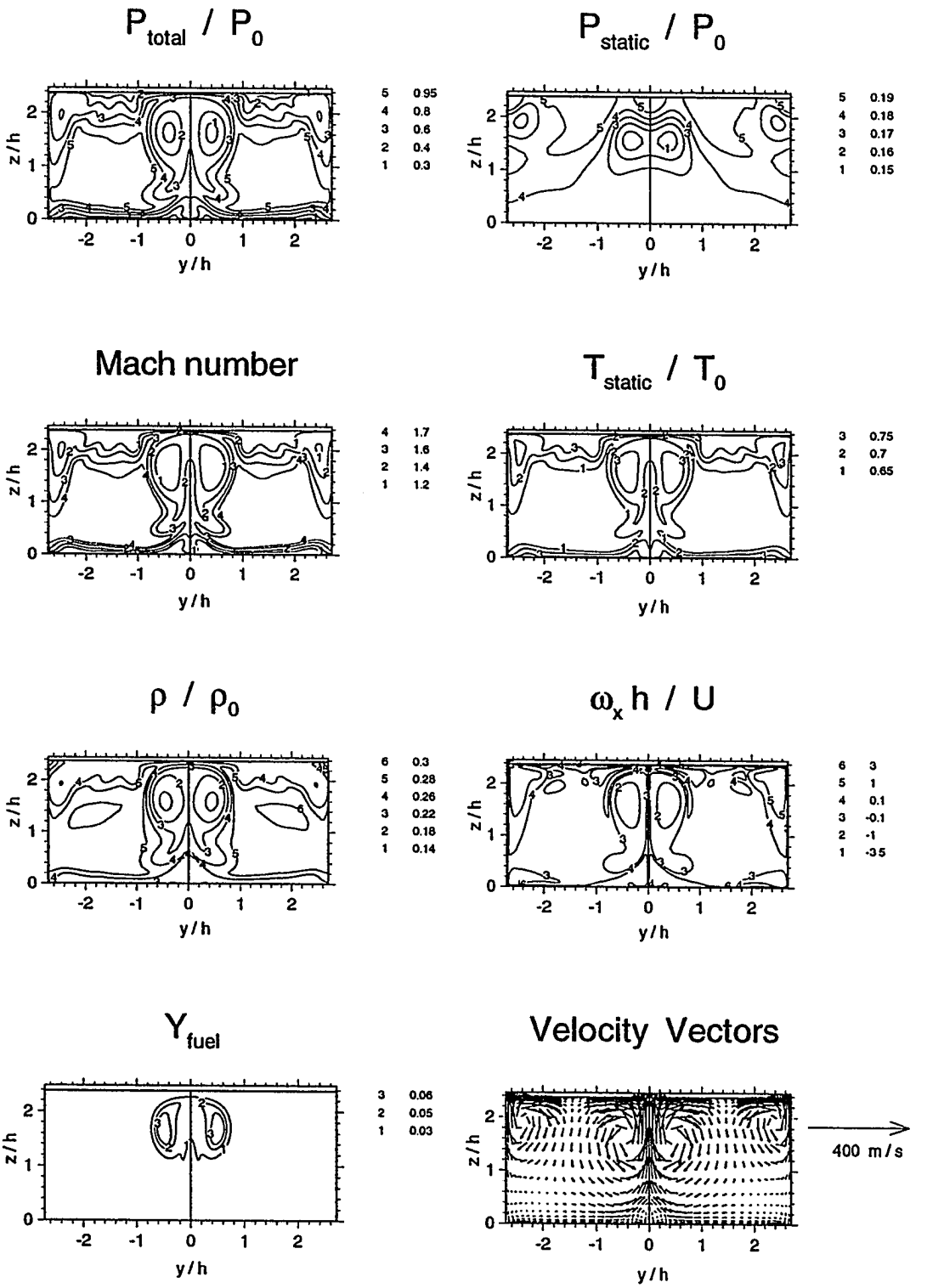


Fig. 5.55 Numerical simulation data of the main flow and helium injection at x/h = 10.

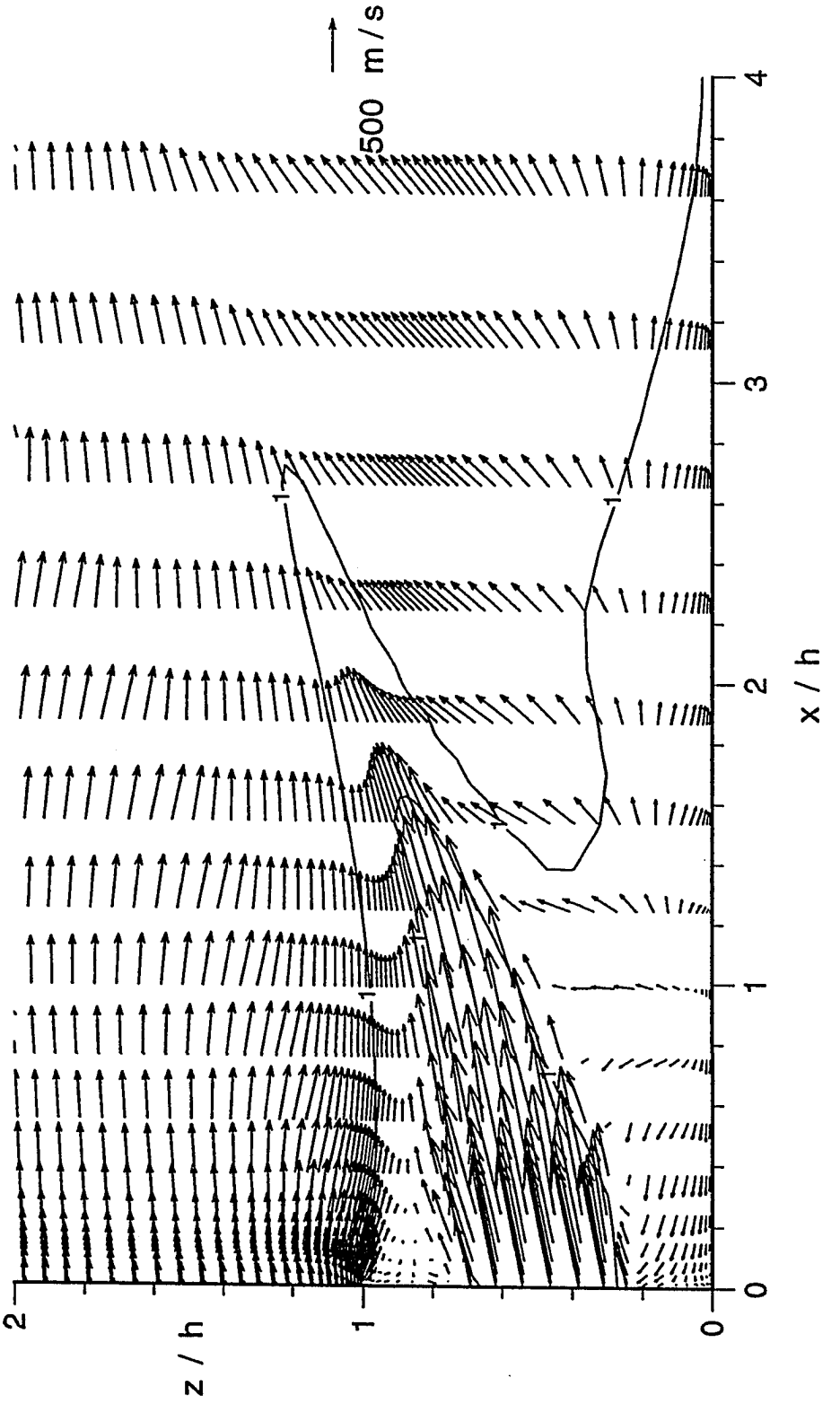


Fig. 5.56 Closeup of the velocity field and M = 1 contour near the ramp base
Main flow and helium injection

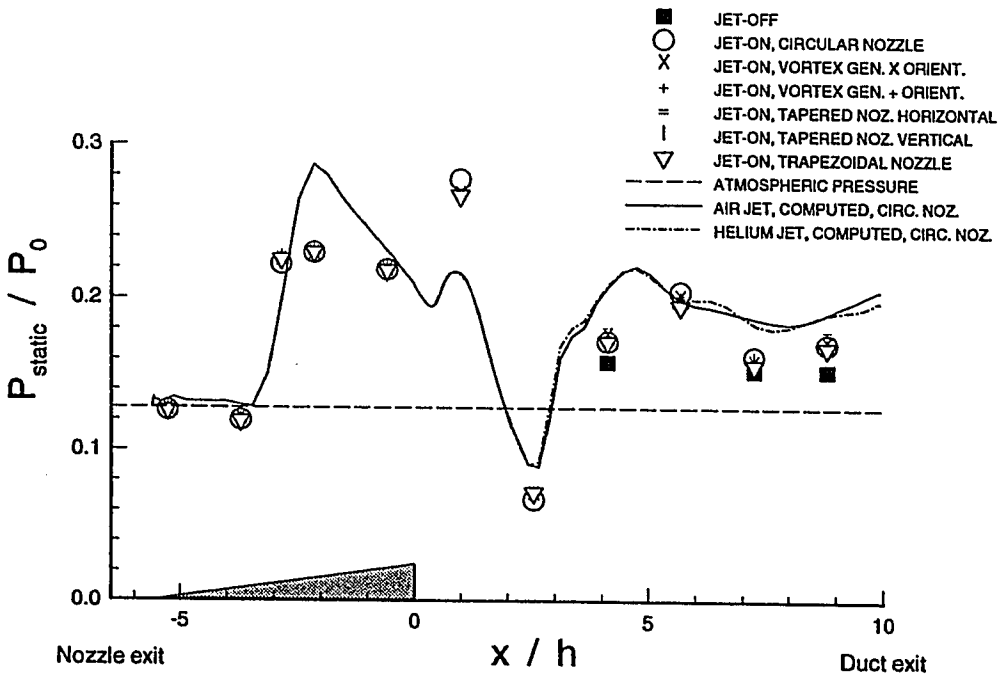


a. Top wall centerline

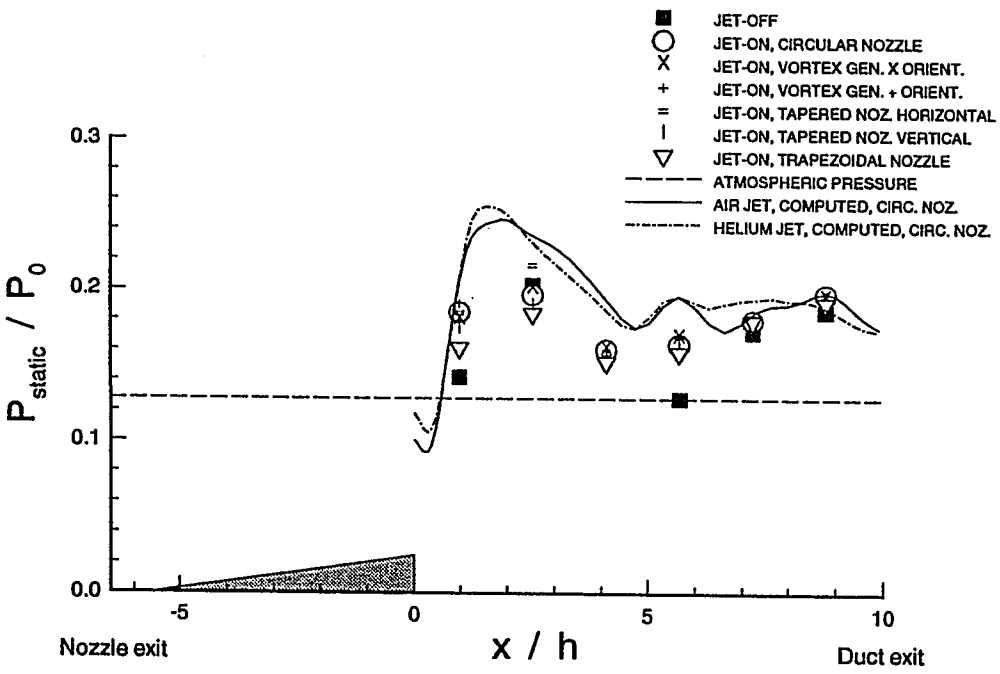


b. Bottom wall centerline

Fig. 5.57 Static pressure distribution on the top and bottom walls
A comparison between experimental and numerical simulations data

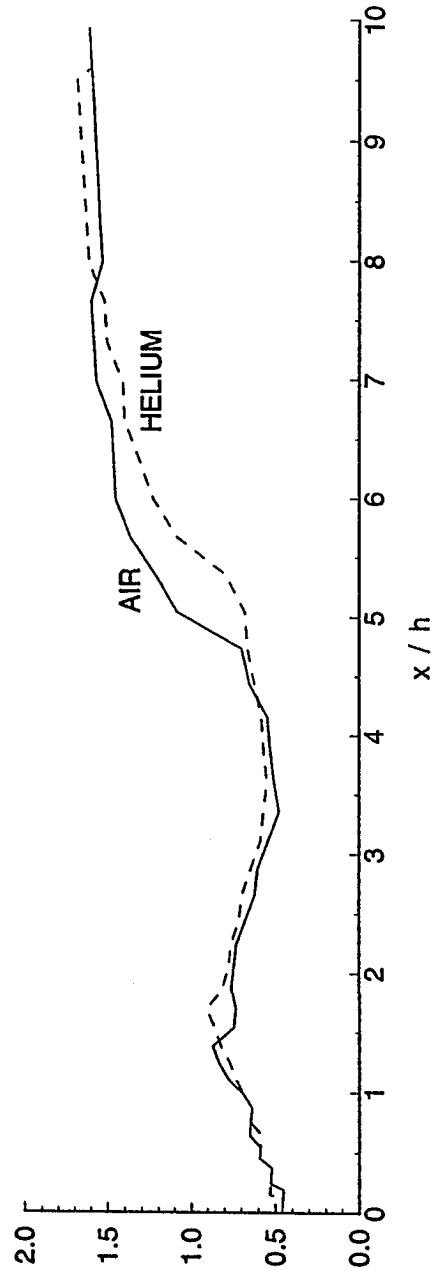


a. Maximum mass fraction location -- z - direction

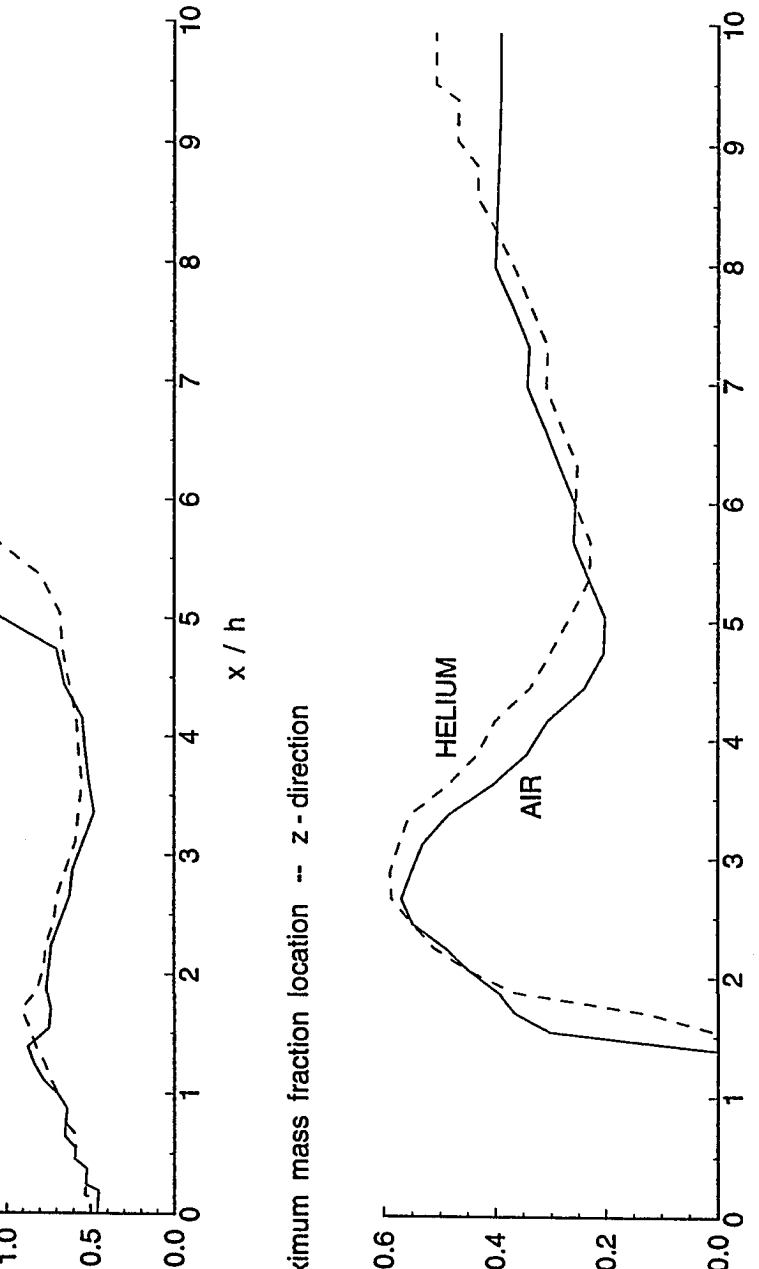


b. Maximum mass fraction location -- y - direction

Fig. 5.58 Injectant maximum mass - fraction location from numerical simulations

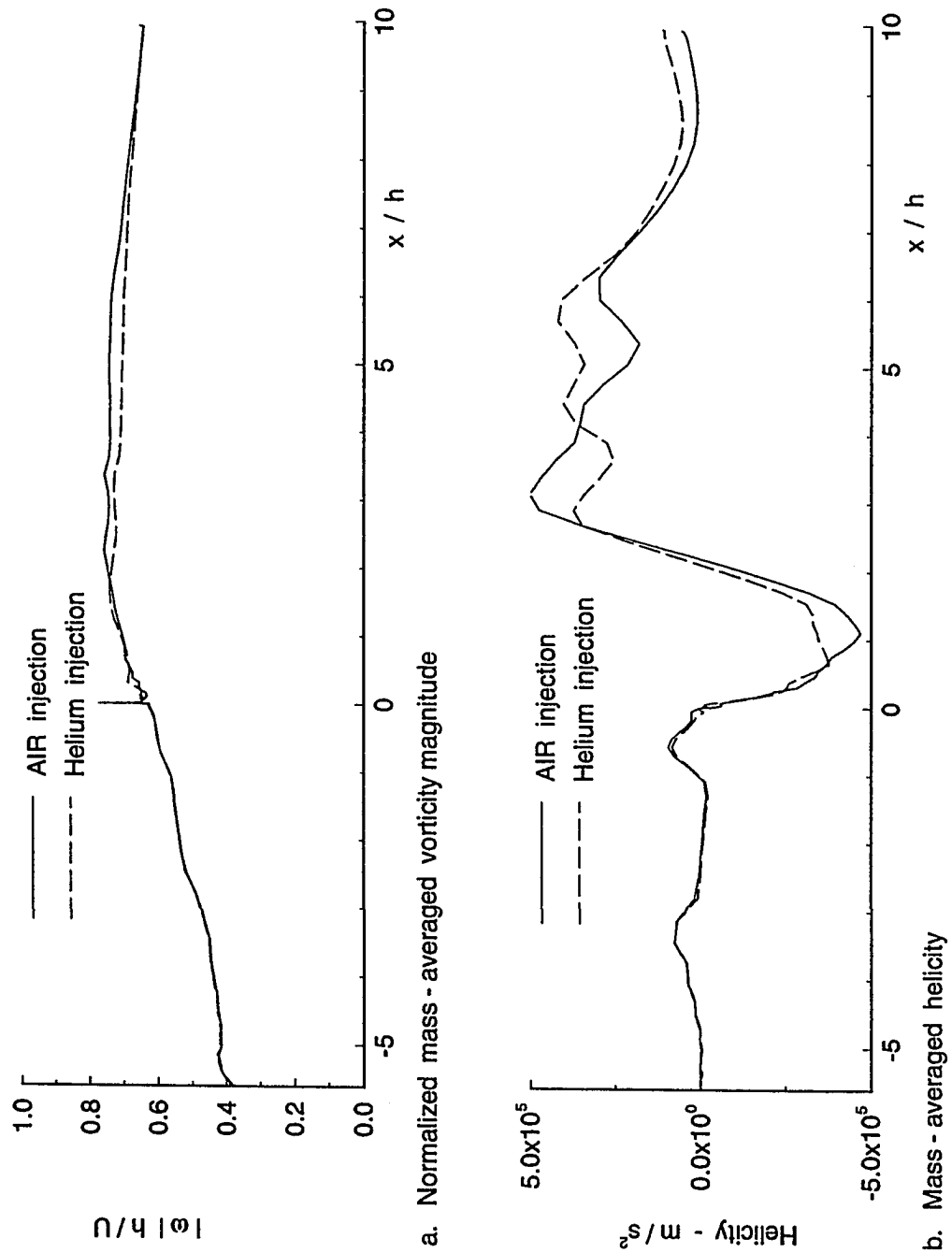


Fig. 5.59 Vorticity magnitude and helicity from numerical simulations

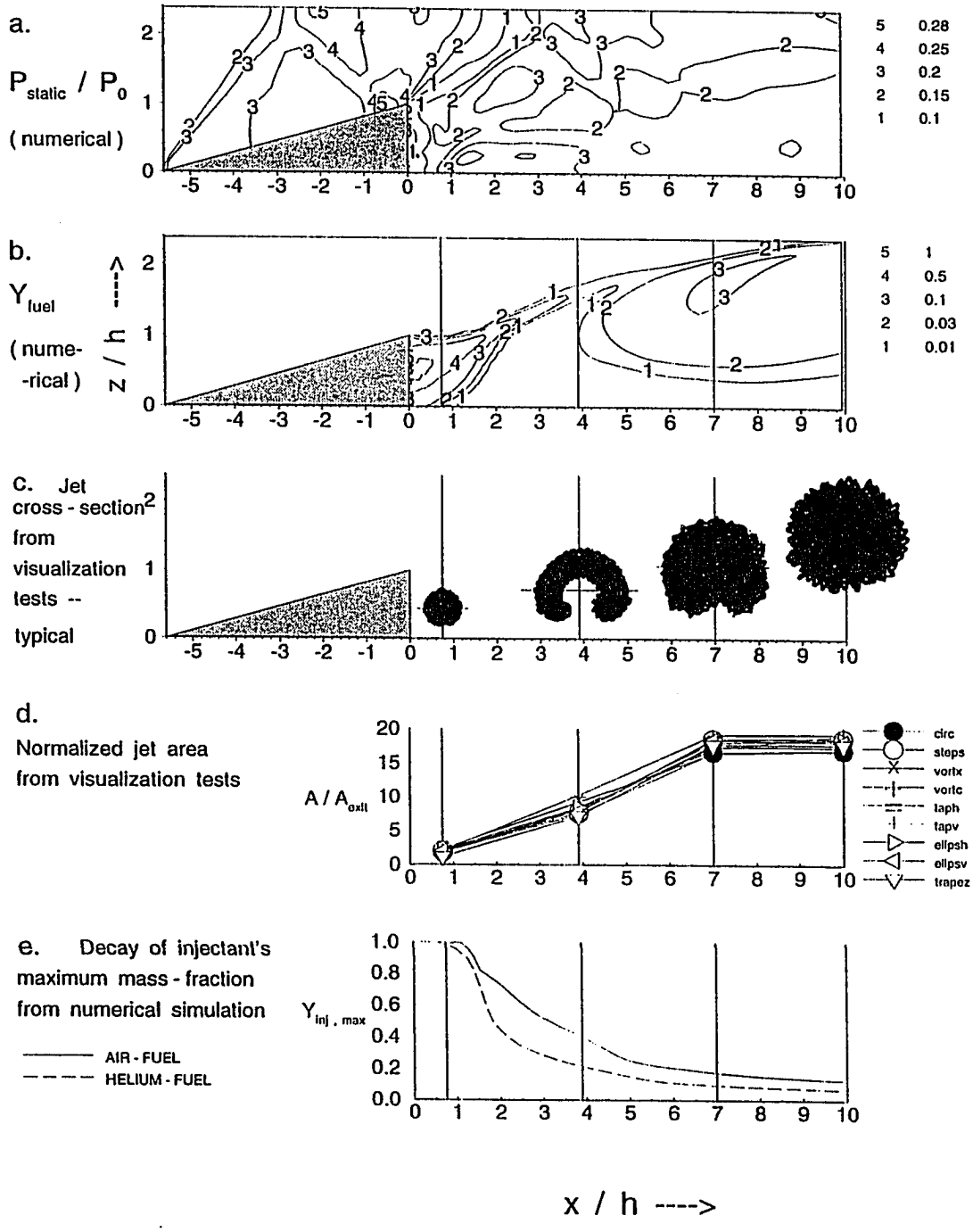


Fig. 5.60 The flow - field behavior

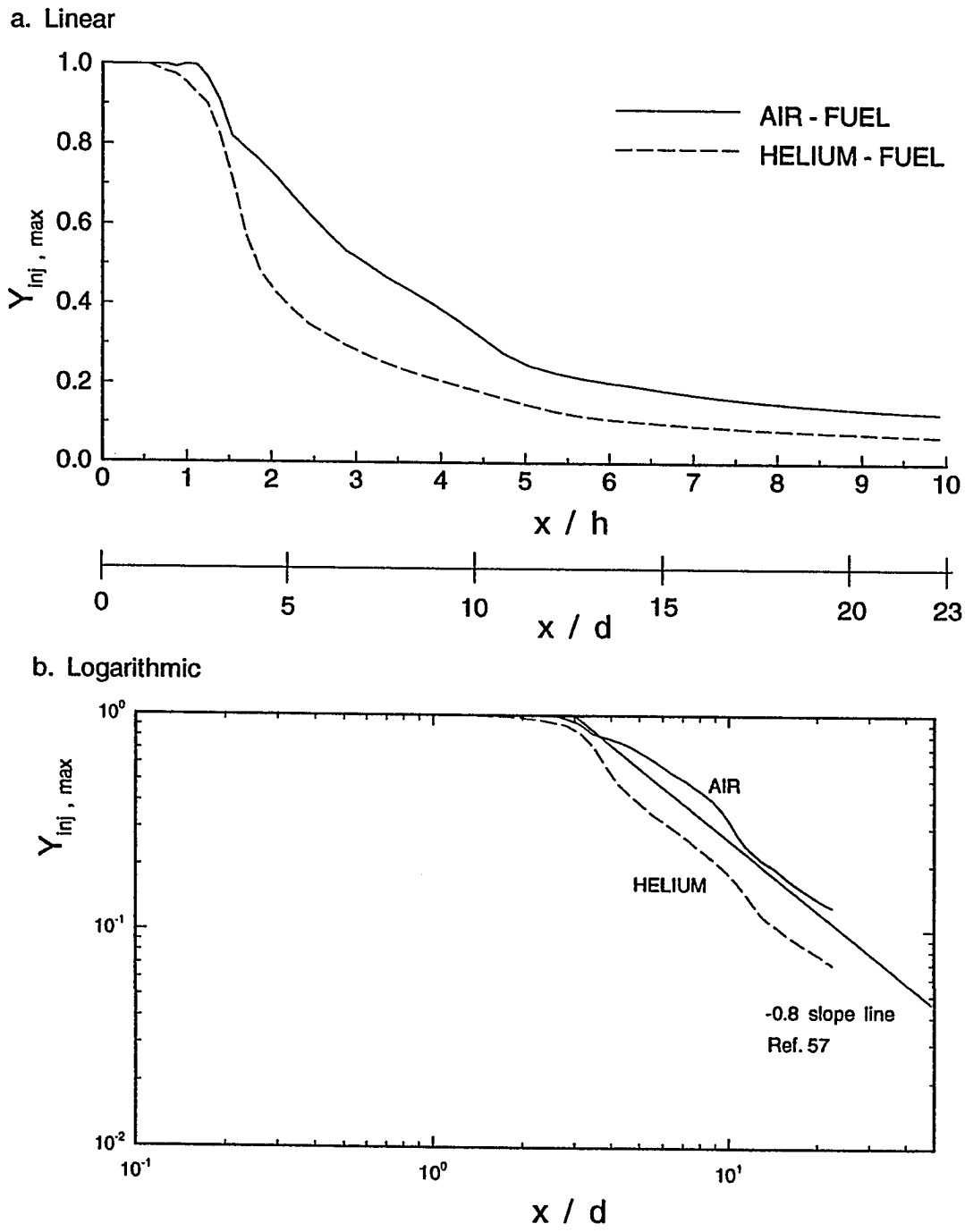


Fig. 5.61 Decay of injectant's mass - fraction from numerical simulations

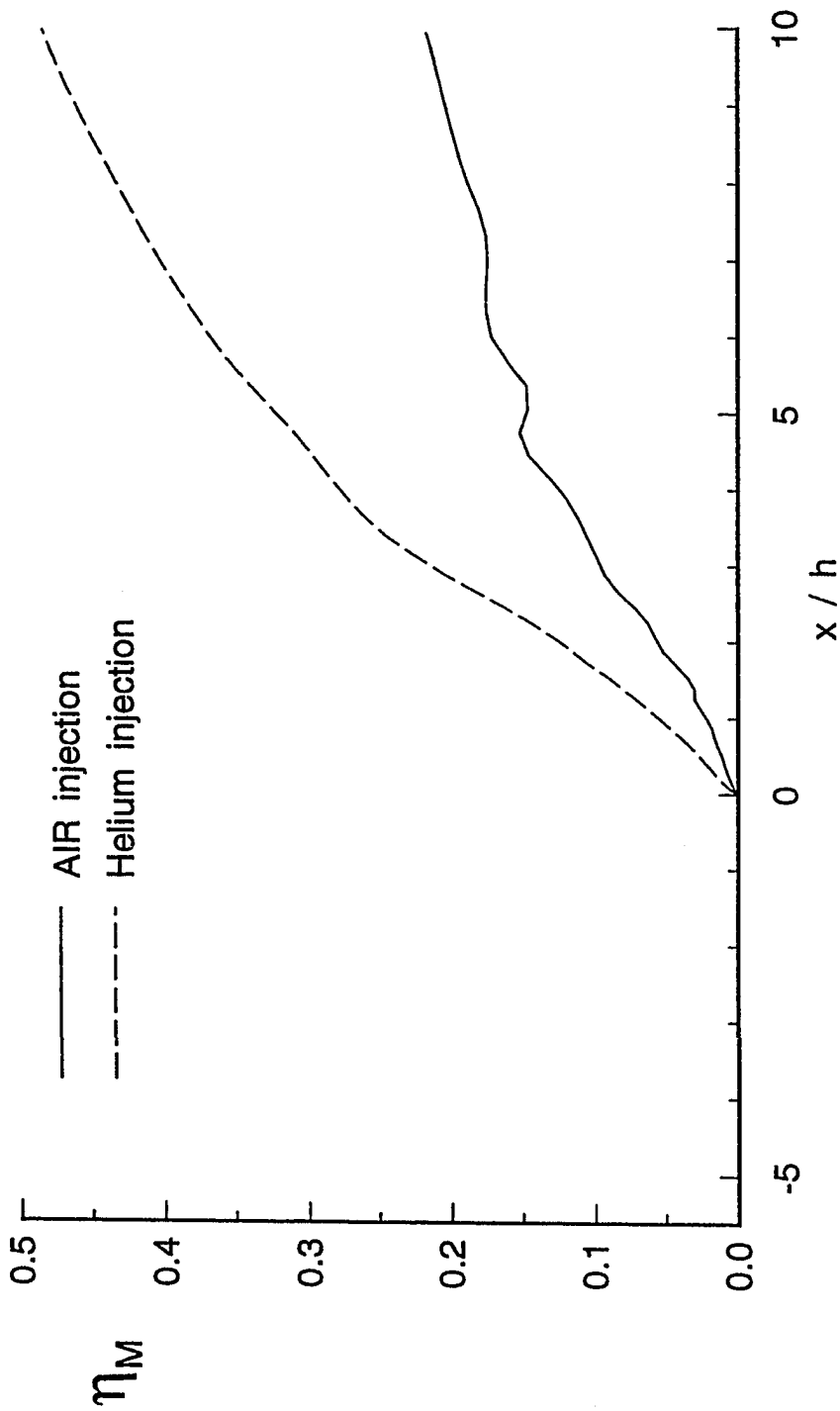


Fig. 5.62 Mixing efficiency from numerical simulations

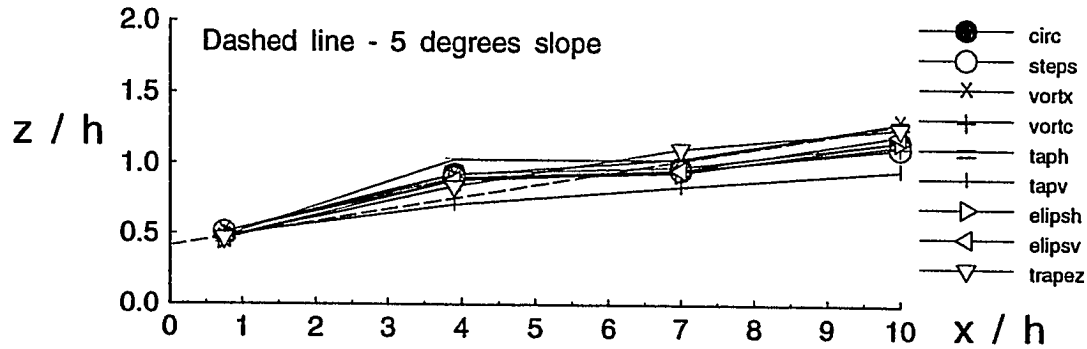


a. Injectant's cross-section area centroid z-coordinate from visualization tests

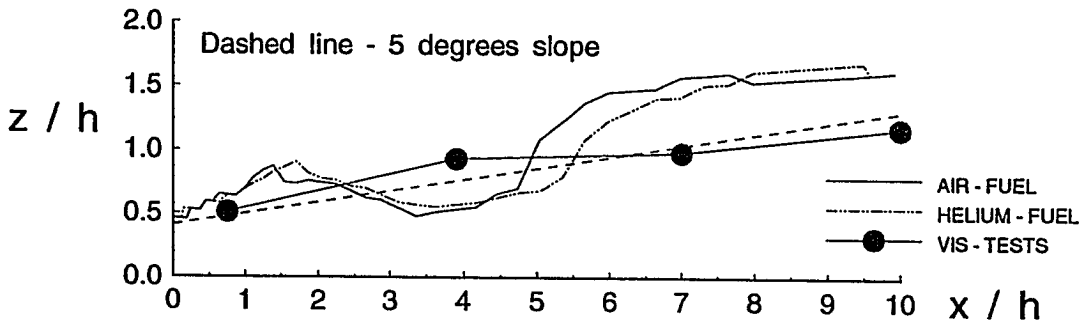


b. Injectant's maximum mass fraction z-coordinate from numerical simulation

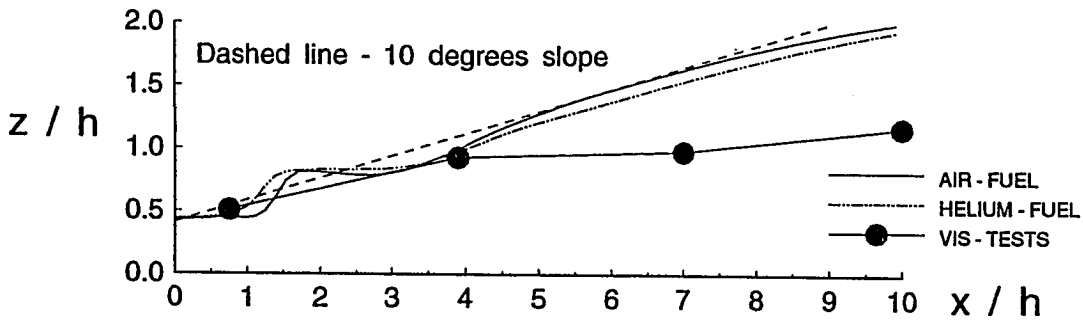


c. Injectant's mass centroid z-coordinate from numerical simulations

Fig. 5.63 Jet penetration

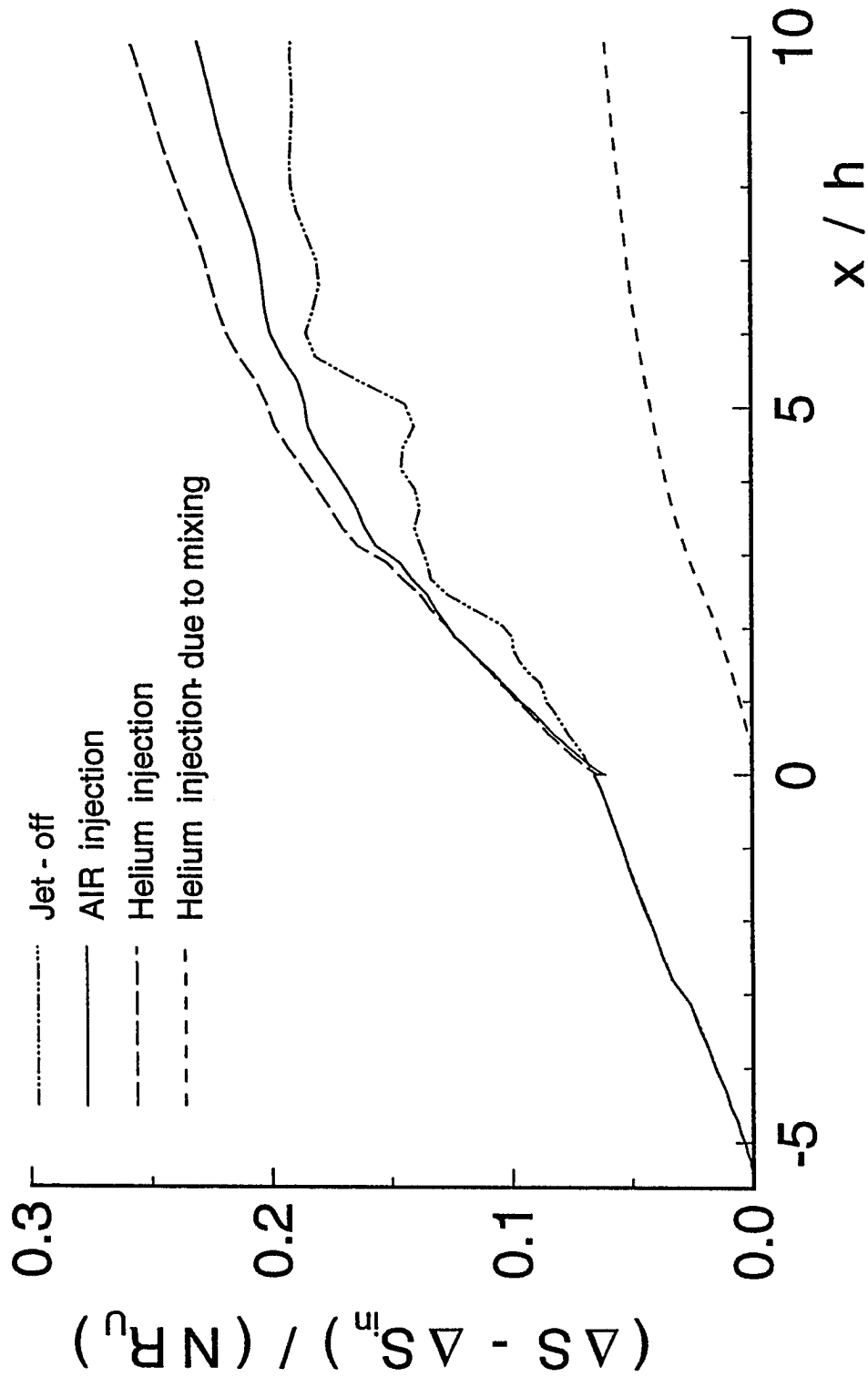


Fig. 5.64 Normalized mass - averaged entropy from numerical simulations

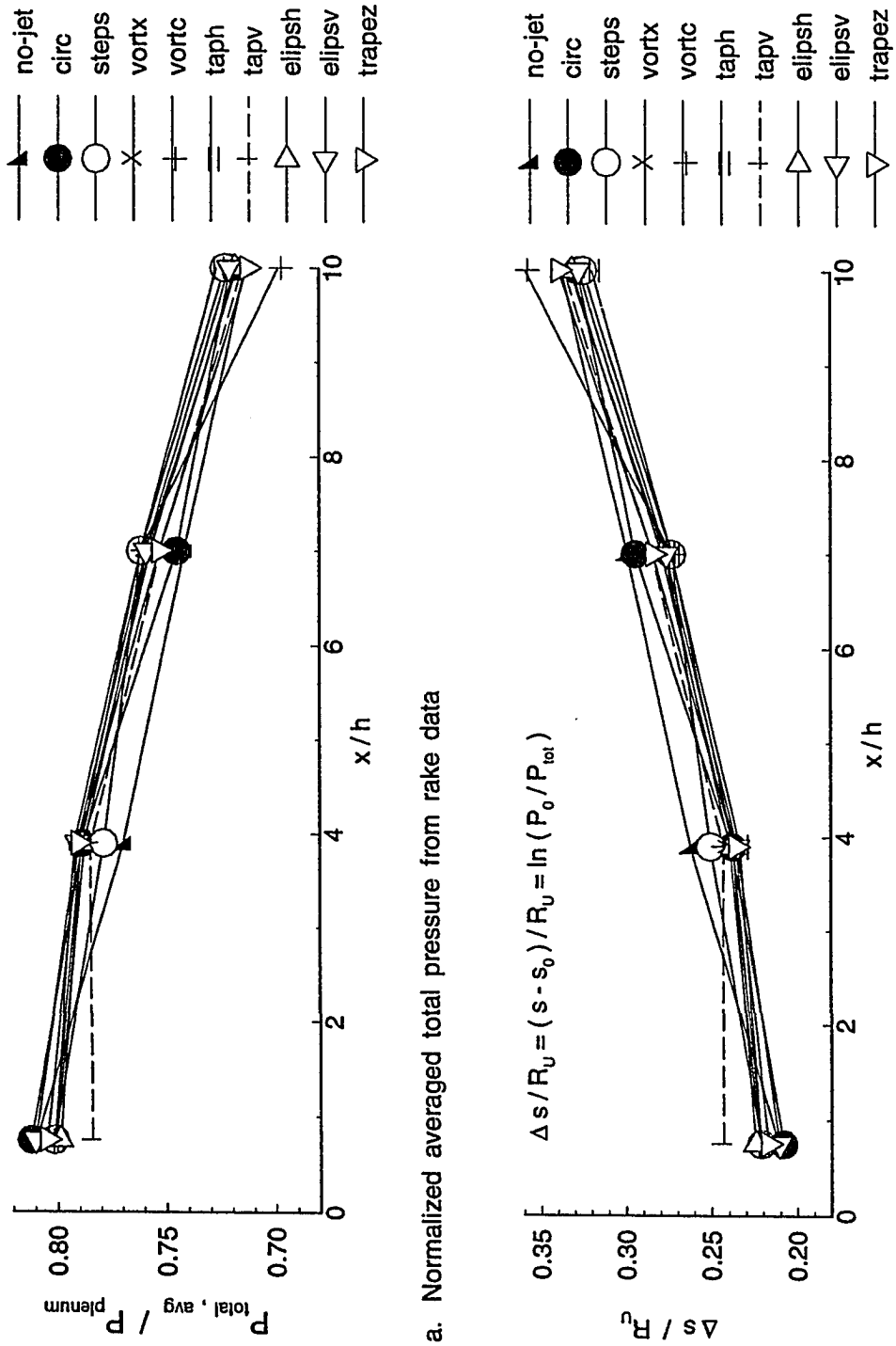


a. Normalized averaged total pressure from rake data

b. Increase in entropy from experimental data

Fig. 5.65 Calculated losses from experimental data

# Chapter 6

# CONCLUSIONS AND RECOMMENDATIONS

## 6.1 Summary

This study addressed the interaction between wall mounted swept-ramp fuel injector and injector nozzle configurations in a Mach two supersonic flow. The injector nozzles were designed to enable a constructive coupling between the injectant flow and the vortical flow generated by the ramp. Short combustor residence time, a requirement for fuel injection nearly-parallel to the main flow in the combustor, and an overall sensitivity of the vehicle performance to the propulsion system motivated the investigation. It follows previous studies on preconditioning free jet flows, and on contoured wall injectors based on the swept-ramp configuration. Injector performance was evaluated in terms of mixing, losses, and jet penetration. The investigation techniques included :

1. A planar Mie scattering technique for direct visualization of the mixed fluid between the supersonic main flow and the supersonic jet. This passive scalar method gives clear identification of the jet/mainstream interface in each of the

four visualized cross planes and in the side views. The method is simple and safe to use.

2. An image processing method which allows extraction of quantitatve information from the visualization images. This information, which is based on geometric properties – area, perimeter, compactness, and centroid – is used to characterize mixing and penetration and to compare the different injector inserts.

3. Twelve rake-mounted probes for flow field survey : four pitot pressure probes, four cone static pressure probes, and four total temperature probes. Given the measurements from these twelve probes, Mach number, density, and static temperatures were determined.

4. A three-dimensional Navier-Stokes code for solving the complex, three-dimensional flow field. Good agreement was observed between the experimental data and the calculations. The numerical simulation results complemented and clarified the experimental findings.

## 6.2 Conclusions

The following conclusions are supported by both experimental and computational results.

1. Six different nozzle inserts ( nine configurations ) were tested, and the results indicate that there is a coupling effect between the preconditioned jet flow and the vortical flow generated by the ramp. This coupling effect enhanced the near-field mixing. All the nozzle inserts demonstrated a better mixing performance relative to the baseline configuration ( the circular nozzle insert ), showing that

the coupling effect does enhance the mixing.

2. The major stirring occurs in the vicinity of the ramp base, $\overline{x} \leq 3.9$ ( $x/d \leq 8.8$ ), where the flow is dominated by the strong vortical flow field generated by the swept-ramp. Well downstream of the ramp base, $\overline{x} \geq 7$ ( $x/d \geq 16$ ), the quasi-axisymmetric flow pattern indicates a "loss of memory" of the near-field stirring. In this region, the flow appears to be controlled by small-scale turbulence. The transition between the vortex-driven mixing in the near-field to small-scale mixing in the far-field occurs in the region $8.8 < x/d < 16$, a behavior observed in other injection schemes too [ e.g. normal injection ].

3. Only minor differences were noticed among the various fuel nozzles, indicating that the injectant mixing well downstream of the injectors ( $\overline{x} \geq 7$ ) is nearly independent of fuel jet geometry, injectant molecular weight, and shear level or initial convective Mach number.

4. Side views of the jets in the vicinity of the ramp base suggest some streamwise large scale organization.

5. The mixing performance and the losses are mainly determined by the ramp, the injector geometry having little effect on total pressure loss.

6. The injectant penetrates the main flow at an average angle that equals the initial injection angle ( 10° ), suggesting that the penetration can be controlled by changing the injection angle.

7. Even though the differences were minor, at $\overline{x} = 10$ the jet from the nozzle with the vortex generators in cross orientation shows the largest perimeter length

together with the largest area and the largest compactness factor, indicating the best mixing characteristics in comparison with the other inserts.

8. Due to the increased lateral spreading, the tapered-slot nozzle with the vertical slot orientation, could not be accurately characterized because it spread out of the field of view. However, this nozzle appears to have a significant mixing potential. The jet from the tapered-slot nozzle with vertical slot throat spread laterally, and was captured by the two vortices generated by the ramp. These vortices further stretch the jet sidewise, almost splitting it into two separate jets. This behavior improves the near-field stirring by increasing the interface between the jet and the main flow.

9. The tapered-slot nozzle, together with the nozzle with vortex generators, are the two candidates recommended for further research.

To summarize, the main flow appears to be the dominant factor in this configuration, the coupling effect between the main flow and the preconditioned jet flow being weak, but showing some potential for enhancing the near-field mixing. The injector inner geometry proved to have secondary effects on the performance of the injection scheme. Therefore, conditioning of the main flow will have the highest impact on the combustor's performance, causing high losses. In order to keep the losses low, conditioning of the fuel should be used. Conditioning of the fuel and the coupling effect between the main flow and the fuel flow could enhance the near-field mixing, although the adverse pressure gradient in the combustor may alter the far-field mixing.

## 6.3 Recommendations and Suggestions for Further Work

This section presents recommendations and suggestions for future work based on both the limited scope of the current tests and the sparse database available from other investigations. The recommendations are based largely on knowledge derived from the time-mean investigation, performed with spatial resolution much larger than that required to determine molecular-scale mixing. As already mentioned, an important design parameter of the combustor is the length required for complete mixing of air and fuel at the molecular level. Mixing length is significant because the specific impulse produced by the combustor decreases and the scramjet engine installed weight increases as the distance for complete mixing increases. Because rapid and efficient mixing are essential for acceptable scramjet performance, improved mixing augmentation should be persued.

Because the vortical-flow field generated by the ramp is responsible for the main stirring in the near-field, jet mixing should be initiated in the shortest possible length. In the present study, a subsonic bubble was generated by the ramp base. The jet discharged into this bubble which isolated the jet from interacting with the vortical flow field. Only at $\bar{x} \approx 1.5$ does the jet start to interact with the surrounding flow. Reducing the base area, by making the jet exit area almost equal to the base area, will reduce this bubble resulting in a faster interaction between the jet and the surrounding flow.

Two injector inserts emerged as deserving further study : the insert with vortex generators in cross orientation and the tapered-slot insert with the vertical slot throat. The investigated nozzle with vortex generators had four rectangular tabs. The vortex

generator tab apparently acts as a "winglet" and produces a pair of trailing vortices which have the same sense of rotation as the trailing vortices originating from the sides of a wing. In order to increase the strength of these vortices, different shapes and sizes of tabs should be investigated, most likely to be in the form of delta wing with the base of the triangle attached to the nozzle circumference, and the apex leaning downstream or upstream ( see Fig. 6.1a ). The upstream leaning apex will generate vortices of opposite sign to the ones generated by the downstream leaning apex, and also will cause an outward bulge in the jet cross section instead an inward indentation, like in the downstream case. Apparently, the shape of the cross-section of the jet, and the vorticity distribution within the injectant can be controlled by a proper number, shape, angle of attack, and size of the tabs. The jet should be distorted in such a manner that it would be captured by the pair of ramp-generated vortices very close to the injection port.

For the tapered-slot nozzle, different aspect ratios of the slot should be investigated to ensure the most favorable interaction between the jet and the vortical flow field. The most favorable interaction would be the splitting of the jet into two separate smaller jets immediately downstream of the injection port. Based on the conclusion that the injectant should be captured and split by the pair of vortices in order to improve the near-field stirring, an alternate design emerges. In this design, two separate jets would be injected at the ramp base as seen in Fig. 6.1b. They can be slightly inclined sidewise too, to improve the transverse penetration towards the ramp-generated vortices. Each injectant could be preconditioned by applying swirl of the same rotation as the ramp-generated vortices. This treatment will strengthen the axial vorticity in the flow field improving the near-field stirring.

There are also practical difficulties associated with manufacturing and operating injectors in extremely high enthalpy flows such as within a scramjet combustor. From the three inserts mentioned above, the tapered-slot nozzle is the easiest to manufacture. From the operational point of view the nozzle with vortex generators is the worst because its performance depends on tab geometry, the effectiveness of which is questionable, over long periods of time in such a harsh environment.

The influence of the boundary layer thickness and the turbulence intensity remain unresolved as it is extremely difficult to make such measurements in compressible flows with adequate spatial resolution and accuracy. It is felt that further studies are required to evaluate these two effects on the mixing performance.

## 6.4 Closure

The present study demonstrated that there is a coupling effect between the preconditioned jet flow and the vortical flow generated by the ramp, the preconditioning of the fuel jet having secondary effect on the global mixing performance. This coupling effect, and the consequent mixing can be enhanced by properly designed fuel injectors.

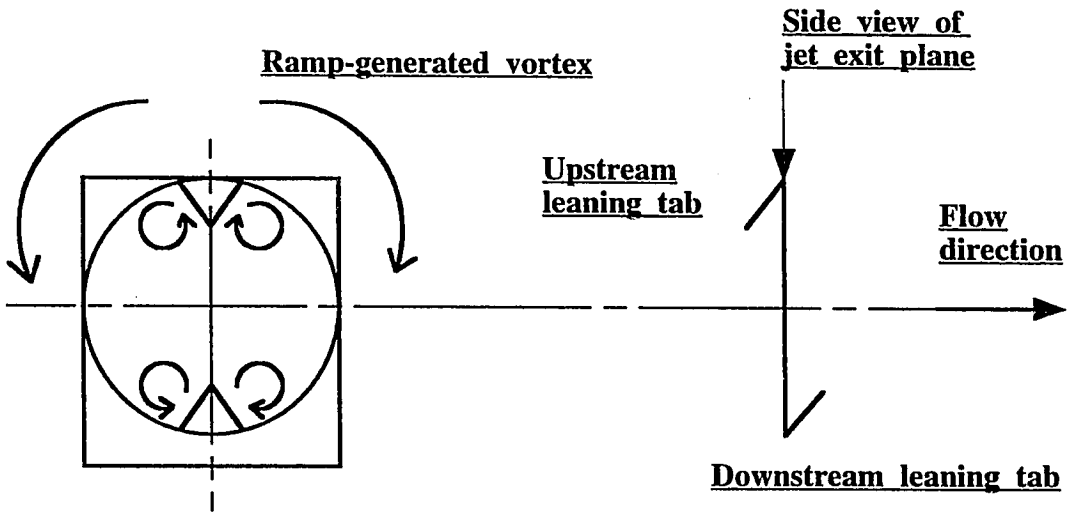


a. Injector nozzle with vortex generators ( delta tabs )

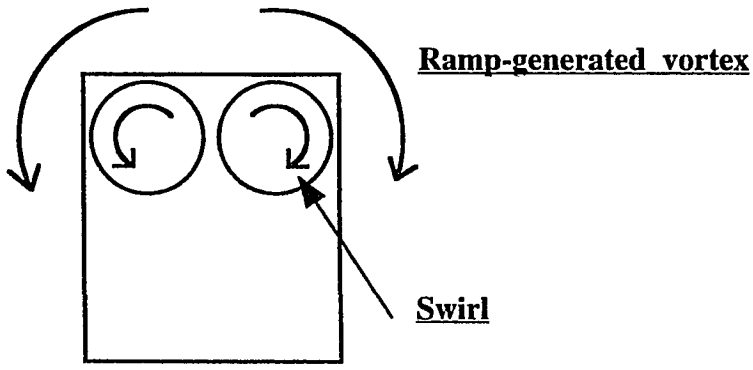


b. Double injector with swirl

**Fig. 6.1 Suggestions for further studies**

# REFERENCES


[1] Heiser, W. H., and Pratt, D. T. with Daley, D. H., and Mehta, U. B., "Hypersonic Airbreathing Propulsion," *AIAA Education Series*, AIAA, Inc., 370 L'Enfant Promenade SW, Washington, DC 20024-2518, 1991, pp. 14–16.

[2] Billig, F. S.,"Research on Supersonic Combustion," AIAA Paper 92-0001, January 1992.

[3] Papamoschou, D., and Roshko, A., "The Compressible Turbulent Shear Layer: an Experimental Study," *Journal of Fluid Mechanics*, Vol. 197, 1988, pp. 453–477.

[4] Elliot, G., and Samimy, M., "Compressibility Effects in Free Shear Layers," AIAA Paper 90-0705, January 1990.

[5] Brown, G. L., and Roshko, A., "On Density Effects and Large Structure in Turbulent Mixing Layers," *Journal of Fluid Mechanics*, Vol. 64, part 4, 1974, pp. 775–816.

[6] Bogdanoff, D. W., "Compressible effects in Turbulent Shear Layers," *AIAA Journal*, Vol.21, No. 6, 1983, pp. 926–927.

[7] Papamoschou, D., "Structure of the Compressible Turbulent Shear Layer," *AIAA Journal*, Vol. 29, No. 5, 1991, pp. 680–681.

[8] McIntyre, S. S., and Settles, G. S., "Optical Experiments on Axisymmetric Compressible Turbulent Mixing Layers," AIAA Paper 91-0623, January 1991.

[9] Goebel, S. G., and Dutton, C. J., "Experimental Study of Compressible Turbulent Mixing Layers," *AIAA Journal*, Vol. 29, No. 4, 1991, pp. 538–546.

[10] Gruber, R. M., Messersmith, N. L., and Dutton, C. J., "Three-Dimensional Velocity Measurements in a Turbulent, Compressible Mixing Layer," AIAA Paper 92-3544, July 1992.

[11] Ragab, S. A., and Wu, J. L., "Instabilities in the Free Shear Layer Formed by Two Supersonic Streams," AIAA Paper 88-0038, January 1988.

[12] Sandham, N. D., and Reynolds, W. C., "Three-Dimensional Simulations of Large Eddies in the Compressible Mixing Layer," *Journal of Fluid Mechanics*, Vol. 224, 1991, pp. 133–158.

[13] Fourguette, D., and Dibble, R. , "Time Evolution of the Shear Layer of a Supersonic Axisymmetric Jet at Matched Conditions," AIAA Paper 90-0508, January 1990.

[14] Nixon, D., Keefe, L. R., and Kuhn, G. D., "The Effects of Compressibility on a Supersonic Mixing Layer," AIAA Paper 90-0706, January 1990.

[15] Dimotakis, P. E., "On the Convection Velocity of Turbulent Structures in Supersonic Shear Layers," AIAA Paper 91-1724, June 1991.

[16] Zeman, O., "Dilatation Dissipation : The Concept and Application in Modeling Compressible Mixing Layers," *Physics of Fluids A : Fluid Dynamics*, Vol. A2, 1990, pp. 178–188.

[17] Zeman, O., "Similarity in Supersonic Mixing Layers," *AIAA Journal*, Vol. 30, No.5, 1992, pp. 1277–1283.

[18] Elliot, G., and Samimy, M., "Pressure Based Real-Time Measurements in Compressible Free Shear Layers," AIAA Paper 90-1980, July 1990.

[19] Elliot, G., and Samimy, M., "Compressibility Effects in Free Shear Layers," *Physics of Fluids A*, Vol. 2, No. 7, 1990, pp. 1231–1240.

[20] Hall, J. L., Dimotakis, P. E., and Rosemann, H., "Some Measurements of Molecular Mixing in Compressible Turbulent Shear Layers," AIAA Paper 91-1719, June 1991.

[21] Clemens, N. T., Paul, P. H., Mungal, M. G., and Hanson, R. K., "Scalar Mixing in the Supersonic Shear Layer," AIAA Paper 91-1720, June 1991.

[22] Northam, G. B., Greenberg, I., and Byington, C. S., "Evaluation of Parallel Injector Configurations for Supersonic Combustion," AIAA Paper 89-2525, July 1989.

[23] Northam, G. B., Capriotti, D. P., Byington, C. S., and Greenberg, I., "Mach 2 and Mach 3 Mixing and Combustion in Scramjets," AIAA Paper 91-2394, June 1991.

[24] Riggins, D. W., Mekkes, G. L., McClinton, C. R., and Drummond, J. P., "A Numerical Study of Mixing Enhancement in a Supersonic Combustor," AIAA Paper 90-0203, January 1990.

[25] Riggins, D. W., and McClinton, C. R., "A Computational Investigation of Flow Losses in a Supersonic Combustor," AIAA Paper 90-2093, July 1990.

[26] Riggins, D. W., and McClinton, C. R., "Analysis of Losses in Supersonic Mixing and Reacting Flows," AIAA Paper 91-2266, June 1991.

[27] Davis, D. O., and Hingst, W. R., "Progress Towards Synergistic Hypermixing Nozzles," AIAA Paper 91-2264, June 1991.

[28] Hartfield, R. J., Jr., Hollo, S. D., and McDaniel, J. C., "Experimental Investigation of a Supersonic Swept Ramp Injector Using Laser Induced Iodine Fluorescence," AIAA Paper 90-1518, June 1990.

[29] Donohue, J. M., Haj-Hariri, H., and McDaniel, J. C., "Vorticity Generation Mechanisms in Parallel Injection Schemes for Supersonic mixing," AIAA Paper 92-3286, July 1992.

[30] Donohue, J. M., McDaniel, J. C., and Haj-Hariri, H., "Experimental and Numerical Study of Swept Ramp Injection into a Supersonic Flowfield," AIAA Paper 93-2445, June 1993.

[31] Marble, F. E., "Investigations into Shock-Induced Enhancement of Mixing and Combustion in Supersonic Burners," AD-A231750, California Institute of Technology, Pasadena, CA 91125, 1991.

[32] Waitz, I. A., "An Investigation of Contoured Wall Injectors for Hypervelocity Mixing Augmentation," Ph.D. Thesis, California Institute of Technology, Pasadena, CA, 1991.

[33] Waitz, I. A., Marble, F. E., and Zukoski, E. E., "A Systematic Experimental and Computational Investigation of a Class of Contoured Wall Fuel Injectors," AIAA Paper 92-0625, January 1992.

[34] Waitz, I. A., Marble, F. E., and Zukoski, E. E., "Vorticity Generation by Contoured Wall Injectors," AIAA Paper 92-3550, July 1992.

[35] Gutmark, E., Schadow, K. C., and Wilson, K. J., "Noncircular Jet Dynamics in Supersonic Combustion," *Journal of Propulsion*, Vol. 5, No. 5, 1989, pp. 529–533.

[36] Gutmark, E., Schadow, K. C., and Wilson, K. J., "Subsonic and Supersonic Combustion Using Noncircular Injectors," *Journal of Propulsion*, Vol. 7, No. 2, 1991, pp. 240–249.

[37] Schadow, K. C., Gutmark, E., Parr, T. P., Parr, D. M., and Wilson, K. J., "Enhancement of Fine Scale Mixing for Fuel Rich Plume Combustion," AIAA Paper 87-0376, January 1987.

[38] Samimy, M., Reeder, M., and Zaman, K. B. M. Q., "Supersonic Jet Mixing Enhancement by Vortex Generations," AIAA Paper 91-2263, June 1991.

[39] Samimy, M., Zaman, K. B. M. Q., and Reeder, M., "Effect of Tabs on the Flow and Noise Field of an Axisymmetric Jet," *AIAA Journal*, Vol. 31, No. 4, 1993, pp. 609–619.

[40] Zaman, K. B. M. Q., Reeder, M. F., and Samimy, M., "Supersonic Jet Mixing Enhancement by "Delta-Tabs"," AIAA Paper 92-3548, July 1992.

[41] Yu, K., Kraeutle, K., Wilson, K., Parr, T., Smith, R., Gutmark, E., and Schadow, K., "Supersonic Flow Mixing and Combustion Using Ramp Nozzle," AIAA Paper 92-3840, July 1992.

[42] Gutmark, E., Bowman, H. L., and Schadow, K. C., "Flow and Acoustic Features of a Supersonic Tapered Nozzle," *Experiments in Fluids*, 13, 1992, pp. 49–55.

[43] Swithenbank, J., and Chigier, N. A., "Vortex Mixing for Supersonic Combustion," *Proceedings of 12th International Symposium on Combustion*, Poitiers, France, July 14-20, 1968, Combustion Institute, Pittsburgh, PA, 1969, pp. 1152–1162.

[44] Settles, G. S., "Supersonic Mixing Enhancement by Vorticity for High Speed Propulsion," NASA-CR 188 920, October 1991.

[45] Cutler, A. D., and Levey, B. S., "Vortex Breakdown in a Supersonic Jet," AIAA Paper 91-1815, June 1991.

[46] Cutler, A. D., Levey, B. S., and Kraus, D. K., "An Experimental Investigation of Supersonic Swirling Jets," AIAA Paper 93-2922, July 1993.

[47] Kraus, D. K., "An Experimental Investigation of Mixing Enhancement in a Simulated Scramjet Combustor by Use of Swirling Jets," Master of Science Thesis, The School of Engineering and Applied Science of the George Washington University, 1993.

[48] Mays, R. B., Thomas, R. H., and Schetz, J. A., "Low Angle Injection Into a Supersonic Flow," AIAA Paper 89-2461, July 1989.

[49] Fuller, E. J., Mays, R. B., Thomas, R. H., and Schetz, J. A., "Mixing Studies of Helium in Air at Mach 6," AIAA Paper 91-2268, June 1991.

[50] Cox, S. K., Fuller, R. P., Schetz, J. A., and Walters, R. W., "Vortical Interactions Generated by an Injector Array to Enhance Mixing in Supersonic Flow," AIAA Paper 94-0708, January 1994.

[51] Aso, S., Okuyama, S., Kawai, M. and Ando, Y.,"Experimental Study on Mixing Phenomena in Supersonic Flows with Slot Injection," AIAA Paper 91-0016, January 1991.

[52] Hollo, S. D., McDaniel J. C., and Hartfield, R. J., Jr., "Quantitative Investigation of Compressible Mixing : Staged Transverse Injection into Mach 2 Flow," *AIAA Journal*, Vol. 32, No. 3, 1994, pp. 528–534.

[53] Li, C., Kailasanath, K., and Book, D. L., "Mixing Enhancement Due to Pressure and Density Gradients Generated by Expansion Waves in Supersonic Flows," AIAA Paper 91-0374, January 1991.

[54] Domel, N. D., and Thompson, D. S., "A Two Dimensional Numerical Simulation of Shock Enhanced Mixing in a Rectangular Scramjet Flowfield with Parallel Hydrogen Injection," AIAA Paper 91-0377, January 1991.

[55] Clemens, N. T., and Mungal, M. G., "Effects of Sidewall Disturbances on the Supersonic Mixing Layer," *Journal of Propulsion*, Vol. 8, No. 1, 1992, pp. 249–251.

[56] Kumar, A., Bushnell, D. M., and Hussaini, M. Y., "Mixing Augmentation Technique for Hypervelocity Scramjets," *Journal of Propulsion*, Vol. 5, No. 5, 1989, pp. 514–522.

[57] Thomas, R. H., Schetz, J. A., and Billig, F. S., "Gaseous Injection in High Speed Flow," *Ninth International Symposium on Air Breathing Engines*, Athens, Greece, September 3–8, 1989, AIAA Paper 90-17446.

[58] Swithenbank, J., Eames, I., Chin, S., Ewan, B., Yang, Z., Cao, J., and Zhao, X., "Turbulent Mixing in Supersonic Combustion Systems," AIAA Paper 89-0260, January 1989.

[59] Mungal, M. G., and Frieler, C. E., "The Effects of Damköhler Number in a Turbulent Shear Layer," *Combustion and Flame*, 71, 1988, pp. 23–34.

[60] Menon, S., and Fernando, E. M., "A Numerical Study of Mixing and Chemical Heat Release in Supersonic Mixing Layers," AIAA Paper 90-0152, January 1990.

[61] Sekar, B., and Mukunda, H. S., "A Computational Study of Direct Simulation of High Speed Mixing Layers without and with Chemical Heat Release," *Proceedings of 23rd International Symposium on Combustion*, Orleans, France, July 22–27, 1990, Combustion Institute, Pittsburgh, PA, 1991, pp. 707–713.

[62] Planche, O. H., and Reynolds, W. C., "Heat Release Effects on Mixing in Supersonic Reacting Free Shear Layers," AIAA Paper 92-0092, January 1992.

[63] Vuillermoz, P., Oran, E. S., and Kailasanath, K., "Effect of Damköhler Number on a Supersonic Reactive Mixing Layer," AIAA Paper 92-0337, January 1992.

[64] *Hewlett Packard 3497A Data Acquisition/ Control Unit : Operating, programming and configuration manual*, Manual No. 03497-90019, Hewlett-Packard Company, P.O.Box 301, Loveland, Colorado 80537, USA, 1982.

[65] *Omega : The Temperature Handbook*, Omega, One Omega Drive, Box 4047, Stamford, CT 06907, USA, 1993.

[66] *Quantel International, YG 580 Series, SF Version, Actively Q-Switched Nd:YAG Laser*, QIOM 110, Quantel International, 3150 Central Expressway, Santa Clara, CA 95051, USA, June 1983, Rev 9/88.

[67] *Photometrics - AT200 CCD Camera System, Hardware Reference Manual, 570075 rev A, and PMIS Image Processing Software User's Manual, 570074 ver 1.5*, Photometrics Ltd., 3440 East Britannia Drive, Tucson, Arizona 85706, USA, 1992.

[68] *TransEra : HTBasic, User's guide, Manual No. HMAN/U, Fifth revision, and Reference manual, Manual No. HMAN/R, Fifth revision*, TransEra Corporation, Provo, Utah, USA, 1990.

[69] *Compumotor Plus User Guide, Indexer/Drive Version*, p/n 88-007488-02 D, Compumotor Division, Parker Hannifin Corporation, 1989.

[70] Wegener, P. P., Clumpner, J. A., and Wu, B. J. C., "Homogeneous Nucleation and Growth of Ethanol Drops in Supersonic Flow," *The Physics of Fluids*, Vol. 15, No. 11, 1972, pp. 1869–1876.

[71] Hirleman, E. Dan, "Nonintrusive Laser-Based Particle Diagnostics," *Combustion Diagnostic by Nonintrusive Methods*, Edited by McCay, T. D., and Roux, J. A., Volume 92, Progress in Astronautics and Aeronautics, AIAA, New York, 1984, pp. 177–207.

[72] Eckbreth, A. C., "Laser Diagnostics for Combustion Temperature and Species," *Energy and Engineering Science Series*, Vol. 7, Abacus Press, Kent, UK, 1988, pp. 209–210.

[73] Wegener, P. P., and Stein, G. D., "Light Scattering Experiments and Theory of Homogeneous Nucleation in Condensing Supersonic Flow," *Proceedings of 12th International Symposium on Combustion*, Poitiers, France, July 14–20, 1968, Combustion Institute, Pittsburgh, PA, 1969, pp. 1183–1191.

[74] Shirinzadeh, B., Hillard, M. E., and Exton, J. R., "Condensation Effects on Rayleigh Scattering Measurements in a Supersonic Wind Tunnel," *AIAA Journal*, Vol. 29, No.2, 1991, pp. 242–246.

[75] Siegel, R., and Howell, J. R., *Thermal Radiation Heat Transfer*, Third edition, Hemisphere Publishing Corporation, 1992, pp. 578–581.

[76] McCartney, E. J., *Optics of the Atmosphere, Scattering by Molecules and Particles*, John Wiley and Sons, New-York, 1976, pp. 176–191.

[77] Clemens, N. T., and Mungal, M. G., "A Planar MIE Scattering Technique for Visualizing Supersonic Mixing Flows," *Experiments in Fluids*, Vol. 11, 1991, pp. 175–185.

[78] Fernando, E. M., and Menon, S., "Mixing Enhancement in Compressible Mixing Layers : An Experimental Study," *AIAA Journal*, Vol. 31, No. 2, 1993, pp. 278–285.

[79] Shirinzadeh, B., Jeffrey Balla, R., Hillard, M. E., Anders, J. B., Exton, J. R., and Waitz, I. A., "Study of Rayleigh Scattering for Visualization of Helium-Air Mixing at Mach 6," *International Congress on Instrumentation in Aerospace Simulation Facilities*, Rockville, Maryland, USA, October 27-31, 1991, IEEE Publication 91CH3028-8, pp. 246–253.

[80] Squires, K. D., and Eaton, J. K., "Particle Response and Turbulence Modification in Isotropic Turbulence," *Physics of Fluids A* Vol. 2, No. 7, 1990, pp. 1191–1203.

[81] Clumpner, J. A., "Light Scattering from Ethyl Alcohol Droplets Formed by Homogeneous Nucleation," *The Journal of Chemical Physics*, Vol. 55, No. 10, 1971, pp. 5042–5045.

[82] Samimy, M., and Lele, S. K., "Particle-Laden Compressible Free Shear Layers," AIAA Paper 90-1977, July 1990.

[83] Melling, A., "Seeding Gas Flows for Laser Anemometry," AGARD-CP-399, 1986, pp. 8.1–8.11.

[84] White, F. M., *Viscous Fluid Flow*, McGraw-Hill Inc., New-York, 1991, pp. 27–32.

[85] Dowling, D. R., and Dimotakis, P. E., "Similarity of the Concentration Field of Gas-phase Turbulent Jets," *Journal of Fluid Mechanics*, Vol. 218, 1990, pp. 109–142.

[86] Bird, R.B., Stewart, W.E., and Lightfoot, E.N., *Transport Phenomena*, John Wiley and sons Inc., New York, 1960, pp. 19–25 and pp. 510–512.

[87] Rosensweig, R. E., Hottel, H. C., Williams, G. C., "Smoke Scattered Light Measurements of Turbulent Concentration Fluctuations," *Chemical Engineering Science*, 15, 1961, pp. 111–129.

[88] Fuchs, N. A., *The Mechanics of Aerosols*, Pergamon Press, New-York, 1964, pp. 288–294.

[89] Hidy, G. M., and Brock, J. R., *The Dynamics of Aerocolloidal Systems*, Pergamon Press, Oxford, 1970, pp. 319–324.

[90] Buil, C., *CCD Astronomy, Construction and Use of an Astronomical CCD Camera*, Willmann-Bell, Inc., P.O.Box 35025, Richmond, Virginia 23235, 1991.

[91] Baldwin, B. S., and Lomax, H.,"Thin Layer Approximation and Algebraic Model for Separated Turbulent Flows," AIAA Paper 78-257, January 1978.

[92] Eklund, D. R., Northam, G. B., and Fletcher, D. G., "A Validation Study of the SPARK Navier-Stokes Code for Nonreacting Scramjet Combustor Flow Fields," AIAA Paper 90-2360, July 1990.

[93] Eggers, J. M., "Turbulent Mixing of Coaxial Compressible Hydrogen-Air Jets," NASA TN D-6487, 1971.

[94] Drummond, J. P., "Mixing Enhancement of Reacting Parallel Fuel Jets in a Supersonic Combustor," AIAA Paper 91-1914, June 1991.

[95] Eklund, D. R., and Stouffer, D. S., "A Numerical and Experimental Study of a Supersonic Combustor Employing Swept Ramp Fuel Injectors," AIAA Paper 94-2819, June 1994.

[96] McBride, B. J., Heimel, S., Ehlers, J. G., and Gordon S., "Thermodynamic Properties to 6000 K for 210 Substances Involving the First 18 Elements," NASA SP-3001, 1963.

[97] Suehla, R. A., "Estimated Viscosities and Thermal Conductivities of Gases at High Temperatures," NASA-TR R-132, 1962.

[98] Arp, V.D., and McCarty R.D., "Thermophysical Properties of Helium-4 from 0.8 to 1500 K with Pressures to 2000 MPa," NIST Technical Note 1334, NASA CR-186992, 1989.

[99] Drummond, J. P., Rogers, R. C., and Hussaini, M. Y., "A Detailed Numerical Model of a Supersonic Reacting Mixing Layer," AIAA Paper 86-1427, June 1986.

[100] Drummond, J. P., and Hussaini, M. Y., "Numerical Simulation of a Supersonic Reacting Mixing Layer," AIAA Paper 87-1325, June 1987.

[101] Carpenter, M.H., "Three-Dimensional Computations of Cross-Flow Injection and Combustion in a Supersonic Flow," AIAA Paper 89-1870, June 1989.

[102] Chitsomboon, T., Northam, G. B., Rogers R. C., and Diskin, G. S., "CFD Prediction of the Reacting Flowfield Inside a Subscale Scramjet Combustor," AIAA Paper 88-3259, July 1988.

[103] Anderson, D. A., Tannehill, J. C., and Pletcher, R. H., *Computational Fluid Mechanics and Heat Transfer,* Hemisphere Publishing Corp., McGraw-Hill, New York, 1984, pp. 247–251.

[104] Shapiro, A. H., *The Dynamics and Thermodynamics of Compressible Fluid Flow,* The Ronald Press Company, New-York, 1954, pp. 153–154 and pp. 653–654.

[105] Sims, J. L., "Tables for Supersonic Flow Around Right Circular Cones at Zero Angle of Attack," NASA-SP-3004, 1964.

[106] Sims, J. L., "Tables for Supersonic Flow of Helium Around Right Circular Cones at Zero Angle of Attack," NASA-SP-3078, 1973.

[107] *Tecplot Version 6 User's Manual,* Amtec Engineering, Inc., P.O.Box 3633, Bellevue, WA 98009-3633, USA, 1993.

[108] *PV-WAVE 4.0, Command Language Reference and Command Language User's Guide,* Precision Visuals, Inc., Boulder, Colorado, USA, 1992.

[109] *The KBVision System, Tutorial, Programmer's Reference, and Users's Guide,* Release 2.5.2, Amerinex Artificial Intelligence Inc., 409 Main Street, Amherst, MA 01002, USA, February 1993.

[110] Leonard, D. M., "Analysis of Objects in Binary Images," NASA Contractor Report 4420, Contract NAS1-19038, December 1991.

# VITA

Yaacov Haimovitch is a graduate of the Technion – Israel Institute of Technology, in Haifa, Israel, where he got his B.Sc. ( 1979 ) and M.Sc. ( 1981 ) degrees, both in Aeronautical Engineering. Since then he worked as a research scientist in rocket propulsion, thermal protecting systems and gas dynamics. His expertise includes computational ( CFD ) as well as experimental methods. In 1991 he came to NASA Langley Research Center, Fluid Mechanics Division, Experimental Methods Branch, to perform the research for his doctoral studies. He is a member of the Israeli Aeronautics and Astronautics Society, a senior member of AIAA, and a member of the Phi Kappa Phi society. He has published a number of papers in journals and proceedings of international conferences.